PART I. EXPERIMENTAL AND THEORETICAL STUDIES ON HETEROGENEOUS DIFFUSION FLAMES

PART II. SPECTROSCOPIC STUDIES OF FLAMES

Thesis by

Allen E. Fuhs

In Partial Fulfillment of the Requirements

For the Degree of

Doctor of Philosophy

California Institute of Technology

Pasadena, California

1958

ACKNOWLEDGEMENTS

The author takes pleasure in expressing his deepest appreciation to Dr. S. S. Penner, whose advice and suggestions have been invaluable to the progress of this research.

Financial support for this research program has been provided by the Daniel and Florence Guggenheim Foundation in the form of a Guggenheim Jet Propulsion Fellowship granted to the author for the academic year 1956-1957, by the California Institute of Technology through tuition scholarships for the years 1954-1956, and by the Office of Ordnance Research, United States Army, under Contract No. DA-04-495-Ord-446. Grateful acknowledgement is made to these three organizations.

ABSTRACT

Three topics concerned with heterogeneous diffusion flames are considered in Part I.

Experiments have been conducted to determine the interference effects during burning for droplet arrays. The burning rate law applicable for single droplets has been found to be valid also for two-, five-, and nine-droplet arrays.

A heterogeneous diffusion flame formed between liquid sodium and gaseous titanium tetrachloride was found to deposit small particles of titanium on the combustion chamber wall. The burning rate of liquid sodium, which is related to the rate of production of titanium, was determined experimentally.

The scaling procedures developed by several authors for liquid-fuel rocket engines have been generalized. In these theoretical studies we have used the functional results derived in our investigations of droplet burning. The generalized analysis indicates that an attempt to maintain complete similarity on scaling results in contradictions. For this reason a program on selected scaling procedures is indicated.

In Part II the apparent emission profiles of a turbulent flame are described in terms of a wrinkled laminar flame model. A distribution function, which assigns a probability for the occurrence of the laminar flame at a particular position within the turbulent flame brush, determines the apparent emission profiles. The inverse problem of determining the probability function from observed emission profiles has also been solved.

It is possible to correlate the ratio of the apparent spectral intensities of two rotational lines with the equivalence ratio of a laminar flame. Assuming that this correlation applies also to other flames, we have determined the equivalence ratio in the critical zone of a reverse-jet stabilized flame in a duct. The equivalence ratio as a function of radial distance from the duct axis has also been measured. The results indicate that there appears to be a single equivalence ratio curve at blow-off, regardless of jet composition, provided the blow-off velocity is considered to be a function of critical zone equivalence ratio.

TABLE OF CONTENTS

PAGE

Acknowledgements i

Abstract ii

Table of Contents iv

List of Tables x

List of Figures xii

List of Symbols xix

PART I. EXPERIMENTAL AND THEORETICAL STUDIES ON HETEROGENEOUS DIFFUSION FLAMES

A. Interference Effects During Burning in Air for Stationary n-Heptane, Ethyl Alcohol, and Methyl Alcohol Droplets 1

1. Introduction 1

2. Experimental Studies on the Burning in Air of Two Stationary Fuel Droplets 4

a. Apparatus 4

b. Experimental Results Relating to Flame Shape and Burning Rate 6

3. Correlations for Evaporation Constants 7

a. Correlations for n-Heptane Droplets 14

b. Correlations for Ethyl and Methyl Alcohol Droplets 16

4. Dimensional Analysis Relating to the Burning of Liquid Droplets 16

a. The Burning of Single Droplets 17

b. Two Droplets Burning in Close Proximity 20

5. Experimental Studies on the Burning in Air of More Complex Stationary Fuel Droplet Arrays 20

a. An Array of Five Droplets 20

b. An Array of Nine Droplets 21

6. Conclusions 23

B. Diffusion Flames for the Production of Titanium from Sodium and Titanium Tetrachloride 24

1. Introduction 24

2. Burning Rate Calculations for Heterogeneous Diffusion Flames 25

3. Some Experiments for Estimating the Mass Burning Rate of Liquid Sodium in an Atmosphere of Titanium Tetrachloride 30

a. Description of Apparatus and Experimental Procedure 30

b. Experimental Results 31

4. A Suggested Apparatus for the Study of Production Rates of Titanium in Laminar Diffusion Flames Formed from Sodium and Titanium Tetrachloride 33

5. Gaseous Diffusion Flames 37

C. Scaling of Liquid Fuel Rocket Engines 38

1. Introduction 38

2. Generalized Scaling Rules 40

a. Similarity of Steady Aerothermochemistry 43

(1) Relation between geometric scale factor, n_L, and thrust scale factor, n 44

(2) Scale factor for the orifice hole diameter 45

(3) Scale factor for the linear flow velocity 45

(4) Scale factor for the chamber pressure 46

(5) Scale factor for the nozzle throat diameter 46

(6) Scale factor for the feed system 47

b. Similarity of Regenerative Cooling System 47

c. Similarity of Sweat Cooling 49

d. Low-frequency Stability 49

e. High-frequency Stability 52

3. Summary of Results and Discussion 53

4. Application of Results to a Program for Testing Scaling Procedures for High-frequency Stability 60

PART II. SPECTROSCOPIC STUDIES OF FLAMES

A. Apparent Emission Intensities from a Wrinkled Laminar Flame Model of a Turbulent Flame 64

1. Introduction 64

2. A Model for the Determination of Apparent Emission Profiles 65

3. Calculation of the Apparent Emission Profiles for Different Probability Functions $p(x_1)$ 68

a. Apparent Emission Profiles for Infinite Values of $\underline{c}$ 68

(1) Profiles for the hot-peak probability function 68

(2) Profiles for the cold-peak probability function 70

(3) Profiles for a symmetrical triangular probability function 71

b. Apparent Emission Profile for Finite Values of $\underline{c}$ and $p(x_1) = \frac{1}{\alpha}$ for $0 \leqslant x_1 \leqslant \alpha$ 73

c. Comparison of the Apparent Emission Profiles 74

4. Determination of the Probability Function from Measured Apparent Emission Profiles 75

5. Determination of $p(x_1)$ from the Experimental Data of Reference 3 78

a. Numerical Calculation of the Parameters $\underline{a}$ and $\underline{c}$ 79

b. Probability Function from a Gaussian Representation of the Apparent Emission Profiles 83

6. Discussion and Conclusions 88

B. Experimental Study of Reverse-Jet Flame Stabilization by the Spectral Intensity Ratio Method 91

1. Introduction 91

2. Experimental Evidence Indicating the Existence of a Critical Zone 91

3. A Discussion of the Spectral Intensity Ratio Method 93

4. Experimental Determination of Local Equivalence Ratio in a Reverse-Jet Stabilized Flame 99

a. Experimental Determination of Spectral Intensity Ratios as a Function of Equivalence Ratio 99

b. Description of the Apparatus and Procedure for Obtaining Local Equivalence Ratios 101

5. Experimental Results 102

a. Equivalence Ratio in the Critical Zone at Blow-Off 102

b. Local Equivalence Ratio as a Function of Radius 103

(1) Stabilized flame 104

(2) Pilot flame 104

c. Equivalence Ratio for an Open Flame Stabilized by a Reverse Jet 105

6. Conclusions 105

APPENDIX TO PART I. SPRAY FORMATION AND SPRAY COMBUSTION

1. Introduction 108

2. Atomizing Devices 109

3. Spray Characteristics 112

   a. Rosin-Rammler Distribution Function 119

   b. Nukiyama-Tanasawa Distribution Function 121

   c. Log-probability Distribution Function 121

   d. Log-probability Distribution Function with Upper Limit 122

   e. Square-Root Distribution Function 123

4. Measurement of Spray Characteristics 125

5. Instability and Disintegration of Liquid Jets and Sheets 128

6. Deformation and Breakup of Drops 136

7. Coalescence of Drops 145

8. Spreading and Mixing of Sprays 148

9. Evaporation of Sprays 152

10. Prediction of Spray Characteristics 166

11. Spray Formation in Rocket Motors 173

12. Combustion of Single Drops and of Drop Arrays 181

13. Combustion of Sprays 189

14. Summary and Conclusions 201

References 203

Figures 217

LIST OF TABLES

PART I

I.	Experimental Results for Two n-Heptane Droplets Burning in Still Air	8
II.	Experimental Results for Two Ethyl Alcohol Droplets Burning in Open Air	10
III.	Experimental Results for Two Methyl Alcohol Droplets Burning in Open Air	12
IV.	Average Values of Evaporation Constant (K) for Nine-Droplet Arrays of n-Heptane and Methyl Alcohol as Fuels Burning in Still Air	22
V.	Estimated Ratio of the Steady Mass Burning Rate, $\dot{m}_F$, to Drop Radius, r_ℓ, for Liquid Sodium in Different Atmospheres	29
VI.	The P-T Scaling Rules for Liquid-fuel Rocket Engines	54
VII.	Crocco's Second Scaling Rule for Liquid-fuel Rocket Engines	55
VIII.	Barrère's Scaling Rule for Liquid-fuel Rocket Engines	57

PART II

I.	The Effect of Jet Composition on Flame Stability	92
II.	Effect of Turbulence on Specific Intensity	98
III.	Observed Equivalence Ratio for an Open Flame Stabilized by a Reverse Jet	106

APPENDIX TO PART I

I.	Definitions of Mean Diameters	115
II.	Cumulative and Distributive Forms of Four Droplet Distribution Functions	117
III.	Mean Drop Diameters Calculated According to Four Different Methods	120
IV.	Critical Velocity for Breakup of Drops of Different Diameters	139
V.	The Influence of Impingement Angle on Sauter Mean Diameter	177
VI.	Dependence of Ignition Lag on Ambient Temperature and Drop Diameter	188
VII.	Values of K and K' for Different Fuels	190
VIII.	Burning Velocities of Aerosols	198

LIST OF FIGURES

PART I

1. Schematic Arrangement of Flame Interference Experiment with Two Droplets Burning in Close Proximity 218
2. Photograph of Two n-Heptane Droplets Burning in Air (D_1^o = 0.181 cm, D_2^o = 0.174 cm, C^o = 0.114 cm) 219
3. Schematic Diagram of the Apparatus Used for Droplet Ignition 220
4. Experimental Results for Two n-Heptane Droplets Burning in Still Air (D_1^o = 0.194 cm, D_2^o = 0.166 cm, C^o = 0.020 cm) 221
5. Plots of D^2 vs Time and C vs Time for Two n-Heptane Droplets Burning in Still Air for Various C^o 222
6. Plots of D^2 vs Time and C vs Time for Two n-Heptane Droplets Burning in Still Air for Various C^o 223
7. Plots of D^2 vs Time for Two n-Heptane Droplets Burning in Still Air for Various C^o 224
8. Plots of D^2 vs Time for Two Ethyl Alcohol Droplets Burning in Open Air for Various C^o 225
9. Plot of D^2 vs Time for Two Ethyl Alcohol Droplets Burning in Open Air for Various C^o 226
10. Plots of D^2 vs Time for Two Methyl Alcohol Droplets Burning in Open Air for Various C^o 227

11. Variation of the Average Evaporation Constant with C^o for n-Heptane Droplets with Different Initial Average Diameters, $\overline{D}^o$ 228

12. Average Evaporation Constant vs Initial Droplet Spacing for Ethyl Alcohol 229

13. Average Evaporation Constant vs Initial Droplet Spacing for Methyl Alcohol 230

14. Dependence of the Evaporation Frequency, $\overline{K}'$, on $C^o/\overline{D}^o$ 231

15. Variation of $\overline{K}$ with $\overline{D}^o$ for Ranges of Values of $C^o + \overline{D}^o$ (Methyl Alcohol) 232

16. Variation of $\overline{K}$ with $\overline{D}^o$ for Ranges of Values of $C^o + \overline{D}^o$ (Ethyl Alcohol) 233

17. Drop Diameter Squared vs Time for the Center Drop (D_c^2) of a Five-Drop Array of Ethyl Alcohol Burning in Open Air 234

18. Schematic Diagram of Apparatus Used for Sodium-Titanium Tetrachloride Diffusion Flame Experiments 235

19a. End View of Liquid Sodium Droplet Supported by Heating Wires 236

19b. Top View Showing the Liquid Sodium 236

20. Schematic Diagram of an Apparatus for the Study of Heterogeneous Diffusion Flames Formed Between Liquid Sodium and Titanium Tetrachloride 237

21. Flame Boundary for an Overventilated Diffusion Flame Formed Between Sodium and Titanium Tetrachloride 238

22. Flame Boundary for an Underventilated Diffusion Flame Formed Between Sodium and Titanium Tetrachloride 239

PART II

1. Turbulent Flame Formed Above a Rectangular Exit Port and a Representative Observation Section (Schematic) 241

2. Schematic Illustrations of the Important Lengths Defining Emission from a Turbulent Flame Composed of a Wrinkled Laminar Flame 242

3. Model of a Steady-state Laminar Flame 243

4. Dependence of Energy Per Second Received on the Separation Between the Slit Center and the Laminar Flame Center 244

5. Regions Within Which the Equations for $E(x_o)$ Are Valid 245

6. Computational Regions for Products and Reactants Using a Symmetrical Triangular Probability Function 246

7. Reproduction of Figure 10 from Reference 3. Percent Transmitted Intensity as a Function of Distance from the Flame Centerline 247

8. Computational Regions for $E_P(x_o)$ Using Finite c Value 248

9. Instrumental Response When Observations Are Made with a Slit Width $b \geqslant a$ for Various Probability Functions with Infinite c 249

10. Comparison of the Apparent Product Emission Profile for Various Values of the Ratio c/α 250

11. Graphs of the Functions $I_R(x_o - x_1)$, $I_P(x_o - x_1)$ for Finite c and $I_P(x_o - x_1)$ for Infinite c 251

12. The Real and Imaginary Parts of the Fourier Transform of the Apparent Emission Profiles Plotted as a Function of ω 252

13. Graph of the Integrand of P_s for $\omega = 0.333\pi$ 253

14. Representation of the Apparent Emission Profiles by Gaussian Curves 254

15. Graph of the Function $\varphi(x)$ Defined by Equation 50 255

16. Radial Distance from the Duct Axis for a Stoichiometric Main Stream and a Stoichiometric Jet 256

17. Schematic Illustration of the Apparatus Used for Obtaining the Calibration Curves 257

18. Apparent Emission Intensity as a Function of Wavelength 258

19. Spectral Intensity Ratio as a Function of Equivalence Ratio for the Line with Center at 4737Å to the Line with Center at 4324Å 259

20. Spectral Intensity Ratio as a Function of Equivalence Ratio for the Line with Center at 4737Å to the Line with Center at 4252Å 260

21. Spectral Intensity Ratio as a Function of Equivalence Ratio for the Line with Center at 5129Å to the Line with Center at 4324Å 261

22. Spectral Intensity Ratio as a Function of Equivalence Ratio for the Line with Center at 5635Å to the Line with Center at 4324Å 262

23. Spectral Intensity Ratio as a Function of Equivalence Ratio for the Line with Center at 6191Å to the Line with Center at 4324Å 263

24. Schematic Illustration of the Apparatus Used for Studies of a Reverse-Jet Stabilized Flame 264

25. Observed Equivalence Ratio in the Critical Zone at Blow-Off for an Air Jet 265

26. Blow-Off Velocity as a Function of Main Stream and Critical Zone Equivalence Ratios 266

27. Local Equivalence Ratio as a Function of Radius for a Rich Main Stream ($\varphi = 1.16$) and Various Jet Compositions 267

28. Local Equivalence Ratio as a Function of Radius for a Lean Main Stream ($\varphi = 0.92$) and Various Jet Compositions 268

29. Local Equivalence Ratio in a Pilot Flame as a Function of φ_{ms} and Radial Distance 269

APPENDIX TO PART I

1. Schematic Illustration of Various Types of Atomizers 271
2. Histogram Showing Size Distribution of Fragments 272
3. Probability Distribution Function for Drop Sizes 273
4. Cumulative Form of Representation of Drop Sizes 273
5. Disintegration of a Liquid Jet 274
6. Effect of Weber Number on Growth Rate 274
7. Comparison of Theory and Experiments; Growth Rate as a Function of Frequency 275
8. Effect of Viscosity on W_{crit} for a Drop Suddenly Exposed to an Air Stream 275
9. Total and Liquid Fuel Distribution Downstream of an Iso-octane Spray in a Duct 276
10. Isothermals Surrounding an Evaporating Drop in a Forced Convection Experiment 276
11. Experimentally Determined Drop Surface Temperatures 277
12. The Fraction of Spray Evaporated (or Burnt) as a Function of Time 277
13. Percentage of Unevaporated (or Unburnt) Fuel as a Function of $\sqrt{Kt_r} / \overline{D}$ and δ for Sprays Obeying the Rosin-Rammler Distribution Law 278
14. Effect of Sheet Thickness on the Wavelength Corresponding to Maximum Growth 279

15.	Atomization Curves for Intermittent Sprays from Impinging Jets and from a Single Jet	280
16.	Effect of Changes in Orifice Diameter and Chamber Pressure on Sauter Mean Diameter	281
17.	The Effect of Injection Pressure on Sauter Mean Diameter	282
18.	Effect of Ambient Air Temperature on the Evaporation Constant, K	283
19.	Distribution of Drop Sizes in the Combustion Zones for Kerosene Drops	284
20.	A Qualitative Representation of the Temperature Which Drops Experience in a Burning Spray	285
21.	Entrainment of the Chamber Gases and the Resulting Velocity Profiles	285
22.	The Transmission Spectrum of Cyclohexane and the Emission Spectrum of a Luminous Propane-Air Flame	286
23.	Maximum Pressure Curves for Propane-Air and Kerosene Mist-Air Mixtures in a Constant Volume Combustion Bomb	287
24.	Lean Limit Air-Fuel Ratio as a Function of Particle Size	287
25.	Weak Flame Extinction Limit as a Function of Fuel Volatility for Fine and Coarse Sprays	288

LIST OF SYMBOLS

PART I

Symbol	Meaning
A	Amplitude of initial disturbance; a constant appearing in Masugi's equation for W_{crit}; cross sectional area of a duct or streamtube, cm^2.
C	Any constant; diameter of regenerative cooling coils; minimum spacing between surfaces of adjacent droplets, cm.
D	Drop diameter, cm.
D	Diffusion coefficient, cm^2/sec.
$\overline{D}$	Size constant for spray distribution functions, cm.
D_I	First Damköhler number, $(L/v)/\tau$.
E	Energy.
F	Spray mixing factor; total propellant injection rate.
Gr	Grashof number, $D^3\rho^2 g\,\beta'\Delta T/\eta^2$.
G(r, s, t)	Particle concentration spectrum; the number of particles of radius, r, in unit volume per unit interval of drop radius, dr.
J	Inertia parameter for low frequency stability.
J_n	Bessel function of first kind of order n.
K	Evaporation constant, cm^2/sec.

K'	An apparent evaporation constant which includes ignition lag and burning time; evaporation "frequency."
L	A characteristic length of a rocket motor; distance from fuel injector; length of jet prior to breakup; scale of turbulence.
M	Mach number.
N	Percent of the spray which has evaporated; total number of drops.
N(D)	Numerical cumulative function, the fraction of drops in a spray with diameter less than D.
Nu	Nusselt number, hD/λ.
P	Chamber pressure.
Q	Total heat transferred; volume flow rate, cm^3/sec.
R	Gas constant based on a gram of gas; nominal mixture ratio, weight of fuel divided by weight of fuel plus oxidizer; sum of radii of two colliding drops.
Re	Reynolds number, $\rho VD/\eta$.
R(r, s, t)	Growth rate, time rate of change of particle radius.
S	Displacement.
Sc	Schmidt number, $\eta/\rho D$.
SMD	Sauter mean diameter.
T	Absolute temperature, degrees Kelvin; time interval.

U	Mean flow velocity; velocity of sound.
V	Velocity; volume .
V(D)	Volume cumulative function, the volume fraction of the spray with drops less than D in diameter.
Vi	Viscosity group or stability number, $\eta_\ell / \sqrt{\rho_\ell \sigma D}$.
W	Input or nominal weight flow rate; Weber number, $\rho V^2 D/\sigma$; weight cumulative function for analytical description of sprays.
Y_j	Mass fraction of species j.
a	Flame shape parameter, cm; parameter in the log probability with upper limit distribution function; thickness of fluid sheet; a constant.
b	"Frequency" group, (3/2) ($\pi \eta D/m$); flame shape parameter, cm; a constant.
c	Correction factor for spray sampling, which occurs in formula for spray mixing factor, F.
c_p	Specific heat at constant pressure, calorie/^{o}K gm.
d	Orifice diameter; diameter of the inner tube for the Na(g) and $TiC\ell_4$(g) diffusion flames.
d'	Diameter of outer concentric tube in gaseous Na-$TiC\ell_4$ diffusion flame.
exp	Exponential.
f(D)	Any function of drop diameter.
g	Gravitational constant, cm/sec^2.

h	Characteristic atomizer dimension; displacement of gas-liquid interface from equilibrium position; film heat transfer coefficient, calorie/sec ^{o}K cm^{2}.
$h(D)$	Any function of drop diameter.
i	Current, amperes.
k	Proportionality constant in Langmuir's evaporation equation, g/cm-sec.
ℓ	Orifice length; the effective length of propellant supply pipes as used in rocket stability analysis.
m	Mass; a constant.
$\dot{m}$	Mass burning (evaporation) rate, g/sec.
m'	A constant which relates chamber pressure to delay time or ambient pressure to drop burning time.
n	Number density; number of samples; a constant; a ratio of the quantity for the large rocket motor to the same quantity for the model; wave number of the disturbing wave.
$n(D)$	Numerical probability distribution; the number of drops of size D per unit size interval.
p	Absolute pressure, atmosphere.
q	Heat transfer per unit area of surface; standard enthalpy difference between reactants and reaction products, calories/gm.

r	Drop radius; local mixture ratio weight of fuel divided by weight of fuel plus oxidizer; radius.
s	Distance along a duct or streamtube.
t	Time, seconds.
v	Velocity; volume, cm^3 or $micron^3$.
v(D)	Volume probability distribution.
w	Wall thickness of rocket chamber; local weight flow rate.
x	Distance along the fluid sheet; number of moles of $C\ell_2$ added to combustible mixture of Na and $TiC\ell_4$.
y	Natural logarithm of ratio $D/\overline{D}$ used in log probability distribution function.
z	Distance along the axis of the circular duct used for the diffusion flame.
α	A constant which determines influence of Weber number on mean drop size.
β	Growth rate factor, sec^{-1}; a constant which determines influence of Reynolds number on mean drop size.
β'	Coefficient of thermal expansion, $\frac{1}{V}\ \frac{\partial V}{\partial T}\Big)_P$.
γ	Ratio of specific heats, c_p/c_v.
Δ	A finite increment.

δ	Distribution parameter or uniformity index; a constant which relates mean drop size to delay time.
$\Delta\ell$	Specific latent heat of evaporation of fuel droplet, calories/gm.
ε	Eddy diffusivity; energy dissipated in turbulent motion per unit time and per unit mass; fraction of total propellant flow used for sweat cooling.
η	Coefficient of viscosity, g/cm-sec; an efficiency.
θ	Impingement angle for impinging jets; spray cone angle.
$\varkappa_o$	Permittivity of free space.
λ	Microscale of turbulence; thermal conductivity, calorie/cm sec ^{o}K; wavelength.
μ	Micron equal to 10^{-6} meter.
ν	Frequency; ratio of mass of fuel to mass of oxidizer at stoichiometric composition; kinematic viscosity, cm^2/sec.
ρ	Density, gm/cm^3.
σ	Surface tension, dyne/cm.
τ	Chemical conversion time; ignition lag time; relaxation time for a drop; time delay between injection and conversion of propellants to heat.
$\mathcal{V}$	The ratio of the coolant mass flow per unit area of surface to the main stream mass flow per unit area.

ϕ	Parameters used in the equation for flame surface of a gaseous diffusion flame in concentric ducts, the products 1/2 d are the roots of the Bessel function of first kind of order 1, cm^{-1}; nozzle potential volts.
φ(Vi)	Function of stability number.
ω	Angular frequency, sec^{-1}.
$\bar{}$	(Bar over a symbol) Average value.

Subscripts

A	Air .
act	Activation .
b	Completion of burning.
c	Collision; refers to chamber conditions; value at flame surface; center drop of an array.
crit	Critical value.
d	Drop.
eff	Effective value.
F	Fuel.
f	Feed or supply system; free.
g	Gas.
h	Referred to a nozzle dimension as a characteristic length.
i	Index equal to 0, 1, 2, 3 . . .
in	Inlet.

ℓ	Liquid; value at liquid surface; value for liquid phase.
m	Maximum; model.
max	Maximum value.
nm	Refers to numerical median.
O	Oxidizer.
o	Initial value; lower value (as compared to upper value); value at ∞.
P	Reaction product.
p	An index equal to 0, 1, 2, 3 . . .
q	An index equal to 0, 1, 2, 3 . . .
r	Residence (time).
s	Steady acceleration.
T	Total.
t	Transient.
v	Vapor.
vm	Refers to volume median.
W	Wave.
1	Larger of two drops; the first of a series of constants.
2	Smaller of two drops.

Superscripts

*	Maximum.
o	Initial value.

PART II

Symbol	Meaning
A_P	Irradiancy received from product emission per unit width of observation slit.
A_R	Irradiancy received from radical emission per unit width of observation slit.
E_{max}	Maximum value of the average energy per second passing through the collimating slits.
$E(x_o)$	The average energy per second passing through the collimating slits when the observation section is at x_o.
$I(x_o-x_1)$	Energy per second received by an instrument having an observation section of width 2b positioned at x_o.
K	A dimensionless ratio defined as $g(\lambda_R)A_P/g(\lambda_P)A_R$.
L	Length of the exit port; effective geometric length of the column of emitters.
N	Concentration of molecules in a particular energy state.
P_ω	Spectral absorption coefficient, cm^{-1} $atmos^{-1}$.
$P_c(\omega)g(\lambda_P)$	Real part of Fourier transform of the apparent product emission profile.

$P_s(\omega)g(\lambda_P)$	Imaginary part of Fourier transform of the apparent product emission profile.
R	Duct radius, inches.
$R_c(\omega)g(\lambda_R)$	Real part of the Fourier transform of the apparent radical emission profile.
$R_s(\omega)g(\lambda_R)$	Imaginary part of the Fourier transform of the apparent radical emission profile.
R_ω	Spectral radiancy, watt/cm.
R_ω^o	Blackbody spectral radiancy, watt/cm.
R_L	Line radiancy, watt/cm^2.
$\lvert R_{u\ell} \rvert^2$	Matrix element for upper and lower energy states.
S	Integrated absorption, $cm^{-2}atmos^{-1}$.
T	Absolute temperature, degrees Kelvin.
$T(x_o)$	Percent transmitted intensity.
V_{bo}	Blow-off velocity, feet/second.
V_{bo}^*	Maximum blow-off velocity, feet/second.
X	Optical depth, cm atmos.
a	Half width of the region of luminosity due to radical emission within a steady-state laminar flame.
b	Half width of the observation section.
c	Distance downstream to which the product radiation from the laminar flame radiates; velocity of light.

g	Statistical weight.
g*	Value of g at $\omega = \omega'$.
$g(\lambda)$	A function which accounts for the variation of film sensitivity with wavelength and which specifies the calibration factor.
$g(\lvert\omega - \omega'\rvert)$	Slit function.
h	Planck's constant, erg-sec.
h(x)	A function of x equal to $\sigma(m-x)^2$.
k	Boltzmann's constant, erg/^{o}K.
m	Coordinate of E_{max}.
p	Partial pressure of the emitters.
$p(x_1)$	Probability function which measures the probability of the occurrence of the center of the laminar flame at a particular coordinate, x_1, within the turbulent flame region.
x	Distances through the turbulent flame brush. The origin is at the cold gas side.
x_o	Coordinate of the center of the observation section.
x_1	Coordinate of the center of the region of radical emission from a steady-state laminar flame.
y	Coordinate measured parallel to long dimension of burner port.
α	Approximate thickness of the turbulent flame brush.

δ	A ratio of $2A/\alpha^2$; one half of the wave number interval over which P_ω is non-zero.
$\Delta\omega$	One half of the slit width of the spectroscope.
λ	Wavelength of radiation.
ν	An adjustable parameter used in the derivation of equation 23; frequency of radiation, cycles/second.
ξ	$x_o - x_1$, separation of observation section and the laminar flame center.
σ	Width parameter in the gaussian representation of the apparent emission profiles.
φ	Equivalence ratio, the ratio $(f/a)_{actual}/(f/a)_{stoichiometric}$, where f is mass flow rate of fuel and a is the mass flow rate of air.
φ_{ms}	Equivalence ratio of main stream as determined by flow meter measurements.
φ_{obs}	Local observed equivalence ratio as determined by spectral intensity ratio method.
φ_j	Equivalence ratio of jet as determined by flow meter measurements.
φ_z	Equivalence ratio in critical zone as determined by spectral intensity ratio method.
ω	Wave number of radiation, cm^{-1}.

Subscripts

ℓ	Lower energy state.
u	Upper energy state.
ω	Spectral value.

Superscripts

a	Apparent.
o	Blackbody.
*	Maximum.

PART I. EXPERIMENTAL AND THEORETICAL STUDIES ON HETEROGENEOUS DIFFUSION FLAMES

The term heterogeneous diffusion flame refers to flames in which two or more phases are involved. Heterogeneous diffusion flames assume an important role in industry, especially in the field of jet propulsion. Volume restrictions for jet propulsion devices make it necessary to have high-density fuels; this requirement dictates that the fuel be liquid or solid. Sprays provide the breakup of the liquid "bulk" which is essential for combustion.

Part I is divided into three sections in which topics concerned with heterogeneous diffusion flames are discussed. Experiments conducted for the purpose of determining the interference effects of two, five, or nine droplets burning in close proximity are described in Section A. In Section B the results of exploratory experiments using diffusion flames for a continuous-flow titanium reduction process are reported, and droplet combustion formulae are applied in Section C to a problem related to the scaling of rocket motors. A survey of spray formation and spray combustion is presented in the Appendix to Part I.

A. INTERFERENCE EFFECTS DURING BURNING IN AIR FOR STATIONARY n-HEPTANE, ETHYL ALCOHOL, AND METHYL ALCOHOL DROPLETS*

1. Introduction

A considerable number of theoretical and experimental papers have been published on the burning of single droplets of fuel.[2-5] Experimental

*Most of the material presented in this section has been published and appears in reference 1.

studies have been performed on single droplets suspended from fine quartz fibers and burning in an oxidizing atmosphere.[6] An approximate theoretical prediction of mass burning rate for single droplets can be obtained on the assumption that mass transport by diffusion to the flame surface and heat conduction to the burning droplet control the burning rate.[5]

Recently an attempt has been made by Graves and Gerstein to utilize experimental data for single droplets in the description of burning rates in sprays.[7] These authors started with the results of an important theoretical study carried out some years ago by Probert.[8] Probert made the following assumptions:

(a) The spray particle size follows the Rosin-Rammler distribution law,

$$1 - V = e^{-(D/\overline{D})^{\delta}}, \qquad (1)$$

where V equals the volume fraction or weight fraction of the spray composed of drops with diameters less than D, $\overline{D}$ is called the size constant, and δ is usually referred to as the distribution constant.

(b) The rate of burning of the droplets is taken to be proportional to the first power of the droplet diameter. In this case it is easily shown that

$$D^2 = (D^o)^2 - Kt \qquad (2)$$

where D is the droplet diameter at any time, D^o is the initial diameter, and K, which has the dimensions of area per unit time, is known as the evaporation constant.

Probert has shown how to compute the percentage of unburned fuel as a function of $\sqrt{Kt_r} / \overline{D}$ for values of δ between 2 and 4,

where t_r is the residence time of the burning droplets. Recently correlations similar to those of Probert have been worked out for droplet distribution laws other than the Rosin-Rammler distribution law.[9]

Equation 2, which determines droplet diameter as a function of time, is known to correlate all of the observed results for the steady burning of single fuel droplets in an oxidizing atmosphere.[5] Therefore, it is of obvious interest to determine whether or not the value of the evaporation constant, K, for single droplet theory or experiment has any relation to the value of K appropriate for spray combustion. Graves and Gerstein attempted to answer this question by measuring the combustion efficiency as a function of oxygen concentration for a single tubular combustor using iso-octane as fuel and counter-current injection. They compared observed combustion efficiencies with calculated combustion efficiencies using Probert's theoretical analysis in conjunction with values of K measured for the burning of single droplets. This comparison showed that all of the observed results could not be explained unless spray combustion involves effects, at least for oxygen concentrations below 24 percent, which can be ignored in the burning of single droplets. In connection with the use of single droplet data for studies on spray combustion, it is therefore of obvious importance to carry out laboratory studies on interference between droplets during burning.

Although, as a general rule, statistical arrays are more easily interpreted than small numbers of droplets; such as 2, 4, etc.,

experimental studies on small numbers of droplets may provide a clue for the important physico-chemical processes operative in droplet interference during burning. For this reason experiments have been carried out on the variation of K with droplet size and droplet spacing for two closely spaced droplets.

There is presented in subsection 2 a summary of experimental results obtained from arrays of n-heptane, ethyl alcohol, and methyl alcohol droplets. Attempts at finding simple correlations for the experimentally determined evaporation constants are outlined in subsection 3. Dimensional analysis is used in subsection 4 to try to clarify and interpret the observed data. Experimental results obtained from five- and nine-droplet arrays are discussed in subsection 5.

2. Experimental Studies on the Burning in Air of Two Stationary Fuel Droplets

a. Apparatus

In order to record the flame shape and the decrease in droplet diameter with time, the droplets were suspended on thin quartz fibers which were secured by means of Sauereisen cement to a metal rod. The rod was bent at an angle of 90 degrees at one end to insure a large supporting surface. The rod was supported on a stand by means of a clamp. Rods of various diameters were used for different minimum spacings between the adjacent surfaces of the droplets, C^{o}. (See Figure 1.) The fibers were either enclosed in a circular plastic tube of

several inches diameter or else were burnt in the open air; no significant differences between the burning rates were found in the two cases. Single droplets of fuel were suspended from the fibers by forcing fuel through a hypodermic needle onto the fiber. The droplets were reasonably spherical as shown, for example, in Figure 2. The drops were ignited by using either an automobile ignition system connected to electrodes which straddled the two quartz fibers through holes in the tube (See Figure 3.) or else simply a match.

An electrically driven Arriflex 35 mm movie camera was used for photographing the burning droplets. In order to photograph the flame front, a 100-watt bulb was placed behind and off to one side of the burning drops. This method silhouetted the drops and also left the flame front visible, as shown in Figure 2. A ten-inch adapter tube and telephoto lens were employed in order to obtain as large an image as possible on each frame of film. Kodak Plus X and Kodak Super XX films were used with apertures of f3.2 to f9.

A stroboscope served as timing standard. A ten-inch circular aluminum plate, with three holes placed 120 degrees apart, was secured to a 75 RPM constant speed motor giving 3.75 flashes per second. The stroboscope was placed directly behind the burning drops. The camera speed was adjusted to almost 25 frames per second, as determined from observations of the stroboscope.

A 3/32-inch ball bearing was photographed at the beginning of each 100-foot roll of film used. The image served for calibration and

was obtained under the same focusing conditions as were used for the burning droplets.

The film was measured by using a microfilm recorder and a steel scale graduated in millimeters. Two measurements were made on each drop; namely, the two perpendicular diameters inclined 45 degrees to the major and minor axes in the plane of observation. The mean value of these two readings was recorded as the "effective diameter" of the droplet. It is easily shown that if the major and minor axes do not differ greatly, as was the case in these experiments, then the volume of a sphere with the measured effective diameter is not greatly different from that of the prolate spheroid, which actually corresponds to the shape of the droplets. In most cases measurements were taken from ignition to burn out and recorded approximately every fifth or sixth frame. The flame shape parameters a_1, a_2, b_1, and b_2 (See Figure 1.) were also measured for n-heptane droplets.

b. Experimental Results Relating to Flame Shape and Burning Rate

Experimental studies have been carried out for two stationary n-heptane, ethyl alcohol, and methyl alcohol droplets burning in air. The square of the droplet diameter, D^2, was generally found to be a linear function of the time, t, for each of the burning droplets. The flame shape parameters (for n-heptane droplets) varied remarkably little with time as the droplets burned. Representative experimental results are shown in Figures 4 to 10.

The experimental data obtained for K are summarized in Tables I to III for n-heptane, ethyl alcohol, and methyl alcohol, respectively. The listed values of K were obtained by drawing "best" straight lines through the experimentally determined points except for those cases in which the data were not adequately represented by linear correlations. In some cases the measured results suggested periodic variations of observed parameters.

In several instances, where droplets of greatly different sizes were used, observations were possible on the larger remaining droplet after the smaller droplet had burned out. In most of these cases the slope of the D^2 vs t curve changed rather abruptly for n-heptane droplets and yielded data in fair agreement with the known single droplet results ($K \simeq 0.008$ cm^2/sec) after the smaller droplet had burned completely. For droplets of nearly equal diameters ($D_1^o \simeq D_2^o$) the evaporation constants K_1 and K_2 were found to be nearly equal.

3. Correlations for Evaporation Constants

If the evaporation constant, K, of a stationary fuel droplet suspended from a quartz fiber is modified extensively by the presence of a second droplet burning in close proximity, then one might expect the value of K to depend both on the instantaneous values of the droplet diameters and on the distance between the droplets. Contrary to this idea, it has been found that K is constant, within the experimental limits of accuracy, for two droplets burning in close proximity.

TABLE I. EXPERIMENTAL RESULTS FOR TWO n-HEPTANE DROPLETS BURNING IN STILL AIR

D_1^o, cm	D_2^o, cm	C^o, cm	K_1, cm^2/sec	K_2, cm^2/sec
0.194	0.166	0.020	0.0094	0.0082
0.181	0.174	0.114	0.0096	0.0094
0.166	0.154	0.183	0.0135	0.0130
0.192	0.176	0.230	0.0105	0.0096
0.165	0.142	0.264	0.0136	0.0122
0.182	0.173	0.752	0.0153	0.0141
0.182	0.182	0.892	0.0140	0.0140
0.173	0.173	1.125	0.0139	0.0133
0.182	0.156	1.47	0.0124	0.0115
0.130	0.127	0.222	0.0080	0.0072
0.138	0.134	0.208	0.0068	0.0063
0.135	0.117	0.313	0.0085	0.0085
0.124	0.124	0.235	0.0070	0.0070
0.133	0.122	0.540	0.0091	0.0090
0.136	0.120	0.496	0.0091	0.0068
0.121	0.118	0.384	0.0074	0.0074
0.143	0.142	0.533	0.0118	0.0110
0.141	0.135	0.538	0.0097	0.0093
0.155	0.142	0.496	0.0122	0.0114
0.156	0.147	0.813	0.0123	0.0113
0.156	0.141	0.883	0.0110	0.0112
0.156	0.156	1.10	0.0107	0.0108
0.208	0.155	0.120	0.0107	0.0104
0.209	0.170	0.352	0.0123	0.0109
0.198	0.140	0.375	0.0090	0.0089

TABLE I. CONTINUED

D_1^o, cm	D_2^o, cm	C^o, cm	K_1, cm^2/sec	K_2, cm^2/sec
0.167	0.115	0.520	0.0150	0.0090
0.160	0.131	0.532	0.140	0.0150
0.192	0.148	0.026	-	0.0068
0.208	0.164	0.150	-	0.0124
0.191	0.178	0.246	0.0157	-
0.192	0.180	0.355	-	-
0.202	0.179	0.362	-	-
0.200	0.15	0.466	0.0133	-

TABLE II. EXPERIMENTAL RESULTS FOR TWO ETHYL ALCOHOL DROPLETS BURNING IN OPEN AIR

D_1^o, cm	D_2^o, cm	C^o, cm	K_1, cm^2/sec	K_2, cm^2/sec
0.097	0.091	0.044	0.0067	0.0053
0.100	0.089	0.199	0.0065	0.0065
0.100	0.095	0.438	0.0075	0.0070
0.102	0.097	0.032	0.0052	0.0052
0.104	0.104	0.435	0.0061	0.0063
0.105	0.103	0.298	0.0067	0.0067
0.108	0.102	0.099	0.0063	0.0063
0.111	0.104	0.435	0.0057	0.0053
0.109	0.108	0.773	0.0065	0.0057
0.111	0.109	0.175	0.0073	0.0069
0.111	0.108	0.438	0.0074	0.0082
0.111	0.108	0.295	0.0070	0.0067
0.123	0.111	0.166	0.0068	0.0069
0.123	0.117	0.420	0.0061	0.0066
0.138	0.136	0.184	0.0073	0.0073
0.139	0.137	0.733	0.0073	0.0074
0.143	0.135	0.132	0.0066	0.0076
0.154	0.150	0.175	0.0067	0.0061
0.156	0.149	0.653	0.0074	0.0077
0.157	0.150	0.152	0.0060	0.0059
0.160	0.154	0.181	0.0070	0.0070
0.169	0.169	0.126	0.0070	0.0066

TABLE II. CONTINUED

D_1^o, cm	D_2^o, cm	C^o, cm	K_1, cm^2/sec	K_2, cm^2/sec
0.172	0.171	0.132	0.0080	0.0080
0.172	0.172	0.640	0.0091	0.0081
0.174	0.169	1.010	0.0076	0.0089
0.176	0.172	0.067	0.0064	0.0066
0.177	0.172	0.184	0.0083	0.0086
0.191	0.187	0.175	0.0081	0.0077
0.190	0.188	0.333	0.0074	0.0081
0.193	0.186	0.105	0.0071	0.0069
0.193	0.187	0.181	0.0080	0.0078
0.194	0.193	0.990	0.0084	0.0087
0.199	0.193	0.175	0.0083	0.0083
0.200	0.196	0.496	0.0085	0.0085
0.201	0.201	0.296	0.0079	0.0084
0.207	0.204	0.184	0.0076	0.0076

TABLE III. EXPERIMENTAL RESULTS FOR TWO METHYL ALCOHOL DROPLETS BURNING IN OPEN AIR

D_1^o, cm	D_2^o, cm	C^o, cm	K_1, cm^2/sec	K_2, cm^2/sec
0.149	0.137	0.120	0.0087	0.0078
0.146	0.145	0.128	0.0080	0.0080
0.149	0.148	0.023	0.0077	0.0077
0.149	0.146	0.426	0.0080	0.0076
0.145	0.137	0.642	0.0071	0.0073
0.140	0.136	0.044	0.0065	0.0065
0.180	0.168	0.117	-	0.0077
0.174	0.162	0.426	0.0083	0.0083
0.186	0.169	0.429	0.0084	0.0089
0.160	0.153	0.699	0.0070	0.0076
0.204	0.202	0.061	0.0082	0.0080
0.193	0.189	0.511	0.0093	0.0087
0.212	0.200	0.435	0.0082	0.0085

The observed values of $\overline{K} = (1/2)(K_1 + K_2)$, for droplets in which D_1^o and D_2^o did not differ by more than 20 percent, are plotted as a function of C^o in Figures 11 to 13 for n-heptane, ethyl alcohol, and methyl alcohol, respectively.

Reference to Figure 11 shows that the experimental results fall roughly into two categories depending on the initial average droplet diameter $\overline{D}^o = (1/2)(D_1^o + D_2^o)$. The average evaporation constant increases when C^o is reduced from larger values with negligible droplet interference, presumably because heat losses from the flame surface are reduced by the proximity of a second heat source for sufficiently small values of C^o; $\overline{K}$ reaches a maximum and then decreases again as C^o is made still smaller. A decrease in $\overline{K}$ for very small values of C^o could be produced through the creation of oxygen-deficient atmospheres resulting from increased competition for the oxygen supply furnished by convection and diffusion. On the basis of the proposed picture, the maximum in plots of $\overline{K}$ vs C^o results through a balance between two opposing factors; namely, decreased heat loss and decreased oxygen supply. The proposed interpretation, if applicable to spray combustion, may be of considerable practical importance.

The experimental data for n-heptane droplets plotted in Figure 11 suggest a strong dependence of $\overline{K}$ on $\overline{D}^o$ unless $\overline{K}$ is not really constant and varies continuously during burning. In this connection it should be emphasized that changes of $\overline{K}$ with time correspond to changes of the second derivative in plots of D^2 vs t. These second derivatives, in turn,

are not defined in our studies because of unavoidable scatter of the experimental data.

The observed values of $\overline{K} = 1/2(K_1 + K_2)$ for ethyl and methyl alcohol droplets as a function of C^o (See Figures 12 and 13, respectively.) do not permit any simple grouping into "small" and "large" droplets. It appears furthermore that $\overline{K}$ is a somewhat weaker function of $\overline{D}^o$ for the two alcohols than for n-heptane.

a. Correlations for n-Heptane Droplets

A number of attempts were made to relate $\overline{K}$ with simple functions of C^o, $C^o/\overline{D}^o$, $(C^o + \overline{D}^o)/\overline{D}^o$, etc., in order to reduce the scatter of experimental points for different values of $\overline{D}^o$. These efforts were, however, unsuccessful and suggest that the evaporation constant, K, which is independent of initial droplet diameter in single droplet studies, loses its significance as a basic correlating parameter for two n-heptane droplets burning in close proximity. Whether or not this conclusion applies to sprays cannot be said without further experimental work. In the meantime, however, it appears that, without further proof, the assignment of a value to K based solely on fuel properties and ambient fluid properties is subject to some question. The fact that $\overline{K}$ appears to vary with $\overline{D}^o$ is shown more directly by plotting $\overline{K}$ as a function of $\overline{D}^o$ for a group of experimental data with nearly equal values of $C^o + \overline{D}^o$.

Two burning droplets meet the requirements of geometric similarity when they have the same values of $C/\overline{D}$ and of D_1/D_2. It is

easily shown from plots of $C/\bar{D}$ versus $\bar{D}$ that nearly identical curves are characterized by greatly different values of $\bar{K}$ if the values of $\bar{D}^{o}$ are different. In other words, if $\bar{K}$ is really constant during burning, then the value of the evaporation constant is determined primarily by the initial conditions and only to a lesser extent by geometrical arrangement.

In view of the apparent dependence of $\bar{K}$ on $\bar{D}^{o}$, attempts were made to find a simple function of $\bar{K}$ and $\bar{D}^{o}$ which would depend only on C^{o} or on a known function of C^{o} and $\bar{D}^{o}$. An obvious choice is the ratio $\bar{K}' = \bar{K}/(\bar{D}^{o})^{2}$ to which we shall refer as the evaporation frequency.

In Figure 14 we have plotted $\bar{K}'$ as a function of $C^{o}/\bar{D}^{o}$. Reference to Figure 14 shows that a fair correlation of all of the experimental data has been obtained, the scatter being perhaps smaller in similar plots using C^{o} and $C^{o} + \bar{D}^{o}$ as abscissa than in the plot shown which uses the dimensionless quantity $C^{o}/\bar{D}^{o}$. In the absence of an adequate theory concerning droplet interference, the significance of the observed "correlations" is obscure, as is also any extrapolation to sprays. For this reason we must content ourselves with the observation that, for two n-heptane droplets burning in close proximity, the observed values of $\bar{K}/(\bar{D}^{o})^{2}$ are fairly well represented as a function of either $C^{o}/\bar{D}^{o}$, C^{o} or $C^{o} + \bar{D}^{o}$. Constancy of the evaporation frequency, except for variations in C^{o}, means that the fundamental burning rate law for

fixed values of C^o has the form

$$(\bar{D})^2 = (\bar{D}^o)^2 - \bar{K}'(\bar{D}^o)^2 t. \qquad (3)$$

b. Correlations for Ethyl and Methyl Alcohol Droplets

No outstandingly successful group for correlating the observed data for $\bar{K}$ as a function of $\bar{D}^o$, C^o, or $C^o/\bar{D}^o$ was found for the alcohols. The fact that $\bar{K}$ is sensitive to changes in $\bar{D}^o$ can be seen from Figures 15 and 16 in which curves are shown connecting the experimental results obtained for similar values of $C^o + \bar{D}^o$.

4. Dimensional Analysis Relating to the Burning of Liquid Droplets

Since the experimental data obtained in the present investigations are not intelligible on the basis of existing theoretical studies for the burning of single fuel droplets,[5] it is of interest to re-examine the problem at least qualitatively in an effort to understand the dimensionless groups which govern droplet burning. Detailed theoretical studies for single droplets are taken as a guide in this work. In view of the observed importance of chemical effects, which is emphasized by the differences between the alcohols and n-heptane, we cannot expect a complete answer without introducing explicitly dimensionless groups depending on chemical reaction rates. It is noted, however, that existing theoretical studies must be deficient since, for example, no really satisfactory explanation exists for the variation of burning rate with pressure.

a. The Burning of Single Droplets

The burning of a single stationary fuel droplet in an oxidizing atmosphere involves the following 23 variables: Mass burning rate of fuel droplet, $\dot{m}_F$; ratio of mass of fuel to mass of oxidizer at stoichiometric composition, ν; constant pressure, p; specific latent heat of evaporation of fuel droplet, $\Delta\ell$; standard specific enthalpy difference between reactants and reaction products, q; droplet diameter, D; specific heats at constant pressure, $c_{p,\ell}$, $c_{p,P}$, $c_{p,F}$, and $c_{p,O}$; densities, ρ_ℓ, ρ_F, and ρ_A; temperatures, T_ℓ, T_c, and $T_O = T_A$; thermal conductivities, λ_F and λ_A; viscosity coefficients, η_F, η_O, and η_A; diffusion coefficients, D_F and D_O. Here the subscripts, ℓ, P, F, O, and A, identify liquid fuel, combustion products, gaseous fuel, oxygen, and air, respectively. The temperature, T_c, is the temperature at the reaction surface. In our physical model the system is characterized by average diffusion, viscosity, and thermal conduction coefficients on the fuel and air sides of the flame front. A suitable set of 18 dimensionless groups* is the following: Schmidt number, $Sc = \eta_F / \rho_F D_F$; Prandtl number, $Pr = \eta_F c_{p,F} / \lambda_F$; ρ_ℓ / ρ_F; ρ_A / ρ_F; $c_{p,F}(T_c - T_\ell)/\Delta\ell$; D_O/D_F; λ_O/λ_F; η_O/η_F; η_A/η_F; $c_{p,O}/c_{p,F}$; $c_{p,P}/c_{p,F}$; $c_{p,\ell}/c_{p,F}$;

---

* According to the Buckingham Pi theorem, the number of dimensionless groups usually equals the number of variables minus the number of dimensions. There are five dimensions in the present problem: length, time, mass, temperature, heat.

ν; $q/\Delta\ell$; $(T_c - T_O)/(T_c - T_\ell)$; $p_A/\rho_A R_A T_O$, where R_A is the gas constant per gram of air; the Grashof number,* $Gr = D^3\rho^2 g\beta'(T_c - T_O)/\eta_A^2$, where g is the acceleration of gravity and $\beta' = \frac{1}{V}\frac{\partial V}{\partial T}\Big)_p$ is the coefficient of expansion of air; and K/D_F with $K = -d(D^2)/dt$ as the evaporation constant.

From the conservation of mass equations it is apparent that

$$\dot{m}_F = -\frac{d}{dt}\left(\frac{\pi}{6} D^3 \rho_\ell\right) = \frac{\pi}{4}\rho_\ell DK$$

whence

$$K/D_F = 4\dot{m}_F/\pi\rho_\ell D D_F \quad . \tag{4}$$

From the analytic solution 4 for $\dot{m}_F$ (using constant average values for specific heats and thermal conductivities) it is easily shown that

$$\frac{K}{D_F} = \frac{8(Sc)}{(Pr)}\frac{\rho_F}{\rho_\ell}\frac{\ell n\left[1 + c_{p,F}(T_c - T_\ell)/\Delta\ell\right]}{1 - (r_\ell/r_c)} \tag{5}$$

where r_ℓ/r_c represents the ratio of the radius of the fuel droplet to the radius of the flame surface. The ratio r_ℓ/r_c is a complicated function of several of the dimensionless groups listed previously. By utilizing experimental results obtained for the burning of single droplets we are now able to draw some useful qualitative conclusions.

It has been found that K is constant during burning and is therefore independent of the instantaneous value of D. Reference to the 18

---

* The Grashof number may well involve the diameter of the combustion surface, $2r_c$, rather than $D = 2r_\ell$. Since r_c and r_ℓ are related, this change will not affect the following arguments.

dimensionless groups shows that only Gr, which determines the magnitude of the convection currents, is a function of D. The constancy of K during burning therefore suggests that the convection currents induced during burning have no important effect on K. This observation is in agreement with the result that absolute values calculated for K, without considering the influence of convection, are in fair agreement with experimental measurements.[3] The functional relation given in Equation 5 also involves the assumption that convection effects may be neglected in first approximation.*

Reference to Equation 5 shows that K is a linear function of $\rho_F D_F$ and of other terms which are pressure independent, except possibly for r_ℓ / r_c. It has been found experimentally[4] that K varies as $p^{1/4}$. Hence, in terms of the simple picture used in the derivation of Equation 5, it follows that $1 - (r_\ell / r_c)$ must vary as $p^{-1/4}$ in order to account for the observed variation of K with pressure. In a more general analysis, which does not involve the assumption that chemical reactions are fast compared with the transport processes, a dependence of K on pressure could be introduced through pressure-sensitive chemical reaction rates. There is an obvious difficulty in attempting to account for the pressure variation of K through the influence of the Grashof number and free convection currents. Thus, since K is constant during burning, it must be independent of droplet or combustion surface diameter. But

---

* Convection currents and their influence on the mass burning rate of droplets are also discussed in the Appendix to Part I.[10] This problem has been investigated recently by Kumagai and Isoda.

Gr is a more sensitive function of this length than of pressure. Therefore, the pressure dependence of K should not be attributed to the influence of Gr.

b. Two Droplets Burning in Close Proximity

For two droplets of equal size, whose centers are separated by a distance, $C^o + \overline{D}^o$, we have the additional variable, $C^o + \overline{D}^o$, and the new dimensionless group, $D/(C^o + \overline{D}^o)$, where D is the diameter of the burning droplets. Since it has been found experimentally that K for each of the two droplets is also independent of the instantaneous value of D, it seems likely that convection effects are again of secondary importance. However, K may not be a function of $D/(C^o + \overline{D}^o)$ but rather of the initial drop diameter $\overline{D}^o$ itself (with the exact dependence varying with fuel type). This result is difficult to understand since it suggests that the entire burning process is influenced by the initial configuration unless, of course, K is not really constant during burning but varies so little that its change with time (i.e., the change of the second derivative in a plot of D^2 vs time) cannot be detected with certainty. If K is really constant during burning, then we are dealing again with a fundamental problem similar to that involved in the pressure dependence of K for single droplets. Questions of this sort are not answered by dimensional studies alone.

5. Experimental Studies on the Burning in Air of More Complex Stationary Fuel Droplet Arrays

a. An Array of Five Droplets

Experimental data have been obtained also for the burning of an array of five ethyl alcohol droplets in air. The results of these

experiments are presented in Figure 17. Four of the droplets were located at the corners of a square and the fifth in the center of the square. The square of the diameter for the droplet surrounded by four other droplets was again found to decrease linearly with time with the apparent value of K about 20 percent larger than for similar studies on two droplets burning in close proximity.

b. An Array of Nine Droplets

Nine droplets were arranged in a body-centered cubic array. The diameter of the center droplet was measured as a function of time for various lattice spacings.[11] The results of these experiments are presented in Table IV.

The droplet diameter squared decreased linearly with time which suggests that the appropriate law to use for an analytical treatment of spray combustion is $D^2 = (D^o)^2 - Kt$. The theoretical analysis of spray combustion is discussed more fully in the Appendix to Part I.

In the discussion of the correlation of $\overline{K}$ with C^o illustrated in Figure 11, it was stated that the decrease of $\overline{K}$ with small values of C^o was due to an oxygen-deficiency. Reference to the data given in Table IV, for the case where the droplets are in close proximity and the flames are completely merged, shows that K is reduced about 40 percent below the value for minimum interference. This fact tends to confirm the interpretation of the two-droplet data and illustrates the practical importance of the effect of fuel-rich zones on the burning rate.

TABLE IV. AVERAGE VALUES OF EVAPORATION CONSTANT (K) FOR NINE-DROPLET ARRAYS OF n-HEPTANE AND METHYL ALCOHOL AS FUELS BURNING IN STILL AIR

Fuel	Spacing of Corner Droplets (mm)	Average Value of K (cm^2/sec)	No. of Runs	Flame Shape
n-Heptane	9.5	.0127	2	Separate
n-Heptane	8.5	.0116	9	Separate
n-Heptane	7.5	.01225	8	Separate
n-Heptane	5.8	.0128	10	Partially Merged
n-Heptane	3.6	.0077	7	Completely Merged
Methyl Alcohol	8.5	.0104	1	Separate
Methyl Alcohol	7.5	.0109	7	Separate
Methyl Alcohol	5.8	.0108	7	Partially Merged
Methyl Alcohol	3.6	.00637	7	Completely Merged

6. Conclusions

The most important results obtained from these experimental investigations are the following: (1) Within the limits of experimental accuracy, the evaporation constant, K, is invariant with time for two droplets burning in close proximity and also for the center droplet of a five-droplet and of a nine-droplet array; (2) the absolute value of K is not determined by chemical composition alone but depends also on droplet arrangement. The first conclusion is of considerable practical interest since it supports the type of phenomenological considerations used by Probert for analyzing spray combustion. In general, it appears unlikely that D^2 will not decrease linearly with time, in good approximation, for arrays and sprays which are more complicated than the two-, five-, and nine-droplet arrays. The second conclusion underlines the doubts expressed in the introduction to Section A about the practical value of results derived from studies on single droplets and simple droplet arrays. It appears necessary to determine an effective value of the evaporation constant, K_{eff}, in order to apply an analysis based in part on the burning law, $D^2 = (D^o)^2 - K_{eff}t$. Single droplet and simple droplet arrays cannot provide K_{eff}. However, these simple models indicate the parameters which control the value of K_{eff}.

B. DIFFUSION FLAMES FOR THE PRODUCTION OF TITANIUM FROM SODIUM AND TITANIUM TETRACHLORIDE*

1. Introduction

Currently the production of titanium is a batch process. Titanium ore is found in certain sands in Florida and Australia. These sands are dredged and separated to obtain a concentrate of approximately 90 percent rutile, TiO_2. Coke and rutile are mixed and exposed to hot chlorine gas. The resulting titanium tetrachloride vapor is condensed. It is at this point in the presently used method for the production of titanium that the process becomes batch-type. The available raw material for a continuous flow process for titanium production is $TiC\ell_4$.

Titanium tetrachloride is a yellow liquid at room temperature. It has a boiling point of $136.4^{\circ}C$ and a specific gravity of 1.61. An interesting sidelight is that $TiC\ell_4$ reacts with the moisture in the atmosphere to form a dense smoke; this property has been used by the military to produce smoke screens.

A diffusion flame formed from titanium tetrachloride and sodium might possibly provide a means for the production of titanium. It is, of course, impossible to predict the physical state in which the titanium will be produced without performing relevant experiments.

---

* The author is indebted to Drs. Pol Duwez and S. S. Penner for suggesting the experiments described in this section.

Preliminary calculations of burning rates for heterogeneous diffusion flames (subsection 2) and of flame shapes for homogeneous diffusion flames (subsection 5) have been carried out using the applicable theoretical equations presented in reference 12. Because of large uncertainties in the transport properties for sodium vapor and titanium tetrachloride, it appeared highly desirable to perform some crude experiments which would at least establish the orders of magnitude of the most important parameters. The exploratory experiments and the conclusions derived from the results are described in subsection 3. A suggested program for additional fundamental studies on heterogeneous diffusion flames, which seem simpler for further development than homogeneous diffusion flames, is outlined in subsection 4. These suggested experimental investigations should (a) provide needed fundamental data for intelligent design of small-scale and large-scale combustors for the production of titanium and (b) help to define the experimental conditions, if any, under which titanium is produced in a suitable physical state.

2. Burning Rate Calculations for Heterogeneous Diffusion Flames

For the following approximate calculations, Godsave's[2, 3] simplified relation is used:

$$\dot{m}_F = \frac{4\pi \lambda r_\ell \ln \left[1 + (c_p)_F (T_c - T_\ell)/\Delta\ell \right]}{(c_p)_F (1 - r_\ell / r_c)} \qquad (6)$$

In Equation 6, $\dot{m}_F$ denotes the mass burning rate (in g/sec) of the liquid fuel droplet (corresponding to liquid sodium in the present case); λ is an average thermal conductivity (in cal/cm-sec-^{o}K) for the region between the sodium droplet and the flame surface; $(c_p)_F$ equals the average specific heat at constant pressure of the sodium vapor (in cal/g-^{o}K) between the (surface) temperature of the sodium (taken equal to the normal boiling point of sodium*) and the flame temperature, T_c; $\Delta\ell$ represents the specific latent heat of evaporation of the sodium vapor; r_ℓ and r_c denote, respectively, the radii of the equivalent spherical sodium droplet and concentric flame surface.

The flame temperature, T_c, will be assumed to be equal to the adiabatic flame temperature. In an actual diffusion flame T_c may well exceed the adiabatic flame temperature; however, if proper allowance is made for dissociation, it is unlikely that T_c will be significantly larger than the adiabatic flame temperature. The theoretical calculation of r_ℓ/r_c requires use of the complete theory presented in reference 12 and is greatly complicated by the lack of knowledge concerning appropriate numerical values of the transport parameters. For this reason it is preferable and simpler to utilize the experimental results described in subsection 3 which suggest that

---

* This approximation has no important influence on the calculated values for the mass burning rate.

$$r_\ell / r_c \ll 1 \,. \tag{7}$$

From Equations 6 and 7 it now follows that

$$\dot{m}_F = \frac{4\pi\lambda r_\ell}{(c_p)_F} \ln\left[1 + \frac{(c_p)_F (T_c - T_\ell)}{\Delta\ell}\right] \tag{8}$$

where the only remaining doubtful parameter is λ. The effective value of λ is also best determined empirically.

In the experiments described in the following subsection 3 it was not possible to follow r_ℓ as a function of time. However, the time, t_b, required to burn the sodium droplet completely could be estimated. This result may be used to determine the evaporation constant, K, which is independent of r_ℓ for steady burning. Thus the evaporation constant, K, is defined by the relation

$$r^2 = r_o^2 - (K/4)t \tag{9}$$

where r_o denotes the initial droplet radius. Hence

$$K = 4r_o^2/t_b \tag{10}$$

if t_b is the total burning time. Furthermore from the definition of K and $\dot{m}_F$ it follows that

$$K = 2(\dot{m}_F)_o/\pi \rho_\ell \ (r_o) \tag{11}$$

whence

$$(\dot{m}_F)_o = \frac{2\pi \rho_\ell r_o^3}{t_b} = \frac{4\pi\lambda r_o}{(c_p)_F} \ln\left[1 + \frac{(c_p)_F(T_c - T_\ell)}{\Delta\ell}\right] \qquad (11)$$

or

$$\lambda = \frac{\rho_\ell r_o^2 (c_p)_F}{2t_b \ln\left[1 + (c_p)_F (T_c - T_\ell)/\Delta\ell\right]} \cdot \qquad (12)$$

For the experimental conditions described in subsection 3, $r_o = 0.16$ cm, $t_b = 2.9$ seconds whence, $K = 0.035$ cm^2/sec. Also $(\bar{c}_p)_F = 0.216$ cal/g-^oK, $\rho_\ell = 0.929$ g/cm^3, $T_c = 3100^oK$, $\Delta\ell = 1091$ cal/g, $T_\ell = 1153^oK$, $\lambda = 2.68 \times 10^{-3}$ cal/cm-sec-^oK.

It is unlikely that changes in reactant composition and associated variations in T_ℓ and T_c will cause a profound change in the value of λ determined empirically by utilizing the procedure described above. On the basis of this assumption it is now possible to use Equation 8 to evaluate $\dot{m}_F/r_\ell$ for various typical gas compositions utilizing always a single liquid sodium droplet. The results of relevant calculations are listed in Table V for the following systems: $4Na(\ell) + TiC\ell_4(g)$, $(2x + 4)\,Na(\ell) + TiC\ell_4(g) + xC\ell_2(g)$, $A(g) + 4Na(\ell) + TiC_4(g)$. The mass production rate of Ti (g/sec) is obtained for $TiC\ell_4$ by multiplying the listed data for $\dot{m}_F/r_\ell$ by $0.520\, r_\ell$, for $TiC\ell_4 + xC\ell_2$ mixtures by multiplying by $1.04\, r_\ell / (x + 2)$, and for $TiC\ell_4$ + A mixtures by multiplication with $0.520\, r_\ell$.

TABLE V. ESTIMATED RATIO OF THE STEADY MASS BURNING RATE, $\dot{m}_F$, TO DROP RADIUS, r_ℓ, FOR LIQUID SODIUM IN DIFFERENT ATMOSPHERES

	$TiC\ell_4$	$TiC\ell_4 + xC\ell_2$			$TiC\ell_4 + A$
$T_c(^oK)$*	3100	4000	5000	6000	2500
$10^2 \times \dot{m}_F/r_\ell$ (g/cm-sec)	5.1	7.0	8.9	10.5	3.7

* The values of T_c have been estimated on the assumption that solid Ti and liquid $NaC\ell$ are produced very closely to the flame front.

The burning rate estimates given in Table V should provide a useful semi-quantitative indication of probable conversion rates in heterogeneous diffusion flames. The principal refinements in the numerical values would be expected to arise from corrections to the listed values for λ and T_c. Both of these parameters could be determined more reliably by further development of the experimental procedure described in subsection 3 or, preferably, by utilizing the suggested approach outlined in subsection 4.

The preceding calculations permit no conclusion concerning the physical state in which the titanium will be produced. The experiments outlined in subsection 3 show only that small metallic deposits of Ti are formed but do not define the physical state unambiguously. The

experiments suggested in subsection 4 should, however, settle this important question and, in particular, help to define an optimum choice of experimental conditions.

3. Some Experiments for Estimating the Mass Burning Rate of Liquid Sodium in an Atmosphere of Titanium Tetrachloride

As has been emphasized in the preceding discussion, the principal reason for carrying out preliminary experimental studies was to determine the unknown transport properties. Theoretical estimates of transport properties for the multi-component gas mixture in the region between the sodium droplet and the flame front are limited to order-of-magnitude accuracy.

a. Description of Apparatus and Experimental Procedure

A schematic diagram of the apparatus used in preliminary experiments is shown in Figure 18. It consisted essentially of a spherical glass vessel in the center of which (solid or liquid) sodium could be supported and exposed to gaseous $TiC\ell_4$ diffusing into the reaction chamber.

The glass flask had a diameter of about 23 cm and was provided with flat extension windows through which the flame surface and burning (evaporating) sodium could be photographed by means of a 35 mm Arriflex movie camera. At an angle of 90^{o} to the optical axis, a ground glass plug was located for inserting the sodium pellet. Preliminary experiments with solid sodium supported on quartz fibers showed that satisfactory ignition could not be obtained. For this reason, a pair of tungsten wire filaments, terminating in a No. 24 Brown and Sharpe

constantan wire, were used in subsequent experiments. The wires, when connected to a 6-volt storage battery and a suitable rheostat, served both as supports and as heating coils to melt the sodium and initiate burning; the heating coils were turned off while the sodium burned in an atmosphere of $TiC\ell_4$.

The entire apparatus was flushed with helium and evacuated prior to admitting $TiC\ell_4$. While the $TiC\ell_4$ was diffusing into the reaction flask, the system was closed off. A stable luminous flame was established as soon as the $TiC\ell_4$ entered the reaction vessel. Since the burning rate of heterogeneous diffusion flames is notably insensitive to pressure, no attempt was made to introduce corrections for the variable pressure within the system.

b. Experimental Results

From the photographs obtained during burning it was a simple matter to estimate the effective size of the flame shape. Unfortunately, the liquid sodium was clearly visible only at the beginning of the experiments because the intensely luminous flame front hid it from view during the remainder of the burning period. For this reason, it was not possible to follow the rate of decrease of the sodium pellet with time directly and thereby determine the evaporation constant, K. However, it is a simple matter to obtain K from the considerations described in the previous section. The principal deficiency of the present work is then the failure to verify the conventional burning rate law for heterogeneous

diffusion flames according to which the square of the droplet diameter decreases linearly with time. The validity of this burning rate law has been assumed throughout the present considerations.

The actual shape of the liquid sodium corresponded roughly to a cylindrical section 5 mm in height, 2 mm in radius, and subtending an angle of 105 degrees. (See Figure 19.) The total initial mass of the liquid sodium was 16.7 ± 8.4 milligrams, and the initial radius of an equivalent sphere was 1.6 mm. The total observed burning time, t_b, equals 2.9 ± .3 seconds. The equivalent sphere corresponding to the flame surface had a radius of 6.4 mm and changed little during burning. Hence the experimentally observed ratio of r_ℓ / r_c was less than 1/4, a result which was used in the preceding section to obtain a significant simplification of the burning rate expression.

The principal deficiencies of the experiment are the following:

(1) The liquid droplet was not spherical. On the basis of previous work it appears unlikely that this will produce a significant error.

(2) The evaporation constant, K, although obtained from a valid expression, is defined only if the square of the drop diameter decreases linearly with time. This burning rate law is known to hold for all heterogeneous diffusion flames which have been studied previously but has not been established for the Na - $TiC\ell_4$ system.

(3) The wires supporting the sodium acted as a heat sink during burning (as is suggested, for example, by the fact that the flame front is indented near the wires). Hence the observed values of K must be lower than the value which would be obtained in a steady-state experiment in which conduction heat losses are non-existent. The magnitude of this effect cannot be estimated reliably but corresponds probably to considerably less than a factor of two.

To summarize, although the experiment performed was crude, it is unlikely that the estimate for K is in error by more than a factor of two unless the assumed burning rate law does not apply. Hence it follows also, as shown in the preceding subsection 2, that mass production rates of the order of 3×10^{-2} (g of Ti)/sec can be achieved for each one cm radius porous plug wetted with liquid sodium. A description of a different procedure is now suggested which could well serve as a prototype for large-scale experiments.

4. A Suggested Apparatus for the Study of Production Rates of Titanium in Laminar Diffusion Flames Formed from Sodium and Titanium Tetrachloride

In Figure 20 is shown a schematic diagram of an apparatus designed for the continuous production of titanium from a Na - $TiC\ell_4$ diffusion flame utilizing a single porous plug through which liquid sodium is fed continuously at a rate equal to the mass conversion rate in the flame. The following essential experiments should be performed:

(1) By utilizing porous plugs of different diameters and by measuring the corresponding steady mass conversion rates, it should be possible to verify the basic burning rate law

$$r^2 = r_o^2 - (K/4)t$$

and to measure K directly for a variety of experimental conditions.

(2) Direct spectroscopic measurements should be made of T_c, possibly by utilizing the sodium line reversal method or by using the integrated emission of an isolated spectral line.

(3) The influence of gas composition and cooling rate on the physical state of the titanium produced should be amenable to direct experimental study. The temperature level at which the chamber walls are maintained may have a profound effect on the results.

(4) An obvious extension of the proposed experiment involves the use of multiple arrays of injection plugs for study of interference effects between burners during titanium production. For sufficiently large spacing between plugs, the single-plug data should apply. For closely-spaced plugs, on the other hand, the performance cannot be predicted but will have to be studied experimentally.

A detailed description of the suggested design for studies on continuously fed sodium droplets (See Figure 20.) is now given.

The dry box should be made of thick-walled aluminum with a heavy lucite cover. It must be hermetically sealed and flushed with dry nitrogen before melting the sodium. The container holding the liquid

sodium is made of No. 303 stainless steel with a heavy pyrex cover, which is bolted on after introduction of chunks of metallic sodium. The cooling water is allowed to circulate in order to protect the container top while the heater is operating and warms the lower parts of the container, tubing, and fittings (including the burner tip) to a controlled temperature. The pyrex cover on the sodium storage box permits visual inspection of the molten metal and liquid level.

Next the $TiC\ell_4$ container is filled and excess air pumped off. The combustion chamber and connecting lines should have been evacuated previously. After the sodium has been melted and equilibrium temperatures are attained, a (slight) pressure is applied to the liquid metal by using dry helium, the valve in the supply line to the burner is opened, and sodium is admitted until a liquid film has formed at the burner orifices in the combustion chamber. At this time $TiC\ell_4$ vapor is admitted to the combustion chamber, with the vacuum pump operating through suitably controlled valves. After ignition has occurred, the flow rates of Na and $TiC\ell_4$ are adjusted in such a way as to maintain a stable flame for the given mixture composition. If necessary, the $TiC\ell_4$ container may be heated in order to increase the flow of vapor.

Two or more large cold traps are needed between the combustion chamber and the vacuum pump in order to protect the pump.

All metal parts which are in contact with the sodium must be made of stainless steel. No pipe or tube fittings should be used;

joint flange seals and high-temperature bolts provide the only satisfactory connections. This type of joint requires close tolerances on the dimensions of the rings and grooves. The system must be thoroughly cleaned before use to remove any oils, greases, oxides, etc. The entire apparatus must, of course, be vacuum tight in order to prevent air, and especially moisture, from entering the combustion chamber.

The temperature of the sodium may be monitored by the use of one or more chromel-alumel thermocouples connected to a "Pyrovane" (Minneapolis - Honeywell) temperature controller which actuates the power output from a variac to the glass-covered heating coils surrounding the outside of the sodium container and pipe lines.

In order to interrupt the combustion reactions, it is necessary to cut first the helium pressure on the sodium lines and to shut the valve connection to the $TiC\ell_4$ reservoir. Helium is then admitted to the combustion chamber to force the sodium back through the supply line and past the valve. After turning off both valves to the $TiC\ell_4$ container, the heat may be turned off, and the system shut down. At this time the top of the combustion chamber may be removed safely for examination or cleaning. Liquid nitrogen could be used in the cold traps, removed after shut-down, and the trap contents pumped off with an aspirator and flushed with dry gas before the next experiment is performed.

Facilities for the use of chlorine and/or inert gas for increasing or decreasing the flame temperature are included in the chamber design.

Depending on the operating temperatures in the combustion chamber, solid titanium will be formed and deposited either with or without contamination by solid NaCℓ. The preceding detailed experimental procedure refers to methods for obtaining needed fundamental data and not to techniques for collecting titanium in a desired physical state. This problem can presumably be answered by empirical studies utilizing the suggested chamber design. The bottom part of the combustion chamber, which is removable, may be insulated from the principal parts of the reaction vessel and cooled, if necessary, in order to facilitate the collection of solid deposits. For chamber temperatures above the boiling point of sodium chloride, only solid or liquid titanium should be deposited at the bottom of the container.

5. Gaseous Diffusion Flames

The theory for calculating the flame boundary in laminar diffusion flames formed between reactants flowing with equal linear velocity in concentric cylindrical tubes has been given in reference 12. The flame boundary is defined by

$$\sum_{\phi>0}^{\infty} \frac{1}{\phi} \frac{J_1(\phi \frac{d}{2})\, J_o(\phi r_c)}{\left[J_o(\phi \frac{d'}{2})\right]^2} e^{-\frac{D\phi^2 Z}{U}} = \frac{d'\nu Y_{O,o}}{4d\left[Y_{F,o} + \nu Y_{O,o}\right]} - \frac{d}{4} \qquad (13)$$

Even if the approximations introduced into the derivation of this relation apply for Na - $TiC\ell_4$ flames, no quantitative calculations can be made without knowledge of the effective diffusion coefficient D.

The results of representative calculations on overventilated and underventilated diffusion flames are plotted in Figures 21 and 22, respectively, using the following design variables: $d' = 3$ inches, $d = 1.5$ inches, $U = 0.5$ inches/second. For the system Na - $TiC\ell_4$ it is easily shown that $\nu = 92/190 = 0.485$. The effective diffusion coefficient has been assumed to be 0.05 inches^2/second. The validity of the results shown in Figures 21 and 22 can be assessed only after reliable quantitative estimates for **D** have become available, for example, by proper interpretation of suitable experiments carried out with the apparatus described in subsection 4.

C. SCALING OF LIQUID FUEL ROCKET ENGINES

Most of the ideas presented in this section have been published and appear in reference 13.

1. Introduction

In recent publications on similarity analysis for the scaling of liquid-fuel rocket engines,[14-17] procedures have been developed both for scaling the steady aerothermochemistry and for maintaining similar conditions with respect to low-frequency and high-frequency motor oscillations. An important practical problem concerned with rocket motor development is the result of occurrence of uncontrolled high-frequency motor oscillations. The value of similarity analysis must ultimately be assessed in terms of our ability to design large engines with predictable performance on the basis of small-engine

test experience. In this connection, the most urgent experimental problem is that of determining minimum conditions required for effective practical scaling.

Three separate components, which are changed on scaling, may be considered qualitatively; any combination of these components may be of dominant importance in producing uncontrolled motor oscillations. Thus high-frequency oscillatory combustion involves, in general, the following separate phenomena: (a) a driving mechanism for producing the oscillations; (b) a coupling process which allows sustained oscillations; (c) damping mechanisms for preventing or minimizing motor oscillations.

A study of published scaling procedures shows clearly that it is impossible, except under very special conditions and for particular (and generally invalid) assumptions relating to the factors determining the chemical conversion time, to maintain exact similarity with respect to all phases of motor operation. For this reason, a preliminary experimental program on the development of rational scaling procedures should be designed to show which physicochemical processes are of dominant importance for a particular motor design.

If a strong driving mechanism is generally sufficient to induce unstable motor operation, we may be reduced to a study of microscopic phenomena involving the details of injector performance and combustion reactions. On the other hand, if we can prevent disastrous motor oscillation merely by preventing strong coupling between the driving

and sustaining mechanisms, then motor oscillations can presumably be avoided by retaining an invariant ratio of chemical conversion time to wave propagation time. Finally, it is conceivable that motor oscillation can be prevented by maintaining adequate damping, irrespective of the nature of the driving and sustaining processes. In this case a detailed analysis of the steady aerothermochemistry, of frictional losses, and of damping associated with oscillating gas flow through the nozzle may be required.

It is the purpose of theoretical studies on similitude in engine scaling to provide useful guides for experimental work. Meaningful answers to the questions raised in the preceding paragraphs can only be obtained empirically. To facilitate this program, a concise and more general approach to the scaling problem than has yet been used is presented in the following section. The results contain the rules of S. S. Penner and H. S. Tsien, of L. Crocco, and of M. Barrère as special cases.

2. Generalized Scaling Rules

For a given propellant system with fixed injector temperature the important similarity groups for stable motor operation are the Reynolds (Re) and first Damköhler* (D_1) similarity parameters; the Mach number (M) may become important for high-velocity processes involving oscillations.

---

* The first Damköhler similarity parameter is defined as the ratio of the residence time in the motor of a certain chemical species to the characteristic chemical conversion time for that species.

Here

$$Re = \rho v L/\eta \tag{14}$$

$$D_I = (L/v)/\tau \tag{15}$$

and

$$M = (\rho v^2/\gamma P)^{1/2} \tag{16}$$

where ρ denotes density; v, linear flow velocity; L, a characteristic chamber dimension; η, viscosity coefficient; τ, chemical conversion time; γ, ratio of specific heats; and P, chamber pressure. Except for the orifice diameter, conditions of geometric similarity shall be imposed with respect to all chamber dimensions in order to make all Reynolds numbers constant. For fixed propellants and injection temperature, the coefficients η and γ are fixed whereas ρ becomes effectively equivalent to P. Surface reactions are neglected throughout the following discussion although they may be important in selected motor applications.

The ratio i/i_m, where the subscript m specifies the model, is denoted by n_i; a symbol without a subscript m refers to the large motor. Here i may represent any of the independent variables. For example, $n_L = (L/L_m)$ is the ratio of a length in the large motor to the corresponding length in the model. It is expected, in general, that the ratio of mean droplet diameter, $\overline{D}$, to orifice diameter, h, is a function of the Weber (W) and Reynolds numbers based on the orifice

diameter.* In particular, we assume that

$$\frac{\bar{D}}{h} \sim \frac{1}{W^{\alpha} Re^{\beta}} \sim \left(\frac{h\Delta p}{\sigma}\right)^{-\alpha} (Pvh)^{-\beta} \tag{17}$$

where Δp is injector pressure drop; σ, interfacial tension; and α and β represent parameters which must be determined empirically. Finally, we introduce the hypothesis that the conversion time, τ, is determined through $\bar{D}$ and P:

$$\tau \sim \bar{D}^{\delta} P^{-m'} \tag{18}$$

with δ and m' denoting parameters which must also be obtained experimentally. Note that α and β depend primarily on the injector head design and on the physical properties of the propellants; the influence of operating conditions appears only in the variable, Δp. However the parameters, δ and m', are determined largely by the chemical properties of the propellants relative to the transport properties of the gases. Qualitatively, one may say that α and β characterize the spray formation whereas δ and m' characterize the spray combustion. Equation 18 is known to hold when $m' = 0.2$, $\delta = 2$, for the burning of stationary fuel droplets in an oxidizing medium.[19] A value $\delta = 2$ has been observed also in the burning of monopropellants and premixed bipropellant droplets in an inert atmosphere.[20] Finally, the observed dependence of τ on chamber

---

* For a detailed discussion of this problem as well as for some experimental correlations, see reference 18.

pressure and injection pressure drop for a nitric acid-furfuryl alcohol rocket engine, which follows from equations 17 and 18 with fixed values of h and $\beta = 0$, is in accord with the values[21] $\delta = 2$, $m' = 0.3$, and $\alpha = 0.8$.*

In the following discussion the Mach number will be neglected as a similarity parameter, thereby restricting our analysis to the development of scaling procedures for stably operating rocket engines. This is of practical importance in engine development programs.**

a. Similarity of Steady Aerothermochemistry

The conditions for maintaining constant Reynolds and first Damköhler numbers are

$$PvL = P_m v_m L_m \text{ and } L/v\tau = L_m/v_m \tau_m$$

whence it follows that

$$n_L = 1/n_P n_v \tag{19}$$

and

$$n_L/n_v = n_\tau . \tag{20}$$

Combining equations 19 and 20 we find the universal relation

$$n_\tau = 1/n_P n_v^2 \tag{21}$$

---

* It might be more logical to represent τ as the sum of times associated with evaporation, diffusion, chemical reaction, etc. In the absence of adequate data, however, we shall use the functional form of equation 18.

** In laboratory tests which are designed to test scaling rules rather than to develop engines, it may be important to scale also an unstably operating combustion chamber. In this case the Mach number should not be neglected as an important similarity group.

which has been discussed for chemical reactors, particularly[22, 23] for the case $n_P = 1$.

From equations 17 and 18 we find the following alternate relation for n_γ:

$$n_\gamma = n_\sigma^{\delta\alpha}\ n_h^{\delta(1-\alpha-\beta)} n_P^{-(\delta\beta+m')} n_{\Delta p}^{-\delta(\alpha+\beta/2)}$$

$$= n_\sigma^{\delta\alpha}\ n_h^{\delta(1-\alpha-\beta)} n_P^{-(\delta\beta+m')} n_v^{-2\delta(\alpha+\beta/2)} \qquad (22)$$

where we have assumed that

$$\Delta p \sim v^2,\ n_{\Delta p} = n_v^2 . \qquad (23)$$

Eliminating n_γ between equations 21 and 22 we find

$$n_P^{1-(\delta\beta+m')} n_v^{2-2\delta(\alpha+\beta/2)} = n^{-\delta\alpha} n_h^{\delta(\alpha+\beta-1)}$$

and after using equation 19 to eliminate n_P

$$n_v^{1-2\delta\alpha+m'} = n_\sigma^{-\delta\alpha}\ n_h^{\delta(\alpha+\beta-1)} n_L^{1-(\delta\beta+m')} . \qquad (24)$$

By the use of equations 19 and 24 we find also that

$$n_P^{-1+2\delta\alpha-m'} = n_\sigma^{-\delta\alpha}\ n_h^{\delta(\alpha+\beta-1)} n_L^{2-\delta(2\alpha+\beta)} . \qquad (25)$$

(1) Relation between geometric scale factor, n_L, and thrust scale factor, n

The continuity equation for the rocket chamber is

$$(Pvd^2)/(Pvd^2)_m = n \qquad (26)$$

where d identifies the chamber diameter and n is the thrust scale factor. Hence

$$n_P n_v n_L^2 = n$$

and, using equation 19,

$$n = n_L \quad ; \tag{27}$$

i.e., the geometric and thrust scale factors are identical. The relatively small effect of n_P on thrust, for pressures exceeding the normal operating pressure, is neglected.

(2) Scale factor for the orifice hole diameter

The continuity equation for flow through the orifice holes is

$$(vh^2)/vh^2)_m = n = n_L \tag{28}$$

since the number of orifice holes remains unchanged if geometric similitude is enforced. Hence

$$n_v n_h^2 = n_L \, . \tag{29}$$

We may combine equations 24 and 29 in order to obtain the appropriate scaling rule for the orifice diameter. The result is

$$n_h = n_\sigma^{\frac{\delta\alpha}{2(1+m') - \delta(1+3\alpha-\beta)}} \; n_L^{\frac{2m' - \delta(2\alpha-\beta)}{2(1+m') - \delta(1+3\alpha-\beta)}} \, . \tag{30}$$

(3) Scale factor for the linear flow velocity

The scale factor for the linear flow velocity may be obtained from equations 29 and 30. The result is

$$n_v = n_\sigma^{\frac{-2\delta\alpha}{2(1+m')-\delta(1+3\alpha-\beta)}} n_L^{\frac{2(1-m')-\delta(1-\alpha+\beta)}{2(1+m')-\delta(1+3\alpha-\beta)}} . \quad (31)$$

(4) Scale factor for the chamber pressure

From equations 19 and 29 it is apparent that

$$n_P = n_h^2 / n_L^2 .$$

Hence, using equation 30, we find

$$n_P = n_\sigma^{\frac{2\delta\alpha}{2(1+m')-\delta(1+3\alpha-\beta)}} n_L^{\frac{2\delta(\alpha+1)-4}{2(1+m')-\delta(1+3\alpha-\beta)}} . \quad (32)$$

(5) Scale factor for the nozzle throat diameter

From the continuity equation for flow through the nozzle throat of radius, r, we obtain

$$\frac{(Pr^2)}{(Pr^2)_m} = n = n_L \quad (33)$$

since the linear flow velocity at the nozzle throat is sonic irrespective of the motor size. Hence

$$n_P n_r^2 = n_L \quad (34)$$

and, using equation 32,

$$n_r = n_\sigma^{\frac{-\delta\alpha}{2(1+m')-(1+3\alpha-\beta)}} n_L^{\frac{(3+m')+(\delta/2)(\beta-5\alpha-3)}{2(1+m')-\delta(1+3\alpha-\beta)}} . \quad (35)$$

(6) Scale factor for the feed system

From the continuity equation for the feed system in which the linear flow velocity is v_f and the cross sectional area A_f we obtain

$$(v_f A_f)/(v_f A_f)_m = n = n_L$$

whence

$$n_{v_f} = n_L/n_{A_f} . \tag{36}$$

b. Similarity of Regenerative Cooling System[15]

Since the Reynolds and Prandtl numbers are fixed, the Nusselt heat transfer number also remains the same in the model and in the large engine. Hence the total heat, Q, which must be transferred to the interior motor walls, for chambers operating under similar conditions of temperature, pressure, and internal aerothermochemistry, must be directly proportional to the propellant consumption rate; this, in turn, varies linearly with the geometric scale factor, as has been shown in equation 28. Thus

$$n_Q = Q/Q_m = n_L . \tag{37}$$

Correspondingly, the heat transfer per unit area, q, must obey the scaling requirement

$$n_q = q/q_m = 1/n_L . \tag{38}$$

For motors operating with maintenance of complete similarity, the interior and exterior wall temperatures are fixed. Therefore, since the heat transfer per unit area varies as $1/n_L$, the

temperature gradient must be changed by the same factor; i.e., the wall thickness, w, must be scaled in geometric proportions:

$$n_w = w/w_m = n_L . \tag{39}$$

The heat transfer problem has now been reduced to a determination of the requirements in the cooling passages for transferring heat per unit area in accordance with the scaling condition expressed by equation 38. The Reynolds number in the cooling coils remains fixed if the cooling coils of diameter, C, are also scaled in geometric proportions; viz.,

$$n_C = C/C_m = n_L . \tag{40}$$

In the special case of a regeneratively cooled motor, the cooling passages correspond to the feeding system. For fixed propellants, constant Prandtl, Reynolds, and Nusselt numbers are maintained if

$$v_f\sqrt{A_f}/(v_f\sqrt{A_f})_m = n_{v_f}\sqrt{n_{A_f}} = 1$$

or

$$n_{v_f} = 1/n_L \tag{41}$$

a relation which is evidently consistent with equation 36 if geometric similarity is maintained for the cooling coils.

In practice, the scaling requirements for the wall thickness and cooling coil dimensions may be undesirable because of excessive weight, or they may be inconsistent with design restrictions such as those imposed by similarity analysis for maintenance of low-frequency stability.

The thickness of the outer wall of the cooling coils may be changed at will without affecting any of the other design restrictions obtained from similitude considerations.

c. Similarity of Sweat Cooling

If a fraction, ϵ , of the total propellant flow is used for sweat cooling, this fraction must be maintained at a fixed value as the engine is scaled.

Based on dimensional analysis, Wheeler[24] concluded that the temperature of a sweat-cooled wall is a function of the ratio of coolant mass flow per unit area to main stream mass flow per unit area, υ . Measurements of wall temperature in a short length of porous walled pipe, which were made by Duwez,[25] indicate that this ratio is the principal parameter determining the wall temperature. Rannie[26] developed a theory for predicting the temperature distribution in the laminar sublayer of a sweat-cooled wall; theoretical and experimental results were in agreement. Hence, to maintain fixed wall temperature, it is necessary to fix υ. The main stream mass flow per unit area varies as $1/n_L$, and the coolant mass flow per unit area will vary as $1/n_L$ if ϵ is fixed. The size and number of pores should be adjusted so that the velocity of the coolant normal to the wall is uniform and continuous.

d. Low-frequency Stability

L. Crocco[15] has discussed scaling procedures for a rigid and rigidly supported feeding system neglecting the compressibility of the

propellants. Low-frequency stability depends on several parameters including the ratio of the chemical conversion time, τ, to the residence time, τ_r; the relative pressure drop, $\Delta p/P$ (Δp = pressure drop across injection orifices; P = steady operating pressure in the combustion chamber); and an inertia parameter which equals the ratio of the kinetic energy of the propellants in the feeding system to the work done on the propellants by the pressure drops during the residence time.

The ratio of the chemical conversion time, τ, to the residence time, τ_r, is maintained invariant by enforcing the condition that the first Damköhler similarity group must remain fixed. This requirement has been introduced in the discussion relating to the steady aerothermochemistry and is given explicitly in equation 20. In view of equation 31, the result may be stated in the form

$$n = n_{\tau_r} = n_\sigma^{\frac{2\delta\alpha}{2(1+m') - \delta(1+3\alpha-\beta)}} n_L^{\frac{2(2m' - 2\delta\alpha + \delta\beta)}{2(1+m') - \delta(1+3\alpha-\beta)}} . \quad (42)$$

Next we consider the implications of the low-frequency stability requirement that

$$\frac{(\Delta p/P)}{(\Delta p/P)_m} = \frac{(\Delta p)}{(\Delta p)_m} \frac{P_m}{P} = 1 . \quad (43)$$

Since $\Delta p \sim v^2$, equation 43 is equivalent to the relation

$$(v^2/P)/(v^2/P)_m = n_v^2/n_P = 1 .$$

By using equations 31 and 32 it may then be shown that equation 43 reduces to the condition

$$\frac{-6\delta\alpha}{n_\sigma 2(1+m') - \delta(1+3\alpha-\beta)} \; n_L \frac{4(2-m') - 2\delta(\beta+2)}{2(1+m') - \delta(1+3\alpha-\beta)} = 1 . \tag{44}$$

For $n = 1$, $n_L \neq 1$, equation 44 corresponds to either of the relations

$$\left.\begin{aligned} 2(2-m') &= \delta(\beta+2) \\ \text{or} \qquad & \\ 2(1+m') - \delta(1+3\alpha-\beta) &\Rightarrow \infty . \end{aligned}\right\} \tag{44a}$$

The inertia parameter

$$J = K \frac{\ell_f}{A_f} \frac{F}{P\tau} \frac{P}{\Delta p} \tag{45}$$

must also remain invariant to maintain low-frequency stability.[15] Here K is a constant, ℓ_f represents the equivalent length of the feeding system with cross sectional area, A_f, F is the total propellant injection rate, and the other symbols have their usual meaning. The condition

$$J/J_m = 1 \tag{46}$$

then becomes

$$\frac{(\ell_f/A_f)}{(\ell_f/A_f)_m} = n_p n_\tau / n_L \tag{47}$$

in view of equation 43 and of equations 26 and 27. Using equations 32 and 42 we find the result

$$\frac{(\ell_f A_f)}{(\ell_f A_f)_m} = n_\sigma^{\frac{4\delta\alpha}{2(1+m')-\delta(1+3\alpha-\beta)}} \; n_L^{\frac{(3+\alpha+\beta)+2(m'-3)}{2(1+m')-\delta(1+3\alpha-\beta)}} . \qquad (48)$$

For scaling of the feeding system and cooling coils with maintenance of geometric similarity, the left-hand side of equation 48 evidently reduces to

$$(\ell_f/A_f)/(\ell_f/A_f)_m = 1/n_L .$$

Crocco[15] has indicated the need for extending the analysis presented in this section in order to make allowance for compressibility of the propellants, non-rigid feeding systems and/or non-rigid mountings, systems involving pumps for pressurization, etc. Details concerning studies of this type are best worked out in connection with motor development programs.

e. High-frequency Stability

High-frequency instabilities can presumably be controlled, for operating conditions otherwise similar, if the ratio of the chemical time, τ, is fixed with respect to the wave propagation times, τ_W. But the latter are linear functions of the chamber dimensions for sound waves as well as for shock waves provided the sound velocity remains invariant. Hence, for fixed temperature and γ, the similarity requirement for high-frequency instability may be written in the form

$$n_\tau = n_{\tau_W} = n_L . \qquad (49)$$

It is apparent that the condition expressed by equation 49 is not usually consistent with the similarity requirement for the steady aerothermochemistry or for low-frequency stability, both of which lead to the result given in equation 42.

Equation 49 expresses only the condition for similitude of the driving and coupling forces for oscillations. The forces producing oscillations must be balanced against the damping forces, of which the principal sources must be frictional losses. These, in turn, should be similar as long as the Reynolds number is constant. Damping, associated with the oscillating gas flow through the nozzle, is not similar unless the nozzles are scaled with maintenance of complete geometric similarity. However, for a well designed prototype it appears unlikely that damping through nozzle oscillations plays a dominant role.

3. Summary of Results and Discussion

The Penner-Tsien (P-T) relations correspond to the special case in which $m' = \alpha = \beta = 0$, $n_\sigma = n_p = 1$, and $\delta = 2$; they can be derived from the generalized results formally by letting m' approach infinity. The scaling procedure for the P-T rule is summarized in Table VI.

Crocco's second rule corresponds to the special conditions $\delta = 0$; the results thus obtained are listed in Table VII.

Barrère's scaling rule is based on an empirical expression for γ (derived from motor tests with red fuming nitric acid and furfuryl alcohol)

TABLE VI. THE P-T SCALING RULES FOR LIQUID-FUEL ROCKET ENGINES ($m' = \alpha = \beta = 0$, $n_\sigma = n_p = 1$, $\delta = 2$)

Steady Aerothermochemistry	Regenerative Cooling	Low-frequency Stability	High-frequency Stability
(1) $n = n_L$	(8) $n_{v_f} = 1/n_L$	(12) $n_L^2 = 1$	(14) $n_\tau = n_L$
(2) $n_h = n_L$	(9) $n_q = 1/n_L$	(13) $n_L^2 = 1$	
(3) $n_v = n_L^{-1}$	(10) $n_w = n_L$	(7) $n_\tau = n_L^2$	
(4) $n_p = 1$	(11) $n_C = n_L$		
(5) $n_r = n_L^{1/2}$			
(6) $n_{v_f} = n_L^{-1}$			
(7) $n_\tau = n_L^2$			

These rules are obtained from the general results most simply by setting $n_\sigma = 1$, $m' = \infty$.

TABLE VII. CROCCO'S SECOND SCALING RULE FOR LIQUID-FUEL ROCKET ENGINES

($\delta = 0$, $n_\sigma = 1$)

Steady Aerothermochemistry	Regenerative Cooling	Low-frequency Stability	High-frequency Stability
(1) $n = n_L$	(8) $n_{v_f} = 1/n_L$	(12) $n_L^{2(2 - m')/(1 + m')} = 1$	(14) $n_\tau = n_L$
(2) $n_h = n_L^{m'/(1 + m')}$	(9) $n_q = 1/n_L$		
(3) $n_v = n_L^{(1 - m')/(1 + m')}$	(10) $n_W = n_L$	(13) $\dfrac{(\ell_f/A_f)}{(\ell_f/A_f)_m} = \left(\dfrac{1}{n_L}\right)_{GS} = n_L^{(3 - m')/(1 + m')}$	
(4) $n_p = n_L^{- 2/(1 + m')}$	(11) $n_C = n_L$		
(5) $n_r = n_L^{1/2 + 1/(1 + m')}$		(7) $n_\tau = n_L^{2m'/(1 + m')}$	
(6) $n_{v_f} = \dfrac{n_L}{n_{A_f}} = \left(\dfrac{1}{n_L}\right)_{GS}$			
(7) $n_\tau = n_L^{2m'/(1 + m')}$			

The subscript, GS, identifies results appropriate for scaling with geometric similarity.

which is inconsistent with the assumptions expressed by equations 17 and 18. Thus Barrère starts from the relation

$$\tau \sim \Delta p^{-r'} P^{-m'} \tag{50}$$

which is in agreement with equations 17 and 18 if $\delta\alpha = r'$, $\beta = 0$, $n_\sigma = 1$, and $n_h = 1$ in the relation for $\bar{D}$ only. This last requirement is probably to be attributed to the fact that motor tests were carried out without variations in orifice diameter. The statement $n_h = 1$ in the expression for $\bar{D}$ is inconsistent with Barrère's scaling rule for n_h derived from other considerations. It will be interesting to see if motor tests with variable injection orifices are really correlated better by equations 17 and 18 than by equation 50. The scaling procedure of Barrère can be obtained by repeating the analysis described in detail in the text with equation 50 substituted for equations 17 and 18. The results derived from this study are summarized in Table VIII.

Reference to Tables VI to VIII shows that the scaling requirements for the steady aerothermochemistry are not generally consistent either with those for low-frequency stability or with those for high-frequency stability.* Thus it is impossible to scale with maintenance of complete similarity with respect to all the important variables. From the practical point of view, the most important discrepancy is that between the usually

---

* The only exception is provided by Crocco's second rule in the unlikely case that $m' = 1$; see Table VII.

TABLE VIII. BARRÈRE'S SCALING RULE FOR LIQUID-FUEL ROCKET ENGINES

($\delta = 2$, $\delta\alpha = r'$, $\beta = 0$, $n_\sigma = 1$, $n_h = 1$ in the expression for $\bar{D}/h$)

Steady Aerothermochemistry	Regenerative Cooling	Low-frequency Stability	High-frequency Stability
(1) $n = n_L$	(8) $n_{v_f} = 1/n_L$	(12) $n_L^{\,2\,\frac{2 - (m' + r')}{1 + m' - 2r'}} = 1$	(14) $n_\gamma = n_L$
(2) $n_h = n_L^{\,\frac{m' - r'}{1 - 2r' + m'}}$	(9) $n_q = 1/n_L$		
(3) $n_v = n_L^{\,\frac{1 - m'}{1 - 2r' + m'}}$	(10) $n_W = n_L$	(13) $\frac{(\ell_f/A_f)}{(\ell_f/A_f)_m} \left(= \frac{1}{n_L}\right)_{GS} = n_L^{\,\frac{3 - m' - 2r'}{1 + m' - 2r'}}$	
(4) $n_p = n_L^{\,\frac{-2(1 - r')}{1 - 2r' + m'}}$	(11) $n_C = n_L$		
(5) $n_r = n_L^{\,\frac{1}{2}\,\frac{3 + m' - 4r'}{1 + m' - 2r'}}$		(7) $n_\gamma = n_L^{\,\frac{2(m' - r')}{1 - 2r' + m'}}$	
(6) $n_{v_f} = \frac{n_L}{n_{A_f}} \left(= \frac{1}{n_L}\right)_{GS}$			
(7) $n_\gamma = n_L^{\,\frac{2(m' - r')}{1 - 2r' + m'}}$			

The effect of setting $n_h = 1$ in the expression for $\bar{D}/h$ can be accounted for by repeating the entire analysis. The subscript, GS, identifies results appropriate for scaling with geometric similarity.

contradictory requirements for n_γ in the analysis for the steady aerothermochemistry and for high-frequency stability. As was stated by Penner in an earlier paper [16] and mentioned again in the introduction to the present survey, it is not yet possible to assess the significance of this discrepancy. For this reason a preliminary test program on engine scaling should involve an investigation of high-frequency stability of properly performing engines in which only the scaling rule $n_\gamma = n_L$ is accounted for.

The steady aerothermochemistry and high-frequency stability requirements are satisfied simultaneously if

$$n_\sigma^{\frac{2\delta\alpha}{2(1+m')-\delta(1+3\alpha-\beta)}} n_L^{\frac{2(2m'-2\delta\alpha+\delta\beta)}{2(1+m')-\delta(1+3\alpha-\beta)}} = n_L$$

$$n_\sigma^{\frac{2\delta\alpha}{2(1+m')-\delta(1+3\alpha-\beta)}} n_L^{\frac{2(m'-1)+\delta(1+\beta-\alpha)}{2(1+m')-\delta(1+3\alpha-\beta)}} = 1 . \qquad (51)$$

According to equation 51, variation of n_σ can, in principle, be used to maintain similarity for the steady aerothermochemistry and high-frequency stability. Whether or not this program is practically feasible remains to be seen and cannot, in any event, be decided until reliable empirical information is available, not only on the validity of the functional relations given in equations 17 and 18, but also on the absolute values of the parameters δ, α, β, and m'.

It is interesting to note that equation 51 is satisfied exactly when $n_\sigma = 1$ if either

$$\left.\begin{aligned} 2(1 - m') &= \delta(1 + \beta - \alpha) \\ 2(1 + m') &\neq \delta(1 + 3\alpha - \beta) \end{aligned}\right] \qquad (52)$$

or

$$\left.\begin{aligned} 2(1 + m') - \delta(1 + 3\alpha - \beta) &= \infty \\ 2(1 - m') - \delta(1 + \beta - \alpha) &\neq \infty \end{aligned}\right] . \qquad (53)$$

The latter relation would never be expected to apply.* For $m' = 0$, $\delta = 2$, $\alpha = \beta = 0$, the first expression given in equation 52 is satisfied; however, in this case all the exponents for n_L appearing in the scaling rules for n_h, n_v, n_P, n_r, and n_σ become indeterminate and, furthermore, the second condition given in equation 52 is not satisfied. In fact, the rule $m' = 0$, $\delta = 2$, $\alpha = \beta = 0$ for $n_\sigma = 1$ corresponds simply to the P-T procedure.

According to Barrère's findings for a bipropellant motor utilizing red fuming nitric acid and furfuryl alcohol, $m' = 0.3$, $\delta = 2$, $\delta\alpha = 1.6$, $\beta = 0$. Then

$$2(1 - m') = 1.4$$

and

$$(1 + \beta - \alpha) = 0.4 .$$

Therefore the conditions given in equation 52 are far from satisfied.

Extensive tests yielding a correct functional form for γ are the first requirement of an intelligent scaling program. Important steps in

---

* The statement given in equation 53 should not be confused with the formal procedure used to derive the P-T results from the generalized expressions by setting $m' = \infty$.

this direction have already been made by Crocco and Barrère, but additional quantitative experimental work, for a variety of propellant systems, is urgently needed.

4. Application of Results to a Program for Testing Scaling Procedures for High-frequency Stability

From the preceding discussion it is apparent that an experimental program aimed at verification or rejection of the various scaling rules needs a rocket motor with interchangeable components in order to change selectively certain ratios, n_i. Interchangeability of rocket components gives the maximum number of experiments in the most economical manner. Three components can be used; namely, the injector head, combustion chamber, and nozzle.

Suppose, however, that one wishes to test only one of the scaling procedures; namely, that for high-frequency stability. The question then arises, How complex must the rocket motors be to provide an adequate test of the scaling procedures? The following discussion answers this question.

In order to test the validity of the scaling rule, one wants to vary systematically the variables while maintaining the equality of the ratios given in equation 49. A method which uses the minimum number of different components is to change the injector head and retain the same combustion chamber and nozzle. This means that

$$n_L = n_{\tau_W} = n_\tau = 1 \ . \tag{54}$$

Combining equations 22 and 54 and letting $n_\sigma = 1$, the following equation can be derived:

$$n_h \delta(1 - \alpha - \beta)\, n_P - (\delta\beta + m')\, n_v - 2\delta(\alpha + \beta/2) = 1 .$$

From the continuity equations for the injector head and the chamber for the special case where n_L is unity, one obtains

$$n_P = n_h^2 .$$

Combination of the preceding two equations leads to the relation

$$n_{\Delta p} = n_v^2 = n_h^{\frac{2m' - \delta(1 - \alpha - 3\beta)}{\delta(\alpha + \beta/2)}} . \qquad (55)$$

To test the scaling rule a series of experiments should be conducted with Δp_m varied over as large a range of values as possible. The orifice holes in the injector are drilled out to give a new value for n_h. Call the rocket motor with the smaller injector orifice diameter the model. A new series of experiments are run, once again varying Δp over as wide a range as possible.

Suppose that high-frequency instability occurred at a particular value of Δp_m. If the high-frequency scaling rule is valid and if the conversion time is given correctly by equation 22, then the same instability should occur for the injector pressure drop

$$\Delta p = \Delta p_m n_h^{\frac{2m' - \delta(1 - \alpha - 3\beta)}{\delta(\alpha + \beta/2)}} .$$

As previously stated, it is necessary to determine the dependence of the conversion time, τ, on the numerous variables before conclusive statements as to the validity of certain scaling rules can be made.

PART II. SPECTROSCOPIC STUDIES OF FLAMES

One of the characteristic features of combustion reactions is the emission of radiation. Spectroscopic studies may be used, in principle, to reveal information about the nature of stable and transient chemical species (for example, C_2, CH, OH, and HCO), population temperatures and departures from thermal equilibrium, translational temperatures, etc.

One of the least understood problems in combustion is the nature and structure of turbulent flames. In recent years a number of papers have been published on the spectral emission properties of turbulent flames and the implications of these studies insofar as turbulent flame structure is concerned. In view of the extensive spectroscopic facilities available for our investigations, we started an experimental program with the idea of extending and clarifying the observational data. During the period devoted to the construction of the turbulent burner, the writer in collaboration with F. A. Williams[1] performed a theoretical study suggested by Dr. S. S. Penner which was designed to clarify the theoretical implications of spectral emission data on turbulent flames. In particular, it was our purpose to determine if spacial separation of radical emission could provide a significant criterion for proving or disproving that a turbulent flame consists of a wrinkled laminar flame. Our joint paper with F. A. Williams[1] showed that the answer was negative. In the following Part II, Section A, we present a more detailed discussion and extension of the earlier theoretical study which shows that spacial separation of radical emission cannot be used either to prove or disprove that a turbulent flame is composed of wrinkled laminar flames.

Since our theoretical studies on spectral emission did not produce significant suggestions for important spectroscopic studies of turbulent flames, the experimental program was changed to an examination of the flame-holding region formed with the reverse-jet flame holders. These experimental studies are described in Part II, Section B.

A. APPARENT EMISSION INTENSITIES FROM A WRINKLED LAMINAR FLAME MODEL OF A TURBULENT FLAME*

1. Introduction

In current turbulent flame theories we consider the wrinkled laminar flame as a valid description for a restricted range of conditions. These conditions are characterized by the magnitude of a parameter which has been defined by Kovasznay[2] and which equals the ratio of a typical velocity gradient in the approaching cold flow to a typical velocity gradient in a laminar flame. For low values of the parameter, the turbulent flame may be represented by the superposition of rapidly fluctuating wrinkled laminar flame fronts. It is of interest to examine the apparent emission profiles that are to be expected from a turbulent flame composed of continuous wrinkled laminar flames.

Experimental evidence to support various turbulent flame theories has been proposed.[3, 4] In this section we present a possible interpretation for one of these experiments; namely, for observed emission profiles.

---

* The material in this section has been published as Technical Report No. 22, United States Army Contract, DA-04-495-Ord-446, March, 1958, and has also been submitted for presentation at the Seventh International Combustion Symposium, London, August, 1958.

2. A Model for the Determination of Apparent Emission Profiles

Consider an open turbulent flame which is burning above a rectangular exit port as illustrated in Figure 1. A set of collimating slits defines the rectangular observation section, which cuts one leg of the turbulent flame brush. The observation section will be traversed by the rapidly moving luminous laminar flame fronts. The apparent emission intensity depends on the concentration of emitters within the field of view. Reference to Figure 2 shows that this concentration varies with time as the wrinkled laminar flame weaves in and out of the observation section.

The measured intensities are always averages over space and, for slow recording, also over time. The radiation from a turbulent flame composed of continuous wrinkled laminar flames may be described by using a laminar flame of fixed optical depth, X, and assigning a probability function, $p(x_1)$, which measures the probability of occurrence of the center of the laminar flame at a particular coordinate (measured, for example, along the stream lines with origin at the cold-gas side of the turbulent flame brush), x_1, within the turbulent flame region.

The model which is proposed here involves two-dimensional wrinkling, i.e., the location of the wrinkled laminar flame is completely specified by a function $f(x,y)$ where the coordinate y is measured parallel to the long dimension of the burner port. The model does not account for any change in $f(x,y)$ over a distance measured normal to the xy plane and equal to the height of the observation section.

In order to locate the center of a three-dimensional wrinkled laminar flame, it is necessary to use three coordinates. However, we believe that a model using two-dimensional wrinkling will reveal the essential features of the radical and product emission profiles.

As an approximation to the emission intensities from a steady-state laminar flame, it is assumed that the radicals (e.g., C_2 or CH) radiate with equal intensity over a region of width $2\underline{a}$ measured along the x-direction. Outside of this region the emitted intensity from the radicals is zero. At the center of this region, the emission intensity from the products (e.g., H_2O) rises to a constant value and extends a distance $\underline{c}$ downstream. (See Figure 3.) The center of the region of reactant emission is located at $x = x_1$. Let $2\underline{b}$ be the width of the observation section, the center of which is located at x_o. The total energy per second, I, received by the spectrograph entrance slit from the observation section will now be calculated. For fixed values of $\underline{b}$ and L the energy per second passing through the collimating slits of the instrument depends only on $(x_o - x_1)$, i.e., on the separation between the slit position and the position of the center of the laminar flame. (See Figure 4.) In Figure 3, A_P and A_R are constants and equal the energy per second received by unit width of slit. The subscripts, P and R, refer to products and radicals, respectively. Self-absorption of the distributed emitters is neglected, and only the usual case $b \geq a$ is considered.

The energy per second which is emitted from the products and passes through the slits is

$$I_P(x_o - x_1) = \begin{cases} 2bA_P & \text{for } x_o - x_1 \geqslant b \\ A_P(b + x_o - x_1) & \text{for } b \geqslant x_o - x_1 \geqslant -b \\ 0 & \text{for } -b \geqslant x_o - x_1 \end{cases} \qquad (1)$$

Similarly, for the reactants,

$$I_R(x_o - x_1) = \begin{cases} 0 & \text{for } x_o - x_1 \geqslant b + a \\ A_R\left[b + a - (x_o - x_1)\right] & \text{for } b + a \geqslant x_o - x_1 \geqslant b - a \\ 2aA_R & \text{for } b - a \geqslant x_o - x_1 \geqslant -(b - a) \\ A_R\left[b + a + x_o - x_1\right] & \text{for } -(b - a) \geqslant x_o - x_1 \geqslant -(b + a) \\ 0 & \text{for } -(b + a) \geqslant (x_o - x_1) \,. \end{cases} \qquad (2)$$

The center of the laminar flame at x_1 is assumed to satisfy the inequality $0 \leqslant x_1 \leqslant \alpha$, where α is nearly the width of the turbulent flame brush. The space- (and time-) averaged energy per second passing through the slits is

$$E(x_o) = \int_0^{\alpha} p(x_1)\, I(x_o - x_1)\, dx_1 \,. \qquad (3)$$

Assuming a linear response of the measuring instrument, the readings will be proportional to $E(x_o)$. The probability function is assumed to be non zero only in the range $0 \leqslant x_1 \leqslant \alpha$ and is normalized in such a way that $\int_0^{\alpha} p(x_1)dx_1$ equals unity. The apparent emission profiles have been calculated [1] for the case where it is equally likely to find the laminar flame anywhere within the turbulent flame zone; the probability function associated with this case is identified as the square probability function.

The calculations based on the square probability function will be compared, in the following section, with results derived for other distribution functions.

3. Calculation of the Apparent Emission Profiles for Different Probability Functions $p(x_1)$

When the width of the laminar flame region defined by the emission due to products, c, is nearly equal to the width of the turbulent flame brush, α, then the apparent product emission profiles for the turbulent flame are qualitatively the same as those calculated using an infinite value for c. The emission profiles will now be determined for infinite c using three probability functions, all of which are triangular. The emission profiles will also be computed for a finite value of c using a square probability function.

a. Apparent Emission Profiles for Infinite Values of c

The first probability function considered has the peak probability on the burned-gas side ("hot-peak probability function"), the second has the peak on the unburned-gas side ("cold-peak probability function"), and the third is symmetrical about the center of the turbulent flame brush.

(1) Profiles for the hot-peak probability function

The probability function is given by

$$p(x) = \begin{cases} 0 & \text{for } x < 0 \\ (2x/\alpha^2) & \text{for } 0 \leqslant x \leqslant \alpha \\ 0 & \text{for } \alpha < x \end{cases} \qquad (4)$$

where α is, for all practical purposes, the thickness of the turbulent flame brush.

Combining equations 1 through 4, a piecewise solution can be obtained. It is convenient for purposes of identification to divide the turbulent flame zone into several regions and to number these regions consecutively. The regions are shown in Figure 5 for both the products and the reactants. The numbers of the regions are used as subscripts to the average received energy in order to indicate the physical location of the center of the slit (x_o) with respect to the turbulent flame in which the equation for $E(x_o)$ is valid.

To illustrate the derivation, consider the solution for $E_R(x_o)$ valid in region 5. Here

$$E_{R5} = \int_{x_o-(b+a)}^{x_o-(b-a)} \delta_R x_1 \left[b+a-(x_o-x_1)\right] dx_1 + \int_{x_o-(b-a)}^{x_o+(b-a)} \delta_R a x_1 dx_1 + \int_{x_o+(b-a)}^{\alpha} \delta_R x_1 \left[b+a+x_o-x_1\right] dx_1 \tag{5}$$

where $\delta_R = 2A_R/\alpha^2$. The portion of the integral from $x_1 = 0$ to $x_1 = x_o - (b + a)$ is zero because there is zero illumination of the slit.

$E_R(x_o)$ is given by the following equations:

$$
\begin{aligned}
E_{R1} &= 0 \\
E_{R2} &= (\delta_R/6)(b+a+x_o)^3 \\
E_{R3} &= (\delta_R/6)\left[(b+a+x_o)^3 - (x_o+b-a)^3\right] \\
E_{R4} &= (\delta_R/6)\left[(x_o+b+a)^3 - (x_o+b-a)^3 - (x_o-b+a)^3\right] \\
E_{R5} &= (\delta_R/6)\left[(x_o+b+a)^3 - (x_o+b-a)^3 - (x_o-b+a)^3 + (x_o-b-a)^3\right] \\
E_{R6} &= (\delta_R/6)\left[(x_o-b-a)^3 - (x_o-b+a)^3 - (x_o+b-a)^3\right] + A_R(x_o+b+a) - \frac{2}{3}A_R\alpha \\
E_{R7} &= (\delta_R/6)\left[(x_o-b-a)^3 - (x_o-b+a)^3\right] + 2A_R a \\
E_{R8} &= (\delta_R/6)\left[(x_o-b-a)^3\right] + \frac{2}{3}A_R\alpha - A_R(x_o-a-b) \\
E_{R9} &= 0 \ .
\end{aligned}
\tag{6}
$$

For the products the following equations apply:

$$
\begin{aligned}
E_{P1} &= 0 \\
E_{P2} &= (\delta_P/6)(x_o + b)^3 \\
E_{P3} &= (\delta_P/6)\left[(x_o + b)^3 - (x_o - b)^3\right] \\
E_{P4} &= -(\delta_P/6)(x_o - b)^3 - \frac{2}{3}A_P\alpha + A_P(x_o + b) \\
E_{P5} &= 2bA_P \ .
\end{aligned}
\tag{7}
$$

(2) Profiles for the cold-peak probability function

The probability function for this case is given by

$$
p(x) = \begin{cases} 0 & \text{for } x < 0 \\ (2/\alpha)(1 - x/\alpha) & \text{for } 0 \leq x \leq \alpha \\ 0 & \text{for } \alpha < x \ . \end{cases}
\tag{8}
$$

We use again the nomenclature defined in Figure 5. It is interesting to note that the function $E_R(x_o)$ associated with the hot-peak probability

function is the mirror image of the function $E_R(x_o)$ associated with the cold-peak probability function. Hence it is necessary to determine only the function $E_P(x_o)$. In Figure 5 the peak for p(x) is now at the unburned-gas side of the turbulent flame brush. The results for $E_P(x_o)$ are:

$$E_{P1} = 0$$

$$E_{P2} = (\delta_P/6)\left[3\alpha(x_o + b)^2 - (x_o + b)^3\right]$$

$$E_{P3} = (\delta_P/6)\left[3\alpha(x_o + b)^2 - (x_o + b)^3 - 3\alpha(x_o - b)^2 + (x_o - b)^3\right] \qquad (9)$$

$$E_{P4} = A_P(x_o + b) - \frac{1}{3}A_P\alpha - (\delta_P/6)\left[3\alpha(x_o - b)^2 - (x_o - b)^3\right]$$

$$E_{P5} = 0 \ .$$

(3) Profiles for a symmetrical triangular probability function

In this case the probability function p(x) is

$$p(x) = \begin{cases} 0 & \text{for } x < 0 \\ 4x/\alpha^2 & \text{for } 0 \leqslant x \leqslant \alpha/2 \\ (4/\alpha^2)(\alpha - x) & \text{for } \alpha/2 \leqslant x \leqslant \alpha \\ 0 & \text{for } \alpha < x \ . \end{cases} \qquad (10)$$

It is necessary to consider new computational regions which are shown in Figure 6.

The probability function and $I_R(x_o - x_1)$ (See Figure 11.) are now symmetrical. Hence it is only necessary to ascertain $E_R(x_o)$ for $x_o \leqslant \alpha/2$ and to use the relation

$$E_R(x_o) = E_R(\alpha - x_o) \ . \qquad (11)$$

Applying the same procedure as before, the following results are obtained:

$$E_{P1} = 0$$

$$E_{P2} = (\delta_P/3)(x_o+b)^3$$

$$E_{P3} = (\delta_P/3)\left[(x_o+b)^3 - (x_o-b)^3\right]$$

$$E_{P4} = (\delta_P/3)\left[3\alpha(x_o+b)^2 - (x_o+b)^3 - (x_o-b)^3 + \alpha^3/4 - (3\alpha^2/2)(x_o+b)\right] \qquad (12)$$

$$E_{P5} = (\delta_P/3)\left[3\alpha(x_o+b)^2 - (x_o+b)^3 - 3\alpha(x_o-b)^2 + (x_o-b)^3 - 3\alpha^2 b\right]$$

$$E_{P6} = (\delta_P/3)\left[3\alpha^2 x_o - \alpha^3 - 3\alpha(x_o-b)^2 + (x_o-b)^3\right]$$

$$E_{P7} = 2bA_P \quad .$$

If we call the values for E_R, calculated by using the hot-peak probability function, E'_{R1}, E'_{R2}, E'_{R3}, etc., then it is possible to relate these to the first four regions of the apparent emission profile for the reactants using the symmetrical triangular probability function. Thus

$$E_{R1} = 0$$

$$E_{R2} = 2E'_{R2}$$

$$E_{R3} = 2E'_{R3}$$

$$E_{R4} = 2E'_{R4}$$

$$E_{R5} = 2E'_{R5} \qquad (13)$$

$$E_{R6} = (\delta_R/3)\left[3\alpha(x_o+b+a)^2 - (x_o+b+a)^3 - (x_o+b-a)^3 + (x_o-b-a)^3 - (x_o-b+a)^3 - (3\alpha^2/2)(x_o+b+a) + \alpha^3/4\right]$$

$$E_{R7} = (\delta_R/3)\left[3\alpha(x_o+b+a)^2 - (x_o+b+a)^3 + (x_o+b-a)^3 - 3\alpha(x_o+b-a)^2 + (x_o-b-a)^3 - (x_o-b+a)^3 - 3\alpha^2 a\right] \quad .$$

b. Apparent Emission Profile for Finite Values of $\underline{c}$ and

$p(x_1) = \frac{1}{\alpha}$ for $0 \leqslant x_1 \leqslant \alpha$

The function $E_R(x_o)$ is independent of $\underline{c}$. However, $E_P(x_o)$ does depend on the value of $\underline{c}$. $E_P(x_o)$ has been calculated for finite values of $\underline{c}$ in the range $b \leqslant c \leqslant \alpha - 2b$. Reference to Figure 7, which is a reproduction of Figure 10 appearing in reference 3, shows that the product emission falls to zero in a distance of about 4.5 mm after reaching its maximum value. These results suggest that $\underline{c}$ should be finite although for $c \geqslant (\alpha + 2b)$ the essential features of $E_P(x_o)$ are unchanged as the infinite tail of product radiation is cut off in any case. For $c < (\alpha + 2b)$ the character of $E_P(x_o)$ changes. When a finite $\underline{c}$ is used, $I_P(x_o - x_1)$ becomes

$$I_P(x_o - x_1) = \begin{cases} 0 & \text{for } x_o - x_1 \leqslant -b \\ A_P(b + x_o - x_1) & \text{for } -b \leqslant x_o - x_1 \leqslant b \\ 2bA_P & \text{for } b \leqslant x_o - x_1 \leqslant c - b \\ A_P\left[c + b - x_o + x_1\right] & \text{for } c - b \leqslant x_o - x_1 \leqslant c + b \\ 0 & \text{for } c + b \leqslant x_o - x_1 \end{cases} \quad (14)$$

New computational regions are defined in Figure 8.

Since the values of $E_P(x_o)$ are the same in regions 1, 2, and 3 regardless of the value of $\underline{c}$, it is only necessary to determine $E_P(x_o)$ for regions 4 to 9. The apparent product emission profiles based on a square probability function and using a finite value for $\underline{c}$ are found to be

$$
\begin{aligned}
E_{P1} &= 0 \\
E_{P2} &= (A_P/2\alpha)(x_o + b)^2 \\
E_{P3} &= 2A_P b x_o/\alpha \\
E_{P4} &= (A_P/2\alpha)\left[\, 4bc - (x_o - b - c)^2 \,\right] \\
E_{P5} &= 2bA_P c/\alpha \quad .
\end{aligned}
\tag{15}
$$

For the special case when p(x) is symmetrical about $\alpha/2$, $E_P(x_o)$ for a finite $\underline{c}$ is symmetrical about $1/2(\alpha + c)$. Hence the profile in region 6 can be calculated by using suitable values of x_o in the equation for E_{P4}; similarly, the profile in region 7 can be calculated using E_{P3}, etc.

c. Comparison of the Apparent Emission Profiles

The solid curves in Figure 9 refer to the apparent emission profiles obtained by using a square probability function and infinite $\underline{c}$.[1] The dotted curves refer to results obtained in the present investigations. The same numerical values were used for A_P, A_R, $\underline{a}$, $\underline{b}$, and α.

When $\underline{c}$ is not infinite, the location and the magnitude of the maximum of the apparent product emission profile, E_{Pmax}, depends on the value of $\underline{c}$. For the square probability function, the peak value of the apparent product emission profile occurs at $x_o = 1/2(\alpha + c)$; the peak value for the apparent reactant emission profile occurs at $\alpha/2$. (See Figure 10.) Hence the separation of the profile peaks for the square probability functions is $c/2$. The foregoing statements can be generalized for symmetrical probability functions. (See subsection 5.)

The dependence of E_{Pmax} on the value of $\underline{c}$ is illustrated in Figure 10 for a square probability function. As indicated in Figure 10, E_{Pmax} equals $2bA_P(c/\alpha)$; the peak value is directly proportional to $\underline{c}$.

4. Determination of the Probability Function from Measured Apparent Emission Profiles

The determination of the probability function $p(x_1)$ from measured apparent emission profiles is the inverse of the problem considered in subsection 3. The problem involves the solution of equation 3 for $p(x_1)$. Reference to equation 3 shows that it is a linear integral equation of the first kind.

When $E(x_o)$ has an analytical representation, it is possible to solve for $p(x)$ by the use of Fourier transforms. The Fourier transforms involving the coupled functions $\overline{f}(\omega)$ and $f(z)$ are

$$\overline{f}(\omega) = \frac{1}{\sqrt{2\pi}} \int_{-\infty}^{\infty} f(z) \exp(i\omega z)dz$$

$$f(z) = \frac{1}{\sqrt{2\pi}} \int_{-\infty}^{\infty} \overline{f}(\omega) \exp(-i\omega z)d\omega . \qquad (16)$$

Representing $I(x_o - x_1)$ in terms of its Fourier transform $\overline{I}(\omega)$ and combining the result with equation 3 leads to the expression

$$E(x_o) = \frac{1}{\sqrt{2\pi}} \int_0^{\alpha} \left(\int_{-\infty}^{\infty} \overline{I}(\omega) \exp\left[-i\omega(x_o - x_1)\right] p(x_1)d\omega \right) dx_1 . \qquad (17)$$

Interchanging the order of integration yields the result

$$E(x_o) = \frac{1}{\sqrt{2\pi}} \int_{-\infty}^{\infty} \bar{I}(\omega) \exp(-i\omega x_o) d\omega \int_{0}^{\alpha} p(x_1) \exp(i\omega x_1) dx_1 \ . \qquad (18)$$

Reference to equations 4 and 10 shows that $p(x_1)$ vanishes except in the range $0 \leqslant x \leqslant \alpha$. Therefore we may change the limits of integration in equation 18 from $x = 0$ and $x = \alpha$ to $x = -\infty$ and $x = \infty$. This results in

$$E(x_o) = \int_{-\infty}^{\infty} \bar{I}(\omega) \exp(-i\ x_o) \bar{p}(\omega) d\omega \ . \qquad (19)$$

But we may express $E(x_o)$ also in terms of its transform; equating the resulting expression to the right-hand side of equation 19, we find*

$$E(x_o) = \frac{1}{\sqrt{2\pi}} \int_{-\infty}^{\infty} \bar{E}(\omega) \exp(-i\omega x_o) d\omega = \int_{-\infty}^{\infty} \bar{I}(\omega)\bar{p}(\omega) \exp(-i\omega x_o)\ d\omega \ . \qquad (20)$$

According to equation 20, the Fourier transform of the probability function may be expressed in terms of $\bar{E}(\omega)$ and $\bar{I}(\omega)$ as follows:

$$\bar{p}(\omega) = \frac{1}{\sqrt{2\pi}} \frac{\bar{E}(\omega)}{\bar{I}(\omega)} \ . \qquad (21)$$

---

* Equation 20 can be written down immediately using the convolution (Faltung) theorem for Fourier Transforms once the limits for the integration over x have been changed to $-\infty$ and ∞ .

Inversion of $\bar{p}(\omega)$ then gives $p(x_1)$ in terms of the transforms of $E(x_o)$ and $I(x_o - x_1)$, viz.,

$$p(x_1) = \frac{1}{2\pi} \int_{-\infty}^{\infty} \left[\bar{E}(\omega)/\bar{I}(\omega) \right] \exp(-i\omega x_1) d\omega . \qquad (22)$$

Equation 22 is valid provided $\bar{I}(\omega) \neq 0$ in the interval $-\infty < \omega < \infty$; the solution is valid when $\bar{I}(\omega) = 0$ if $\bar{E}(\omega)$ simultaneously becomes zero but the ratio remains finite. The functions $I_P(x_o - x_1)$ and $I_R(x_o - x_1)$ are plotted in Figure 11 for the emission model shown in Figure 3. In order to evaluate the transform for I_P when $\underline{c}$ is infinite, we replace the constant value $2bA_P$ in equation 1, which equals I_P for $(x_o - x_1) \geqslant b$, by $2bA_P \exp(-\nu\xi)$ where $\xi = x_o - x_1$ and ν is an adjustable parameter. The Fourier transform for $I_P(\xi)$ is

$$\bar{I}_P(\omega) = \frac{1}{\sqrt{2\pi}} \int_{-b}^{b} A_P(b + \xi) \exp(i\omega\xi) d\xi + \frac{1}{\sqrt{2\pi}} \int_{b}^{\infty} 2A_P b \exp(-\nu\xi + i\omega\xi) d\xi . \qquad (23)$$

The second integral has the value $-\left[2A_P b/(i\omega - \nu)\right] \exp\left[(i\omega - \nu)b\right]$ which reduces to $-(2A_P b/i\omega)\exp(i\omega b)$ in the limit as ν approaches zero. The complete transform for infinite $\underline{c}$ becomes

$$\bar{I}_P(\omega) = \frac{2A_P}{\sqrt{2\pi}} \frac{i \sin\omega b}{\omega^2} . \qquad (24)$$

The Fourier transform for I_R is

$$\bar{I}_R(\omega) = \frac{4A_R}{\sqrt{2\pi}\,\omega^2} \sin\omega a \sin\omega b \ . \qquad (25)$$

When $\underline{c}$ is finite, the transform of I_P can be obtained from equation 25 by noting that I_P and I_R are similar if the origin for I_P is translated by $c/2$ in the positive ξ-direction. Hence, using the translational property of Fourier transforms, $\bar{I}_P$ is given by

$$\bar{I}_P(\omega) = \frac{4A_P}{\sqrt{2\pi}\,\omega^2} e^{i\omega c/2} \sin\omega b \sin\frac{1}{2}\omega c \ . \qquad (26)$$

In accord with our postulated model (Compare equation 22.) we should obtain the same value for $p(x_1)$ from $\bar{E}_R(\omega)/\bar{I}_R(\omega)$ and from $\bar{E}_P(\omega)/\bar{I}_P(\omega)$.

5. Determination of $p(x_1)$ from the Experimental Data of Reference 3

In this subsection two topics will be considered. First, a procedure will be described for estimating $\underline{a}$ and $\underline{c}$. Combining the experimentally determined product and radical profiles with the postulated functions I_P (for finite $\underline{c}$) and I_R, the equality of the Fourier transforms $\bar{p}_P(\omega) = \bar{p}_R(\omega)$ may be used to derive a formula for the laminar flame half width $\underline{a}$. The measured separation between the peaks of the radical and product profiles gives a value for the width $\underline{c}$. The separation between the peaks will be equal to $c/2$ whenever $p(\alpha/2 - x) = p(\alpha/2 + x)$, $I_R(-x_o + x_1) = I_R(x_o - x_1)$, and $I_P\left[\frac{c}{2} - (x_o - x_1)\right] = I_P\left[\frac{c}{2} + (x_o - x_1)\right]$. These seemingly complex conditions will be clarified in a later paragraph.

The second topic is concerned with the derivation of a formula for $p(x_1)$ when the apparent emission profiles $E(x_o)$ are nearly gaussian. After obtaining an analytical representation for $E(x_o)$, its Fourier transform $\bar{E}(\omega)$ is obtained. Using $\bar{E}(\omega)$ and the appropriate intensity transform $\bar{I}(\omega)$ from equation 25 or 26, we obtain $p(x_1)$ from equation 22. The probability function $p(x_1)$ will necessarily be symmetrical about the center of the turbulent flame ($x = \frac{1}{2}\alpha$) for gaussian profiles $E(x_o)$ whenever I_R and I_P have an axis of symmetry.

a. Numerical Calculation of the Parameters a and c

We proceed to use the fact that the Fourier transforms $\bar{p}_R(\omega)$ and $\bar{p}_P(\omega)$ are equal in order to estimate an effective value for the laminar flame half width a .

From the separation of the peak intensities for CH and H_2O, the parameter c is found to be 10.4 mm. We will now consider under what conditions the separation of peaks is equal to c/2. If m_P is the coordinate of the peak of the apparent product emission profile, then

$$\frac{\partial E_P(m_P)}{\partial x_o} = 0 = \int_0^{\alpha} p(x_1) \frac{\partial I_P(m_P - x_1)}{\partial x_o} dx_1 . \qquad (27)$$

Also if m_R is the coordinate of the peak of the apparent radical emission profile, then

$$\frac{\partial E_R(m_R)}{\partial x_o} = 0 = \int_0^{\alpha} p(x_1) \frac{\partial I_R(m_R - x_1)}{\partial x_o} dx_1 . \qquad (28)$$

Assume that $p(\frac{\alpha}{2} - x) = p(\frac{\alpha}{2} + x)$. Change the variable of integration by letting $x_1 = \frac{\alpha}{2} + z$ from which it follows

$$\int_{\frac{\alpha}{2}}^{\frac{\alpha}{2}} p(\tfrac{\alpha}{2} + z) \frac{\partial I_P(m_P - \frac{\alpha}{2} - z)}{\partial x_o} \, dz \, . \tag{29}$$

If $I_P\left[\frac{c}{2} - (x_o + x_1)\right] = I_P\left[\frac{c}{2} + (x_o + x_1)\right]$ then the derivative in equation 29 will be an odd function of z only if $m_P = \frac{c}{2} + \frac{\alpha}{2}$; the derivative must be odd in order for the integral to vanish. If $I_R(-x_o + x_1) = I_R(x_o - x_1)$ then the derivative of I_R with respect to x_o in equation 28 will be an odd function of z only if $m_R = \alpha/2$. Therefore

$$\int_{\frac{\alpha}{2}}^{\frac{\alpha}{2}} p(\tfrac{\alpha}{2} + z) \frac{\partial I_R(m_R - \frac{\alpha}{2} - z)}{\partial x_o} \, dz \tag{30}$$

will vanish. The separation of peaks is $m_P - m_R = c/2$.

The data presented in Figure 7 were used to obtain numerically the values of $\overline{E}_R(\omega)$ and $\overline{E}_P(\omega)$. The curve for H_2O was assumed to represent the products whereas the curve for CH was used for the radicals. Since the curves given in Figure 7 are photographic records, it is necessary to account for the variation of the sensitivity of the film with wavelength. Also, in order to relate $E(x_o)$ to the percentage of the transmitted intensity $T(x_o)$ which is plotted in Figure 7, a suitable calibration factor must be specified. We write

$$E(x_o) = g(\lambda)\left[\, 1 - .01T(x_o) \,\right] \quad . \tag{31}$$

where $g(\lambda)$ then accounts for the variation of film sensitivity with wavelength and for the calibration factor.

Separation of $\bar{E}_R(\omega)$ into its real and imaginary parts leads to

$$\bar{E}_R(\omega) = \frac{1}{\sqrt{2\pi}} \int_{-\infty}^{\infty} E_R(x) \cos\omega x dx + \frac{i}{\sqrt{2\pi}} \int_{-\infty}^{\infty} E_R(x) \sin\omega x dx \quad . \tag{32}$$

It is now convenient to introduce the following notation:

$$g(\lambda_R)R_c(\omega) = \frac{1}{\sqrt{2\pi}} \int_{-\infty}^{\infty} E_R(x) \cos\omega x dx = \frac{g(\lambda_R)}{\sqrt{2\pi}} \int_{-\infty}^{\infty} \left[\, 1 - (.01)T_R(x) \right] \cos\omega x dx,$$

$$g(\lambda_R)R_s(\omega) = \frac{1}{\sqrt{2\pi}} \int_{-\infty}^{\infty} E_R(x) \sin\omega x dx = \frac{g(\lambda_R)}{\sqrt{2\pi}} \int_{-\infty}^{\infty} \left[\, 1 - (.01)T_R(x) \right] \sin\omega x dx. \tag{33}$$

Similar symbols will be utilized to represent the real and imaginary parts of the Fourier transform of the apparent product emission profile, i.e., $\bar{E}_P(\omega) = g(\lambda_P)(P_c + iP_s)$.

Combining equations 21, 25, 26, and 31 to 33, and using equation 21 for both products and radicals, we find that

$$\frac{g(\lambda_R)}{A_R} \frac{R_c + iR_s}{\sin\omega a} = \frac{g(\lambda_P)}{A_P} \frac{P_c + iP_s}{\exp(\frac{1}{2} i\omega c) \sin(\omega c/2)} \quad . \tag{34}$$

It is interesting to note that the equality $\bar{p}_P(\omega) = \bar{p}_R(\omega)$ does not depend on the value of the slit half width b. The real part of equation 34 is

$$\frac{KR_c}{\sin\omega a} = P_c \cot(\omega c/2) + P_s \quad , \tag{35}$$

while the imaginary part becomes

$$\frac{KR_s}{\sin\omega a} = P_s \cot(\omega c/2) - P_c \quad . \tag{36}$$

In equations 35 and 36 we have introduced the parameter

$$K = \frac{g(\lambda_R)A_P}{g(\lambda_P)A_R} \quad .$$

The transforms required in equations 35 and 36 have been evaluated. The results of the numerical integrations are presented in Figure 12.

The laminar flame half width a is determined from either equation 35 or equation 36 by using two different values of ω, i.e., ω' and ω''. A numerical value for the ratio $\sin\omega' a/\sin\omega'' a$ is obtained and the unknown parameter K is eliminated. In this manner a has been found to have the reasonable value 0.3 mm.

In the limit as ω approaches zero, equation 35 becomes

$$K = \frac{2P_c a}{R_c c} \quad . \tag{37}$$

As $\omega \longrightarrow 0$ equation 36 reduces to

$$K = \frac{2a\int xE_P(x)dx}{c\int xE_R(x)dx} \quad . \tag{38}$$

Once a and c are known, K may be evaluated. The numerical value obtained from equation 38 is 0.081.

For values of $\omega > 0.2\pi$, P_c, P_s, R_c and R_s rapidly approach zero because of cancellation of areas as $\cos\omega x$ or $\sin\omega x$ in the integrands oscillate rapidly. This is illustrated in Figure 13 which shows the integrand of P_s for $\omega = 0.333\pi$. For large ω, it is difficult to determine P_c, P_s, R_c, and R_s accurately.

The apparent slit half-width b is determined through the relation

$$\int_{-\infty}^{\infty} \omega^2 \frac{P_c \cos\omega(x + \frac{c}{2}) + P_s \sin\omega(x + \frac{c}{2})}{\sin\omega b \, \sin(\omega c/2)} d\omega = K \int_{-\infty}^{\infty} \frac{\omega^2 (R_c \cos\omega x + R_s \sin\omega x)}{\sin\omega a \, \sin\omega b} d\omega \tag{39}$$

which may be derived from equations 22, 25, and 26.

In a properly executed experiment the parameters b and K are known from the experimental conditions. The parameters a and c are properties of the (wrinkled) laminar flame used to represent the turbulent flame.

b. Probability Function from a Gaussian Representation of the Apparent Emission Profiles

Frequently it is possible to obtain an analytical representation of experimental data (e.g., the data of reference 3) by using a gaussian curve for the apparent intensity, i.e.,

$$E(x_o) = E_{max} \exp\left[-\sigma (x_o - m)^2 \right] . \tag{40}$$

In equation 40, m is the coordinate of the maximum value of the emission profile E_{max}, and σ is a parameter which determines the width of the profile; both σ and m are related to α, the width of the turbulent flame brush.

The apparent emission profiles obtained from reference 3 have been fitted to a gaussian curve. (See Figure 14.) Both the apparent product and radical emission profiles are very well described near their peak values. However, the tail of the radical profile falls to zero more sharply than the gaussian curve.

The Fourier transform of equation 40 is

$$\bar{E}(\omega) = \frac{E_{max}}{\sqrt{2\sigma}} \exp\left[- (\omega^2/4\sigma) + im\omega \right] . \tag{41}$$

Substitution of equation 41 into equation 22 leads to

$$p(x_1) = \frac{E_{max}}{2\pi\sqrt{2\sigma}} \int_{-\infty}^{\infty} \frac{\exp\left[- (\omega^2/4\sigma) + i\omega(m - x_1) \right]}{\bar{I}(\omega)} d\omega . \tag{42}$$

The symmetry properties of $p(x_1)$ can be readily determined from equation 42. When the radical emission is used to calculate the probability function, then

$$p(x_1) = \frac{E_{max}}{2\pi\sqrt{2\sigma}} \int_{-\infty}^{\infty} \frac{\exp\left[- (\omega^2/4\sigma) + i(\alpha/2)\omega - i\omega x_1 \right]}{\bar{I}_R(\omega)} d\omega . \tag{43}$$

Also

$$p(\frac{\alpha}{2} - x_1) = \frac{E_{max}}{2\pi\sqrt{2\sigma}} \int_{-\infty}^{\infty} \frac{\exp\left[-(\omega^2/4\sigma) + i\omega x_1\right]}{\bar{I}_R(\omega)} d\omega \ , \qquad (44)$$

and

$$p(\frac{\alpha}{2} + x_1) = \frac{E_{max}}{2\pi\sqrt{2\sigma}} \int_{-\infty}^{\infty} \frac{\exp\left[-(\omega^2/4\ ) - i\omega x_1\right]}{\bar{I}_R(\omega)} d\omega \ . \qquad (45)$$

By letting $\omega = -\omega$ in equation 45 the equality $p(\frac{\alpha}{2} + x_1) = p(\frac{\alpha}{2} - x_1)$ can be established provided $\bar{I}_R(\omega) = \bar{I}_R(-\omega)$. When the probability function is calculated from the product emission

$$p(x_1) = \frac{E_{max}}{2\pi\sqrt{2\sigma}} \int_{-\infty}^{\infty} \frac{\exp\left[-(\omega^2/4\sigma) + i(1/2)(\alpha + c - 2x_1)\omega\right]}{\bar{I}_P(\omega)} d\omega. \qquad (46)$$

Reference to equation 26 shows that $\bar{I}_P(\omega)$ equals the product of $\exp(i\omega c/2)$ and an even function of ω. The factor $\exp(i\omega c/2)$ appears in numerator and denominator and can be cancelled. Again it is possible to show that $p(\frac{\alpha}{2} + x_1) = p(\frac{\alpha}{2} - x_1)$.

Substitution of equation 25 into equation 42 leads to

$$p(x_1) = \frac{1}{8\sqrt{\pi\sigma}} \frac{E_{max}}{A_R} \int_{-\infty}^{\infty} \frac{\omega^2 \exp\left[-(\omega^2/4\sigma) + i(m - x_1)\omega\right]}{\sin\omega a \sin\omega b} d\omega \qquad (47)$$

for the probability function based on radical emission. A graph of the integrand of equation 47 reveals that the contributions to the integral for $\omega > 0.2\pi$ are negligibly small. This result suggests the desirability of expanding the denominator in a series about $\omega = 0$. The integral of equation 47 may then be evaluated. Expanding $(\sin \omega a)(\sin \omega b)$ and neglecting terms of the order of ω^3, or higher, equation 47 becomes

$$p(x_1) = (Q/ab) \int_{-\infty}^{\infty} \exp\left[- (\omega^2/4\sigma) + i\omega(m - x_1)\right] d\omega$$

$$+ \frac{Q(a^2 + b^2)}{6ab} \int_{-\infty}^{\infty} \omega^2 \exp\left[- (\omega^2/4\sigma) + i\omega(m - x_1)\right] d\omega \qquad (48)$$

where Q equals $E_{max}/(8\sqrt{\pi\sigma}\ A_R)$. The first integral is easily evaluated and yields a gaussian curve. Expressing the imaginary exponential of the second integral in terms of trigonometric functions gives

$$\int_{-\infty}^{\infty} \omega^2 \exp\left[- (\omega^2/4\sigma)\right] \cos(m - x_1)\omega\, d\omega \ .$$

Expanding the cosine in an infinite series will give integrals which can be readily determined. The probability function is

$$p(x_1) = \frac{E_{max}}{4abA_R} \varphi(x_1) \qquad (49)$$

where

$$\varphi(x_1) = e^{-\sigma(m - x_1)^2} + \frac{1}{3}(a^2 + b^2) \sum_{n=0}^{\infty} (-1)^n \frac{(m - x_1)^{2n}}{n!} (2n + 1)\sigma^{n+1} \tag{50}$$

The infinite series may be simplified. Introducing the quantity $h = \sigma(m - x_1)^2$, we find

$$p(x_1) = \frac{E_{max}}{4abA_R} \left[1 + \frac{1}{3}(a^2 + b^2)\sigma(1 - \sigma h) \right] e^{-h} \tag{51}$$

The probability function has also been derived including terms in ω^4 for the series expansion of $(\sin \omega a)(\sin \omega b)$. The details will not be shown; however, the probability function in this case is

$$p(x_1) = \frac{E_{max} e^{-h}}{4abA_R} \left\{ 1 + \frac{a^2 + b^2}{3}\sigma(1 - \sigma h) - \frac{\sigma^2}{30}\left[b^4 + (10/3)a^2b^2 + a^4 \right](4h^2 - 12h + 3) \right\}. \tag{52}$$

The third term within the brackets is on the order of 10^{-6} for values of h within the turbulent flame brush. The probability function associated with the apparent emission profile which can be represented by a gaussian curve is a constant times the equation for the profile plus small terms. The small terms depend on a, b, and σ. The function $\varphi(x)$ is plotted in Figure 15 for a = 0.3 mm, b = 0.6 mm, and σ = 0.0412 mm^{-2}. The probability function can also be determined from $E_P(x_o)$. It is necessary to include terms to ω^8 for the series expansion of $(\sin\omega b)\left[\sin(\omega c/2) \right]$.

The probability function based on the apparent product emission profile must equal the probability function calculated from the apparent radical emission profile. At $m = x_1$, the formula for the probability function is simplified and provides a convenient expression for calculating b. Thus

$$b = \frac{c}{2} K \frac{\left[1 - T_{Rmin}\right]}{\left[1 - T_{Pmin}\right]} \frac{\left[1 + (1/12)(4a^2 + c^2)\sigma_P\right]}{\left[1 + (1/3)(a^2 + b^2)\sigma_R\right]} \qquad (53)$$

corresponds to equation 39. To evaluate b from equation 53, an average value of K from equations 37 and 38, values for minimum transmitted intensity from Figure 7, and values for a and c as found previously were used. The effective value of b for the published data is 0.59 mm.

For a gaussian representation, the tails of the apparent emission profiles extend to infinity. One would expect the probability function to be so small outside of the visible turbulent flame brush that no measurable radiant energy is observed in this region.

6. Discussion and Conclusions

The apparent emission profiles have been calculated for several different probability functions. Reference to Figure 9 shows the dependence of the apparent emission profiles on the probability function, $p(x_1)$. The similarity between the radical profiles and the probability function is apparent.

The analysis based on a square probability function and a finite value of $\underline{c}$ reveals the following information. The distance downstream over which the reaction products radiate, $\underline{c}$, has two effects on the apparent product emission profiles. The value of E_{Pmax} and the coordinate at which E_{Pmax} occurs depend on $\underline{c}$. For values of $\underline{c}$ larger than the thickness of the turbulent flame brush plus the slit width, E_{Pmax} is independent of $\underline{c}$. For values of $c < (\alpha + 2b)$, E_{Pmax} is proportional to $\underline{c}$.

If the probability function is symmetrical (for the model which has been assumed here), the separation of the peaks of the product and radical profiles is $c/2$.

A formula has been derived for the probability function in terms of the ratio $\overline{E}(\omega)/\overline{I}(\omega)$. Using the experimental data described in reference 3, we have estimated the flame parameters $\underline{a}$ and K. An approximate formula for $p(x_1)$ has been derived for the profiles which can be described analytically by an equation of the form (constant) $\exp\left[-\sigma(m - x)^2\right]$. Whenever $\overline{I}_P(\omega)$ and $\overline{I}_R(\omega)$ are symmetrical, then $p\left[(\alpha/2) - x\right] = p\left[(\alpha/2) + x\right]$ for gaussian profiles.

The significance of the calculated probability functions $p(x_1)$ for the interpretation of turbulent flame properties cannot be assessed at the present time. We have only shown that it is possible to correlate observed emission profiles in terms of a model describing a turbulent flame as resulting from the superposition of wrinkled laminar flames.

Our analysis and correlations neither prove nor disprove the validity of the wrinkled laminar flame hypothesis.

In this paper we consider only the separation of radical and product emission profiles. It should be noted, however, that a separation of the C_2 and CH emission profiles is also to be expected on the basis of the wrinkled laminar flame model provided the laminar flame emission profiles for these two radicals do not have distributions with the same center of gravity. Dr. K. Wohl has recently discussed the separation of CH and C_2 emission profiles.* The preceding remarks should not be interpreted to mean that we are of the opinion that the observed spatial separation of CH and C_2 emission profiles should actually be interpreted in terms of the wrinkled laminar flame model for turbulent flames.

---

* Data presented at the 1958 Meeting of Project Squid, Pittsburgh, Pennsylvania.

B. EXPERIMENTAL STUDY OF REVERSE-JET FLAME STABILIZATION BY THE SPECTRAL INTENSITY RATIO METHOD

1. Introduction

In order to stabilize a flame in a high-velocity stream of combustibles, it is necessary to provide a continuous ignition source. The recirculation zone associated with an obstacle placed in the flow is a low-velocity region of hot, burned, gases which ignites the reactants continuously. The obstacle may be a bluff body, an array of bluff bodies, a recess in the duct wall, or a small jet opposing the main flow. A flame stabilized by a reverse jet has been studied using the spectral intensity ratio method which presumably gives the local equivalence ratio. The restrictions on the application of this method will be discussed.

Reverse-jet flame stabilization introduces several new variables and hence new design possibilities. Among the new variables are jet momentum, composition, temperature, and mass flow rate. Since the jet has a pronounced effect on flame stability, the jet variables may be optimized to fit the widely varying operating conditions in ramjets and afterburners.

2. Experimental Evidence Indicating the Existence of a Critical Zone[5-10]

Calculations show that the reverse jet contributes only about 0.01 of the mass flow of the main stream. Yet changing the jet

composition from pure air to an air-fuel mixture produces a large effect in the stability curves (blow-off velocity as a function of equivalence ratio). Typical data, which were obtained by Eustis and Mraz,[8] are given in Table I.

TABLE I. THE EFFECT OF JET COMPOSITION ON FLAME STABILITY

Fluid in Jet	Maximum Blow-off Velocity, V^*_{bo}, fps	Equivalence Ratio at V^*_{bo}
Air	165	1.4
Stoichiometric air-fuel	>220	0.9 (approx.)
167 percent of theoretical fuel	180	0.55

In order to account for the pronounced change in the stability curves, it seems reasonable to assume that there is a critical zone which determines flame holding properties. The jet flow, while only a very small fraction of the main stream flow, must contribute a large fraction to the flow entering the "critical zone." The critical zone is a region of turbulent mixing located directly behind the nose of the flame.

Optimum flame stability occurs for a stoichiometric jet and main stream. When the main stream is not stoichiometric, Noon[9]

found that the equivalence ratio in the critical zone, φ_z, at the maximum blow-off velocity, V^*_{bo}, is unity regardless of jet temperature. Penner and Williams[10] have extended the concept by stating that at V^*_{bo}, φ_z is a constant characteristic of the fuel-air system.

Experimental results will be shown which suggest that actually there is one stability curve relating V_{bo} to φ_z for a given fuel and duct geometry.

3. A Discussion of the Spectral Intensity Ratio Method

To apply the spectral intensity ratio (SIR) method for determining local equivalence ratios, it is only necessary to measure SIR as a function of φ for a known fuel-air input to a laminar flame. However, in order to extrapolate the calibration curve with some degree of confidence, it is essential to understand how the changes in operating conditions affect SIR.

We proceed to consider the factors which determine the intensity of a spectral line assuming that the population temperature and the effective temperature in the formula for the line radiancy are equal.

A region of optical depth X (cm-atmos) will emit the spectral radiancy

$$R_\omega = R^o_\omega \left[1 - \exp(-P_\omega X) \right]$$

at the wave number ω, where R^o_ω is the spectral radiancy of a blackbody and P_ω (cm^{-1}-$atmos^{-1}$) is the spectral absorption coefficient of the emitter. The spectral blackbody radiancy R^o_ω is the radiant energy

emitted from a given source per unit area of emitter (watt/cm^2) into an angle of 2π steradians.

An isolated spectral line has a line radiancy equal to

$$R_L = \int_{-\infty}^{\infty} R_\omega^o \left[1 - \exp(-P_\omega X) \right] d\omega .$$

For optically thin emitters the line radiancy is approximately

$$R_L = R_\omega^o X \int_{-\infty}^{\infty} P_\omega \, d\omega = R_\omega^o XS$$

where S (cm^{-2}-atmos^{-1}) is the integrated absorption. The integrated absorption, in terms of square of the matrix element for the upper (u) and lower (ℓ) states, is

$$S = \frac{8\pi^3}{3ch} \frac{g_u}{g_\ell} \frac{N_\ell}{p} \omega \left| R_{u\ell} \right|^2 \left[1 - \exp -(hc\omega/kT) \right] .$$

The blackbody radiancy is given by Planck's equation:

$$R^o \, d\omega = \frac{2\pi hc^2 \omega^3}{\exp(hc\omega/kT) - 1} \, d\omega \quad ;$$

the optical depth is

$$X = pL$$

where p is the partial pressure of the emitters (atmos) and L is the effective geometric length (cm). Combining the preceding equations, the integrated line radiancy becomes

$$R_L = \frac{16}{3} \pi^4 \omega^4 L N_u \left| R_{u\ell} \right|^2 .$$

The ratio of integrated radiancies for two lines is

$$\frac{R_{L1}}{R_{L2}} = \frac{\omega_1^4}{\omega_2^4} \frac{N_{u1}}{N_{u2}} \frac{|R_{u\ell}|_1^2}{|R_{u\ell}|_2^2}$$

which reduces, for specified lines, to

$$\frac{R_{L1}}{R_{L2}} = (\text{constant}) \frac{N_{u1}}{N_{u2}} \quad .$$

The preceding equation shows that the spectral intensity ratio is a constant times the ratio of number densities of the emitters in the excited, or upper, energy level.

In our experiments, the apparent peak intensity above the continuum was measured, which in terms of physical quantities for thin radiating regions is

$$R_\omega^a = X \int_{\omega - \Delta\omega}^{\omega + \Delta\omega} R_{\omega'}^o P_{\omega'} \, g(|\omega - \omega'|) \, d\omega'$$

where $g(|\omega - \omega'|)$ is the slit function for the instrument and includes suitable geometric and recorder calibration factors. The superscript a is used to indicate that we are measuring an apparent value of the spectral radiancy. The blackbody radiancy is nearly constant over the width of the slit, $2\Delta\omega$; hence R_ω^a is approximately

$$R^a_\omega = R^o_\omega X \int_{\omega - \Delta\omega}^{\omega + \Delta\omega} P(\omega')\, g(|\omega - \omega'|)\, d\omega' \ .$$

Additional simplifications to the preceding equation can be made which are the result of the following conditions satisfied in our experiment. For diffraction grating instruments, the slit function is an even function. When $\omega' = \omega$, the quantity g as a function of ω has zero slope. Outside a wave number interval 2δ, the intensity of the spectral line is not measurable. If the instrumental slit width greatly exceeds the line width, then the slit function is nearly constant for $|\omega - \omega'| \leq \delta$. The apparent peak intensity is then

$$R^a = R^o X g^* \int_{\omega - \delta}^{\omega + \delta} P(\omega')\, d\omega' = R^o X g^* S$$

where g* is the value of g at $\omega' = \omega$. Using the equation derived previously for the ratio of integrated line radiancies, it is apparent that

$$\frac{R^a_{\omega 1}}{R^a_{\omega 2}} = (\text{constant}) \frac{N_{u1}}{N_{u2}} \ .$$

The apparent spectral peak intensity ratio measured above the continuum and the true spectral radiancy ratios are identical except possibly for a

change in the numerical constant which results from a possible wavelength dependence of the receiver used for measurement.

In a flame the excitation is not necessarily thermal but may be the result of chemical reactions which produce molecules in excited states (chemiluminescence). In particular the radiation from C_2 and CH must be associated with the combustion reactions. We assume that SIR is a function only of the local equivalence ratio. This same assumption has been made without proof also by several other investigators. In view of our preceding discussion, the validity of this assumption is uncertain.

John and Summerfield[11] have measured the effect of turbulence on the radiation intensity from propane-air flames. Turbulence may reduce the (apparent) specific intensity (radiation intensity divided by fuel flow rate) as much as 50 percent for fuel-lean mixtures. For a turbulent flame enclosed in a duct, the relative changes of C_2 and CH intensity are nearly equal. The results given in Table II were obtained by John and Summerfield [11] using a propane-air flame stabilized by a bluff body.

A test for the extrapolation of the calibration curve obtained from a laminar flame to the reverse-jet flame may be made by using a stoichiometric main stream. The results of these tests are shown in Figure 16. Each point shown is the result of several different SIR measurements. The average is shown as a circle and the range of values are indicated by the lines. We infer from these data that SIR

TABLE II. EFFECT OF TURBULENCE ON SPECIFIC INTENSITY

Velocity fps	Equivalence Ratio	Decrease in CH(4300Å) Specific Intensity	Decrease in C_2 (5150Å) Specific Intensity
155	.90	.29	.32
	.80	.31	.34
	.70	.50	.45
60	.90	.17	.18
	.80	.16	.22
	.70	.17	.17

does not necessarily yield correct absolute values for the reverse-jet flame. However, relative values of φ are probably given correctly because changes in jet composition produce the expected changes in the measured values of φ. Fortunately, the interpretation of the data does not depend in an important way on the absolute value of φ.

Radiation measurements were made by Clark and Bittker[12] to determine the extent to which radiant intensity could be used to measure flame velocities. There is a relation between surface area and radiation intensity for laminar flames burning at fixed equivalence ratio; the radiation per unit area of a laminar flame depends only on the equivalence ratio. Using the preceding conclusion, John, Wilson, and Summerfield[13] correlated spectral intensity ratio with the equivalence

ratio of a laminar flame stabilized by a bluff body in a duct. To obtain the correlation, interference filters with a band width of about 100Å were used. One filter was centered to pass the emission from CH produced by the transition $^2\Delta \rightarrow {}^2\pi$ (0, 0), and the other filter transmitted the emission from C_2 associated with the transition $^3\pi \rightarrow {}^3\pi$ (1, 1). Using the correlation of SIR with φ, John, Wilson, and Summerfield[13] investigated preferential diffusion in flame stabilization. Later Wilson, John, and Summerfield[14] studied the effect of boundary layer flow on flameholding by using the SIR method.

4. Experimental Determination of Local Equivalence Ratio in a Reverse-Jet Stabilized Flame

In this subsection the apparatus and procedure for obtaining the calibration curve and the local equivalence ratio are described.

a. Experimental Determination of Spectral Intensity Ratios as a Function of Equivalence Ratio

The apparatus which was used to determine the spectral intensity ratios as a function of the equivalence ratio of a laminar flame is illustrated in Figure 17. An image of the inner cone was formed on the slit of a diffraction grating spectroscope. By masking the slit, the radiation from the tip and the base of the inner cone was not permitted to enter the spectroscope. Spectral intensity ratios determined from any part of the straight portion of the inner cone were the same for identical fuel-air input to the flame.

The following rotational lines were selected for the computation of intensity ratios:

Wavelength, Å	Transitions	Emitter
4252	$^2\Delta \rightarrow {}^2\Pi$ (0, 0)	CH
4312	" "	CH
4324	" "	CH
4737	$^3\Pi \rightarrow {}^3\Pi$ (1, 0)	C_2
5129	" (1, 1)	C_2
5165	" (0, 0)	C_2
5635	" (0, 1)	C_2
6191	" (0, 2)	C_2

These lines were selected because they are well isolated and because, for a given equivalence ratio, the spectral intensity ratios based on these lines were reproducible to an accuracy of about 5 percent.

In the experimental studies steady-state conditions were established at a fixed equivalence ratio. A wavelength interval including the line was then scanned. A typical recording of apparent intensity as a function of wavelength is shown in Figure 18. These data refer to the electronic transition $^3\Pi_u$ to $^3\Pi_g$ and the vibrational transition $1 \rightarrow 0$ of the radical C_2. The height of the peak was measured above the continuum. (See Figure 18.)

The results of the calibration from the laminar flames are shown in Figures 19 to 23. It is important to recognize that the calibration

curves can be applied only to measurements of SIR made by the same instrument. The spectroscope in this case was a Jarrell Ash diffraction grating spectroscope using a RCA 1P28 photomultiplier tube for detection. The spectroscope has an f number of 6.5 and a linear dispersion of 18 Å/mm.

b. Description of the Apparatus and Procedure Used for Obtaining Local Equivalence Ratios

In order to view the flame, particularly the critical zone, it proved to be convenient to use a mirror system as shown in Figure 24. A mirror was located on an adjustable mount within the plenum chamber so that the flame was viewed along the axis of the duct.

A six-stage centrifugal compressor supplied the primary air. Commercial grade propane (95 percent propane with higher hydrocarbons as impurities) was used as fuel. Facilities were provided for a jet of air, oxygen, nitrogen, or fuel-air mixtures. Ignition was accomplished by means of an automobile spark plug. Two duct sizes were used: 1 (1/4) inch diameter and 2 inch diameter standard pipe. Mixing of the fuel and air in the main stream was assured with a mixing chamber which had a porous metal (Poroloy) sheet across the flow. The plenum chamber had three paper blow out patches.

Steady-state operating conditions were established in the duct. By adjusting the mirror and masking off a portion of the spectroscope slit height, the radiation from a small portion of flame surface was selected for study. The size of the segment of the flame surface was an

area about 1/8 inch long by several hundred microns wide. The radiation entering the slit was scanned with the spectroscope; a large enough wavelength interval on either side of the line was taken so as to determine the magnitude of the continuum radiation.

5. Experimental Results

Two types of experiments were conducted. The equivalence ratio in the critical zone at blow-off was determined, and the local equivalence ratio as a function of radial position was measured.

a. Equivalence Ratio in the Critical Zone at Blow-Off

Measurements at blow-off require patience. To obtain meaningful results the flame must be burning long enough to have steady-state conditions throughout the apparatus; it must burn an additional interval of time sufficiently long to complete the spectroscopic measurements. At blow-off and for φ very near to blow-off, the flame tends to go out.

With an air jet the observed equivalence ratio in the critical zone, φ_z, is less than the main stream equivalence ratio, φ_{ms}. For the rich blow-off limit, φ_z is considerably smaller than the main stream equivalence ratio. (See Figure 25.)

Addition of fuel to the jet shifts the blow-off curves toward the lean side. Substitution of pure oxygen for air in the jet shifts the blow-off curves toward richer mixtures. This agrees with the results which other investigators have reported.[5-9] When the jet is a stoichiometric fuel-air mixture, then φ_z is larger than φ_{ms} for lean

fuel-air mixtures in the approach streams. This result is illustrated in Figure 26 by the points represented as squares. As with an air jet, the pure oxygen jet gives φ_z less than φ_{ms}. No data were obtained for an oxygen jet or an air-fuel jet at the rich blow-off limit. When the main stream is rich and the jet is pure oxygen, the flame temperatures are very high making it impossible to achieve a steady-state temperature without damage to the equipment.

In subsection 2 the conclusion was stated that in the critical zone the local equivalence ratio at V^*_{bo} was the same for any jet composition. An extension of this idea is the statement that at blow-off, for any jet composition, there is <u>one</u> stability curve provided V_{bo} is plotted as a function of φ_z. In Figure 26 the values of V_{bo} have been plotted as a function of φ_{ms} and φ_z. At lower velocities, 30 to 50 ft/sec, and in the velocity interval near 100 ft/sec, the experimental points for φ_z fall on one curve. This is consistent with the idea of <u>one</u> stability curve, $V_{bo} = V_{bo}(\varphi_z)$, regardless of jet composition. There is considerable scatter in the points at 80 ft/sec.

b. Local Equivalence Ratio as a Function of Radius

The equivalence ratio was measured as a function of radius. These data yield a comparison of the equivalence ratio in the critical zone with the equivalence ratio in other regions of the flame. When the jet-stabilized flame is viewed parallel to the duct axis, the depth of luminous gas increases with increasing radius. (Refer to Figure 24.)

We have performed experiments to establish the equivalence ratio gradient for a stabilized flame and also the φ_{obs}-gradient (spectroscopically determined values) for a pilot flame.

(1) Stabilized flame

In Figure 27 curves of the observed equivalence ratio as a function of radial distance from the duct axis are presented. For a rich main stream φ_{obs} remains constant to a radius R/3. Here R is the duct radius. At larger radii it decreases. Also the three curves obtained with different jet compositions are plotted together for comparison in Figure 27. The air jet and the oxygen jet give results which are practically indistinguishable. When fuel is added to the jet, φ_{obs} is higher by about 5 percent near the center of the duct; near the duct walls φ_{obs} merges with the other curves. The fact that φ_{obs} for the air-fuel jet is constant from the axis to R/3 may be explained if the assumption is made that the jet tip, and hence the critical zone, precesses about the duct axis. The precession of jet tip has been observed by Agoston, Noon, and Witherly.[15]

In Figure 28, $\varphi_{obs}(r)$ has been plotted for a lean main stream. In this case the local equivalence ratios are nearly independent of radial distance.

(2) Pilot flame

It was not possible to maintain a flame when the jet consisted of pure fuel and the main stream of air only; however, it was possible to burn a "pilot-flame" by having a fuel-air jet with equivalence ratio

φ_j = 2.8 and φ_{ms} = 0. The observed equivalence ratios φ_{obs} for the pilot flame are plotted in Figure 29. The luminous portion of the pilot flame did not fill the duct.

When there was no fuel in the main stream, the flame burned with uniform equivalence ratio. Addition of fuel to the main stream (φ_{ms} = 0.26 and φ_{ms} = 0.47) resulted in larger apparent equivalence ratios for the center of the flame. Addition of more fuel to the main stream causes an upward shift of the curve. Near the center of the duct, the flame burns locally at leaner mixtures.

c. Equivalence Ratio for an Open Flame Stabilized by a Reverse Jet

For the series of experiments involving an open flame, the main stream, which was an air-fuel mixture, emerged as a jet from a nozzle with an opening of 2 inches by 1/2 inch. The flame holding jet was located 16 inches vertically above the main stream nozzle. The open flame was stabilized between the outlets of the nozzle and the jet at a position which was determined by the jet pressure.

Air from the surroundings was entrained by the main stream and by the jet, diluting the combustibles. In order to maintain a flame, the nozzle flow had to be considerably richer than stoichiometric. The results are summarized in Table III.

6. Conclusions

The spectral intensity ratio method for determining equivalence ratio must use a calibration curve which is preferably obtained under operating conditions similar to those of the test flame. When extrapolated

TABLE III. OBSERVED EQUIVALENCE RATIO FOR AN OPEN FLAME STABILIZED BY A REVERSE JET

Velocity at Outlet of Nozzle ft/sec	Jet Pressure psig	Fluid in Jet	Input Equivalence Ratio	Equivalence Ratio in Critical Zone
42	14	Air	2.12	1.02
39	12	Air	2.19	1.08
38	12	Air	2.12	1.01
40	14	Air	2.29	1.05
40	14	Air	2.29	1.06
40	9	Air	2.49	1.05
53	10	Air	1.57	0.76
53	10	N_2	1.56	0.79
53	10	O_2	1.57	0.79
40	10	O_2	2.18	1.06
40	10	N_2	2.17	1.05
40	10	Air	2.18	1.04
45	10	Air	1.68	0.83

to flames burning under conditions unlike those of the calibration flame, the absolute value for φ may be in error; however, relative values of φ are probably given correctly.

The equivalence ratio is nearly independent of radial distance for lean flames. For rich flames the equivalence ratio decreases near the duct wall. Jet composition influences φ near the axis of the duct and also affects the equivalence ratio at larger radii.

The importance of the critical zone is illustrated by the experimental result that there appears to be a single stability curve relating the blow-off velocity V_{bo} to φ_z, regardless of jet composition. Unfortunately our equipment was usable only for studies of the lean blow-off tail of the stability curve; however, more extensive experiments may well reveal that the blow-off velocity is a unique function of φ_z regardless of jet composition.

APPENDIX TO PART I. SPRAY FORMATION AND SPRAY COMBUSTION*

1. Introduction

Atomization is the process of reducing a large volume of liquid to a fine spray with the result that the surface-to-volume ratio is greatly increased. The chemical reactions of combustion require the intimate molecular mixing of the fuel and oxidizer; atomization is an important preliminary to the combustion of liquid fuels.

The production of atomized fuel involves the following interacting processes:

(1) The atomizer imparts kinetic energy to the sprayed fluid forming the jet, cone, or sheet of liquid which penetrates the ambient fluid.

(2) Disintegration of the sheet, cone, or jet of fluid into ligaments occurs as the result of drag of ambient fluid and disruptive components of velocity within the sprayed fluid.

(3) The relative velocity between drops of sprayed fluid and ambient fluid may cause further disintegration into smaller drops.

(4) Under certain conditions drops collide and coalesce to form larger drops or else more extensive breakup.

Combustion of the spray introduces other processes (and complications) which are considered in subsections 12 and 13.

In spite of the extensive experimental and theoretical studies already completed, there is not enough information available to design

* The survey presented in this appendix was supported, in part, by the United States Air Force Office for Advanced Study under Contract AF 18(603)-107.

a combustion chamber without resorting to trial-and-error techniques. There are numerous reasons for our inability to describe completely the combustion of sprays. Many physical properties affect the results; the detailed mechanisms and the interaction between reaction processes are complex. In addition, there are numerous experimental difficulties. Ingenious devices for quantitative work have been invented, but these have limitations as to ranges of droplet size, droplet velocity, or other variables which can be employed.

Drop formation is not studied exclusively by combustion engineers. For example, meteorologists are interested in the shattering of falling raindrops, and chemical engineers use sprays in the process industries. Significant contributions to our understanding of spray formation and combustion have come from workers in these allied fields.[1]

2. Atomizing Devices

The atomizers which will be discussed in this subsection are illustrated in Figure 1.

When used as an atomizer the simple orifice operates at high pressure (300 to 600 atmospheres). One application is for fuel injection in both diesel and gasoline engines. Disintegration of a chaotic nature begins at the lip of the orifice.

A secondary fluid, such as compressed air or steam, may be used. The flow passage for the auxiliary fluid is concentric with and exterior to the liquid orifice. This arrangement gives satisfactory sprays

over wide ranges of operating conditions; however, it is limited to applications where the secondary fluid is readily available. Highly viscous liquids can be broken up by an atomizer using a secondary fluid.

For liquid-propellant rocket motors, which have large flow rates at high pressure, it is common practice to use impinging jets for spray formation. The spray from a pair of impinging streams is characterized by its sheetlike spatial distribution and relatively large drops (200 μ to 400 μ). Important factors which determine the characteristics of impinging jet sprays are relative stream momentum, relative stream cross-sectional area, impingement distance, impingement angle, and velocity profile within the jets.

Another atomizer design which finds application in liquid rocket engines is the splash plate. Impact of the jet from a plain orifice upon a plate provides the breakup of the liquid bulk. By varying the geometry of the jet and plate, it is possible to focus the spray.

Swirl-type atomizing nozzles impart a tangential component of velocity to the fluid so that when it leaves the orifice the fluid spreads into a hollow cone. As the conical sheet of liquid progresses from the nozzle, waves of increasing amplitude develop. A ring of liquid breaks away as a result of the wave instability. The ring itself is unstable and breaks up; the larger drops are formed from lobes on the ring. Larger drops traveling at a high velocity relative to the airstream will disintegrate into smaller drops.

Centrifugal atomization provides a means for obtaining a spray with uniform drops.[2-4] A liquid jet is directed along the axis of a whirling disc and impinges upon the center of the disc. Friction between the disc and the fluid causes a film which moves outward due to the centrifugal force. The manner in which the fluid leaves the periphery of the disc depends on the angular velocity.[5] At low rotational velocity a ridge forms which has bulges. These bulges are thrown off as drops; this process corresponds to the "direct drop formation" stage. Increasing speed of the disc causes thin strips of liquid to be flung from the disc. These strips are unstable and break up into drops; this process corresponds to the "disintegration by ligament formation." With higher speed and higher liquid flow rates a film forms which extends beyond the disc. Along the edge of this whirling film ligaments or "fingers" of liquid are torn off. In addition there is drop formation at the film edge. This last process represents the "disintegration by film formation" stage or phase.

Centrifugal atomization is largely a research device at the present time rather than an atomizer for practical applications in power plants. In order to obtain really uniform drop sizes it is necessary to use a disc mounted on a shaft with very precise bearings. Representative conditions for centrifugal atomization are the following:[6]

fuel supply: 12 cc/min;

disc diameter: 2 inches;

disc speed: 8000 RPM;

drop size: $90\mu \pm 5\mu$ (with 90 percent of the drops within this size range).

Some research applications require drops of large size, for example 10 mm. One method to produce large drops is to use a vibrating disc with a groove. The groove is tilted slightly from the horizontal. Vibration causes small drops on the surface of the disc to coalesce and move along the groove. Another technique for producing large drops is to connect a piston and cylinder to the supply tube of an orifice. Motion of the piston periodically disturbs the liquid causing large, uniform drops.

3. Spray Characteristics

In order to obtain quantitative data, a measurable quantity must be defined. For sprays the distribution of droplet size is an important and meaningful quantity which can be measured. Mean drop diameters are derived quantities. Most of the following discussion is taken from Ranz[7] and Mugele and Evans.[8]

Drops in a spray range in size from the smallest drops which still have a distinct phase boundary to the largest drops the size of which is limited by the critical Weber number. A lower limit for average drop diameter is 5μ to 6μ ; of course, drops smaller than 5μ occur in sprays as a result of the breakup mechanisms. (See Figure 2.) The fundamental spray variables, from the point of view of size

distribution, are the upper limit for drop size, D_m, the lower limit, D_o, a mean drop diameter, $\bar{D}$, and the deviation from the mean, δ .

The variation in drop size is obtained from experimental data by counting the number of drops in a size range D to D + ΔD followed by normalization using the total number of drops. The successive fractions $\Delta n/\Delta D$ form the histogram or numerical probability distribution, n(D). In the limit as ΔD becomes infinitesimally small, the histogram becomes a smooth curve. An analytical expression which represents this curve is necessary for the purposes of mathematical analysis. The volume probability distribution, $\Delta v/\Delta D$, is an alternate representation which is obtained from the numerical probability distribution function, n(D), by weighting each class interval, ΔD, by a D^3 factor. Integration of the numerical or volume probability distribution, n(D) or v(D), leads to the cumulative distribution function, N(D) or V(D). In Figures 3 and 4 are shown typical graphical representations of drop-size distributions. It should be noted that weighting n(D) by D^3 to give v(D) causes a large difference in the range having largest percentage of volume of drops. In the graph being considered here, the range 2 to 10 μ has the greatest number of drops and the range 10 to 60 μ has the greatest volume. The number distribution is important for ignition, and the volume distribution for combustion rates.

One large drop causes difficulty in volume analysis. A sample, upon which the v(D) is based, may contain less than 0.1 percent of all the drops. One drop of unusually large size in the sample exerts a

strong influence on the v(D). Bitron[9] encountered this difficulty in his experiments. If a measurement were made of the size distribution of all the drops in the spray zone at any one instant, it need not necessarily be the same as a measurement of the distribution based on flux. Measurement techniques such as employed by Rupe,[10] where sampling tubes or cups are exposed to the spray for a definite interval of time, provide a distribution based on the flux of drops.

Using the numerical probability distribution function, the statistical average of any quantity depending on drop diameter can be found:

$$\overline{h} = \frac{1}{N} \int_0^\infty h(D')n(D')dD' \quad .$$

A general equation for mean drop diameters is

$$D_{qp} = \left\{ \frac{\int_0^\infty D'^q n(D')dD'}{\int_0^\infty D'^p n(D')dD'} \right\}^{\frac{1}{q-p}} \quad .$$

In Table I, which is taken from Mugele and Evans,[8] the various defined mean diameters are related and the field of application is specified.

TABLE I. DEFINITIONS OF MEAN DIAMETERS

p	q	p + q (order)	Name of Mean Diameter	Field of Application
0	1	1	linear	comparisons, evaporation
0	2	2	surface	surface area controlling, i.e., absorption
0	3	3	volume	volume controlling, i.e., hydrology
1	2	3	surface diameter	absorption
1	3	4	volume diameter	evaporation, molecular diffusion
2	3	5	Sauter	efficiency studies, mass transfer, reaction
3	4	7	De Brouckere	combustion equilibrium

If Q is the volume flow rate, then the rate of surface generation is given by

$$\frac{Q}{D_{32}} \quad .$$

The mean drop diameters are not all independent but are related by

$$D_{qp}^{q-p} = \frac{D_{qc}^{q-c}}{D_{pc}^{p-c}}$$

and

$$D_{pq} = D_{qp} \quad .$$

In Table II the distribution functions commonly used to represent atomization data are summarized. Included are the expressions for mean drop diameters. Median drop diameters are easily obtained when data have been plotted in cumulative form as in Figure 4. These drop diameters are

D_{nm} = numerical median diameter

and

D_{vm} = volume median diameter.

Based on the data of Houghton[11] the following numerical values of the mean drop diameters were determined by Ranz:

TABLE II. CUMULATIVE AND DISTRIBUTIVE FORMS OF FOUR DROPLET DISTRIBUTION FUNCTIONS.

Name of Equation	Volume Cumulative V	Volume Distributive $v = \frac{dV}{dD}$	Numerical Cumulative N	Numerical Distributive $n = \frac{dN}{dD}$	Expression for Mean Drop Diameters
Rosin Rammler	$1 - V = e^{-\left(\frac{D}{\bar{D}}\right)^{\delta}}$	$\frac{dV}{dD} = \frac{\delta D^{\delta-1}}{\bar{D}^{\delta}} e^{-\left(\frac{D}{\bar{D}}\right)^{\delta}}$	—	$n = \frac{\delta D^{\delta-4}}{\bar{D}^{\delta-3}\Gamma\left(1-\frac{3}{\delta}\right)} e^{-\left(\frac{D}{\bar{D}}\right)^{\delta}}$	$D_{pq} = \bar{D}\left\{\frac{\Gamma\left(\frac{q-3}{\delta}+1\right)}{\Gamma\left(\frac{p-3}{\delta}+1\right)}\right\}^{\frac{1}{q-p}}$
Nukiyama Tanasawa	$V = \frac{\Gamma(bD^{\delta})\left(\frac{6}{\delta}\right)}{\Gamma\left(\frac{6}{\delta}\right)}$ see note below	$\frac{dV}{dD} = \frac{b^{\frac{6}{\delta}} D^5}{\Gamma\left(\frac{6}{\delta}\right)} e^{-bD^{\delta}}$	—	$\frac{\delta b^{\frac{3}{\delta}}}{\Gamma\left(\frac{3}{\delta}\right)} D^2 e^{-bD^{\delta}}$	$D_{pq} = \bar{D}\left\{\frac{\Gamma\left(\frac{q+3}{\delta}\right)}{\Gamma\left(\frac{p+3}{\delta}\right)}\right\}^{\frac{1}{q-p}}$
Log probability	$V = \frac{1}{\sqrt{\pi}} \int_{-\infty}^{Y\delta} e^{-U^2} dU$	$\frac{dV}{dY} = \frac{\delta}{\sqrt{\pi}} e^{-\delta^2 y^2}$ $y = \ln(D/\bar{D})$	$N = \frac{1}{\sqrt{\pi}} \int e^{-U^2} dU$	$\frac{dN}{dD} = \frac{\delta}{\sqrt{\pi}} e^{-\left(\delta Y + \frac{3}{2\delta}\right)^2}$	$D_{pq} = \bar{D}\, e^{\frac{p+q-6}{4\delta^2}}$
Log probability with upper limit	← same as log probability except			$y = \ln \frac{aD}{D_m - D}$ →	$D_{32} = \frac{D_m}{1 + ae^{(1/4\delta^2)}}$

Note: $\Gamma(bD^{\delta})\left(\frac{6}{\delta}\right) = \int_0^{bD^{\delta}} U^{\frac{6}{\delta}-1} e^{-U} dU \quad ; \quad b = (\bar{D})^{-\delta}$

Name of Diameter	Symbol	Diameter (in microns)
Linear	D_{10}	5.5
Surface	D_{20}	7.5
Volume	D_{30}	10
Sauter	D_{32}	18
Number median	D_{nm}	4.2
Volume median	D_{vm}	24

The "spread" of the distribution curve is described by the difference between the mean and the median diameters. Mathematically the concept of "spread" of the distribution curve is defined precisely by the average deviation from a mean diameter; for example, the deviation from the mean diameter may be defined by

$$\frac{\overline{D - D_{32}}}{D_{32}}$$

where the bar signifies average.

Consider the evaporation of a spray following the Langmuir evaporation equation

$$\frac{dm}{dt} = -kD \quad .$$

For a number of drops of different diameters

$$\frac{d\Sigma m}{dt} = -k\Sigma D \quad .$$

Dividing by the total number of drops gives the result

$$\frac{d\bar{m}}{dt} = -kD_{10} \quad .$$

This is an example of the application of a mean drop diameter.

Size-distribution functions should be of a functional form which is easy to manipulate. There should be as few constants as possible; usually an "average-diameter" constant and a uniformity index are sufficient. For a given set of operating conditions, nozzle geometry, and physical properties, one should be able to find values of the constants for correlating experimental results.

a. Rosin-Rammler Distribution Function[12, 13]

In the volume-cumulative form the Rosin-Rammler distribution function is simply

$$1 - V = \exp - \left[\left(\frac{D}{\bar{D}} \right)^{\delta} \right]$$

where V is the volume fraction of material occurring in drops of diameter less than D; δ is the distribution parameter or the uniformity index; and $\bar{D}$ is the size parameter. Other forms of the Rosin-Rammler distribution function appear in Table II. Originally the Rosin-Rammler function was intended for the description of the size distribution of powdered materials, but it has been used to correlate spray data and has been applied in theoretical investigations.[14-18] A characteristic result from experimental distribution data is $D_{30} \cong D_{21}$. Only for values of δ greater than 3 is this true for the Rosin-Rammler representation. For $\delta = 3$, $D_{30} = 0$ and for $\delta = 2$, D_{20} is negative. Mugele and Evans used the experimental results obtained by Lee[19] and found that the Sauter mean diameter, SMD, predicted by the

Rosin-Rammler function was 85 μ whereas the SMD calculated directly from the histogram was 68.7 μ . Ingebo[20] conducted experiments on spray evaporation and determined D_{20} using several analytical distributions and by direct integration. These are given in Table III.

TABLE III. MEAN DROP DIAMETERS CALCULATED ACCORDING TO FOUR DIFFERENT METHODS

Mathematical Expression	Mean Drop Diameter D_{20} Microns
Rosin-Rammler	21.1
Nukiyama-Tanasawa	41.3
Log-probability	40.7
Direct Integration	41.3

From experimental data one determines δ by fitting the best straight line to a plot of log log $1/(1 - V)$ versus log D; the slope of the best straight line equals δ . Ingebo found δ to be 3.1 for his experiments. A spray with a broad distribution has a small value of δ; the more uniform the spray, the larger δ . The uniformity index δ must be greater than 3 in order to obtain mean drop diameters which have physical significance. Hence the Rosin-Rammler distribution can be

applied only to those sprays with uniformity index $\delta > 3$. For that portion of a histogram representing the larger drops, Bevans[15] found that the Rosin-Rammler distribution more closely fitted the experimental data than did the Nukiyama-Tanasawa equation.

b. Nukiyama-Tanasawa Distribution Function[21]

The Nukiyama-Tanasawa (NT) equation is a drop size distribution function obtained from extensive experiments with an air atomizing nozzle. Table II presents the NT equation in cumulative and distributive forms. Lewis, et al,[22] applied the NT equation to the data obtained from air atomization experiments; although they found the calculated SMD too high, there was good agreement for the distribution of sizes. Applying the NT equation to sprays produced by simple orifices, they found only qualitative agreement.

Direct integration of data from sprays usually gives $D_{30} \cong D_{21}$; these mean values calculated from the NT equation are nearly equal.

Longwell[23] states that the NT equation is applicable to air atomization whereas the Rosin-Rammler is applicable to swirl nozzles.

c. Log-probability Distribution Function

If the classes used to develop the distribution function from experimental data are graded exponentially; i.e., $\Delta D = .01, 0.1, 1.0, 10, \ldots$, instead of linearly; i.e., $\Delta D = 0.1, 0.2, 0.3, 0.4, \ldots$, the distribution resembles the Gaussian distribution. Replacing D as the variable by $y = \ell n\, D/\bar{D}$ gives the log-probability distribution. More

generally the variable y can be represented by $y = \ell n f(D)$, as in the case of the upper limit distribution. The upper limit distribution is more complex than either the Nukiyama-Tanasawa or Rosin-Rammler functions and has not been applied as extensively.

Stange[24] felt that theoretical derivations of the distribution functions would make possible a better choice of the distribution function for the spray from a particular atomizer. Two simple model processes were considered to be operating on initially uniform particles: (a) a p-fold repetition of a simple breakup into two parts and (b) single breakup into n parts. Breakup occurs statistically. The first model leads to the log-probability and the second model to the Rosin-Rammler.

d. Log-probability Distribution Function with Upper Limit

All of the distributions discussed previously predict, with very small probability, drops larger than physically possible. In view of this fact Mugele and Evans suggested a more realistic distribution with cut off at a maximum drop diameter. This introduces a new constant, D_m, making the log probability with upper limit a three-constant distribution function. In the case of the relatively coarse atomization from impinging jets, the "upper limit" distribution may fit the data better. However it is mathematically more complex.

Bitron used the upper limit equation to fit the histogram representing atomization by supersonic air jet. Typical values of the constants for the upper limit equation, which is given in Table II, were a = 1.045, D_m = 22.5 microns, δ = 0.634. Using these values the predicted

D_{32} or SMD is 7.65 μ. Bitron also used the equation for SMD developed by Nukiyama and Tanasawa and obtained 7.2 μ. Direct integration of experimental data gave 7.2 μ.

e. Square Root Distribution Function

Ranz[7] describes a volume distribution function used to analyze drop sizes from pressure swirl nozzles and centrifugal sprayers; the square root distribution function is

$$\frac{dV(D)}{dD} = \frac{\delta}{\sqrt{\pi}} e^{-\delta^2 \frac{D}{D_{vm}}} .$$

The uniformity constant, δ, is obtained from the formula

$$\ell n\, D_{nm} = \ell n\, D_{vm} - (3/2)^2 .$$

If the cumulative plots are available, the constants characterizing the distribution are easily obtained.

In the remaining paragraphs of this subsection other spray characteristics will be considered.

An obvious reason for interest in the penetration of sprays is its connection with the distribution of fuel, both in the liquid and gaseous phases within the combustion chamber. Spray penetration is also an important factor in the ignition of propellants. Various authors have defined spray penetration in different ways. Giffen and Muraszew[1] consider a spray with a horizontal axis and define spray

penetration as the shortest distance between the nozzle and a plane normal to the spray axis which has been reached by the drops at a given moment. Rupe[10] defines spray penetration as follows: "Penetration is the maximum distance from the nozzle orifice traveled by any spray particle when the spray is directed vertically upwards." Ranz[7] defines spray penetration as the radial position from the nozzle reached by spray liquid in a given time, t. Rupe[10] defines a final or maximum penetration; whereas Giffen and Ranz define penetration as a radial distance which is a function of time.

Cone angle is the angle within which a certain percent of the liquid passes. The results of experiments concerned with spray cone angle have been presented by Söhngen and Grigull.[25] The nozzles were made up of different combinations of housings and swirl producing inserts. The nozzles differed systematically as to length and diameter of the discharge orifice, diameter of the radial drillings in the swirl inserts and depth of swirl chamber. For a given nozzle configuration, flow, fuel and injection pressure were varied, and the cone angle was measured.

Automization experiments conducted by Lee[19] with intermittent sprays revealed that from four to eighteen million drops are produced by one cycle of the injector. Dispersion is the instantaneous location of the millions of drops in spray and their motion; it is analogous to configuration space in the kinetic theory of gases.

4. Measurement of Spray Characteristics

The measurement of drop size distributions can be a tedious job. Numerous ingenious devices have been invented; several are described here.

Rupe[10] developed an electronic counter which gives an accuracy, compared to a direct drop count, of a few percent. Cups, containing a liquid immiscible to the sprayed liquid, are exposed to the spray for a regulated time. Drops settle to the bottom of the cup and are photographed. The photographs are enlarged and placed on the turntable of the counter. The turntable also translates horizontally along a lead screw so that the photograph is scanned. Three phototubes with suitable optics are focused to look at a certain diameter circle; the diameter is adjustable. If all three phototubes "see" the same color, a count is recorded. The procedure is to start with a small diameter adjustment for the tubes. Scan the photograph, increase the diameter of circle which gives a count, and then rescan. A cumulative distribution is obtained in this manner.

The wax-sieve method[17] uses molten wax as the sprayed fluid. By adjusting the temperature, the viscosity and surface tension of the liquid wax can be varied. When wax is sprayed, it cools and solidifies. The solid wax particles can be sieved for size.

Another technique similar in concept is the settling weight method developed by Taylor and Harmon.[26] A bath of liquid is

maintained at the temperature of dry ice. This bath is exposed to the spray; the drops solidify in the bath and settle out on a shutter mechanism. When all drops have settled upon the shutter, it is opened. Below the shutter is a pan resting on a balance; this pan collects and weighs the drops. The weight-time curve can be translated into a drop size distribution since the time of fall is a function of drop size.

Slides coated with magnesium oxide are also employed to obtain drop size distributions. Impact of a drop causes a crater on the slide. The size of the crater is related to the drop diameter. With this method it is necessary to apply a correction for the collection efficiency of the slide. Smaller drops can follow the streamlines around the slide.

Photography has been used for counting and sizing drops. York and Stubbs[27] took silhouette photographs of sections of the spray, using a camera with open shutter and flash illumination of about one microsecond. The photographs were projected with 100X magnification from drop to screen and were counted and measured. A certain blurring of the photograph defined the boundaries of the depth of field; drops within these limits were counted. In order to determine velocities two flashes separated by a known time interval record two images of the drops on the same photographic plate. Using the measured spray distribution the mass flow from a nozzle was calculated; the calculated and observed mass flows were within 20 percent. Among the parameters which have an important influence on the accuracy of the method are the

number of photographs, the location of the sample fields, and the number of drops counted. Bolt and Boyle[6] used a similar technique for their studies of combustion of a spray from a centrifugal atomizer.

Ranz and Hofelt[28] have developed a rectangular jet impaction system for obtaining cumulative volumes versus drop sizes in a spray. Inertial impaction theory was the basis for the design of equipment and analysis of test data. The development impactor gave a means for determining the relative measure of drop sizes in the range 60μ to 90μ.

Optical sizing of drops is limited to about one micron. An optical method avoids the problems associated with any method whereby the drops collide with the measuring device. Not all drops strike the collector. Also high velocity impact results in shattered drops and a false size distribution.

A lapse of time occurs between spraying and counting; therefore, vapor pressure of the spray liquid at room temperature should be less than one millimeter of mercury to prevent the complications of an evaporating spray sample.

A rapid sizing technique is needed. Some measurable quantity which is a function of one of the mean drop diameters is the basis for most rapid techniques. Sauter[29] measured photometrically the weakening of a ray of light transmitted through the spray. Light scattering and absorption experiments provide directly the mean value

of the drop diameter but no information on size distributions. When the nozzle is maintained at an electrical potential, the spray is charged. Assuming the capacity of an isolated sphere applies to the drops in a spray, an expression for D_{31} can be derived

$$D_{31} = \sqrt{\frac{12 \chi_o Q \phi}{i}}$$

where χ_o is permittivity of free space; ϕ, nozzle potential; Q, volume flow rate; and i, the current carried by the spray.

Cone angle can be measured by placing a row of test tubes with their openings on an arc of a circle whose center is at the nozzle. Each test tube is parallel to the spray axis. Measurement of penetration is more or less obvious.

5. Instability and Disintegration of Liquid Jets and Sheets

As the velocity of a liquid jet increases, there are several distinct stages of disintegration. At the lower velocities the breakup of the jet is regular; in fact, with viscous fluids; e.g., glycerine, it is possible to use a stroboscope to stop the motion. The stages characterized by the regular manner of breakup are amenable to theoretical analysis; however, these low velocity jets are not practical for atomizers. A practical atomizer operates at the stage where breakup is irregular and chaotic. Unfortunately this manner of disintegration is not easily analyzed.

One of the earliest theoretical studies of the disintegration of liquid jets was carried out by Rayleigh,[30] who considered a non-viscous fluid with potential flow. There are two causes of instability; one is the result of surface tension forces, and the second is the aerodynamic forces arising from the interaction between the jet and the ambient fluid. When disintegration is due to capillary forces, the drops formed are about twice the diameter of the jet. A spherical drop has less surface area than the segment of cylindrical jet from which it is formed. When the aerodynamic forces are no longer negligible, the instability of the waves in the jet is aggravated. Decreased pressure at the crest and increased pressure in the trough tend to increase wave amplitude. The amplitude grows exponentially, at least in first approximation.

Haenlein[31] conducted experiments using nozzles with a length-to-bore ratio of 10:1 and found four stages in the disintegration of a liquid jet:

(1) Drop formation caused by dilation, also called varicose or radially symmetric waves, as illustrated in Figure 5. The waves are due to primary disturbances in the fluid flow and surface tension forces. This stage is characterized by a linear relationship between the length, L, of the jet prior to breakup and the jet velocity, V.

(2) Drop formation caused by dilation waves with air influence. As the jet velocity is increased, the aerodynamic forces of the surrounding air are no longer negligible and tend to accentuate the waves. Also L and V are no longer related linearly.

(3) Drop formation due to waviness of the jet, which is associated with increasing effectiveness of aerodynamic forces and lessened relative influence of surface tension.

(4) Complete disintegration of the jet. The liquid is broken up at the nozzle in a chaotic and irregular manner. There is no sharp demarcation between stages but rather a gradual transition occurs. Unfortunately the complete and immediate atomization stage, which is the normal operating condition for the plain-orifice atomizer, is not easily described. The impinging-jet method of spray formation does not operate with jets in the complete disintegration stage.

A jet sprayed into a vacuum or reduced pressure region will disintegrate although the length of jet to the point of disintegration increases. From this fact it is apparent that breakup of a jet is not caused solely by aerodynamic forces but must be the result, at least in part, of turbulence or other disruptive causes in the fluid itself. Other possible disruptive mechanisms in jet disintegration are vaporization of liquid and vortices produced by the large amount of energy added to the fluid. The disturbances in the flow have a strong influence on jet disintegration and atomization primarily in the early phases of the process. The time required for the jet to breakup is strongly influenced by the nature of the fluid flow. Subsequent breakup is determined largely by aerodynamic forces. Atomization is not an efficient process. The energy necessary to break a large liquid volume into small drops represents only about 0.05 percent of the energy available in the pressure drop across the injector.[1]

Scheubel[32] injected a liquid stream, using water or alcohol as fluids, along the axis of a venturi which had controlled air velocity. This simulated atomization as it occurs in a carburetor. A photographic technique was used to study atomization rates. Ligaments torn from the main stream by high relative air velocity are clearly visible. His photographs, when considered in view of Haenlein's work, suggest that a breakup due to wave motion is also operative. Castleman[33] suggested an explanation for the apparent explosion of a jet of liquid into small drops when exposed to a stream of high-velocity air as follows:

> "A portion of the large mass is caught up (say at a point where its surfaces are ruffled) by the air stream and, being anchored at the other end, is drawn into a fine ligament. This ligament is quickly cut off by the rapid growth of a dent in its surface, and the detached mass, being quite small, is swiftly drawn up into a spherical drop."

He utilized an extension of Rayleigh's theoretical analysis to predict collapse time for a ligament. The calculated collapse times are 10^{-5} seconds or less for ligaments which give 5μ drops. Castleman's mechanism applies whenever the relative speed between the air and the jet is large; the torn ligaments of fluid result from action of the surrounding air.

Some atomizers do not form cylindrical jets of fluid but rather conical sheets. Impingement of two fluid streams also gives a sheet of fluid. The mechanism for the disintegration of liquid sheets has

been studied theoretically and experimentally by York, Stubbs, and Tek[34] who concluded that the formation of unstable waves at the interface between the sprayed and ambient fluids is the major factor in the breakup of a sheet of liquid into drops.

At the boundary between a liquid and a gas there is a balance of forces as expressed by the equation

$$p_\ell - p_g = -\sigma \frac{\partial^2 h}{\partial x^2}$$

where p is the pressure; the subscripts ℓ and g identify liquid and gas, respectively; h is the displacement of liquid from the equilibrium position; σ equals the surface tension; x is the distance along fluid sheet. In order to formulate the problem, a two-dimensional infinite sheet of fluid of finite thickness is considered. The liquid sheet separates the two gas regions. By neglecting viscous effects and assuming irrotational flow, the velocities can be obtained from a velocity potential. Using calculated velocities and Bernoulli's equation, the pressures may then be estimated and the displacements, h, determined. As in the case of a liquid jet, an exponential increase in wave amplitude occurs under certain conditions. The amplitude increase is given by

$$h(t) = A \exp(\beta t)$$

where h(t) is the amplitude at time, t; A represents the amplitude of the initial disturbance; and β is a number which determines the growth

rate of the disturbance. If the amplitude of the initial disturbance, A, were known, then the time for disintegration could be calculated from the relation

$$t = \frac{1}{\beta} \ln \frac{a}{A}$$

where a is the thickness of the fluid sheet. A graph, based on the analysis of York, Stubbs, and Tek,[34] is plotted in Figure 6 and shows the relation between growth-rate factor, wavelength, and Weber number.

Increasing the flow rate from a swirl atomizer causes disintegration nearer the nozzle and increases the irregularity of breakup. The wavelength for instability decreases with increased flow rates. The wavelengths for maximum growth are associated with high velocity and hence high energy.

York, Stubbs, and Tek found that the infinite flat sheet model used in theoretical analysis was not approximated closely by a conical spray. Also the agreement between theoretical and experimental results was only qualitative. Hagerty and Shea[35] extended the studies on disintegration of liquid sheets by working with a spray approximately 6 inches wide and 1/16 inch thick formed from a narrow slit orifice. Waves of any desired frequency could be imposed upon the sheet. The analysis was also extended to include dilation waves which are the result of out-of-phase wave motion of the two faces. Using

photographs of the flat liquid sheet, experimental values of growth rate factor, β , were obtained and compared (See Figure 7.) with the theoretically predicted curve calculated from the following equation:

$$\beta = \left[\frac{(n^2 V^2 \rho_g / \rho_\ell) - (n^3 \sigma / p_\ell)}{\tanh na} \right]^{1/2} .$$

In the preceding expression, n is wave number of a disturbing wave, V is the velocity of the liquid relative to the gas, σ equals the surface tension, ρ_g and ρ_ℓ represent, respectively, the densities of gas and liquid, and a is the sheet thickness. It was also concluded: (a) that only two wave types are possible: a "sinuous" wave with phase angle zero and a dilational wave with phase angle zero and a dilational wave with phase angle π; (b) that the lowest stable frequency is given by

$$\nu = \frac{\rho_g V^3}{2\pi\sigma} = \frac{WV}{2\pi a}$$

where W is again the Weber number; and (c) that the growth rate for sinuous waves exceeds that of the dilational waves. The analysis by York, Stubbs, and Tek of wave growth in liquid sheets and the belief that frequency and wavelength of the ripples are perhaps related to the size range of the drops produced may apply also to impinging jet formation. Waves have been observed in spray formation from impinging jets.[36-38]

When the vapor pressure of the injected liquid exceeds the ambient pressure, a marked fanning or disintegration of the jets occurs at the orifice. In the case of a rocket motor with a LOX (liquid oxygen) impinging jet spray, disruption of the jet may occur before impingement. Schmidt[39] investigated experimentally the relation between spray cone angle, the chamber pressure, and the vapor pressure, neglecting the influence of drop size. The range of the variables in experiments on $CC\ell_4$ and H_2O were:

Δp (injection pressure): from 1 to 4 atmospheres;

p_c (chamber pressure): from 0.15 to 2.0 inches of mercury;

p_v (vapor pressure): from 2.4 to 8.5 inches of mercury;

ℓ/d (orifice length-to-diameter ratio): 3.13.

Schmidt's experiments were not conducted at pressure levels comparable to rocket motor chamber pressures. Extrapolation of relevant data suggests that LOX spray characteristics would change enormously for a small change in p_c near $p_c = p_v$. Also since p_v is a function of temperature, a change in the injection temperature of LOX when $p_c = p_v$ would again result in large changes of the spray characteristics.

Summarizing the discussion on the disintegration of liquid jets or sheets, we note that the initial work of Rayleigh has been extended by a number of authors to include more complicated boundary conditions than were considered in the original work. The theoretical studies involve the growth of the amplitude of an initial disturbance until the sheet or jet of liquid is disrupted and ligaments are formed. Drops

result from the ligaments or "fingers" of fluid. In order to use potential flow in the analysis, it is customary to neglect viscous effects. The inviscid approximation may account for the fact that the Weber number seems to be of dominant theoretical importance in determining the breakup of sheets.

Continuing the discussion of drop formation, attention is now directed to the shattering of drops in a high-velocity gas stream.

6. Deformation and Breakup of Drops

As was mentioned previously, one can think of the over-all process of fuel atomization as being separated into several interacting mechanisms, among which is the additional disintegration of the larger droplets produced by high relative gas velocity. For swirl or orifice injectors and for impinging jet injectors, this mechanism is appropriately named secondary atomization. Carburetion and air atomization depend on the high-velocity gas stream to perform both initial disintegration of the "bulk" of the fluid and the breakup of large drops. In order to study this phase of atomization it is convenient to observe a single drop or a train of drops. Different experimental techniques are used to investigate the breakup of large drops: (a) free fall from towers or in stairwells; (b) droplets suspended in vertical windtunnels with air velocity adjusted to hold the drop stationary; and (c) a shock tube for supersonic velocities. The breakup of drops gives information which, with suitable extrapolations, can be useful in spray analysis.

Lane[40] has shown experimentally and Hinze[41] has shown

theoretically that differences exist between the case where the drop is subject to steady acceleration (free fall) and the case where a drop is suddenly exposed to a high-velocity gas stream. The criterion for determining which type of breakup will occur is given by the ratio

$$\frac{t_{buildup}}{t_{oscillation}}$$

where $t_{buildup}$ is the time required for the buildup of the velocity of the air relative to the drop. The period of drop oscillation in its principal mode is $t_{oscillation}$. Shock breakup occurs if this ratio is small compared to unity, and the steady-acceleration breakup occurs if this ratio is large.

Steady acceleration produces two types of breakup, the "bursting bag" and the natural breakup. The "bursting bag" breakup of a drop has been described by Lane as follows:

> "As it came under the influence of the airstream, the drop was seen to become increasingly flattened, and at a critical velocity of the air it was blown out into the form of a hollow bag attached to a roughly circular rim. Bursting this bag produced a shower of very fine droplets, and the rim, which contained at least 70% of the mass of the original drop, broke up later into much larger drops."

The natural breakup mechanism involves the smooth transition of a large parent drop into two main drops with one or two smaller drops.

Magarvey and Taylor[42] conducted free fall experiments using a train of drops of uniform size and found that the wake of successive drops had no effect on the mechanism of breakup. Water drops 7 to 8 mm in diameter were stable in free fall at the terminal velocity. Water

drops 7 to 10 mm were observed to break up naturally, whereas larger drops, 10 to 12 mm, broke up either naturally or bursting-bag type. The photographs suggest that the bursting-bag breakup results from drops less disturbed by vibrations. During fall the drops vibrate, but the data did not suggest that oscillations in planes perpendicular to the airstream were a major factor in the breakup mechanism. However, in the case of bursting-bag breakup, there were lobes formed on the rim, each of which produced a drop. The number of lobes, and hence the number of large drops formed from the rim, was related to the vibrations. In Figure 2 a histogram is shown of the size distribution of small droplets formed from disintegration of a large drop.

A drop suddenly exposed to a fast airstream breaks up in a manner different from the "bursting bag". Lane[40] described the "shock" breakup as follows:

> "This mode of break-up is strikingly different from that observed at the critical velocity in a steady stream of air. Instead of the drop being blown out into a thin hollow bag anchored to a rim, it is deformed in the opposite direction and presents a convex surface to the flow of air. The edges of the saucer shape are drawn out into a thin sheet and then into fine filaments which, in turn, break into drops."

Table IV which shows the critical velocity for breakup of drops of decreasing size was taken from Lane.[40] The constancy of the term $V_s^2 D$ suggests that there is a parameter which would be useful as a drop stability parameter; this quantity is the Weber number. The following heuristic argument illustrates the significance of the Weber

TABLE IV. CRITICAL VELOCITY FOR BREAKUP OF DROPS OF DIFFERENT DIAMETERS

D, mm	Critical Velocity, m/sec, for Steady Acceleration V_s	"Shock" Acceleration V_t	$V_s^2 D$
4.0	12.5	12.0	625
3.0	14.4	12.1	622
2.0	17.5	12.6	612
1.0	24.7	16.0	610
0.5	35.0	24.0	612

number: deformation of a droplet results from the balance of the aerodynamic forces represented by $(1/2)\rho V^2$ and the surface tension forces, which are related to σ/D. Forming a dimensionless group from these two forces, one gets the Weber number:

$$W = \frac{\rho V^2 D}{\sigma} .$$

The critical Weber number, W_{crit}, for shock breakup is somewhat smaller than W_{crit} for steady-acceleration breakup. Lane found that for a 50 μ drop the ratio of the W_{crit} for shock breakup to W_{crit} for steady-acceleration breakup was about 0.48. Hinze[41] has given values for the two cases under consideration as 13 and 22, giving a ratio of 0.69.

Lane obtained correlation for critical breakup velocity of drops of different fluids by using the empirical relation

$$V \sim \sqrt{\frac{\sigma}{D}} \quad \text{for } 28 < \sigma < 475 \text{ dynes/cm}$$

where V is the critical velocity of the air relative to the drop, D is drop diameter, and σ , the surface tension. This also confirms the use of W_{crit} as a criterion for breakup.

A drop suddenly exposed to a high velocity airstream has an unbalanced pressure distribution along its surface which causes acceleration of the drop. Different segments of the drop are accelerated to a different extent; hence the acceleration forces acting on the drop produce deformation in addition to the deformation caused along the drop by that part of the pressure distribution balanced by surface

tension forces. The deformation when $W \cong W_{crit}$ is more conformable to pressure distribution alone, whereas the deformation when $W \gg W_{crit}$ is more conformable to what might be expected of acceleration effects alone. Moreover for $W \gg W_{crit}$ a kind of stripping off of the drop surface takes place owing to waves and ripples formed there.

Hinze[43] has given a more thorough discussion of the forces acting on a droplet. Externally the drop is acted upon by the dynamic pressure of the ambient fluid and by viscous stresses. Deformation requires internal flow which produces internal forces; namely, viscous stresses and dynamic pressure. Surface tension exerts a strong influence on drop breakup. Dimensional analysis leads to the Weber number and a viscosity group

$$Vi = \frac{\eta_\ell}{\sqrt{\rho_\ell \sigma D}}$$

which is preferable to the Reynolds number since it is independent of the velocity and a function only of droplet properties. Hinze suggests a relation of the form

$$W_{crit} = W^{o}_{crit}\left[1 + \varphi(Vi)\right]$$

where the function $\varphi(Vi)$ approaches zero as the liquid viscosity approaches zero; hence W^{o}_{crit} is the critical Weber number for zero viscosity. This result may be compared with Ohnesorge's[44] conclusion that the correct relation should be

$$W_{crit} = 4.25 \times 10^{4}\ Re^{-0.4} \quad .$$

Masugi,[45] on the basis of theoretical calculations, has predicted that

$$W_{crit} = \frac{f(Re)}{1-AVi}$$

where f(Re) is a function of Reynolds number and A is a constant. Here Vi represents again the viscosity group, which in Masugi's nomenclature is called the stability number. Masugi has suggested the relation

$$W_{crit} = \frac{7.57}{1-4.4\ Vi} .$$

Illustrated in Figure 8 is the effect of viscosity on W_{crit} for the case of a drop suddenly exposed to an airstream.

Lane has found that for a dibutyl phthalate drop exposed to supersonic velocities in a shock tube, a limiting value of 15μ for the mean drop size is approached as shock velocity is increased. This means that above a certain velocity the Weber number fails as a criterion for breakup since the mean drop diameter approaches a constant as the velocity becomes very large. Masugi conducted experiments using a suction nozzle and water drops. For a range of drop diameters from 400 to 2000μ, the measured critical Weber number varied from 7.2 to 6.7, the higher Weber number corresponding to the smaller drops. Since the time of velocity buildup was about one tenth of the natural vibrational period of the drops, these values of W_{crit} may be considered to correspond to the "shock" case. For the range of drop diameters from 100μ to 700μ, Hanson, Domick, and Adams[46] found the following empirical relations for disintegration of a drop in a shock tube:

$D \sim V^{-1.497}$ for distilled water and

$D \sim V^{-1.706}$ for methyl alcohol.

Also obtained was a relation between critical Weber number and drop diameter with the value of W_{crit} increasing as D decreased.

A drop may have initially a high velocity and $W > W_{crit}$. Drag slows the drop and the time of breakup relative to slowing may be such that the drop is decelerated to a non-critical Weber number without disintegration.

In order to apply the critical Weber number as a useful parameter for the prediction of stability of a drop it is necessary to know the type of flow. The available experimental values refer to parallel flow. It is possible that irregular ambient fluid flow patterns can be characterized by a suitable average value of W_{crit}.

Hinze[43] has discussed emulsification in turbulent flow for liquid-liquid systems. However the concepts introduced by Hinze may apply also to disintegration of liquids by a gaseous ambient fluid. Dynamic pressure, rather than viscous shearing forces, cause breakup in turbulent flow. According to Hinze:

> "These dynamic pressure forces are caused by changes in velocities over distances at the most equal to the diameter of the drop. In regard to the area just around the drop, the plane hyperbolic and Couette flow patterns are the ones most likely to be responsible for breaking up the largest drops."

The kinetic energy of a turbulent fluctuation increases with increasing wavelength. Thus velocity differences due to fluctuations with a wavelength equal to twice the drop diameter will produce a higher dynamic pressure than those due to fluctuations with shorter wavelength. If

these fluctuations are assumed to be responsible for the breakup of drops,

$$W_{crit} = \frac{\rho_g \overline{V^2} D_{max}}{\sigma}$$

where $\overline{V^2}$ is the average value across the whole flow field of the squares of velocity differences over a distance equal to D_{max}, ρ_g is the density of the gas, and σ is the surface tension. To relate the average kinetic energy to this distance, one considers the simplest case; namely, an isotropic homogeneous turbulence. For this case of turbulence the main contributions to the kinetic energy are made by fluctuations where the Kolmogoroff[47] energy distribution law is valid. In this region the turbulence pattern is determined solely by the energy input per unit mass per unit time, ε ; it can be shown that

$$V^2 = C_1(\varepsilon D)^{2/3}$$

where $C_1 = 2.0$ according to Batchelor. For sufficiently small values of the viscosity group, it follows that

$$\frac{\rho_g D_{max}}{\sigma} \; C_1(\varepsilon D_{max})^{2/3} = \text{constant} = W_{crit},$$

and that

$$D_{max} \sim (\rho_g/\sigma)^{-3/5} \varepsilon^{-2/5} .$$

The concepts just described may apply to a rocket motor chamber, with ε representing the energy dissipated in turbulent motion. If D_{max} were large relative to the mean drop diameter when ambient fluid is quiescent, then turbulence would insure that the tail of the distribution curve on the large-drop side would be chopped off at D_{max}

and W_{crit} data from parallel flow studies would apply. If the value of D_{max} is approximately equal to the mean drop size for parallel-flow, then the spray characteristics would be determined largely by the turbulent flow patterns in the chamber.

Theoretically, the investigations of drop disintegration in a high-velocity gas stream involve the same difficulties as studies on jet or sheet disintegration. In order to linearize the equations, it is again necessary to make the major assumption of small deformation. Nevertheless, these theoretical investigations may indicate trends and assist in correlating experimental data in a rational manner. Another difficulty is associated with the fact that pressure distributions on the deformed drops, unlike those on spheres, are not well-known.

7. Coalescence of Drops

Turbulent flow of the gas surrounding the drops of spray causes drop collisions. The paths followed by the larger drops deviate from the streamlines of the gas flow which the smaller drops follow more closely. Hence in irregular flow with high enough concentration of drops it seems reasonable that some trajectories cross. Also, all drops do not have the same velocity and the faster drops can collide with the slower drops; however, not every collision of drops would necessarily be inelastic and result in coalescence.[48] Those drops that do collide and "stick" would in general have a Weber number less than critical despite the increased diameter.[23] The Nukiyama and Tanasawa[21] equation for SMD, which is discussed more fully in subsection 10, has

two terms, one of which accounts, in part, for the agglomeration of drops. Since the Nukiyama and Tanasawa equation is based on results for an air atomizing nozzle, it was possible to establish a criterion for the magnitude of the effect due to the coalescence of drops in terms of the ratio of the volume flow rates of air to liquid, Q_A/Q_ℓ. When this volume ratio is less than 5000, increases in drop size due to coalescence become observable.

Considering a cubic spacing for the drops and calculating the volume of air associated with each drop, one finds that Q_A/Q_ℓ equal to 5000 corresponds to a drop spacing of about 14 diameters. The mean drop size increases due to agglomeration when the spacing is of this order.

Three mechanisms were considered by Saffman and Turner[49] to account for the collision and coalescence of drops in turbulent clouds; these are:

(1) Spatial variations of the turbulent motion cause relative velocities between the drops. This is a process whereby drops of equal size collide.

(2) Each drop moves relative to the surrounding air due to the fact that the inertia of a drop differs from that of the air which it displaces. Neighboring drops of unequal size will have unequal velocities.

(3) Gravitational forces may cause differential drop velocities. It is necessary to consider the distortion of flow due to the presence of a drop. A measure of this distortion is the collision efficiency

$$\eta_c = \frac{\text{actual number of collisions}}{\text{number of collisions in absence of flow distortion}} .$$

Obviously η_c depends on the nature of the flow. For the case of two approaching drops of approximately the same size, the value of η_c is assumed to be unity; i.e., distortion of the flow does not influence the collision rate.

Assuming isotropic turbulence and η_c equal to unity, the collision rate due to spatial variations of turbulence is

$$N = n_1 n_2 (r_1 + r_2)^3 \left[\frac{8\pi\varepsilon}{15\nu}\right]^{1/2} ,$$

which is valid for r_1/r_2 less than two. In the preceding equation, n_i is the number density of drops of radius, r_i, ε is the rate of energy dissipation per unit mass due to turbulence, and ν is the kinematic viscosity. Numerical integration of the collision rate gives the time rate of change of drop size distribution due to spatial variations of velocity in turbulent flow.

Extending the analysis to include all three mechanisms, Saffman and Turner[49] have derived the formula

$$N = \frac{2R^2 n_1 n_2}{\sqrt{2\pi}} \left[\underbrace{\frac{\varepsilon R^2}{9\nu}}_{\substack{\text{spatial} \\ \text{variation} \\ \text{of velocity}}} + \underbrace{\left(1 - \frac{\rho_g}{\rho_\ell}\right)^2 (\tau_1 - \tau_2)^2 \left\langle \left| \frac{Du}{Dt} \right|^2 \right\rangle}_{\substack{\text{inertial effect due to} \\ \text{unequal drop sizes}}} + \underbrace{\frac{g^2}{3}\left(1 - \frac{\rho_g}{\rho_\ell}\right)^2 (\tau_1 - \tau_2)^2}_{\text{gravity}} \right]^{1/2}$$

where $R = (r_1 + r_2)$, ρ_g = density of gas, ρ_ℓ = density of the drop, τ_i = relaxation time* of a type i drop,

---

* The relaxation time is derived from small drops obeying Stokes law and is equal to $2r^2/\nu_\ell$.

$$\left\langle (Du/Dt)^2 \right\rangle = 1.3\sqrt{\frac{\varepsilon^3}{\nu}}$$

the mean square acceleration due to turbulence, and g = gravitation constant. Within the brackets are three terms; below each term we have identified the physical mechanism described by the term. The equation for N is not valid when r_1/r_2 differs greatly from unity. By taking the ratio of terms within the brackets, it is possible to determine under what conditions a particular mechanism will predominate.

Under certain conditions the drops of a spray will coalesce due to turbulent flow; it may well be that a regular flow disturbance also results in changes of drop size. Miesse[50] has conducted an experiment which indicates that this is indeed the case. Miesse investigated the effect of ambient pressure oscillations on the disintegration and dispersion of a liquid jet by imposing a high-intensity acoustic field on the jet. The effect of a localized sound source directed perpendicular to the stream was to disperse the droplets in a diverging sinusoidal configuration; the effect of an axial cavity resonance directed parallel to the stream was to coalesce the droplets as a result of the velocity variation of successive fluid particles. Coalescence of drops due to pressure oscillations may be a contributing factor to combustion instability.

8. Spreading and Mixing of Sprays[23, 51-54]

Prediction of spray spreading and mixing is primarily a fluid-mechanical problem. The initial spreading of the spray is due to the momentum given to the drops by the nozzle. Mixing of the evaporated

spray is the result of molecular and turbulent diffusion. The kinetic theory of gases can be used to explain molecular diffusion. In turbulent flow most of the mixing is a result of the turbulence; the gross motion of discrete masses of fluid accounts for more mixing than molecular diffusion. Vapors, either from the fuel or from the oxidizer, have a density of the same order of magnitude as the gaseous mixture within the combustion chamber and can, therefore, follow the motion of the turbulent eddies which are characterized by an intensity of turbulence and a scale of turbulence. Drops, on the other hand, because of their larger inertia follow the turbulent motion with a lessened amplitude.

The random motion of the eddies relative to the average motion of the mixture produces material transport. It is possible to use equations analogous to those applicable to molecular diffusion for the description of turbulent transfer:

$$\dot{m} = -(\varepsilon + D)\nabla c_v - \varepsilon_d \nabla c_d$$

where $\dot{m}$ is the mass rate of transport per unit area, ε and D are the eddy and molecular diffusivities, respectively, ε_d is drop eddy diffusivity, and ∇c_v and ∇c_d are the concentration gradients for vapor and drops respectively. The eddy diffusivity depends on the flow conditions in the stream. Experimental results indicate that, as a first approximation, ε may be treated as a constant in the turbulent core of a stream. The eddy diffusivity is related to the scale and intensity of turbulence by

$$\mathcal{E} = L\sqrt{\overline{U^2}}$$

$$L = \int_0^T \frac{\overline{U_t U_{t+T'}}}{\sqrt{\overline{U_t^2}}\sqrt{\overline{U_{t+T'}^2}}}\, dT'$$

where L is the scale of turbulence, $\sqrt{\overline{U^2}}$ is rms of the velocity deviations from the mean velocity, and the integrand is the correlation of velocities measured at two different locations simultaneously.

In order to estimate the eddy diffusivity of drops, we assume that the drag on the drops follows Stokes law and that the turbulent motion is sinusoidal; in this case

$$m\ddot{S} = 3\pi\eta D(U_m \cos\omega t - \dot{S})$$

where S is the displacement, m stands for the mass of a drop of diameter, D, η is the viscosity of gas, and U_m equals the maximum eddy velocity. The steady-state solution to the above equation is

$$S = \frac{2b(2b\sin\omega t - \omega\cos\omega t)}{\omega^2 + 4b^2}$$

where $b = 3/2\,(\pi\eta D/m)$. The amplitude of the gas motion relative to a mean position is

$$S_o = \int_0^{\pi/2} U_m \sin\omega t\, dt = \frac{U_m}{\omega}.$$

The ratio of gas amplitude to the amplitude of the drop trajectory is

$$\frac{S}{S_o} = \frac{2b(2b \sin \omega t - \omega \cos \omega t)}{\omega^2 + 4b^2} .$$

Maximizing the displacement ratio leads to

$$\frac{S_{max}}{S_o} = \sqrt{\frac{4b^2}{\omega^2 + 4b^2}} .$$

The frequency of the drop motion is the same as that of the gas motion so that the velocity of the drop is reduced in the same proportion as the displacement. Since the eddy diffusivity is a product of velocity and displacement,

$$\frac{\varepsilon_d}{\varepsilon} = \left[\frac{S_{max}}{S_o}\right]^2 = \frac{4b^2}{\omega^2 + 4b^2} = \frac{1}{1 + \left[\frac{\omega m}{3\pi\eta D}\right]^2}$$

which provides an estimate of the ratio of drop diffusivity to the eddy diffusivity in the gas stream. Experiments conducted by Longwell and Weiss[53] indicate that $\varepsilon_d/\varepsilon$ for unvaporized fuel in a 6-inch duct may be approximately one half. Their analysis includes a theoretical prediction for the fuel distribution downstream of point and ring sources. For a point source the distribution is gaussian.

Bahr[54] investigated experimentally spreading and evaporation downstream of a contrastream fuel injector in a duct. His results agree with the gaussian prediction of Longwell and Weiss. A typical total and liquid fuel distribution from Bahr's experiments is shown in Figure 9.

The degree of mixing to be expected in rocket motors can be inferred from motion pictures of combustion in a transparent 100-pound thrust rocket engine burning LOX and hydrocarbons which were taken

by Bellman, Humphrey, and Male.[55] Various injectors, e.g., parallel jets and impinging jets, were used to study different combustion patterns. With parallel-jet injection a striated pattern of smooth stream flow, as indicated by the intensity of luminosity, was observed. In fact, the location of fuel and oxidizer jets could be determined from the striations. Increasing the number of jets resulted in more uniform combustion, and turbulence-producing projections increased the apparent mixing and circulation of propellants. Low levels of turbulence and small values of ε_d must apply for striated flow and nonuniform combustion.

9. Evaporation of Sprays

It is apparent that the various spray variables are interdependent. Mixing of fuel vapors depends on the previous evaporation; evaporation depends on mixing since it determines, in part, the local vapor concentration. For convenience the many processes are being discussed separately.

Determination of evaporation rates of a spray poses a difficult problem. Evaporation depends on the local temperature, the local vapor concentration, fluid properties, and local turbulence characteristics. To gain fundamental information various models have been studied experimentally and theoretically:

(a) single spherical drop of pure liquid

(1) in still air

(2) in free convection

(3) in forced convection

(b) deformed drops in forced convection.

When the pure liquid is replaced by a mixture, such as JP-5, then an additional equation must be introduced to account for the non-linear variation of vapor pressure with temperature and the time-varying composition. Complete sprays have been investigated theoretically by assuming a certain initial size distribution and an evaporation law from which subsequent variations in size distribution can be predicted. Experimental studies of the changes in size distribution with time for a spray subjected to a turbulent flow field have been conducted.

For some applications of sprays, for example in the process industries, the evaporation of the spray is the final problem, but in combustion "cold-flow" spray studies are still an approximation to the ultimate problem. Of course, in ignition studies the "cold-flow" investigations are important.

A single drop of pure liquid evaporating in still air follows the evaporation formula

$$D^2 = D_o^2 - Kt$$

where D is drop diameter at time, t, D_o is the initial drop diameter, and K is an evaporation constant which can be predicted theoretically. This equation has been confirmed by numerous experiments.[6,88,89] From the equation $D^2 = D_o^2 - Kt$ it follows that the lifetime of a drop evaporating in still air is proportional to D_o^2. When the drop is exposed to forced or free convection currents, the gradients of temperature and concentration become a function of the polar angle. This is illustrated in Figure 10. It is evident that in the region of the forward stagnation

point, the temperature gradients are greater than at other points. The Nusselt number, in terms of which heat and mass transfer can be expressed, is a function of the angle measured from the upstream stagnation point. The point values of the Nusselt number can be replaced by a suitable average value. For free convection the average Nusselt number has been determined empirically to be:

$$\text{Nusselt number for heat transfer} = Nu = 2.0 + C_1 Pr^n Gr^m$$

$$\text{Nusselt number for mass transfer} = Nu' = 2.0 + C_2 Sc^n Gr^m$$

where C_1, C_2, n, and m are constants, Pr is the Prandtl number, Gr is the Grashof number, and Sc is the Schmidt number. For a single water drop Ranz and Marshall[56] found $C_1 = C_2 = 0.60$, $n = 1/3$, and $m = 1/4$.

For forced convection the correlations for the Nusselt number are:

$$Nu = 2.0 + C_3 Pr^n Re^m$$

$$Nu' = 2.0 + C_4 Sc^n Re^m$$

where C_3 and C_4 are constants and Re is the Reynolds number. Ranz and Marshall found $C_3 = C_4 = 0.60$, $n = 1/3$, and $m = 1/2$ for an isolated water drop evaporating in dry air. Hsu, Sato, and Sage[57] point out that m increases from 0.5 to 0.8 with increasing turbulence. In the limit as $Re \rightarrow 0$, i.e., for still air, Nu and $Nu' \rightarrow 2.0$. This is consistent with the formula stated for drop evaporation in still air.

Frössling[58] applied the heat and mass transfer equations and a modified Navier Stokes equation to the problem of an evaporating drop

with a boundary layer. It was determined that Nu and Nu' are equal when Pr Re in Nu is replaced by Sc Re in Nu'. [A ratio of the average value of $(p_T - p_v)/p_T$ across the transfer path has been equated to unity, where p_T is total pressure and p_v is the partial pressure of the vapor.] The same functional form for Nu and Nu' follows from the fact that the heat and mass transfer equations are identical when Pr Re has been replaced by Sc Re. When the boundary layer controls the rate of transfer of mass or heat, in general, Nu has the same form as Nu'.

Experimentally Ingebo[59] investigated the evaporation of different pure liquid drops which had latent-heat values from 50 to 500 gram-calories/gram and which were subjected to forced convection with air temperatures in the range 30°C to 500°C. Correlation was obtained using the following empirical expression:

$$\mathrm{Nu} = \left[\frac{\lambda_A}{\lambda_v}\right]^{0.5}\left[2 + 0.303(\mathrm{Re\ Sc})^{0.6}\right] = \frac{hD}{\lambda}$$

where λ_A and λ_v are the thermal conductivity of air and vapor, respectively, evaluated at an average film temperature.

In order to find the rates of evaporation it is necessary to know the drop temperature, since the vaporization rate $\dot{m}$ is given by

$$\dot{m} = \frac{h}{\Delta\ell}\,\Delta T = \frac{\lambda\,\mathrm{Nu}A}{\Delta\ell\,D}\,\Delta T$$

where h is film coefficient, A is the drop surface area, $\Delta\ell$ is the latent heat of vaporization, and ΔT is the temperature difference between the drop and surrounding fluid. The mass transfer equation can be used equally well to calculate $\dot{m}$; when it is used, the vapor

partial pressures are essential information. The connection between the mass and heat transfer rate equations is an equation relating vapor pressure to temperature, $p_v(T)$. Surface temperatures of evaporating drops have been measured by Kobayasi[60] using thermocouples; typical results are illustrated in Figure 11. For very high gas temperatures, such as occur in a rocket combustion chamber, the error in assuming the drop temperature equal to the temperature at the boiling point is negligible.

For a blend of two pure liquids Kobayasi[60] obtained a curve with a knee or kink (two straight line segments at different slope) when the evaporation data were plotted as drop diameter squared versus time. This indicates that one component evaporates completely prior to the complete evaporation of the drop.

Skin friction on the surface of the drop results in a circulation within the drop. Aerodynamic forces on a drop cause deformation and oscillation of the drop. Calderbank and Korchinski[61] have studied experimentally the effects of drop circulation on evaporation rates as compared to the effects of drop oscillation on evaporation rates. Internal circulation increases diffusivity within the drop relative to molecular diffusivity but does not affect the drag coefficient or the heat transfer coefficient. Drop vibration increases the drag coefficient, the heat transfer coefficient, and the effective diffusivity within the drop. No precise data were obtained to define the circulation regime. Savic[62,63] states that circulation is probably absent in drops of a size usually found in fuel sprays, unless the temperature is high enough to

reduce the surface tension below a critical level. Suppression of circulation in small drops is due to a surface-active layer, the extent of which is governed by the balance between interfacial tension and the integral of viscous surface shear. The development of circulation from rest in a drop was calculated for two conditions, viz., when the internal viscosity is high compared to viscosity of the ambient fluid and when internal viscosity is low; the ratio of the two conditions differs by a factor of four. Circulation may affect ignition delay times.

Circulation reduces the boundary layer thickness according to Conkie and Savic.[64] Application of Reynolds analogy between heat transfer and skin friction indicates a substantial increase in heat transfer coefficient due to circulation. The theoretical results obtained by Conkie and Savic[64] do not agree with the conclusions of Calderbank and Korchinski[61] based on experiments.

One method for investigating the evaporation of a spray is to inject the liquid into an airstream within a duct and to sample the spray at stations downstream. Using this technique Bahr[54] arrived at the empirical relation for the percent evaporated N:

$$\frac{N}{100 - N} = 9.35\left(\frac{T_{in}}{1000}\right)^{4.4}\left(\frac{V_{in}}{100}\right)^{0.80} p_{in}^{-1.2}\,\Delta p^{0.42} L^{0.84} \quad .$$

The symbols in the equation for N are:

T_{in} inlet air temperature, ^{o}R

V_{in} inlet air velocity, ft/sec

p_{in} inlet air pressure, inches of mercury absolute

Δp injection pressure, psi

L axial distance from fuel injector, inches.

There is a strong dependence on temperature. Evaporation depends on airstream velocity since it affects residence time, atomization of the fuel, and heat transfer coefficients. An increase of injection pressure has opposing effects: On one hand, greater pressure gives higher injection velocities; on the other hand, increased injection pressure results in finer atomization. The spray used by Bahr was iso-octane. Experiments have been conducted by Foster and Ingebo[65] with a less volatile fuel, JP-5, for which the results are

$$N = 7.4L^{0.38}\Delta T^{0.28}\left[\frac{U_A + U_F}{100 + U_A}\right]^2$$

where ΔT equals air temperature minus wet-bulb temperature of the fuel drop, U_A is the airstream velocity, and U_F, the injection velocity of the fuel.

Ingebo[20] made simultaneous measurements of drop velocities and drop size distribution of an iso-octane spray which was injected contrastream to the air flow in a duct. Velocities of the drops were determined by means of an optical system which utilized a rotating mirror. The angular velocity of the rotating mirror was adjusted until the image of the moving drops remained sharply focused. Angular velocity of the mirror could be correlated with the drop velocities. Using the drop size distribution, Ingebo determined the evaporation

rates and found agreement with Bahr's experiments. The heat transfer coefficients, inferred from the evaporation rates, could be correlated in terms of single-drop results.

Hanson[66] investigated the effect of turbulence on the drop size distribution of an evaporating spray at a point.* Turbulence makes point distributions less uniform; i.e., the size distribution curve less peaked, whereas the distribution for the complete spray remains unchanged. This means that a spray without turbulence in the surrounding gas has regions where the drops of a certain size are concentrated. Turbulence spreads out the distribution. Drop evaporation reduced the drag coefficient relative to a non-evaporating drop at the same Reynolds number.

A theoretical treatment of spray evaporation and combustion has been given by Shapiro and Erickson[67] who show how the size distribution changes during evaporation, combustion, or acceleration. The general differential equation governing the concentration of particles as a function of size, position, and time will now be given for one dimensional duct-type flow as formulated by Shapiro and Erickson. Consider the flow of a discrete particle cloud in a duct or stream tube (the latter referring to the particle flow) of variable cross-sectional area A. Let s denote distance along the duct or stream tube,

---

* Actually not at a point, of course, but within a volume very small compared with total spray volume.

G the particle concentration spectrum,* U the particle speed, and R a growth rate which is given by

$$R = \frac{Dr}{Dt}$$

where D( )/Dt signifies substantial derivative and r is drop radius. For evaporation or combustion R has negative values. U, G, and R are specified by the drop radius, location, and time, i.e., G = G(r, s, t,), U = U(r, s, t) and R = R(r, s, t). It is necessary to derive an expression which indicates the rate at which particles change from sizes smaller than r to sizes larger than r. Consider all the particles smaller than r in unit volume at time t. During the time interval dt, all particles will have grown at their appropriate growth rates. The increase of diameter of those particles initially at size r is dr = Rdt. It follows that the number of particles grown larger than r is

$$dn = \frac{dn}{dr}\, dr = GR\,dt \quad .$$

For the time rate of change one divides by dt and obtains the expression:

$$\left[\begin{array}{l}\text{number of particles per unit time} \\ \text{and volume becoming larger than r}\end{array}\right] = GR \quad .$$

Set up a control space within the duct with surfaces at s and s + ds. Count numerically only those particles in the size range from r to r + dr. At the control surface s the values for this range of r are U, G, and R. At the control surface s + ds the values are U + (∂U/∂s)ds, G + (∂G/∂s)ds, etc. In order to account for the particles it is necessary to consider:

---

* G is the number of particles of radius r in unit volume of space per unit interval of drop radius; i.e., G = dn/dr.

(a) convective fluxes in and out of control space,

(b) growth fluxes in and out of the size range,

(c) rate of change of particle number within the control space and size interval.

Considering (a):

(rate of entry into control space) = UAGdr;

(rate of exit from control space) = $UAGdr + \frac{\partial}{\partial s}(UAGds)dr$.

Considering (b):

(birth rate within control space) = GRAds;

(death rate within control space) = $GRAds + \frac{\partial}{\partial r}(GRAds)dr$.

Considering (c):

(time rate of change of particle number) = $\frac{\partial}{\partial t}(Gdr)(Ads)$.

Setting the time rate of change equal to the net convective flux and the net rate of creation, the following differential equations result:

$$A\frac{\partial G}{\partial t} = -\frac{\partial}{\partial s}(UAG) - A\frac{\partial}{\partial r}(GR)$$

and

$$\frac{1}{G}\frac{DG}{Dt} = \frac{1}{G}\left[\frac{\partial G}{\partial t} + U\frac{\partial G}{\partial s} + R\frac{\partial G}{\partial r}\right] = -\frac{\partial U}{\partial s} - \frac{U}{A}\frac{dA}{ds} - \frac{\partial R}{\partial r} \quad .$$

Since G = G(r, s, t), it follows that

$$\frac{dG}{dt} = \frac{\partial G}{\partial t} + \frac{\partial G}{\partial s}\frac{ds}{dt} + \frac{\partial G}{\partial r}\frac{dr}{dt} \quad ,$$

and since ds/dt = U and dr/dt = R for particles of <u>fixed</u> identity, it follows that

$$\frac{DG}{Dt} = - G \left[\frac{\partial U}{\partial s} + \frac{U}{A} \frac{dA}{ds} + \frac{\partial R}{\partial r} \right] .$$

Shapiro and Erickson solve this differential equation for several special cases; the case of interest here is the evaporation or combustion of a cloud in a very large medium. The assumptions are:

(a) uniformly moving cloud of particles

(b) growth rate R is independent of location or time and depends only on r ($R = K/r$)

(c) the concentration or spectrum depends only on r and t

(d) growth flux GR depends only on r and t.

One of the features of the solution is

$$G = \frac{dn}{dr} = \frac{\exp - (Kt/\overline{D}^{\,2})}{\overline{D}} \left[\begin{array}{c} \text{initial size} \\ \text{distribution} \end{array} \right] .$$

Solutions for three different models of sprays are plotted in Figure 12. One solution is for the Nukiyama-Tanasawa equation and can be considered as representative of an actual spray. The second solution is for a spray model in which all drops initially have a diameter of D_{31}, the volume-diameter mean value. As evaporation or combustion progresses, the size of the initial particles decreases but remains uniform; i.e., all the drops of the same initial group are of equal but decreasing size. This is the conventional model used to replace size distributions for simplified spray analysis. The third solution is for a model in which the actual spectrum is replaced by a spray of drops of variable number but of uniform and constant size,

with the number of drops decreasing at a rate proportional to the rate of evaporation or combustion. In the plot of fraction evaporated or burned versus time, Figure 12, the model of variable number but constant size drops most nearly approaches the result based on the Nukiyama-Tanasawa distribution.

The evaporation of liquid sprays has been examined theoretically by Probert[14] using two assumptions:

(a) The size distribution in the spray follows the Rosin-Rammler distribution for which the cumulative form is:

$$1 - V = \exp\left[-\left(\frac{D}{\overline{D}}\right)^{\delta}\right]$$

where V is the volume fraction of spray occurring in drops with diameter less than D, δ is the distribution constant which determines the breadth of the distribution, and $\overline{D}$ is a reference drop size. The distribution peak occurs at $\overline{D}$.

(b) The time history of a drop initially of diameter, D_o, is given by

$$D^2 = D_o^2 - Kt \quad .$$

Using these assumptions Probert arrived at the following integral for the fraction unevaporated as a function of time

$$\text{fraction unevaporated} = -\frac{\delta}{\overline{D}} \int_{\sqrt{Kt}}^{\infty} D^{\delta - 4}(D^2 - Kt)^{3/2} \exp\left[-\left(\frac{D}{\overline{D}}\right)^{\delta}\right] dD \quad .$$

Integration leads to the curves presented in Figure 13. The interpretation of these curves and their relation to combustion will be discussed in subsection 12.

The rates of evaporation of small drops of the order of a micron in diameter deviate from the law $D^2 = D_o^2 - Kt$. Small drops have been observed by Monchick and Reiss[68] to obey a law of the form

$$\frac{dr}{dt} = \frac{a}{1 + br} ,$$

which has been predicted by the theories of Fuchs and Frisch and Collins. In the expression a and b are constants, and r is the drop radius.

Ingebo[69] conducted experiments with single drops of liquid over a limited range of pressure, from 450 to 1500 mm Hg, and found that the heat-transfer coefficient was independent of the static pressure of the system. In the study, the effect of pressure on the vaporization rate was determined by the effect of pressure on the surface temperature of the drop.

The previous discussion has presented the evaporation process from the gross macroscopic heat- and mass-transfer viewpoint. It is also possible to treat evaporation from the standpoint of thermodynamics and the kinetics of the microscopic processes occurring in the liquid and vapor phases.

Penner[70-73] has shown that the Eyring theory of absolute reaction rates might be applied to the evaporation process. Initially an expression for calculating the maximum possible rate of isothermal

vaporization of a liquid drop was developed. This equation, which was derived assuming that evaporation is a first order process; i.e., the rate of evaporation is proportional to the number of exposed molecules at the surface, is

$$\frac{dr}{dt} = -(e)\sqrt{\frac{2\Delta\ell}{kT\gamma}}\ U \exp\left[-\frac{\Delta\ell}{kT}\right]$$

where the symbols have the following meaning:

r = drop radius

t = time

e = base of natural logarithm and is equal to 2.718

$\Delta\ell$ = heat of vaporization

k = Boltzmann constant

T = absolute temperature

γ = specific heat ratio

U = velocity of sound in the liquid.

The results agree well with the measured rates found for most nonpolar liquids.

Another equation was derived in terms of absolute rate theory. Molecules in the liquid are "particles in a box," that is, there is a potential which tends to constrain the molecules to the drop. The contributions to the partition function due to the vibration, rotation, and electronic states are the same for molecules in the vapor or in the liquid. The evaporation rate is proportional to the ratio of partition function for the activated complex to that for the normal molecule. The result is

$$\left[\begin{matrix}\text{molecules evaporated} \\ \text{per second}\end{matrix}\right] = \frac{1}{V_f^{1/3}} \sqrt{\frac{kT}{2\pi m}} \exp\left[-\frac{\Delta E_{act}}{kT}\right]$$

where ΔE_{act} is the activation energy and m is the mass of the molecule. The free volume of the molecules in the liquid V_f is defined as the total volume integral of that portion of the potential energy of the molecules in the liquid which is due to thermal displacements of the center of mass of the molecule from its equilibrium position.

In summary, the evaporation of single drops in still air can be described theoretically with good agreement with experiment provided the transport properties are known accurately. When convection is considered, the non-linear equations prevent derivation of theoretical expressions, except in special cases; it is necessary to resort to empirical formulae. Similarly, the evaporation of sprays has been described by empirical expressions which have been determined only for simpler systems such as a single injector in a duct. The ratio of heat transferred by radiation to the heat transferred by conduction is usually negligibly small and has not been considered here. Phenomena which tend to increase the complexity of the evaluation of spray evaporation are drop circulation, deformation, and vibration.

10. Prediction of Spray Characteristics

Spray characteristics such as drop-size distribution, penetration, cone angle, drop-size uniformity, etc., are influenced by the following factors: physical properties of sprayed fluid, physical

properties of the ambinet fluid, geometry of the atomizer including the supply system, and the flow conditions of the ambient fluid. The prediction of spray characteristics from a knowledge of the above four factors provides impetus for current research.

In order to focus attention on a particular example, consider the swirl atomizer described previously. Observation of the conical liquid sheets from the swirl chamber suggest that an estimate of the linear mean drop size can be made. Waves form near the nozzle, and those with wavelength for maximum growth cause periodic thickening of the fluid sheet in a direction normal to the flow direction. Rings break off from the conical sheet, and the instability of cylindrical ligaments gives additional breakup into drops. The estimate for the linear mean drop size is obtained by considering the volume of liquid in a ring; this estimate is:

$$r = (1.06)(a\,\lambda^*)^{1/2}$$

where r equals the linear mean radius of the drops formed, a is the sheet thickness, and λ^* is the wavelength for maximum growth rate, which can be estimated from Figure 14. Figure 14 is based on the analysis of York, Stubbs, and Tek.[34] Actually a swirl atomizer produces a range of sizes, and the preceding simplified estimate cannot, of course, disclose information as to drop-size distribution. Not only is it necessary to know the drop-size distribution, but it is necessary to know the velocity of the drops formed from the ring in order to predict the sizes of drops resulting from secondary atomization. The information is not available from this approach.

Empirically a formula has been developed for the mean drop size from an atomizer using a secondary fluid. Examination of this formula may reveal a clue as to the most fruitful method of attack on the problem of predicting mean drop size. Air-atomization, which depends on high gas velocity to break up the bulk of the fluid and the larger drops, has been studied by Nukiyama and Tanasawa[21] who obtained an empirical equation for the volume to surface mean drop diameter or Sauter mean diameter, SMD; i.e.,

$$SMD = 585 \frac{\sqrt{\sigma}}{V\sqrt{\rho_\ell}} + 597 \left[\frac{\eta_\ell}{\sqrt{\sigma \rho_\ell}} \right]^{0.95} \left[\frac{10^3 Q_\ell}{Q_A} \right]^{1.5} .$$

In the preceding relation it is necessary to specify units since the constants have dimensions. The parameters have the following meaning:

$\frac{Q_\ell}{Q_A}$ = liquid to air volume flow rate ratio;

η_ℓ = liquid viscosity coefficient in dyne-sec/cm^2;

σ = surface tension in dyne/cm;

SMD = Sauter mean diameter in microns;

V = air velocity in m/sec;

ρ_ℓ = liquid density in g/cm^3.

The first term in the expression is proportional to the square root of a Weber number. The second term includes a factor closely related to the viscosity group or stability number discussed earlier. The factor

Q_ℓ / Q_A can be interpreted as representation of effect due to coalescence of droplets. A prediction formula for the SMD from a secondary-fluid atomizer must include the concept of critical Weber number, account for viscosity effects, and provide for drop coalescence.

The empirical equation of Nukiyama and Tanasawa for SMD has been verified by other experimenters; e.g., by Golitzine[74] and Lewis, et al.[22] Bitron[9] verified the Nukiyama-Tanasawa equation for supersonic air jets over a narrow range of variables. In Bitron's experiments there was a supersonic air jet directed in the x-direction and an intersecting liquid jet moving in the y-direction. Masugi[45] has used the critical Weber number to derive a theoretical formula for the mean drop size. The concept employed was that the atomization process continues until all drops have velocity or diameter such that the Weber number is less than critical. Atomization can be said to be complete when a given generation of drops has $W < W_{crit}$. Masugi's formula gives the ratio of the initial linear mean drop size to the final linear mean drop size. Since the initial Weber number and linear mean drop size must be known, this does not represent a complete prediction formula.

Due to the fact that there are many variables which influence the spray characteristics, use of dimensional analysis may provide insight to the problem. This discussion follows closely that of Shafer

and Bovey[75] and Kanevsky.[76] For a swirl atomizer, if the geometry remains fixed from nozzle to nozzle, one length can characterize the geometry of the system. The following variables are assumed to define the mean drop size:

Symbol	Meaning	Dimensions
$\bar{D}$	the mean drop size	L
h	characteristic atomizer dimension	L
η_ℓ	viscosity of sprayed liquid	$ML^{-1}T^{-1}$
η_A	viscosity of ambient fluid	$ML^{-1}T^{-1}$
ρ_ℓ	density of sprayed liquid	ML^{-3}
ρ_A	density of ambient fluid	ML^{-3}
Δp	injector pressure drop	$ML^{-1}T^{-2}$
θ	spray cone angle	- -
σ	surface tension of sprayed liquid	MT^{-2}

If the geometry of the atomizer parts change, as for example was done in the experiments of Söhngen and Grigull,[25] it is necessary to introduce lengths for swirl chamber, tangential feed holes, etc. Parameters which characterize the flow of the gases surrounding the atomizer are ignored. Pressure within the spray chamber has not been included. One final variable which is neglected is the temperature; however, temperature is introduced indirectly through the dependence of η_A, η_ℓ, σ, ρ_A, and ρ_ℓ on temperature. For an evaporating spray, temperature effects would not be negligible.

There are three dimensions, M, L, and T, and nine variables. From this it follows that there should be six dimensionless groups. Previous discussion has indicated that the Weber number is an important group. The viscosity group, Vi, which was also discussed in subsection 6 is

$$Vi^2 = \frac{W}{Re^2} \quad .$$

Rather than use Vi, it will be more convenient to use the Reynolds number, Re. The following six groups are chosen:

$$\frac{\bar{D}}{h} \; , \; \frac{\eta_\ell}{\eta_A} \; , \; \frac{\rho_\ell}{\rho_A} \; , \; \theta \; , \; W, \; Re \quad .$$

Since the injector pressure drop Δp is proportional to $\rho_\ell V^2$, it is possible to express W and Re in terms of Δp:

$$W = h\Delta p/\sigma \quad \text{and} \quad Re = L\sqrt{\rho_\ell \Delta p} \; / \eta_\ell \quad .$$

Any group can be represented as a function of the remaining five dimensionless groups. The mean drop diameter is the variable of interest; hence

$$\frac{\bar{D}}{h} = \psi \left[W, \; Re, \; \theta \; , \; \frac{\eta_\ell}{\eta_A}, \; \frac{\rho_\ell}{\rho_A} \right] \quad .$$

For a fixed geometry and for a particular liquid sprayed into a particular atmosphere, the function ψ reduces to

$$\frac{\overline{D}}{h} = \psi \left[W, \, Re \right] \quad .$$

Shafer and Bovey[75] were able to correlate the data obtained by Rupe[10] from a swirl atomizer. For various Re, $\overline{D}/h$ was a function of W within ± 10 percent.

An equation has been developed by Harman[77] which can be used under specified conditions to determine the volume-to-surface mean drop diameter, D_{32}, of a high speed spray issuing from a simple orifice. Diesel injectors and showerhead rocket injectors use the simple orifice atomizer. An energy balance was used to ascertain the dimensionless parameters which are important in determining the mean diameter. By using the experimental data of other investigators, the following formula was developed:

$$\frac{h}{D_{32} W} = 3 \times 10^{-4} \frac{\left[\frac{\eta_g^2}{\sigma \rho_\ell h} \right]^{0.3} \left[\frac{\eta_\ell}{\eta_g} \right]^{1.38}}{\left[\frac{U \eta_\ell}{\sigma} \right]^{1.45} \left[\frac{\rho_\ell}{\rho_g} \right]^{0.052}}$$

where ρ and ρ_g are liquid and gas densities, U is mean linear velocity of jet at the orifice outlet, η_ℓ and η_g are the liquid and gas viscosities, h is orifice diameter, W is Weber number, and σ is the surface tension.

This equation correlates satisfactorily the data of several investigators. It is not a prediction formula in the sense that it was

developed from fundamentals without empirical knowledge; the theory is incomplete. Its value lies in the trends indicated. For example, the D_{32} increases with increasing gas viscosity and decreases with increasing surface tension.

As yet a formula for mean drop size has not been developed without using experimental results. A formula has not been developed to predict drop size distributions with or without empirical information.

11. Spray Formation in Rocket Motors

Injector heads of rocket engines are frequently designed with impinging jets for spray formation. A qualitative comparison of impinging jet, random and hypoid showerhead, splash plate, concentric ring, and swirler insert injectors has been given by Stehling.(78) A summary of important injector systems together with some remarks concerning desirable and undesirable features is presented in a survey paper by Penner and Datner.(79)

In this subsection a summary of the information available in the literature concerned specifically with impinging jets is presented. Atomization by jet impingement is a field which has received only limited study. For example, only meager information has been reported in regard to drop size distributions. Specific information about the combustion behavior of sprays formed by impinging jets is lacking.

Lee(80) compared the volume distribution of drops obtained experimentally using an intermittent, diesel-type impinging-jet atomizer with that obtained using a single jet. The results are presented in

Figure 15. The pressure at the nozzle inlet was the same for both the impinging jet and for the single jet. However the velocity of the impinging jets was probably lower than for the single jet as a result of large pressure loss in the complex passages of the impinging-jet nozzle. It is possible to design a single-jet injector with less pressure loss than that of an impinging-jet injector. The results of these tests showed much poorer atomization for the impinging jet than for the single jet.

One advantage of the impinging jet relative to the single jet is the increased dispersion. It is necessary to recognize that the performance of an injector head does not depend just on the characteristics of one set of jets but depends on the complete injector head. The single jet is the basic element of the showerhead injector; a pair of jets is the basic element of the impinging jet injector. Considering the injector head as a complete unit, the impinging jet-design gives superior dispersion. The photographic investigation of combustion in a two dimensional transparent rocket engine by Bellman, Humphrey, and Male[55] indicates the absence of streaky or localized combustion with impinging-jet atomization.

Fuel and oxidizer combinations can be divided into two categories: (a) The fuel and oxidizer have nearly the same volatility; for example, nitric acid and aniline, and (b) fuel and oxidizer have greatly differing volatility; for example, JP-5 and LOX. When the fuel and oxidizer are

of nearly equal volatility, the liquid phase mixing of a pair of like-unlike impinging streams is of primary importance. When propellants differ greatly in volatility, the drop size distribution becomes important.

Rupe[37] has studied the liquid-phase mixing of a pair of impinging streams. He assumed that an optimum injector system for a bipropellant rocket system mixes components uniformly at a given ratio. In order to characterize the liquid phase mixing, a mixing factor F is defined. The equation for F is

$$F = 100\left[1 - \sum_{0}^{n} \frac{(cw)(R - r)}{WR} - \sum_{0}^{\bar{n}} \frac{(cw)(R - \bar{r})}{W(R - 1)}\right] .$$

In the expression for F the symbols have the following meaning:

c = correction factor =

$$\frac{\text{portion of the spray cross section represented by sample}}{\text{gross sectional area of sampling tube}}$$

w = total local weight flow rate of spray

W = nominal weight flow rate

R = nominal mixture ratio = $(W_F)/(W_O + W_F)$

r = local mixture ratio

n = number of samples.

The bar above a symbol applies to the case when $r > R$. The mixing factor F indicates the percentage of a hypothetical spray with the nominal mixture ratio and the remainder unmixed. F also represents a cumulative weighted average of the departure of the local mixture

ratio from the nominal or input value as determined from a large number of separate points. The value of F attains a maximum value when

$$\frac{(\rho V^2 h)_F}{(\rho V^2 h)_O} = 1 \quad .$$

The subscripts F and O identify the fuel and oxidizer respectively, ρ is the density, V is the jet velocity, and h is the orifice diameter.

The influence of several parameters on the Sauter mean diameter SMD of a spray formed by two impinging jets has been studied experimentally by Kling, Chevalerias, and Maman.[38] Silhouette microphotographs were taken to determine SMD; the field of view of the camera included the drops within a volume of about 10 mm^3. The effect of changes in chamber pressure* P and in orifice diameter h on the SMD for the spray is illustrated in Figure 16. In Figure 17 is given a graph which shows the effect of injector pressure drop on SMD for two levels of chamber pressure. The impingement angle was also varied and the results appear in Table V. The measurements which are given in Table V were made at a point 10 cm downstream of the intersection of the impinging jets; the values of the parameters Δp and P were 4 kg/cm^2 and one atmosphere respectively. The fuel was kerosene at a temperature of 20°C.

---

* The conversion factor for pressure in kg/cm^2 to atmospheres is 0.968; hence, the two units of pressure are nearly equivalent.

TABLE V. THE INFLUENCE OF IMPINGEMENT ANGLE ON SAUTER MEAN DIAMETER

Impingement Angle, 2θ	Orifice Diameter h		
	0.5 mm	1.0 mm	1.2 mm
55^{o}	80μ	135μ	150μ
84^{o}	45μ	70μ	90μ

The time delay τ between the injection of the propellants and their conversion to heat is a determining factor in rocket combustion instability.[81] With certain reasonable assumptions,[82] which are discussed more fully in Part I, Section C, it is possible to relate delay time τ to chamber pressure P and injection pressure drop Δp. The relations are:

$$\tau \sim \overline{D}^{\delta} P^{-m'} ,$$

$$\frac{\overline{D}}{h} \sim W_h^{-\alpha} Re_h^{-\beta} ,$$

and

$$\tau \sim p^{-\alpha\delta} P^{-(\beta\delta + m')} .$$

In the above expressions $\overline{D}$ is the volume-surface mean diameter and α, β, δ, and m' are empirically determined constants. Both Re_h,

the Reynolds number, and W_h, the Weber number, are based on the orifice diameter h as a characteristic length. The two terms in the exponent for P, $\beta\delta$ and m', are determined by different physical processes; m' is determined by the influence of chamber pressure on the heat and mass transfer processes whereas β is determined by the effect of chamber pressure on the atomization process. Using Figure 16 it is possible to infer values for β. In the range of chamber pressure of interest, 5 to 30 atmospheres, one obtains from Figure 16 values* for β ; for h = 1.2 mm, β is approximately 0.51 and is valid for a range of chamber pressure from 5 to 20 atmospheres. For h = 0.8 mm, β is approximately 0.26 and is valid for the same range of chamber pressures. In the range of chamber pressure from 20 to 30 atmospheres, the Sauter mean diameter is independent of chamber pressure, which means β is nearly zero. Similarly one can estimate α using the curves presented in Figure 17; an estimate for α is 0.94 for a chamber pressure of 21 kg/cm^2. Because of the scatter in the experimental points in Figure 17, this value for α is doubtful. Values for α have been reported for other types of sprays. For a simple orifice atomizer Miesse[83] gives a value $\alpha = 1/3$. Shafer and Bovey[75] used the data of Rupe[10] and determined $\alpha = 1/2$ for a swirl atomizer.

---

* The value for β can be determined using the coordinates of two points from the same curve: these coordinates are identified by subscripts 1 and 2. The formula for β and a numerical example for h = 1.2 mm is

$$\beta = \frac{\ell n(SMD_1/SMD_2)}{\ell n(P_2/P_1)} = \frac{\ell n(220/102)}{\ell n(20/5.0)} = 0.51 \ .$$

Kling, Chevalerias, and Maman[38] give values for the exponent m:

Exponent, m	Orifice Diameter, mm
0.3	0.8
0.7	1.2

These data are for the case where the injection pressure is 6 kg/cm^2, liquid sprayed is kerosene, and the impingement angle is 55^0; the range of validity is $2 < P < 30$ kg/cm^2.

The spray formed by two impinging liquid jets was investigated by Heidmann, Priem, and Humphrey.[36] At low flow velocities a liquid sheet forms with a regular wave pattern. Regularly spaced drops are thrown off tangentially from the periphery of the main sheet. The regularity at low flow rates suggests that the problem may be amenable to an analytical treatment. At high flow rates the spray pattern shows waves which appear to project from the point of jet impingement. Impinging-jet atomizers as applied in rocket engines operate at high flow rates.

The frequency of the waves of drops in a fully developed spray was measured; an increase in jet velocity or decreased impingement angle results in increased frequency. It should be noted that the frequency was determined by a stationary measuring device. An increase in jet velocity increases the velocity of wave propagation. A straight line was obtained by Heidmann, Priem, and Humphrey[36] from a plot of waves counted per second versus the component of velocity in the plane of the spray; the wavelength is equal to the slope of the straight

line. Hence the wavelength, which is the spacing between groups of drops, is constant as impingement angle or jet velocity is varied.

The wave pattern from an impinging-jet spray is of interest because of its possible relation to combustion oscillations. The waves of drops with frequencies in the range 1500 to 4000 per second from an impinging-jet spray may contribute to combustion instability. If this were the case, the combustion oscillations and the waves of drops could be "decoupled" by varying either jet velocity or impingement angle. The impingement length L does not affect the drop size distribution. The best use of chamber volume can be had by making impingement length as short as possible; however, excessive heat transfer to the injector head may occur with a small value of L.

Stream characteristics prior to impingement have a strong influence on the spray which is formed. Criteria for a good stream or jet have been given by Rupe:[37]

(a) Jet diameter must equal orifice diameter with a divergence of less than 15 minutes of arc,

(b) Jet must be directionally stable,

(c) Jet must have constant mass flow rate which makes it necessary to avoid flow anomalies like cavitation, hydraulic flip, and flow separation in the nozzle,

(d) It is necessary to have knowledge concerning the free stream velocity profile.

To achieve a good stream fully developed turbulent flow can be induced in the orifice. A length-to-bore ratio of approximately ten and a surface roughness of about 0.65 will give a stable jet. Excessive values of surface roughness or length-to-bore ratio can cause a low value of the discharge coefficient and "flare" of the jet.

12. Combustion of Single Drops and of Drop Arrays

The approach to the problem of spray combustion is similar to that used in the case of evaporation studies. It has included experimental and theoretical work based on the burning of single drops or of simple geometric arrays of drops. The behavior of complete sprays has been investigated both theoretically and experimentally but with less success.

Combustion of single drops in quiescent oxygen-inert gas atmospheres has been described by a number of authors.[84-89] Prediction of the burning rate of single drops involves the solution of a heat and mass transfer problem. Surrounding the drop and concentric with it is a spherical flame front of negligible thickness. Steady-state conditions are assumed. The rates of delivery of fuel and oxidizer to this spherical surface are in stoichiometric proportions. By assuming that the rate of reaction at the flame front is fast compared to the rates of delivery of the combustible gases then it is evident that heat and mass transport control the burning rate. Accurate values of the transport coefficients are essential for obtaining quantitative agreement between theory and experiment. Godsave[88] derived an equation for the mass burning rate $\dot{m}_F$,

$$\dot{m}_F = \frac{4\pi\lambda r_\ell}{C_{P,F}} \frac{\ell n \left[1 + C_{P,F}(T_c - T_\ell)/\Delta\ell \right]}{(1 - r_\ell / r_c)} \quad .$$

In this equation the various symbols have the following meaning: λ = an average value of thermal conductivity, $C_{P,F}$ = specific heat at constant pressure of the fuel vapor, T_c = temperature at the flame front, T_ℓ = temperature at the drop surface, $\Delta\ell$ = specific latent heat of vaporization of the fuel, r_ℓ = drop radius, and r_c = flame front radius. Godsave's theory is essentially incomplete since no method for computing either r_c or T_c was developed. The burning rate is seen to be proportional to the droplet radius if $r_c >> r_\ell$ or if the ratio r_c/r_ℓ is constant. A strong dependence of $\dot{m}_F$ on specific heat and thermal conductivity is indicated by this equation, whereas the temperatures T_c and T_ℓ influence the burning rate weakly. Goldsmith and Penner[89] extended Godsave's equation by showing a proper procedure for calculating the two unknowns in Godsave's equation, T_c and r_c. Also they deleted the assumption of constant λ and C_P.

A modification to the theory for drop burning can be made in order to include the effect of dissociation of the fuel, oxidizer, and/or combustion products. Dissociation reduces the flame temperature and affects the radial distance to the flame zone. Rough calculations made by Goldsmith and Penner[89] show that the net effect of dissociation of the calculated values of $\dot{m}_F$ for benzene-air flames is probably less than 10 percent.

In the event that the chemical reactions are slow so that mass transport is no longer rate-controlling, then it is necessary to amend the theory. This has been done by Lorell, Wise, and Carr.[84] When chemical reactions control the rate of mass conversion, there is a flame zone rather than a very thin flame shell. The temperature in the reaction zone, T_c, is reduced.

The mass burning rate $\dot{m}_F$ is related to the evaporation constant K by the expression

$$K = \frac{2\,\dot{m}_F}{\pi\, r_\ell\, \rho_\ell}$$

where ρ_ℓ is the liquid density.

The effects of ambient conditions on the combustion of drops yield useful information to assist in the analysis of spray combustion. Hall and Diederichsen[90] investigated the influence of chamber pressure on the burning rate of single drops. Increasing the pressure increases the boiling point of the liquid drop, decreases the latent heat of vaporization, and also decreases the density at the boiling points. The total burning time for a given drop is proportional to the pressure raised to the negative power, m: experimental values of m are listed below:

Fuel	Value of the Exponent, m
furfural alcohol	0.2
tetraline	0.2
decane	0.3
amyl acetate	0.3
benzene	0.4

The value 0.4 in the preceding compilation for benzene was obtained by Goldsmith.[85]

As the temperature of the ambient air is increased, the rate of evaporation of fuel drops increases until, at about 700°C for hydrocarbons, spontaneous ignition takes place. Kobayasi[60] measured the burning rates in air of several hydrocarbons up to 900°C. The measured evaporation constants for n-heptane burning in air at various temperatures are listed below:

Temperature, °C	Evaporation Constant (K) cm^2/sec	Source of Data
room temperature	.0084	Goldsmith[85]
135	.0114*	Goldsmith[85]
700	.0121	Kobayasi[60]
700	.0110	Kobayasi[60]
800	.0124	Kobayasi[60]

Kobayasi[86] determined the effects of the ambient air temperature on the evaporation constant, K. The results are shown in Figure 18. The influence of ambient temperature on K for a burning drop is less than the influence on an evaporating, but not burning, drop. For a burning drop the ambient temperature affects K indirectly by its influence on flame temperature.

---

* Average of six runs.

Experimentally Kumagai and Isoda[91] have determined the effect of natural convection currents on the mass burning rate of a single droplet by using a falling combustion chamber. For ethyl alcohol the evaporation constant K is about 0.75 mm^2/sec and remains nearly constant as the acceleration which the system experiences is decreased to 0.25 g. From 0.25 g to zero g (a freely falling combustion chamber), K decreases to a value of 0.46 mm^2/sec. For n-heptane, K for one g was found to be about 1.0 mm^2/sec, decreasing to a value of 0.5 mm^2/sec at zero acceleration. Photographs of the burning drops show a concentric flame surface at zero g; however, even at 0.06 g the flame surface has a marked oval shape.

When the oxygen concentration was increased from the normal value in air to 90 percent by weight, the evaporation constant was found by Goldsmith[85] to increase by a factor of from 3 to 5. Graves[87] has investigated the effect of oxygen concentration on the burning rate of iso-octane and found an increase of approximately 34 percent for an oxygen increase from 17 to 35 percent by volume. Oxygen concentration has a marked effect on the burning rate of single drops.

The drop array studies discussed earlier in Part I, Section A, suggest that a single value of K cannot be assigned which is valid for all the drops in a burning spray; it is necessary to use an average or an effective value of the evaporation constant, K_{eff}. The value of K_{eff} would depend not only on the physical and chemical properties of the fuel and oxidizer but would depend also on the spatial distribution of the drops in a spray.

Studies of single drop or simple geometric arrays of drops can provide valuable information as to trends in spray combustion. Single-drop data give a clue as to whether or not changes in certain spray parameters should improve combustion. For example, one might attempt to accelerate combustion by using an additive. Investigations of single drops indicate that the rate of combustion is controlled by (a) drop-size, (b) heat transfer, (c) mass transfer, (d) latent heat of vaporization, (e) heat capacity of the fuel vapor, and (f) heat of combustion. If the additive did not change at least one of the preceding parameters, then any attempt at changing the burning rate would be futile.

In order to ignite the vapor-air mixture from an evaporating drop, it is necessary to add energy. If the vapor-concentration is too low to have an ignitable mixture, then it is necessary to provide additional energy for increasing the drop temperature. Increased drop temperature results in a higher vapor concentration.

Two methods for adding energy for ignition will be discussed. One way to deliver the energy to the drop and vapor-air mixture is by means of an electrical spark. Compared to spark ignition of a homogenous combustible mixture, ignition of a vapor-air mixture from a drop is many times more complicated. The geometry of the system is important; the spacing of the electrodes, the position of the drop relative to the electrodes, and the drop diameter are the significant geometrical variables. Results obtained from the ignition of premixed combustibles establish a minimum for the energy required. With an optimum spark,

the minimum energy to ignite a benzene vapor-air mixture is 2400 ergs (taken from Lewis and von Elbe,[92] page 413). The equivalence ratio requiring the least energy is 1.75; rich mixtures are more easily ignited. If energy must be added to vaporize additional fuel, there will be a time lag since vaporization does not occur instantaneously. Spark duration is important.

Another technique of supplying the energy is thermal. Kobayasi[86] and Nishiwaki[93] used similar techniques to study the thermal ignition of single drops. A furnace on a track was moved so as to surround the drop which was suspended from a quartz fiber. Motion pictures were taken. Temperatures were high enough within the furnace to ignite the vapor. Nishiwaki states that there are two time intervals, τ_1 and τ_2, the sum of which equals the ignition lag. τ_1 is the time necessary to heat the droplet to its steady-state evaporation temperature. τ_2 is the time from the beginning of steady evaporation to ignition. The data presented in Table VI show the dependence of ignition lag on temperature and drop diameter. Jackson[94] has reported a spontaneous ignition temperature for α-methylnapthlene to be 547°C with a time lag of 24 seconds.

The sequence of events leading to thermal ignition begins with the heating of the drop; the heating continues until an equilibrium temperature is reached. This is followed by a period of steady-state

TABLE VI. DEPENDENCE OF IGNITION LAG ON AMBIENT TEMPERATURE AND DROP DIAMETER

	400°C		550°C		680°C		716°C	
τ_1	1.2	2.1	0.8	1.3	0.6	0.9	0.4	0.5
τ_2	∞	∞	0.8	0.7	0.4	0.3	0.2	0.2
$\tau_1 + \tau_2$	∞	∞	1.6	2.0	1.0	1.2	0.6	0.7

Note: For each temperature there are two columns which give the ignition lag in seconds. The left hand column is for D_o = 1 mm and the right hand column, D_o = 1.4 mm. The fuel is α-methylnapthlene.

evaporation during which the vapors descend.* There is a downward vapor stream, the thickness of which is proportional to the diameter of the drop. Following ignition it requires 0.2 seconds or so to establish the upward convection currents. Steady-state combustion occurs until burnout.

Changing the oxygen concentration in the furnace does not affect τ_1. τ_2 is decreased; the ignition lag, which is the sum of τ_1 and τ_2, is decreased. Movies of a drop, which were taken by Kobayasi,

* The vapors descend provided the density is greater than that of the hot ambient air. This is usually the case because of the lower temperature of the vapors; also the vapors usually have a higher molecular weight.

show that ignition occurs at a point in the surrounding vapors. The flame propagates circumferentially around the drop. Products of combustion lie dormant near the drop until convection currents are built up.

The lifetime of a drop depends on the ignition lag and the burning rate. The burning rate can be determined from the evaporation constant. Kobayasi suggests that K, the evaporation constant defined previously in Part I, Section A, be replaced by an apparent evaporation constant, K', which is defined by

$$\tau = D_o^2 / K'$$

where D_o is the initial diameter and τ is the total lifetime. The total lifetime is the sum of τ_1, τ_2, and τ_b. τ_b is the burning time and equals D^2/K where D^2 is the diameter at ignition. Values of K and K' have been determined by Kobayasi and are given in Table VII. The ignition lag time is incorporated in K'. The idea is similar to that of using K_{eff}.

13. Combustion of Sprays

As mentioned previously in Part I, Section A, one approach to the combustion of a spray is to assume a certain law of combustion, usually $D^2 = D_o^2 - Kt$, and a size distribution for the spray. Probert[14] performed an analysis based on these two facts about the spray. Reference to Figure 13, which is taken from Probert, shows that one of the important spray parameters is $\overline{D}$. For a given spray, that is for

TABLE VII. VALUES OF K AND K' FOR DIFFERENT FUELS

Temperature, ^{o}C	Fuel	K	K'
700	n-heptane	1.10	0.96
700	nitrobenzene	1.02	0.94
800	nitrobenzene	1.00	0.95
735	toluene	0.91	0.74

specified δ and $\bar{D}$, and for a given percentage unevaporated or unburned fuel the dimensionless group $\sqrt{Kt} / \bar{D}$ is fixed. The time, t, required for conversion of the given amount of spray is directly proportional to $\bar{D}^2$ and inversely proportional to K. It appears that the extent of combustion is a sensitive function of the percentage of unburned fuel. A limited volume is provided for combustion and, hence, defines a corresponding residence time in the combustion chamber. Figure 13 indicates that a small fraction of fuel will remain unburned unless the residence time is made much longer than may be practical.

During steady-state burning the rate of evaporation equals the rate of injection. The properties of the evaporating spray determine combustion characteristics rather than those of the injected spray, except insofar as the evaporating spray is derived from the injected spray. Figure 19 illustrates this concept. Probert[14] defines a specific volume by the relation

$$\begin{bmatrix}\text{specific}\\ \text{volume}\end{bmatrix} = \frac{\text{volume of the burning spray}}{\text{spray injection rate}} .$$

In view of the dimensions of specific "volume"; i.e., time, perhaps a better nomenclature might be characteristic spray time. The combustion intensity, which has been defined as

$$\begin{bmatrix}\text{combustion}\\ \text{intensity}\end{bmatrix} = \frac{\text{volume rate of fuel injection}}{\text{chamber volume}} ,$$

is inversely proportional to the specific volume. Probert has determined the specific volume as

$$\begin{bmatrix}\text{specific}\\ \text{volume}\end{bmatrix} = \frac{\overline{D}^2}{2K} \Gamma\left(1 + \frac{2}{\delta}\right)$$

where Γ is the gamma function.

Not all injection nozzles provide a spray with a size distribution which can be specified analytically by the Rosin-Rammler distribution law. Tanasawa[95] has deduced the following empirical expression for the weight* distribution function for a spray from a swirl atomizer

$$\frac{dW}{dD} = a D^{2.5} e^{-bD} .$$

Here a and b are constants which are determined for a particular spray nozzle. The burning rate law used was $D^2 = D_o^2 - Kt$. The

---

* The weight distribution function is related to the volume distribution function in subsection 3. The relation is

$$\frac{dW}{dD} = \rho_\ell \frac{dV}{dD}$$

where ρ_ℓ is the liquid density.

formula for the combustion of a spray, which has a maximum drop size, is

$$\frac{W_b}{W_o} = 1 - \exp\left[-3\left(\frac{Kt}{2\overline{D}^2}\right)^{.75}\left(1 - \frac{Kt}{4\overline{D}^2}\right)^{-0.25} \right]$$

where W_b/W_o is the weight fraction of fuel burned, and $\overline{D}$ is the Sauter mean diameter based on the empirical weight distribution.

The following discussion of the burning in still air is based on the experimental investigation by Wolfhard and Parker[96] of a spray formed from a simple orifice nozzle.

Figure 20 shows qualitatively the temperature distribution along the axis of burning spray. The velocity of the fuel at the injector outlet is of the order of 40 to 50 meters/sec and the transit time from the injector outlet to the flame front is less than a 0.1 second. One can estimate the velocity of the drop-entrained-air mixture downstream by considering conservation of momentum. The momentum of the spray equals the momentum of the drops plus entrained air at points downstream. A flame propagates through the droplet-air mixture at a definite velocity; the flame front will be positioned where the velocity of flame propagation equals the velocity of the air-drop mixture. Figure 21 illustrates the entrainment of surrounding gases and the changing velocity profiles which result.

In the free space between the orifice and the flame front where drop formation is accomplished, heat transfer by radiation is

negligible. Kerosene and other similar hydrocarbons absorb radiant energy in bands displaced from the radiant energy emission peaks, as is indicated in Figure 22 which was taken from Berlad and Hibbard.[97] In the preheat zone large temperature gradients result in sufficiently high rates of heat transfer to vaporize the smaller drops which diffuse into the gases in this narrow zone. Thus an inflammable mixture is formed which maintains the flame front.

Three cases exist for the ratio of drop diameter D to scale of turbulence λ .

(a) $D >> \lambda$ The small scale of turbulence affects the wake and the boundary layer on the surface of the liquid resulting in increased heat and mass transfer, which accelerates combustion. This condition can be approximated by the porous sphere combustion technique.

(b) $D << \lambda$ The drop follows the direction of the local air motion. Large relative motions between the drop and the air are improbable.

(c) $D \cong \lambda$ This condition may be expected to be relatively the most detrimental to flame stability. With turbulent flow, which has turbulent eddies of the same size as the drop diameter, very high local velocities may exist. A drop traversing these turbulent eddies cannot respond to the fluid path and will be subjected to fluctuating velocities. The scale of turbulence is as important as the intensity of turbulence in determining combustion behavior. Furthermore, an optimum spray

particle size may exist for a given scale of turbulence in the combustion chamber.

Experimental investigations of flame emissivities in furnaces, which were conducted by Mayorcas and Riviere,[98] indicate that the greatest change of flame condition is brought about by change in the momentum of the injected fuel. It seems reasonable that increased momentum results in a greater level of turbulence. Increasing the momentum always decreased the emitted radiant energy at all points along the flame length; the temperature in the early part of the flame increased, whereas at points downstream an increase in turbulence decreased flame temperature.

In the next few paragraphs the relation of inflammability limits to drop size will be considered. As the drop size is made smaller and smaller, one would expect the combustion behavior of a spray to approach that of a premixed gaseous flame. At the other extreme, as drops increase in size, the behavior of a burning spray is determined by the diffusion flames associated with the drops.

Using a kerosene spray with SMD from 60 to 150μ, Anson[99] found the lean limits of combustion to be a 15 to 1 air to fuel ratio for 150μ SMD and a 29 to 1 air to fuel ratio for 60μ SMD. Burgoyne and Cohen[100] investigated the fuel-air ratio for stable burning of lean mixtures of suspended liquid tetralin drops. The suspension was formed by an aerosol generator which provided drops of nearly uniform size

from less than 10 μ up to 55 μ in diameter. With the equipment used, the work was limited to 55 μ drops and lean mixtures. The results found for lean limits were 26 to 1 for 10 μ drops and 64 to 1 for 55 μ drops. Above 40 μ, the drops burn individually in their own air envelope and one burning drop ignites adjacent ones. Comparison of flame sizes and burning rates of a large-drop aerosol with similar data for single droplets showed differences which were attributed to the influence of adjacent drops.

Browning and Krall[101] measured the peak pressures in a combustion bomb from which the inflammability limits can be obtained. Figure 23 shows the results of these measurements. Propane has narrower stability limits than a kerosene mist for drops of about one micron diameter, although both have nearly the same lean limit. A mixture of kerosene mist and propane gives a much wider range of ignition limits.

The lean limit of flammability and the peak pressure during constant-volume combustion of wax particles of uniform size have been determined by Browning, Tyler, and Krall.[102] The particles were separated into increments of 10 μ from less than 10 μ up to 90 μ. A weight of wax particles in a definite size range, say 60-70 μ, was placed in a closed loop constant-volume combustion chamber. These particles were agitated by a fan to provide uniform dispersion, and then ignited. Peak pressures were measured.

No rich limit of flammability was observed within the range of the mixtures tested; the observed lean limits are plotted in Figure 24 together with the data of Burgoyne and Cohen and those of Anson. Anson's low values are attributed to the turbulence produced by the spray. Burgoyne and Cohen's wider spread of measured results may be caused by the use of liquid fuel and the use of a quiescent aerosol. Browning, Tyler, and Krall[102] explain the peak at about 60 μ as follows:

> "In suspensions composed of large particles the flame progresses from one droplet to another across a relatively vapor-free space. Each droplet burns to form a diffusion flame, and a sufficient amount of heat must be transferred from particle to particle to allow the flame to progress through the entire mixture. At constant fuel-air ratio a reduction in the size of large particles produces a more closely spaced suspension. Above 60 μ this closer spacing gives conditions more favorable for this type of diffusion flame propagation. As particle size is reduced, higher vaporization rates arise, and a larger amount of the fuel is transformed into vapor. This vapor, in turn, is diffused into spaces between the droplets. The vapor tends to burn in the same fashion as a gaseous fuel, while the particles which are not completely vaporized burn as diffusion flames. A mixed type of combustion results even though ignition might well be sustained by droplet-to-droplet propagation alone. As long as the flame is predominantly of diffusional character, the production of excess vapor prior to combustion is a loss. Thus, more fuel must be available for combustion to proceed. As the droplet size approaches 10 μ, the vapor concentration becomes greater between droplets until a point is reached where successful combustion of the mixture is completely dependent on its gaseous state. The ability of the 60 μ size suspension to burn at the leanest air-fuel ratios is thus brought about by a balance between the rate of vapor production and the ability of the flame to progress from droplet to droplet."

Burgoyne and Cohen[100] introduced an aerosol formed from tetralin drops into the upper end of a 5.4 cm glass tube which was 150 cm in length. When the aerosol was ignited the flame propagated upward, and the character of the flame was observed. Drop sizes below 10 μ gave a continuous blue flame front of parabolic form which progressed smoothly up the tube. There was no sign of individual drop burning. Between 10 μ and 20 μ, white flame centers appeared in the blue flame front; near 20 μ a cellular structure developed with each cell having a white center. Between 20 μ and 40 μ, there was no observable continuous flame front as combustion progressed up the tube. Each yellow or white diffusion flame center was surrounded by a blue flame zone. Near 40 μ the blue flame zones disappeared with only yellow flames in isolated centers remaining. The progress of combustion was less regular than with smaller drops.

Burgoyne and Cohen[100] studied also stationary flames with a burner tube and measured burning velocities. The results are summarized in Table VIII. As the mass concentration increases, the diameter of drops with the same combustion behavior as vaporized fuel decreases for two reasons; in the first place, the burning velocity increases which decreases vaporization time and, in the second place, the partial pressure of the vaporized fuel increases.

The theoretical investigations of Probert,[14] of Shapiro and Erickson,[67] and of Tanasawa[95] assumed a burning law of the form

TABLE VIII. BURNING VELOCITIES OF AEROSOLS

Drop Diameter, μ	Concentration mg/liter	Mass Concentration, Percent of Lower Limit	Number Density of Drops, $Drops/cm^3$	Burning Velocity, cm/sec
8	67	146	2.5×10^5	28
11	84	182	1.2×10^5	42
22	64	188	1.1×10^4	55
34	45	215	2.2×10^3	58
38	48	240	1.7×10^3	58

$$D^2 = D_0^2 - Kt.$$

Experimentally the validity of this law for sprays has been established by Bolt and Boyle.[6] Their investigation was concerned with the evaporation and combustion of a spray of uniform-size fuel drops which was produced by means of a spinning disk atomizer. By variation of operating conditions, the drop size could be varied in the range 70 μ to 130 μ. A flame zone 1 to 1.5 inches wide was stabilized at a radial distance of 6 to 8 inches from the disc axis; drops entered the flame with a velocity of approximately 5 ft/sec. By using a photographic technique, the drop sizes could be followed from an initial size of 90 to 100 μ to drops which had evaporated to 40 to 60 μ. The observed values of K varied from drop to drop; there is no single

burning rate for all drops since each drop "burns" under different conditions. The flame is not associated with an individual drop; rather there is a flame zone and, as the drops pass through it, they leave a trail of vapor. Drop evaporation depends on local temperature, local vapor concentration, and the fuel properties. Combustion depends on local equivalence ratios and local products concentrations. Average values of K for many drops were obtained for the spray burning in air. Representative results are summarized below:

Fuel	Average Evaporation Constant, m cm^2/sec
benzene	0.0033
cyclohexane	0.0066
n-propyl alcohol	0.0046
n-heptane	0.0047

The values for K observed in the spray for n-heptane are one half to one third of the value observed in single-droplet studies. In Figure 19 is illustrated the fact that the initially uniform size distribution is altered rapidly as combustion proceeds.

Whittle[103] investigated the effect of the vaporization rate on the weak (lean) combustion limit of liquid fuel sprays in an aero-type gas turbine combustion chamber. Two degrees of fineness of atomization were used; viz., SMD equal to 60 μ or 140 μ . Different fuels were used in order to vary volatility. The lean limit of combustion was determined for each fuel. These data permitted curves to be drawn.

The curves are given in Figure 25 and illustrate the dependence of the weak flame limit on atomization and volatility. Consider a highly volatile fuel. If the aim is to burn with as lean a mixture as possible, should the fuel be finely or coarsely atomized? A glance at Figure 25 answers this question. The spray with coarse atomization (SMD equal to 140 μ) burns at a leaner mixture ratio. Likewise for a fuel with low volatility, the spray with fine atomization (SMD equal to 60 μ) burns at a lower mixture ratio. A spray of highly volatile, finely atomized fuel requires a richer mixture ratio because rapid combustion eliminates the drops which recirculate as ignition sources. The coarser the atomization of a spray with a given mixture ratio, the more sparse the spatial distribution of the drops; this effect leads to lowered vapor concentrations. Hence, for fuels of low volatility, a finely atomized spray has a weak flame limit using less fuel than a coarsely atomized spray.

In current theories of rocket combustion instability, the time lag between injection and liberation of heat is considered an important parameter. The total time lag can be separated into two general classifications: (a) the chemical time lag and (b) the physical time lag which depends on such processes as atomization, heating of drops, evaporation, mixing, and the preheating of combustibles. Mueller[104] has considered the chemical time lag in nitromethane rocket motors. He determined experimentally the thermal decomposition of nitromethane with and without a small amount of added oxygen. With oxygen the overall

disappearance of nitromethane is not influenced; however, the intermediates, such as hydrogen cyanide, are decomposed more rapidly in the presence of oxygen.

The rate of formation of CO and CO_2 increases with oxygen concentration. This type of experimental evidence suggests the existence of a chemical time lag because

(a) Pure nitromethane, as a monopropellant, requires a large L* or very high chamber pressure for combustion;

(b) Addition of a few percent O_2 permits use of a considerably smaller L* or lower chamber pressure;

(c) The physical time lag is not changed by addition of O_2.

14. Summary and Conclusions

There have been two methods of attack in regard to developing a suitable analysis for describing spray phenomena. One approach is to examine the drops, individually or in simple groupings, with the hope of understanding thoroughly drop technology. Having this information, the next step is to build the spray allowing for the many interactions. The other method is to characterize the spray by a parameter; e. g., a mean diameter, and then to consider the effect of a process which acts on all the drops. This technique is appropriate for the description of evaporation, mixing, etc., but not for the prediction of the spray characteristics such as drop size distribution.

At present it is not possible to predict spray characteristics. Current theories indicate trends only and provide a rational means for correlating data.

Spray combustion is a complex process involving the interaction of many physical and chemical rate processes which are not clearly understood in detail. Quantitative combustion rate measurements under actual burner conditions are difficult to carry out. Although, in principle, it should be possible to build up information on the combustion processes of a complete fuel spray by starting with the knowledge of single-drop behavior, compensating for the effects of drop interference, and allowing for the interaction of the drops with the ambient fluid flow which is often turbulent, it is not possible to derive quantitatively significant results. Nevertheless, our understanding of the essential features of spray combustion has progressed to the point where reasonable semi-empirical correlations can be obtained in terms of the fundamental law for droplet burning and appropriate relations for spray-size distribution.

REFERENCES

PART I

1. J. F. Rex, A. E. Fuhs, and S. S. Penner, "Interference Effects During Burning in Air for Stationary n-Heptane, Ethyl Alcohol, and Methyl Alcohol Droplets," Jet Propulsion, 26 (March, 1956), pp. 179-187.

2. G. A. E. Godsave, "The Burning of Single Drops of Fuel: Part I, Temperature Distribution and Heat Transfer in Pre-Flame Region," National Gas Turbine Establishment (England) Report No. R 66 (1950).

3. G. A. E. Godsave, "The Burning of Single Drops of Fuel: Part II, Experimental Results," National Gas Turbine Establishment (England) Report No. R 87 (1951).

4. A. R. Hall and J. Diederichsen, "An Experimental Study of the Burning of Single Drops of Fuel in Air at Pressures up to Twenty Atmospheres," Fourth (International) Symposium on Combustion (Baltimore: Williams and Wilkins Company, 1953), pp. 837-846.

5. M. Goldsmith and S. S. Penner, "On the Burning of Single Drops of Fuel in an Oxidizing Atmosphere," Jet Propulsion, 24 (1954), pp. 245-251. See also S. S. Penner, Introduction to the Study of Chemical Reactions in Flow Systems (London: Butterworths Publications, Ltd., 1955), Chapter 4.

6. M. Goldsmith and C. K. Perkins, "Experiments on the Burning of Single Drops of Fuel in Oxygen-Inert Gas Mixtures" (Technical Report No. 4, Contract No. DA 04-495-Ord-446, California Institute of Technology, Pasadena, May, 1954).

7. C. C. Graves and M. Gerstein, "Some Aspects of the Combustion of Liquid Fuels," Combustion Researches and Reviews, 1955 (London: Butterworths Publications, Ltd., 1955), Chapter 3.

8. R. P. Probert, "The Influence of Spray Particle Size and Distribution in the Combustion of Oil Droplets," Philosophical Magazine, 37 (1946), pp. 94-105.

9. Y. Tanasawa, "On the Combustion Rate of a Group of Fuel Particles Injected Through a Swirl Nozzle," Technology Reports of Tohoku University, 18 (Sendai, Japan, 1954), pp. 195-208.

10. S. Kumagai and H. Isoda, "Combustion of Fuel Droplets in a Falling Chamber," Sixth (International) Symposium on Combustion (New York: Reinhold Publishing Corporation, 1957), pp. 726-731.

11. J. Kanevsky, "Interference During Burning in Air for Nine Stationary Fuel Droplets Arranged in a Body Centered Cubic Lattice," Jet Propulsion, 26, No. 9 (1956), p. 788.

12. S. S. Penner, Chemistry Problems in Jet Propulsion (Volume I, E. R. Sharp and A. D. Baxter, editors, Division III: Propulsion Systems Including Fuels; T. von Kàrmàn and H. Dryden, chairmen, International Series of Monographs on Aeronautical Sciences and Controlled Flight; London: Pergamon Press, 1957), 394 pp.

13. S. S. Penner and A. E. Fuhs, "On Generalized Scaling Procedures for Liquid Fuel Rockets," Combustion and Flame, 1 (June, 1957), No. 2, pp. 229-240.

14. S. S. Penner, "Models in Aerothermochemistry," I Modelli Nella Tecnica, 1 (Rome: Accademia Nazionale dei Lincei, 1956), pp. 652-669. See also Technical Report No. 13, Contract DA 04-495-Ord-446, California Institute of Technology, Pasadena, 1955).

15. L. Crocco, "Considerations on the Problem of Scaling Rocket Motors," Selected Combustion Problems II (AGARD, London: Butterworths Scientific Publications, 1956), p. 457.

16. S. S. Penner, "Rational Scaling Procedures for Liquid Fuel Rocket Engines," Jet Propulsion, 27 (1957), p. 156.

17. M. Barrère, Similarity of Liquid-fuel Rocket Combustion Chambers (Paris: Office Nationale d'Etudes et de Recherches Aéronautiques, 1956).

18. M. R. Shafer and H. L. Bovey, "Applications of Dimensional Analysis to Spray-Nozzle Performance Data," Journal of Research of National Bureau of Standards, 52 (March, 1954), pp. 141-147.

19, S. S. Penner, Chemical Reactions in Flow Systems (London: Butterworths Scientific Publications, 1955), Chapter 4.

20. M. Barrère and H. Moutet, "Étude Expérimentale de la Combustion de Gouttes de Monergols," La Recherche Aéronautique (Mars-Avril, 1956), Numéro 50, p. 31.

21. M. Barrère, Preliminary experimental results obtained at the Office Nationale d'Etudes et de Recherches Aéronautiques, Paris; personal communication.

22. G. Damköhler, "Einflusse der Stromung, Diffusion und des Warmeuberganges auf die Leistung von Reaktionsofen," Z. Elektrochem., 42 (1936), p. 846.

23. S. S. Penner, Combustion Researches and Reviews 1955 (AGARD, London: Butterworths Scientific Publications, 1956), Chapter 12.

24. H. L. Wheeler, "An Empirical Equation for Heat Transfer in a Tube Sweat-Cooled with a Gas" (California Institute of Technology JPL Progress Report 4-49, 1947).

25. P. Duwez and H. L. Wheeler, "Heat Transfer Measurements in a Nitrogen Sweat-Cooled Porous Tube" (California Institute of Technology JPL Progress Report 4-48, 1947).

26. W. D. Rannie, "A Simplified Theory of Porous Wall Cooling" (California Institute of Technology JPL Progress Report 4-50, 1947).

REFERENCES

PART II.

1. F. Williams and A. E. Fuhs, "Apparent Emission Intensities from a Turbulent Flame Composed of Wrinkled Laminar Flames," Jet Propulsion, 27 (October, 1957), pp. 1099-1101.

2. L. S. G. Kovasznay, "A Comment on Turbulent Combustion," Jet Propulsion, 26 (June, 1956), p. 485. Part of summary, Combustion in Turbulent Flow.

3. M. Summerfield, S. H. Reiter, V. Kebely, and R. W. Mascolo, "The Structure and Propagation Mechanism of Turbulent Flames in High Speed Flow," Jet Propulsion, 25 (August, 1955), pp. 377-385.

4. J. K. Richmond, W. F. Donaldson, J. Grumer, and D. S. Burgess, "Evidence for the Wrinkled Continuous Laminar Wave Concept of Turbulent Burning," American Rocket Society Preprint 517-57 (1957).

5. A. Schaffer and A. B. Cambel, "Continued Investigations of the Opposing Jet Flameholder," Jet Propulsion, 26 (1956), pp. 576-578.

6. A. Schaffer and A. B. Cambel, "The Effect of an Opposing Jet on Flame Stability," Jet Propulsion, 25 (1955), pp. 284-287.

7. A. B. Cambel, "A Review of Flame Stabilization of Gaseous Jets," Unpublished paper, Northwestern University.

8. R. H. Eustis and C. L. Mraz, "Investigations of Jet Flameholders," WADC Technical Note 56-316, April, 1956.

9. A. W. Noon, "Investigations of Jet Flameholders, Part II," WADC Technical Note 56-316, April, 1957.

10. S. S. Penner and F. Williams, "Recent Studies on Flame Stabilization of Premixed Turbulent Gases," Applied Mechanics Reviews, 10 (June, 1957), pp. 229-237.

11. R. R. John and M. Summerfield, "Effect of Turbulence on Flame Radiation," Jet Propulsion, 27 (1957), pp. 169-175, 178-179.

12. T. D. Clark and D. A. Bittker, "A Study of the Radiation from Laminar and Turbulent Open Propane-Air Flames as a Function of Flame Area, Equivalence Ratio, and Fuel Flow Rate," N. A. C. A. Research Memorandum E54F29, August 24, 1954.

13. R. R. John, E. S. Wilson, and M. Summerfield, "Studies of the Mechanism of Flame Stabilization by Spectral Intensity Method," Jet Propulsion, 25 (1955), p. 535.

14. E. S. Wilson, R. R. John, and M. Summerfield, "Spectroscopic Studies of the Effect of Boundary Layer Flow on Flameholding," Jet Propulsion, 27 (1957), pp. 892-894.

15. G. A. Agoston, A. W. Noon, and T. D. Witherly, "Experimental Study of a Reverse-Jet Flameholder," Paper presented at Winter Meeting of the Provisional Western States Section of the Combustion Institute, Pasadena, California, January, 1958.

REFERENCES

APPENDIX TO PART I

1. E. Giffen and A. Muraszew, The Atomization of Liquid Fuels (New York: John Wiley and Sons, Inc., 1953), 246 pp.

2. R. R. May, "An Improved Spinning Top Homogenous Spray Apparatus," Journal of Applied Physics (1951), p. 932.

3. W. H. Walton and W. C. Prewett, "Production of Sprays and Mists of Uniform Drop Size," Proceedings of Physical Society, 62B (1949), p. 341.

4. S. J. Friedman, F. A. Gluckert, and W. R. Marshall, Jr., "Centrifugal Disk Atomization," Chemical Engineering Progress, 48 (1952), p. 181.

5. J. O. Hinze and H. Milborn, "Atomization of Liquids by Means of a Rotating Cup," Journal of Applied Mechanics, 17 (1950), p. 145.

6. J. A. Bolt and T. A. Boyle, "The Combustion of a Liquid Fuel Spray," Transactions of the American Society of Mechanical Engineers, 78 (1956), p. 609.

7. W. E. Ranz, On Sprays and Spraying (Penn State College Bulletin 65, Part I, 1956).

8. R. A. Mugele and H. D. Evans, "Droplet Size Distribution in Sprays," Industrial and Engineering Chemistry, 43 (1951), p. 1317.

9. M. D. Bitron, "Atomization of Liquids by Supersonic Air Jets," Industrial and Engineering Chemistry, 47 (1955), p. 23.

10. J. H. Rupe, "A Technique for the Investigation of Spray Characteristics of Constant Flow Nozzles," Conference on Fuel Sprays, University of Michigan (1949), 14 pp. Also Third (International) Symposium on Combustion (Baltimore: Williams and Wilkins Company, 1948), p. 680.

11. H. G. Houghton, Chemical Engineers Handbook (third edition; McGraw Hill Book Company, Inc., 1950), p. 1175.

12. P. Rosin and E. Rammler, "The Laws Governing the Fineness of Powdered Coal," Journal of the Institute of Fuel, 7 (1933), pp. 29-36.

13. P. Rosin and E. Rammler, Zeitschrift des Vereins Deutscher Ingenieure, 71 (1927), p. 1.

14. R. P. Probert, "The Influence of Spray Particle Size and Distribution in the Combustion of Oil Droplets," Philosophical Magazine, 37 (1946), pp. 94-105.

15. R. S. Bevans, "Mathematical Expressions for Drop-Size Distributions in Sprays," Conference on Fuel Sprays (Ann Arbor: University of Michigan, 1949).

16. J. L. Hopkins, "The Size Distribution of Droplets in a Fuel Spray," Technical Report No. I. C. T/6 (London: Shell Petroleum Co., Ltd., 1946), 20 pp. and 7 figures.

17. J. R. Joyce and J. L. Hopkins, "The Wax Method of Spray Particle Size Measurement," Technical Report No. I. C. T/7 (London: Shell Petroleum Co., Ltd., August, 1946).

18. I. G. Bowen and J. R. Joyce, "The Effects of Cone Angle, Pressure and Flow Number on the Particle Size of a Pressure Jet Atomizer," Technical Report No. I. C. T/17 (London: Shell Petroleum Co., Ltd., March, 1948).

19. D. W. Lee, "Experiments on the Distribution of Fuel in Fuel Sprays," N. A. C. A. Report No. 438, 1932. See also Reports 274 and 281.

20. R. D. Ingebo, "Vaporization Rates and Drag Coefficients for Iso-octane Sprays in Turbulent Air Streams," N. A. C. A. Technical Note 3265.

21. S. Nukiyama and Y. Tanasawa, "An Experiment on the Atomization of Liquid by Means of an Air Stream," Trans. S. M. E. Japan, 4 (February, 1938), p. S-13.

22. H. C. Lewis, D. G. Edwards, M. J. Goglia, R. I. Rice and L. W. Smith, "Atomization of Liquids in High Velocity Gas Streams," Industrial and Engineering Chemistry, 40 (January, 1948), p. 67.

23. J. P. Longwell, "Combustion of Liquid Fuels," Combustion Processes (Volume II, B. Lewis, R. N. Pease, and H. S. Taylor, editors, High Speed Aerodynamics and Jet Propulsion Series, 12 vols.; Princeton, New Jersey: Princeton University Press, 1956), Section J, p. 410.

24. K. Stange, "Size Distribution Laws in Disintegration Processes," Ing. Arch., 21 (1953), p. 368.

25. E. Söhngen and U. Grigull, "Spray Angle of Fuel-Injection Nozzles of Swirl Type Under Steady Injection Conditions," Forsch. Geb. Ing. Wes., (B) 17, No. 3 (1951), pp. 77-82.

26. E. H. Taylor and D. B. Harmon, "Measuring Drop Sizes in Sprays," Industrial and Engineering Chemistry (1954), pp. 1455-1457.

27. J. L. York and H. F. Stubbs, "Photographic Analysis of Sprays," Transactions of the American Society of Mechanical Engineers, 74 (1952), p. 1157.

28. W. E. Ranz and C. Hofelt, Jr., "Determining Drop Size Distribution of a Nozzle Spray," Industrial and Engineering Chemistry, 49 (1957), p. 28.

29. J. Sauter, "Determining Size of Drops in Fuel Mixture of Internal Combustion Engines," N. A. C. A. Technical Memorandum No. 390, December, 1926. Translation from Zeitschrift des Vereins Deutscher Ingenieure, July 31, 1926.

30. Lord Rayleigh, "On the Instability of Jets," Proceedings of London Math. Society, 10 (1878), p. 4.
Theory of Sound (Volume II, New York: Dover Publications, 1945), pp. 360, 376.

31. A. Haenlein, "Disintegration of a Liquid Jet," N. A. C. A. Technical Memorandum 659, February, 1932.

32. F. N. Scheubel, "On Atomization in Carburetors," N. A. C. A. Technical Memorandum 644, 1931, 10 pp.

33. R. A. Castleman, Jr., "The Mechanism of the Atomization Accompanying Solid Injection," N. A. C. A. Report No. 440, 1932, 12 pp.

34. J. L. York, H. F. Stubbs, and M. R. Tek, "The Mechanism of Disintegration of Liquid Sheets," Transactions of the American Society of Mechanical Engineers, 75 (1953), p. 1279.

35. W. W. Hagerty and J. F. Shea, "A Study of the Stability of Plane Fluid Sheets," Journal of Applied Mechanics, 22 (1955), p. 509.

36. M. F. Heidmann, R. J. Priem, and J. C. Humphrey, "A Study of Sprays Formed by Two Impinging Jets," N. A. C. A. Technical Note 3835, 1957.

37. J. H. Rupe, "A Correlation Between the Dynamic Properties of a Pair of Impinging Streams and the Uniformity of Mixture-Ratio Distribution in the Resulting Spray," (California Institute of Technology JPL Progress Report 20-209, 1956); "The Liquid Phase Mixing of a Pair of Impinging Streams" (California Institute of Technology JPL Progress Report 20-195).

38. R. Kling, G. Chevalerias, and A. Maman, L'injection par Jets Concourants Dans les Chambres de Combustion de Fusses a Liquides (Paris, France: Office National d'Etudes et de Recherches Aéronautiques, 9ème Congrès International de Méchanique Appliquée, Bruxelles, Septembre, 1956), 10 pp.

39. J. M. Schmidt, "An Experimental Study of the Behavior of Liquid Streams Injected into a Low-pressure Chamber," (California Institute of Technology JPL Progress Report 4-94, 1949).

40. W. R. Lane, "Shatter of Drops in Streams of Air," Industrial and Engineering Chemistry, 43 (1951), p. 1313.

41. J. O. Hinze, "Critical Speeds and Sizes of Liquid Globules," Applied Scientific Research, A 1 (1947-1949), p. 273.

42. R. H. Magarvey and B. W. Taylor, "Free Fall Breakup of Large Drops," Journal of Applied Physics, 27 (October, 1956), p. 1129.

43. J. O. Hinze, "Fundamentals of the Hydrodynamic Mechanism of Splitting in Dispersion Processes," American Institute of Chem. Journal, 1 (1955), pp. 289-295.

44. W. von Ohnesorge, "Die Bildung von Tropfen und Düsen und die Auflösung flüssiger Strahlen," Zeitschrift fur Angewandte Mechanik und Mathematik, 16 (1936).

45. N. I. Masugi, "Theoretical and Experimental Study of the Deformation and Atomization of a Liquid Drop in a High Velocity Gas Stream," American Rocket Society Preprint 355-56 (1956).

46. A. R. Hanson, E. G. Domik, and H. S. Adams, "An Experimental Investigation of Impact and Shock Wave Breakup of a Liquid Drop," Report 125 (University of Minnesota, Rosemont Aero. Laboratory).

47. A. N. Kolomogoroff, "Dissipation of Energy in the Locally Isotropic Turbulence," C. R. (Doklady) Acad. Sci. U.R.S.S., 32 (1941), p. 16.

48. C. C. Miesse, "From Liquid Stream to Vapor Trail," Proceedings of Gas Dynamics Symposium (Evanston, Illinois: Northwestern University, 1955), p. 17.

49. P. G. Saffman and J. S. Turner, "On the Collisions of Drops in Turbulent Clouds," Journal of Fluid Mechanics, 1 (1956), Part I, p. 16.

50. C. C. Miesse, "The Effect of Ambient Pressure Oscillations on the Disintegration and Dispersion of a Liquid Jet," Jet Propulsion, 25 (1955), p. 525.

51. W. G. Schlinger and B. H. Sage, "Material Transfer in Turbulent Gas Streams," Industrial and Engineering Chemistry, 45 (1953), p. 657.

52. G. K. Batchelor and A. A. Townsend, "Turbulent Diffusicn," Surveys in Mechanics (Cambridge University Press, 1956).

53. J. P. Longwell and M. A. Weiss, "Mixing and Distribution of Liquids in High Velocity Air Streams," Industrial and Engineering Chemistry, 45 (1953), pp. 667-677.

54. D. W. Bahr, "Evaporation and Spreading of Iso-octane Sprays in High-Velocity Air Streams," N. A. C. A. Research Memorandum E53I14, 1953.

55. D. R. Bellman, J. C. Humphrey, and T. Male, "Photographic Investigation of Combustion in a Two-Dimensional Transparent Rocket Engine," N. A. C. A. Report 1134, 1953.

56. W. E. Ranz and W. R. Marshall, Jr., "Evaporation from Drops," Chemical Engineering Progress, 48 (1952), p. 141.

57. N. T. Hsu, K. Sato, and B. H. Sage, "Effect of Shape on the Evaporation of Drops," Industrial and Engineering Chemistry (1954), p. 870.

58. N. Frössling, "On the Evaporation of Falling Droplets," Beitr. Geophys., 52 (1938), pp. 170-216.

59. R. D. Ingebo, "Vaporization Rates and Heat-Transfer Coefficients for Pure Liquid Drops," N. A. C. A. Technical Note 2368, 1951.

60. K. Kobayasi, "A Study on the Evaporation Velocity of a Single Liquid Droplet," Technology Reports of Tohoku University, 18, Number 2.

61. P. H. Calderbank and I. J. O. Korchinski, "Circulation in Liquid Drops," Chemical Engineering Science (1956), pp. 65-78.

62. P. Savic, "Hydrodynamical and Heat Transfer Problems of Liquid Spray Droplets," Quarterly Bulletin (Canada: National Research Council, Division of Mechanical Engineering, January/March, 1953).

63. P. Savic, "Circulation and Distortion of Liquid Drops Falling Through a Viscous Medium," Mechanical Engineering Report MT-22 (Canada: National Research Council, 1953), 56 pp.

64. W. R. Conkie and P. Savic, "Calculation of the Influence of Internal Circulation in a Liquid Drop on Heat Transfer and Drag," Mechanical Engineering Report MT-23 (Canada: National Research Council, 1953), 20 pp.

65. H. H. Foster and R. D. Ingebo, "Evaporation of JP-5 Fuel Sprays in Air Streams," N. A. C. A. Research Memorandum E55K02, 1956.

66. A. R. Hanson, "The Evaporation of a Fuel Spray in an Airstream and Effect of Turbulence on Droplet Size Distribution," Proceedings of Second Midwestern Conference on Fluid Mechanics (Ohio State University, 1952), pp. 415-428.

67. A. H. Shapiro and A. J. Erickson, "On the Changing Size Spectrum of Particle Clouds Undergoing Evaporation, Combustion, or Acceleration," Heat Transfer and Fluid Mechanics Institute, 1956, Preprints of Papers (Palo Alto, California: Stanford University, 1956), pp. 105-133. Also an article of the same title in Transactions of the American Society of Mechanical Engineers (May, 1957).

68. L. Monchick and H. Reiss, "Studies of Evaporation of Small Drops," Journal of Chemical Physics (1954), pp. 831-836.

69. R. D. Ingebo, "Study of Pressure Effects on Vaporization Rate of Drops in Gas Streams," N. A. C. A. Technical Note 2850, 1953.

70. S. S. Penner, "The Maximum Rate of Evaporation of Liquids," Journal of Physical and Colloid Chemistry, 52 (1948), p. 367.

71. S. S. Penner, Additions to the article "Melting and Evaporation as Rate Processes," Journal of Physical and Colloid Chemistry, 52 (1948), p. 1262.

72. S. S. Penner, "On the Kinetics of Evaporation," Journal of Chemical Physics, 56 (1952), p. 475.

73. S. S. Penner, "On Maximum Evaporation Rates of Liquid Droplets in Rocket Motors," Journal of the American Rocket Society, 23 (1953), pp. 85-88, 98.

74. N. Golitzine, "Method for Measuring the Size of Water Droplets in Clouds, Fogs, and Sprays," Note 6, National Aeronautical Establishment, Ottawa, Canada, 1951, 13 pp. 22 figures.

75. M. R. Shafer and H. L. Bovey, "Applications of Dimensional Analysis to Spray-Nozzle Performance Data," Journal of Research of National Bureau of Standards, 52 (March, 1954), No. 3, pp. 141-147.

76. J. N. Kanevsky, "I. Interference During Burning of Body-Centered Cubic Arrays of Nine Fuel Droplets in Air II. Spray Formation and Evaporation," (Technical Report No. 15, Contract DA 04-495-Ord-446, California Institute of Technology, Pasadena, June, 1956), 59 pp.

77. D. B. Harmon, Jr., "An Equation for Predicting a Mean Drop Size in a High Speed Spray," University of California Publications in Engineering, 5, 5 (1955), pp. 145-148.

78. K. R. Stehling, "Injector Spray and Hydraulic Factors in Rocket Motor Analysis," Journal of the American Rocket Society, 22 (1952), p. 132.

79. S. S. Penner and P. P. Datner, "Combustion Problems in Liquid-Fuel Rocket Engines," Fifth (International) Symposium on Combustion (Reinhold Publishing Company, 1955), pp. 11-28.

80. D. W. Lee, "Effect of Nozzle Design and Operating Conditions on the Atomization and Distribution of Fuel Sprays," N. A. C. A. Report No. 425, 1932.

81. L. Crocco and S. Cheng, Agardograph No. 8 (London: Butterworths Scientific Publications, 1956).

82. S. S. Penner and A. E. Fuhs, "On Generalized Scaling Procedures for Liquid Fuel Rockets," Combustion and Flame, 1 (June, 1957), No. 2, pp. 229-240.

83. C. C. Miesse, "Correlation of Experimental Data on the Disintegration of Liquid Jets," Industrial and Engineering Chemistry, 47 (1955), p. 1690.

84. Jack Lorell, Henry Wise, and Russell E. Carr, "Steady State Burning of a Liquid Droplet. II. Bipropellant Flame," Journal of Chemical Physics, 25 (August, 1956), No. 2, pp. 325-331.

85. M. Goldsmith, "Experiments on Burning of Single Drops of Fuel," Jet Propulsion, 26 (March, 1956), pp. 172-179.

86. K. Kobayasi, "An Experimental Study on the Combustion of a Fuel Droplet," Fifth (International) Symposium on Combustion (New York: Reinhold Publishing Co., 1955), pp. 141-148.

87. C. C. Graves, "Burning Rates of Single Fuel Drops and Their Application to Turbojet Combustion Process," N. A. C. A. Research Memorandum E53E22, 1953.

88. G. A. E. Godsave, "The Burning of Single Drops of Fuel: Part I, Temperature Distribution and Heat Transfer in Pre-Flame Region," National Gas Turbine Establishment (England) Report No. R 66 (1950).

89. M. Goldsmith and S. S. Penner, "On the Burning of Single Drops of Fuel in an Oxidizing Atmosphere," Jet Propulsion 24 (1954), pp. 245-251.

90. A. R. Hall and J. Diederichsen, "An Experimental Study of the Burning of Single Drops of Fuel in Air at Pressures up to Twenty Atmospheres," Fourth (International) Symposium on Combustion (Baltimore: Williams and Wilkins Company, 1953), pp. 837-846.

91. S. Kumagai and H. Isoda, "Combustion of Fuel Droplets in a Falling Chamber," Sixth (International) Symposium on Combustion (New York: Reinhold Publishing Corporation, 1957), pp. 726-731.

92. Bernard Lewis and Guenther von Elbe, Combustion, Flames and Explosions of Gases (New York: Academic Press Inc., Publishers, 1951), 795 pp.

93. N. Nishiwaki, "Kinetics of Liquid Combustion Processes; Evaporation and Ignition Lag of Fuel Droplets," Fifth (International) Symposium on Combustion (New York: Reinhold Publishing Co., 1955), pp. 148-158.

94. Joseph L. Jackson, "Spontaneous Ignition Temperatures," Industrial and Engineering Chemistry, 43 (December, 1951), p. 2869.

95. Y. Tanasawa, "On the Combustion Rate of a Group of Fuel Particles Injected Through a Swirl Nozzle," Technology Reports of Tahoku University, 18 (Sendai, Japan, 1954), pp. 195-208.

96. H. G. Wolfhard and W. G. Parker, "Evaporation Processes in a Burning Kerosine Spray," Journal of the Institute of Petroleum, 35 (London, 1949), p. 118.

97. A. L. Berlad and R. R. Hibbard, "Effect of Radiant Energy on Vaporization and Combustion of Liquid Fuels," N. A. C. A. Research Memorandum E52I09, November 13, 1953, 46 pp.

98. R. Mayorcas and M. Riviére, "Description of Trials and Results; Reports of the Burner Trials at Ijmuiden," (paper No. 7), Journal of the Institute of Fuel, 26 (1953), pp. 211-224.

99. D. Anson, "Influence of the Quality of Atomization on the Stability of Combustion of Liquid Fuel Sprays," Fuel, 32 (1953), pp. 39-51.

100. J. H. Burgoyne and L. Cohen, "The Effect of Drop Size on Flame Propagation in Liquid Aerosols," Proceedings of the Royal Society of London, 225A (1954), pp. 375-392.

101. J. A. Browning and W. G. Krall, "Effect of Fuel Droplets on Flame Stability, Flame Velocity, and Inflammability Limits," Fifth (International) Symposium on Combustion (New York: Reinhold Publishing Co., 1955), pp. 159-163.

102. J. A. Browning, T. L. Tyler, and W. G. Krall, "Effect of Particle Size on Combustion of Uniform Suspensions," Industrial and Engineering Chemistry, 49 (1957), p. 142.

103. J. Whittle, "Effect of Vaporization Rate on the Weak Combustion Limit of Liquid Fuel Sprays," Fuel, 33 (1954), p. 153.

104. K. H. Mueller, "Contribution of Chemical Reactions to a Time Lag in Nitromethane Rocket Motors," Jet Propulsion, 25 (1955), p. 468.

FIGURES

PART I

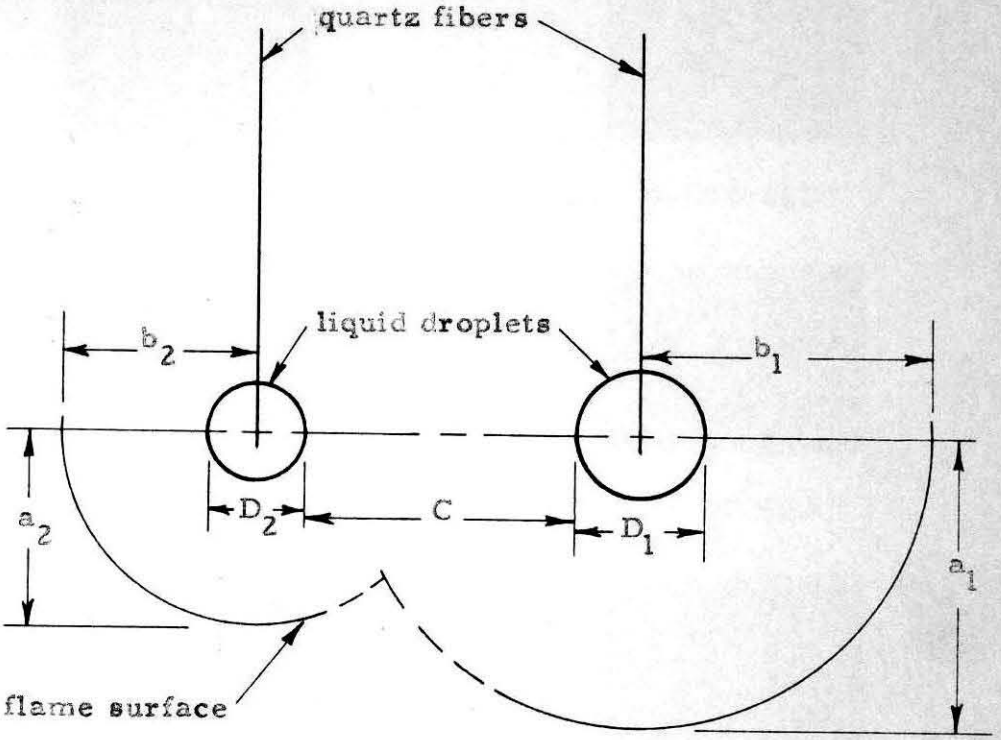

FIGURE 1. SCHEMATIC ARRANGEMENT OF FLAME INTERFERENCE EXPERIMENT WITH TWO DROPLETS BURNING IN CLOSE PROXIMITY.

IGNITION

T=1.44 SEC.

T=0.53 SEC.

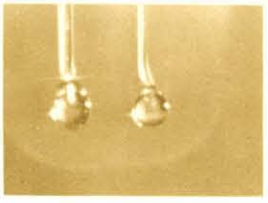

T=1.70 SEC.

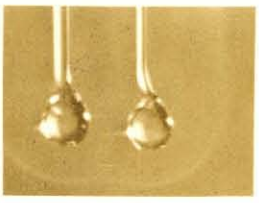

T=0.75 SEC.

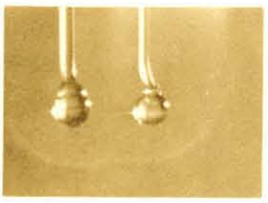

T=1.90 SEC.

T=0.92 SEC.

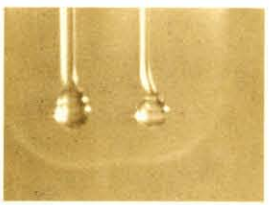

T=2.15 SEC.

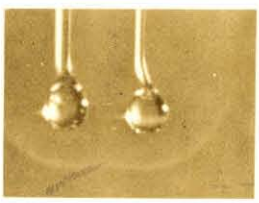

T=1.28 SEC.

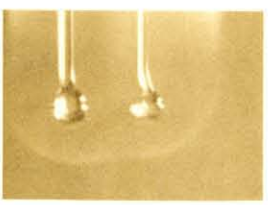

T=2.40 SEC.

FIGURE 2. PHOTOGRAPH OF TWO n-HEPTANE DROPLETS BURNING IN AIR (D_1^o= 0.181cm, D_2^o=0.174cm, C^o=0.114cm)

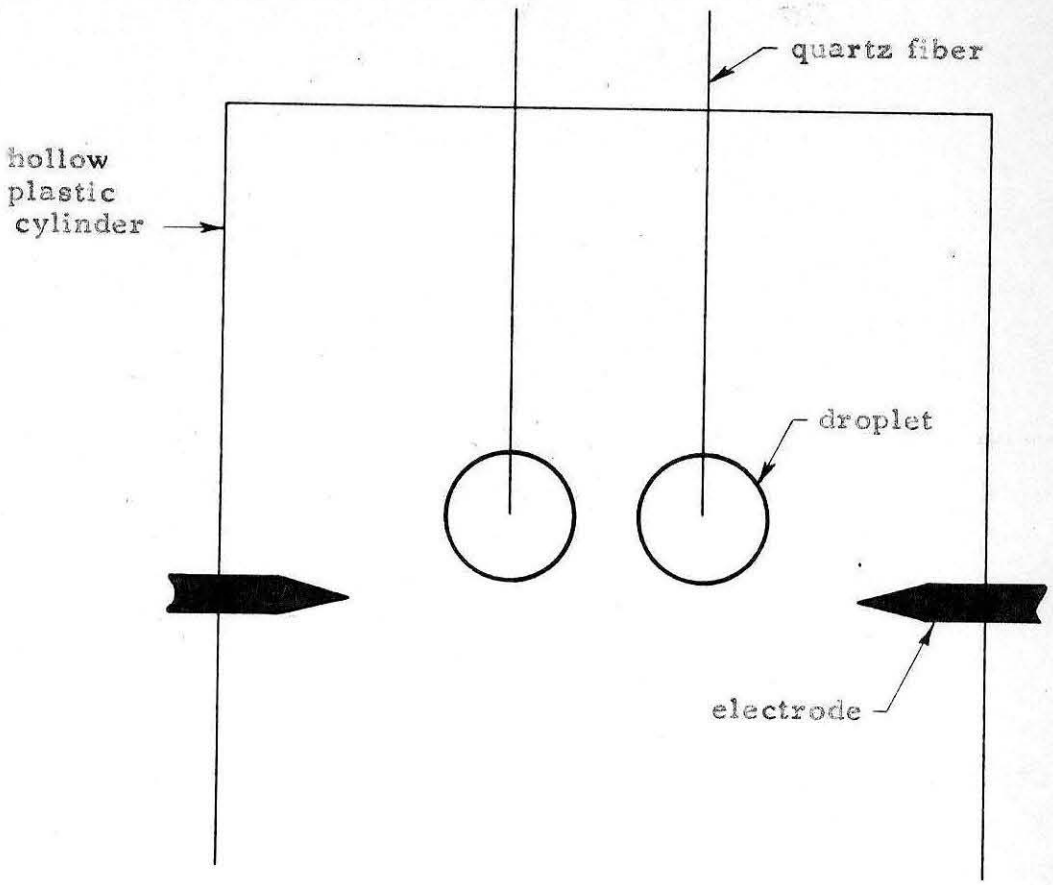

FIGURE 3. SCHEMATIC DIAGRAM OF THE APPARATUS USED FOR DROPLET IGNITION.

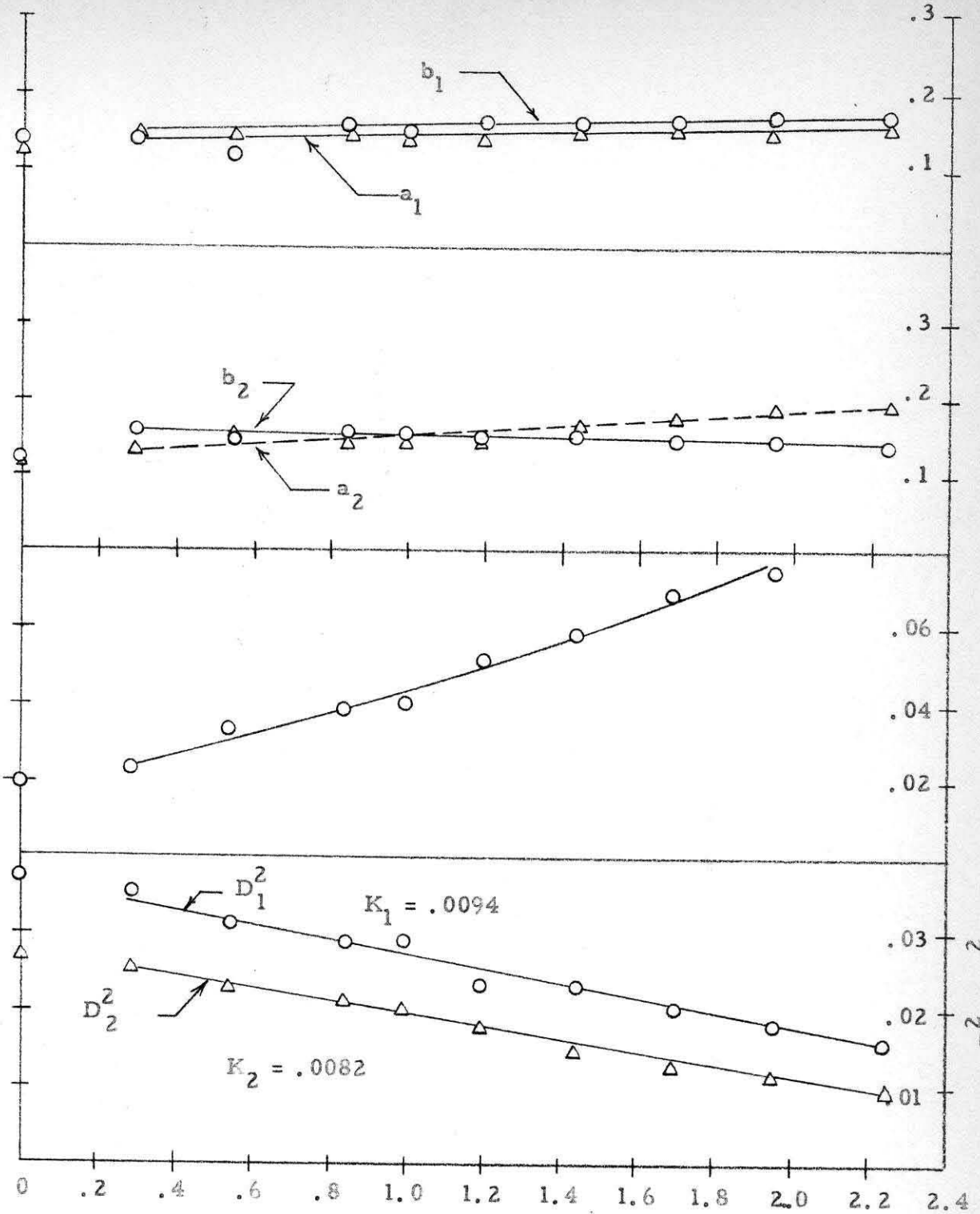

FIGURE 4. EXPERIMENTAL RESULTS FOR TWO n-HEPTANE DROPLETS BURNING IN STILL AIR (D_1^o =0.194 cm, D_2^o =0.166 cm, C^o = 0.020 cm).

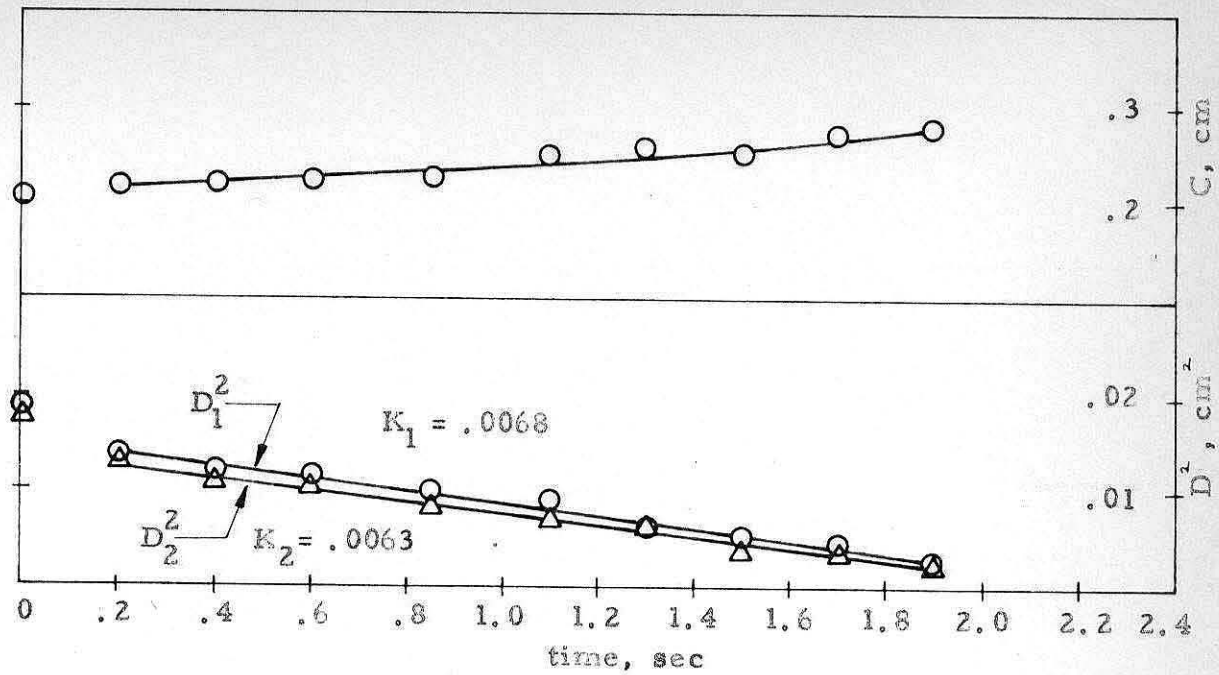

(D_1^o = 0.138 cm, D_2^o = 0.134 cm, C^o = 0.208 cm)

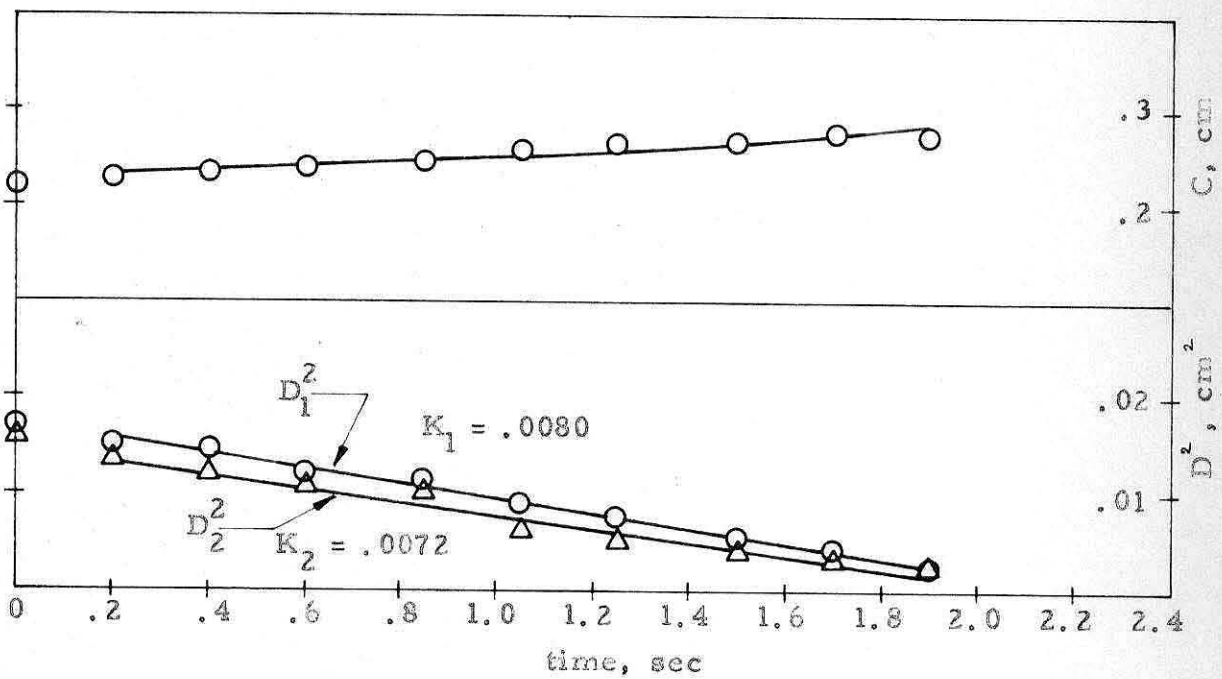

(D_1^o = 0.130 cm, D_2^o = 0.127 cm, C^o = 0.222 cm)

FIGURE 5. PLOTS OF D^2 VS TIME AND C VS TIME FOR TWO n-HEPTANE DROPLETS BURNING IN STILL AIR FOR VARIOUS C^o.

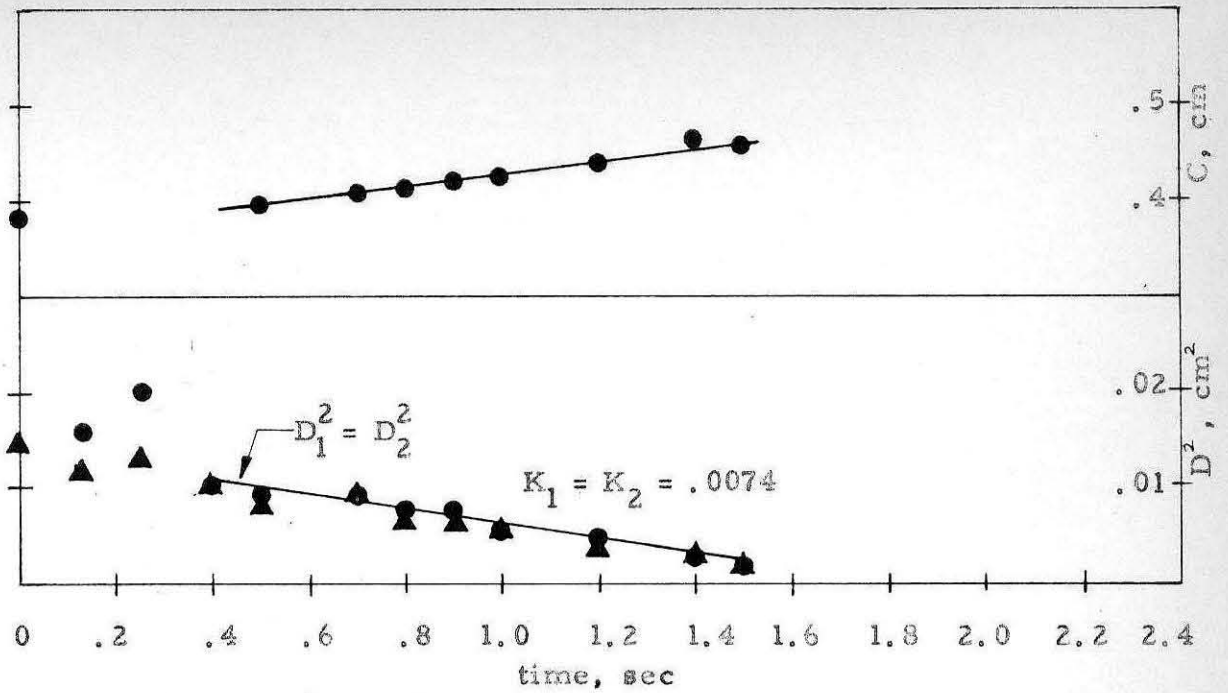

(D_1^o = 0.121 cm, D_2^o = 0.118 cm, C^o = 0.384 cm)

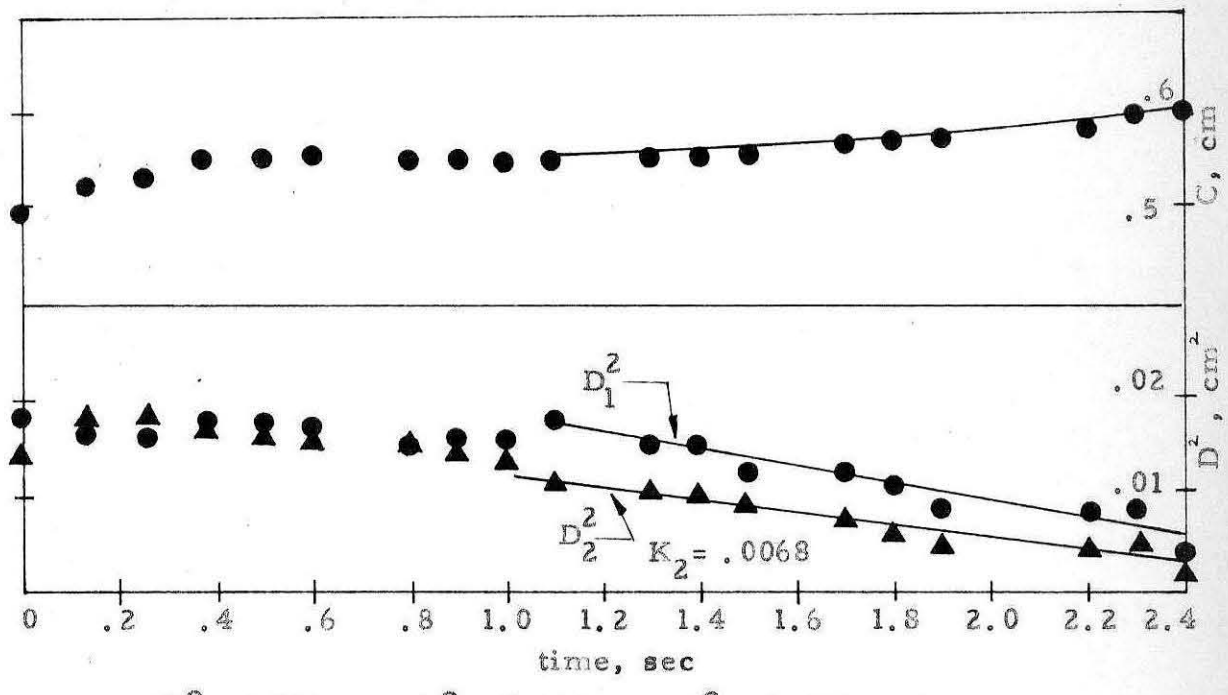

(D_1^o = 0.136 cm, D_2^o = 0.120 cm, C^o = 0.496 cm)

FIGURE 6. PLOTS OF D^2 VS TIME AND C VS TIME FOR TWO n-HEPTANE DROPLETS BURNING IN STILL AIR FOR VARIOUS C^o.

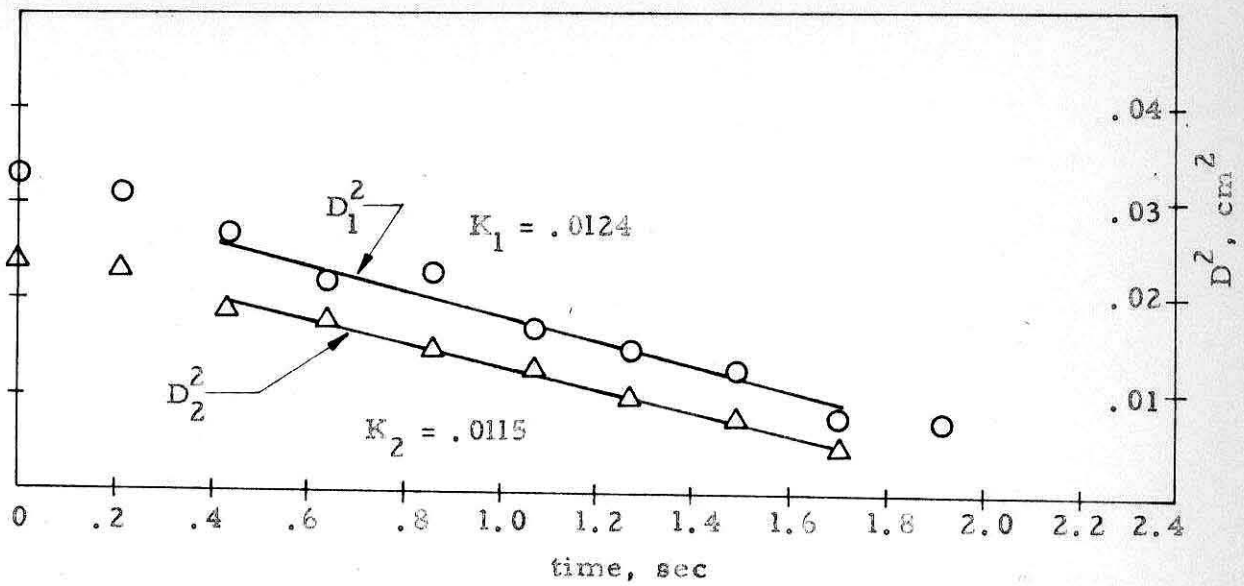

(D_1^o = 0.182 cm, D_2^o = 0.156 cm, C^o = 1.47 cm)

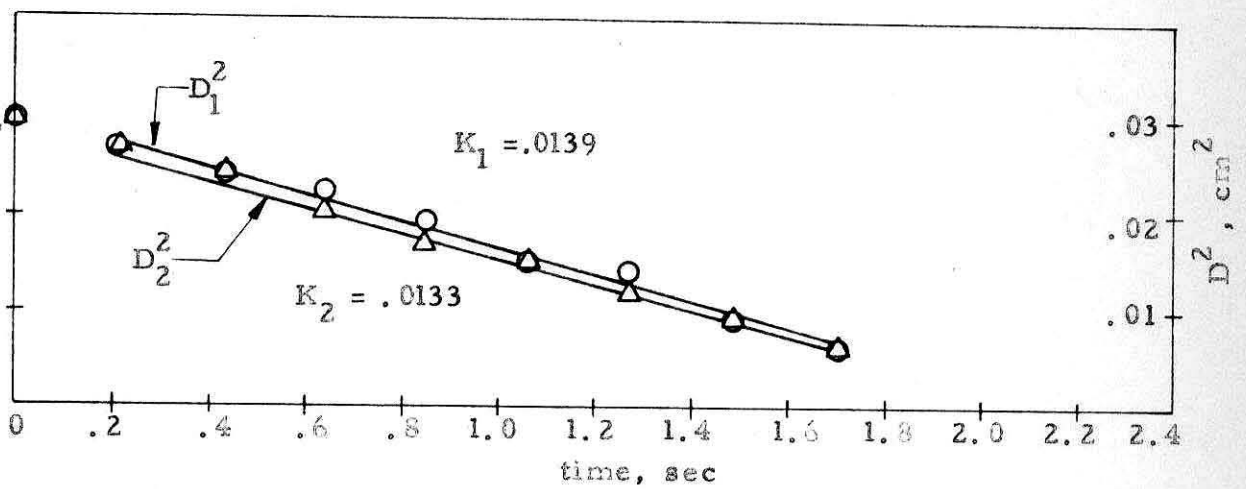

(D_1^o = 0.173 cm, D_2^o = 0.173 cm, C^o = 1.125 cm)

FIGURE 7. PLOTS OF D^2 VS TIME FOR TWO n-HEPTANE DROPLETS BURNING IN STILL AIR FOR VARIOUS C^o.

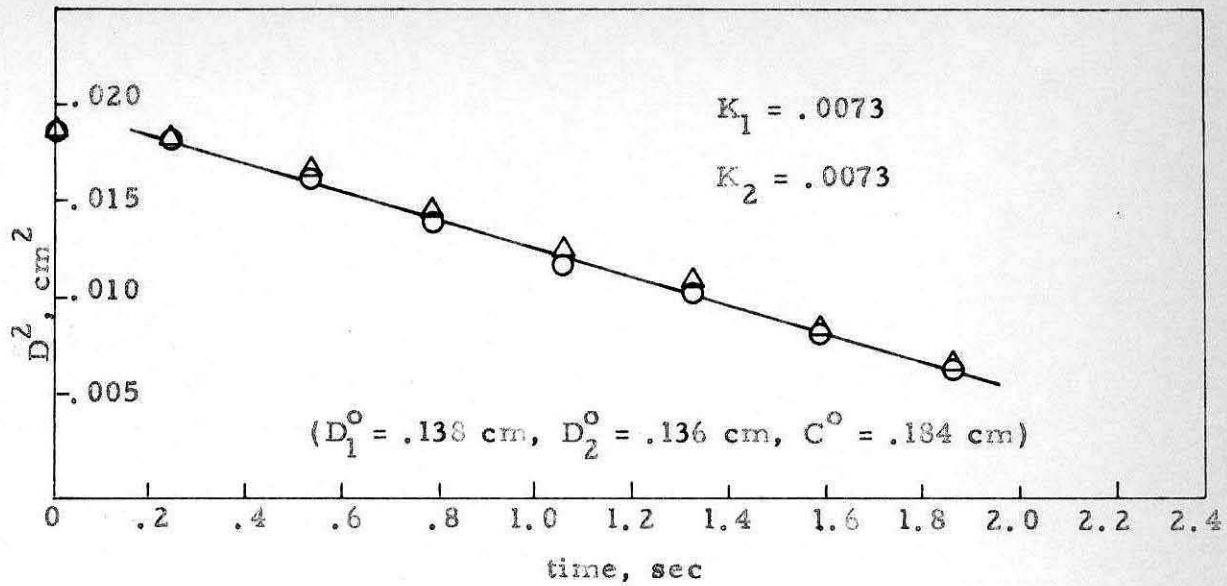

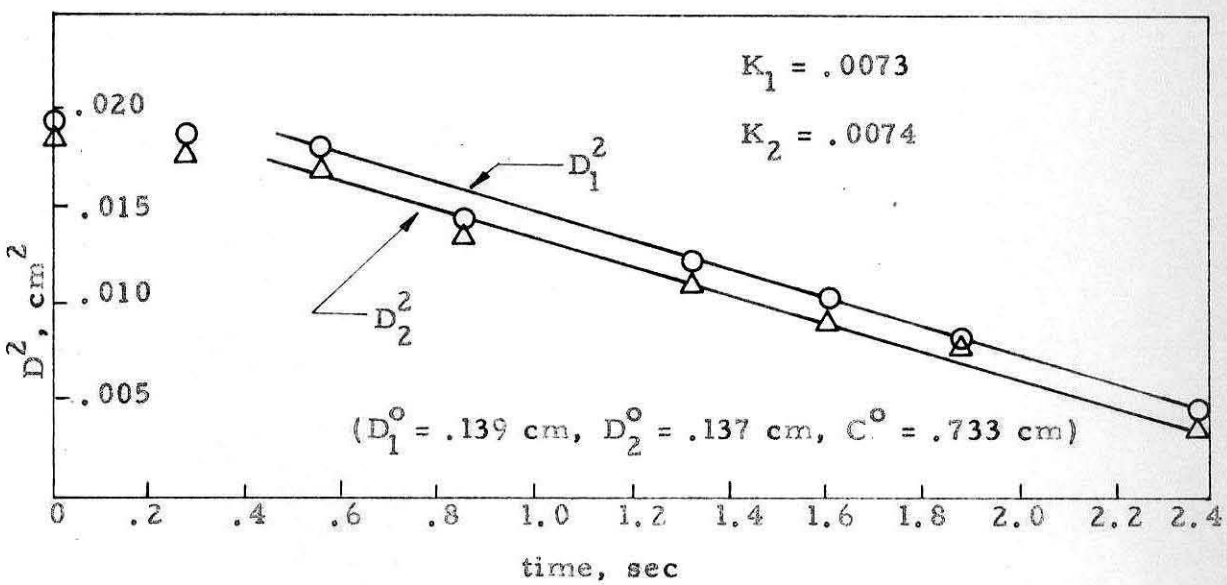

FIGURE 8. PLOTS OF D^2 VS TIME FOR TWO ETHYL ALCOHOL DROPLETS BURNING IN OPEN AIR FOR VARIOUS C^o.

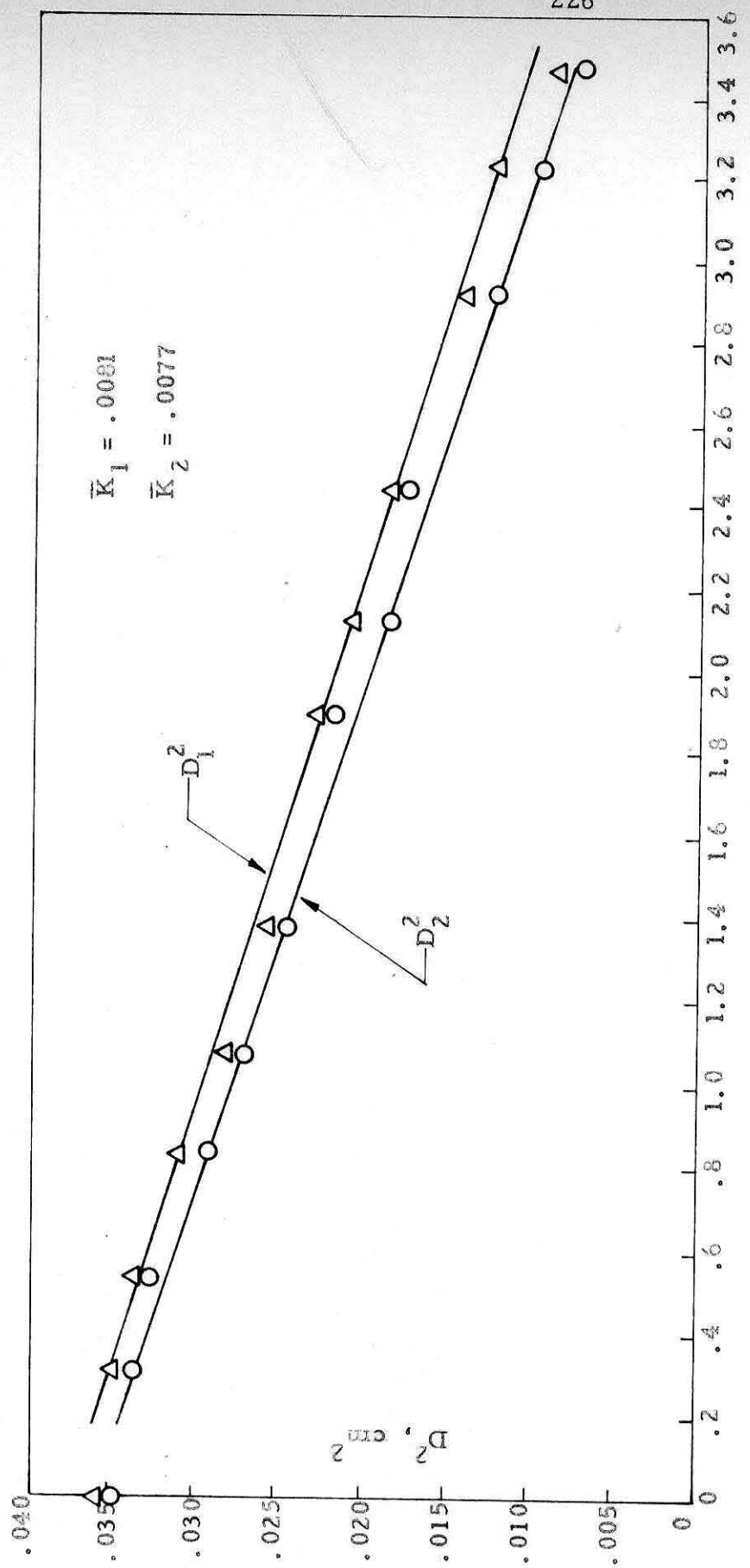

(D_1^o = .191 cm, D_2^o = .187 cm, C^o = .175 cm)

FIGURE 9. PLOT OF D^2 VS TIME FOR TWO ETHYL ALCOHOL DROPLETS BURNING IN OPEN AIR FOR VARIOUS C^o.

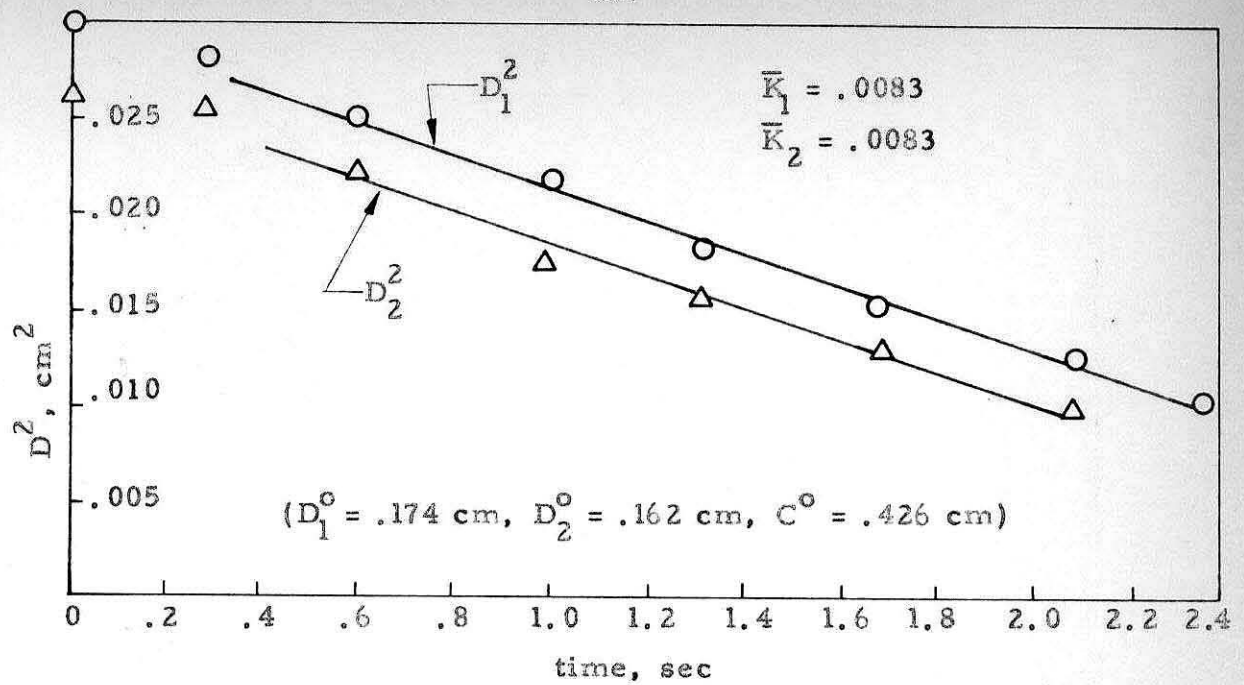

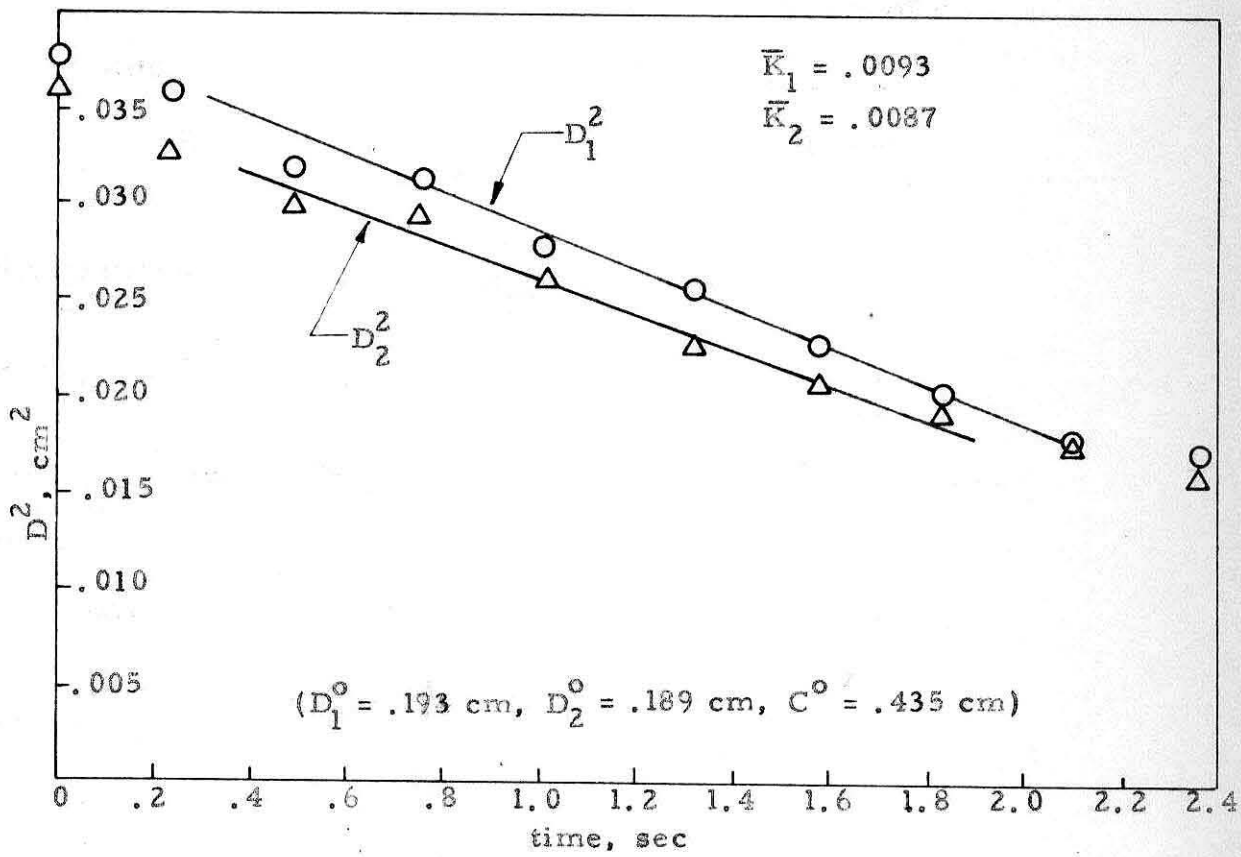

FIGURE 10. PLOTS OF D^2 VS TIME FOR TWO METHYL ALCOHOL DROPLETS BURNING IN OPEN AIR FOR VARIOUS C^o .

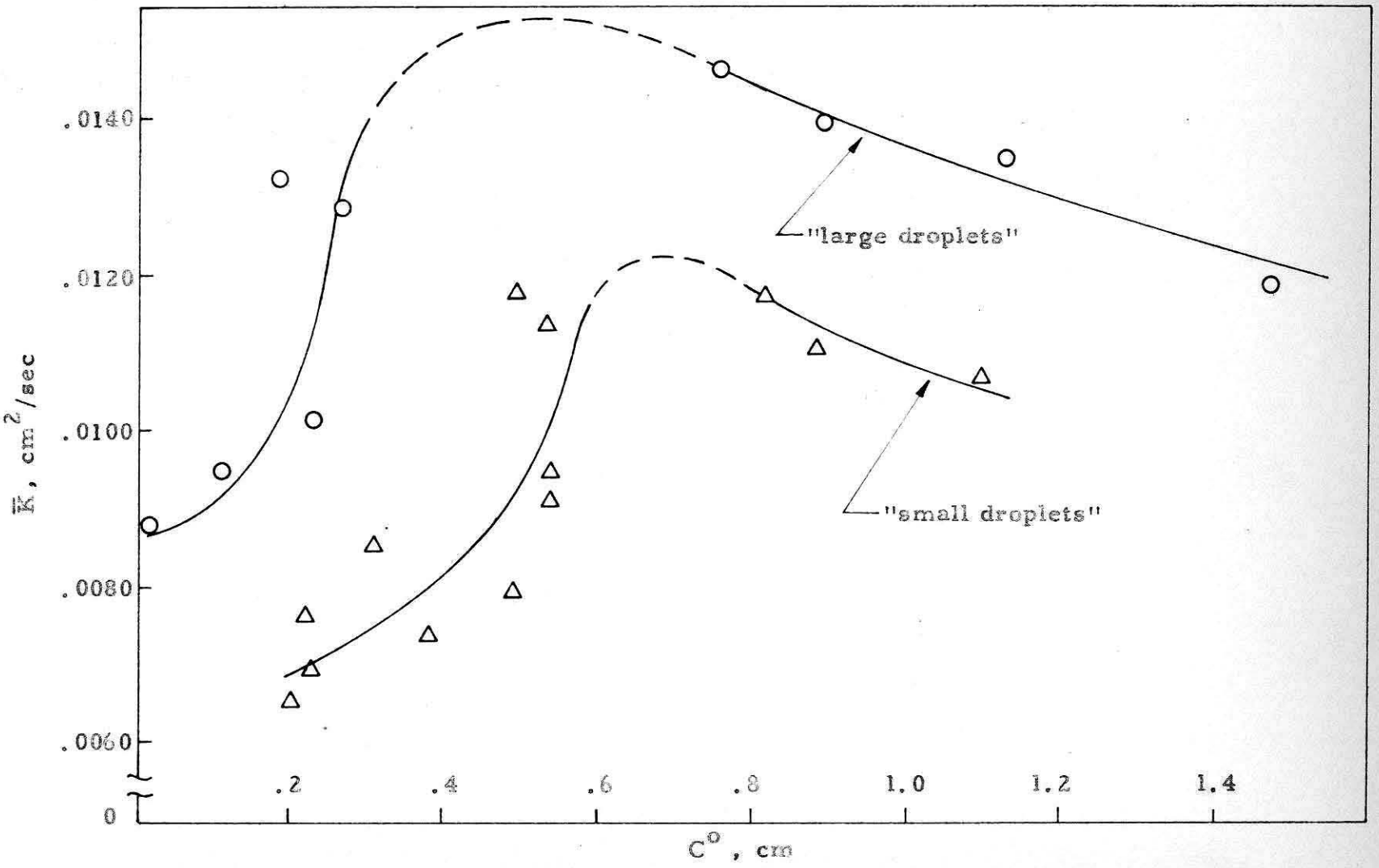

FIGURE 11. VARIATION OF THE AVERAGE EVAPORATION CONSTANT WITH C^o FOR n-HEPTANE DROPLETS WITH DIFFERENT INITIAL AVERAGE DIAMETERS, $\bar{D}^o$.

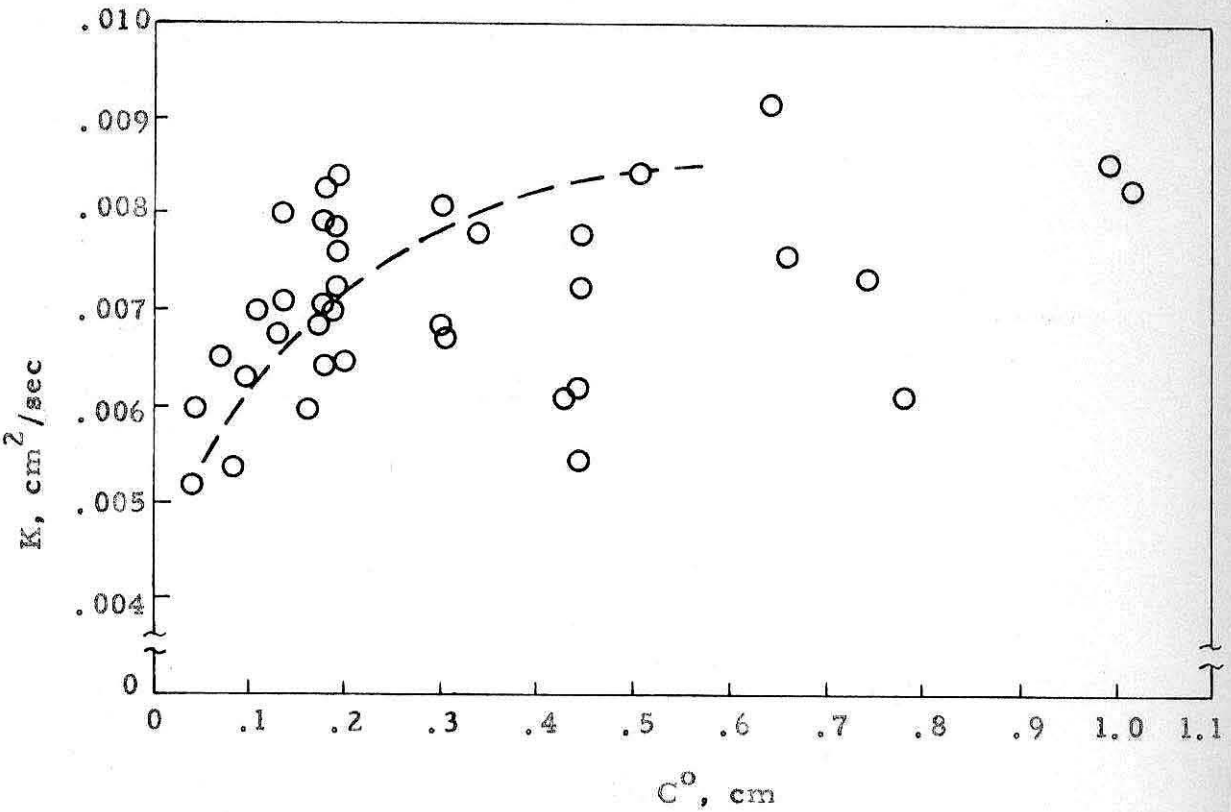

FIGURE 12. AVERAGE EVAPORATION CONSTANT VS INITIAL DROPLET SPACING FOR ETHYL ALCOHOL.

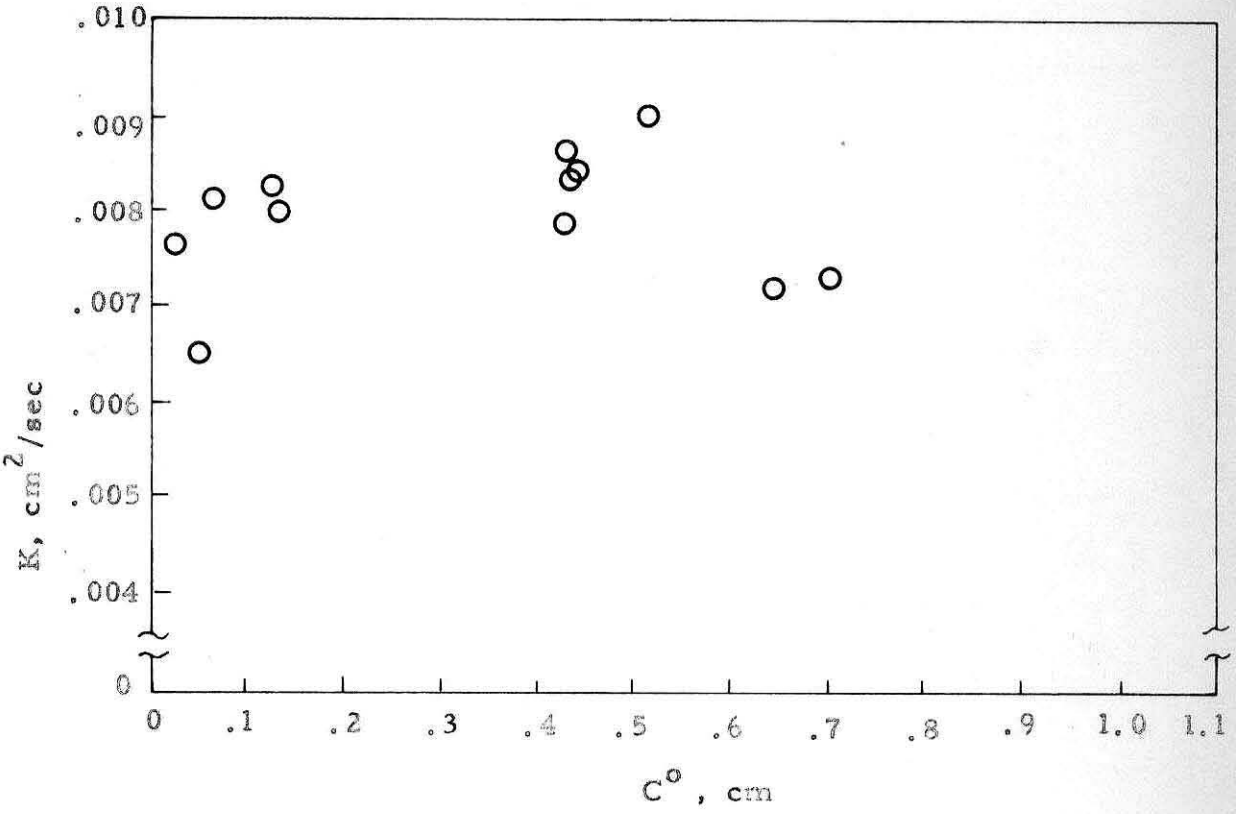

FIGURE 13. AVERAGE EVAPORATION CONSTANT VS INITIAL DROPLET SPACING FOR METHYL ALCOHOL.

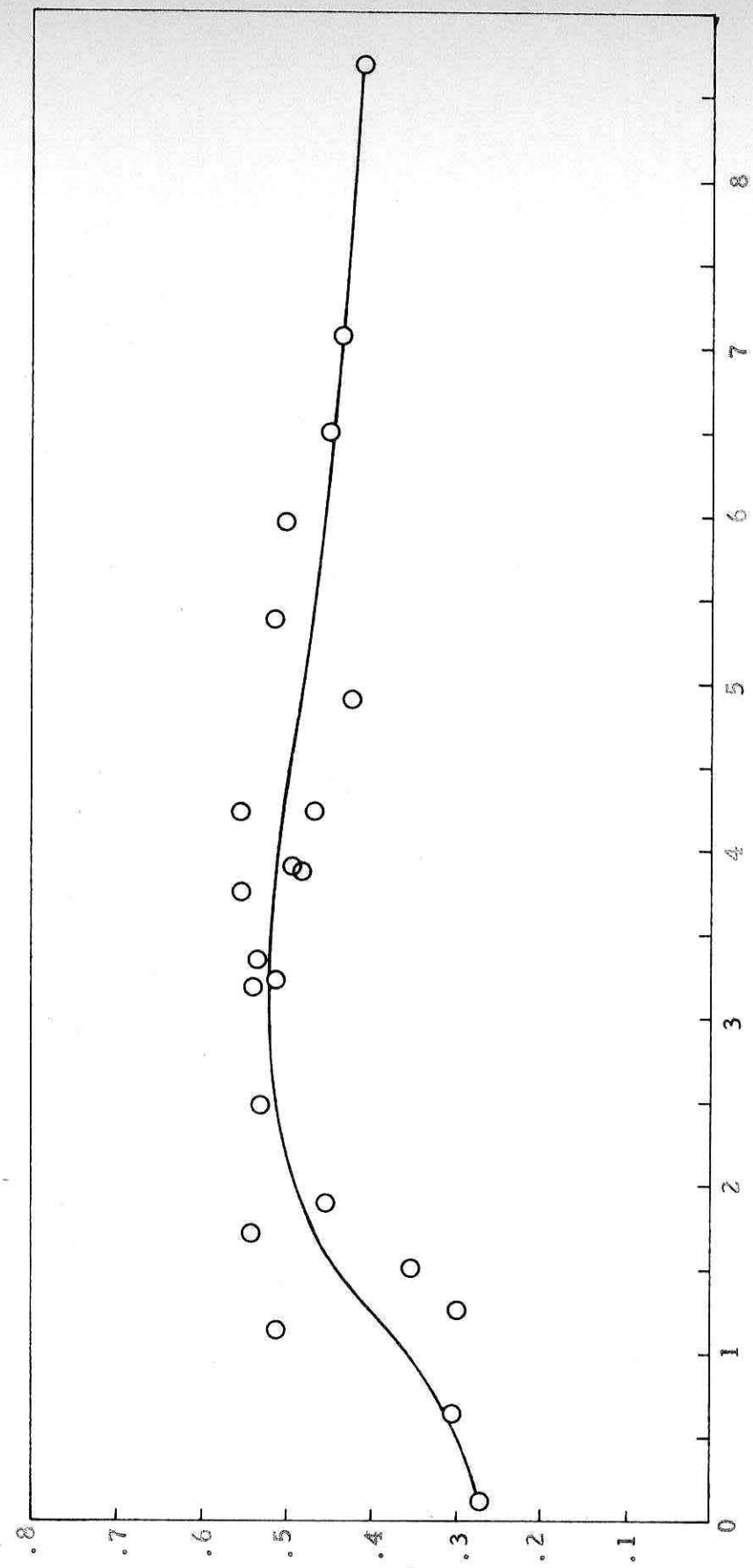

FIGURE 14. DEPENDENCE OF THE EVAPORATION FREQUENCY, $\bar{K}'$, ON $C^o/\bar{D}^o$.

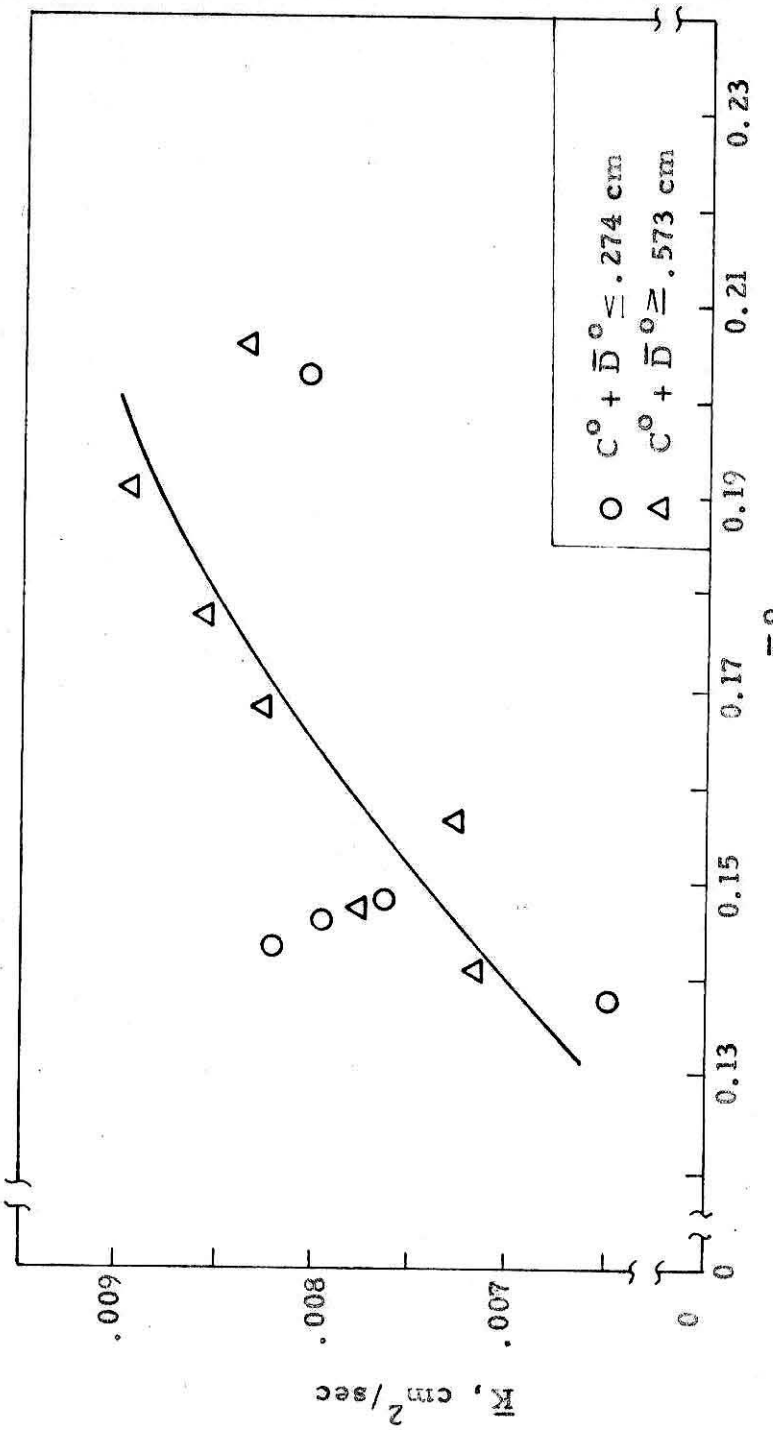

FIGURE 15. VARIATION OF $\bar{K}$ WITH $\bar{D}^\circ$ FOR RANGES OF VALUES OF $C^\circ + \bar{D}^\circ$ (METHYL ALCOHOL).

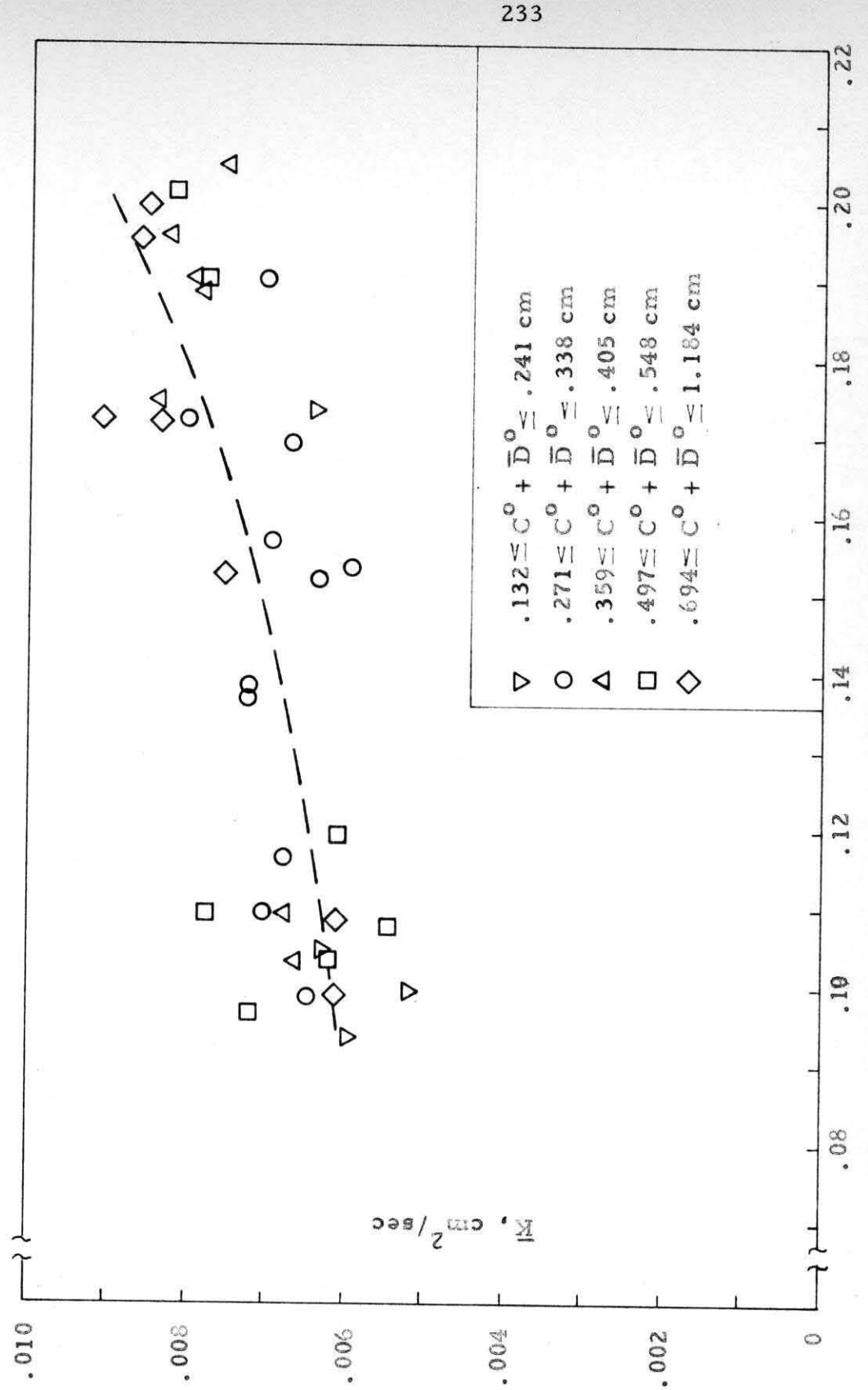

FIGURE 16. VARIATION OF $\bar{K}$ WITH $\bar{D}^o$ FOR RANGES OF VALUES OF $C^o + \bar{D}^o$ (ETHYL ALCOHOL).

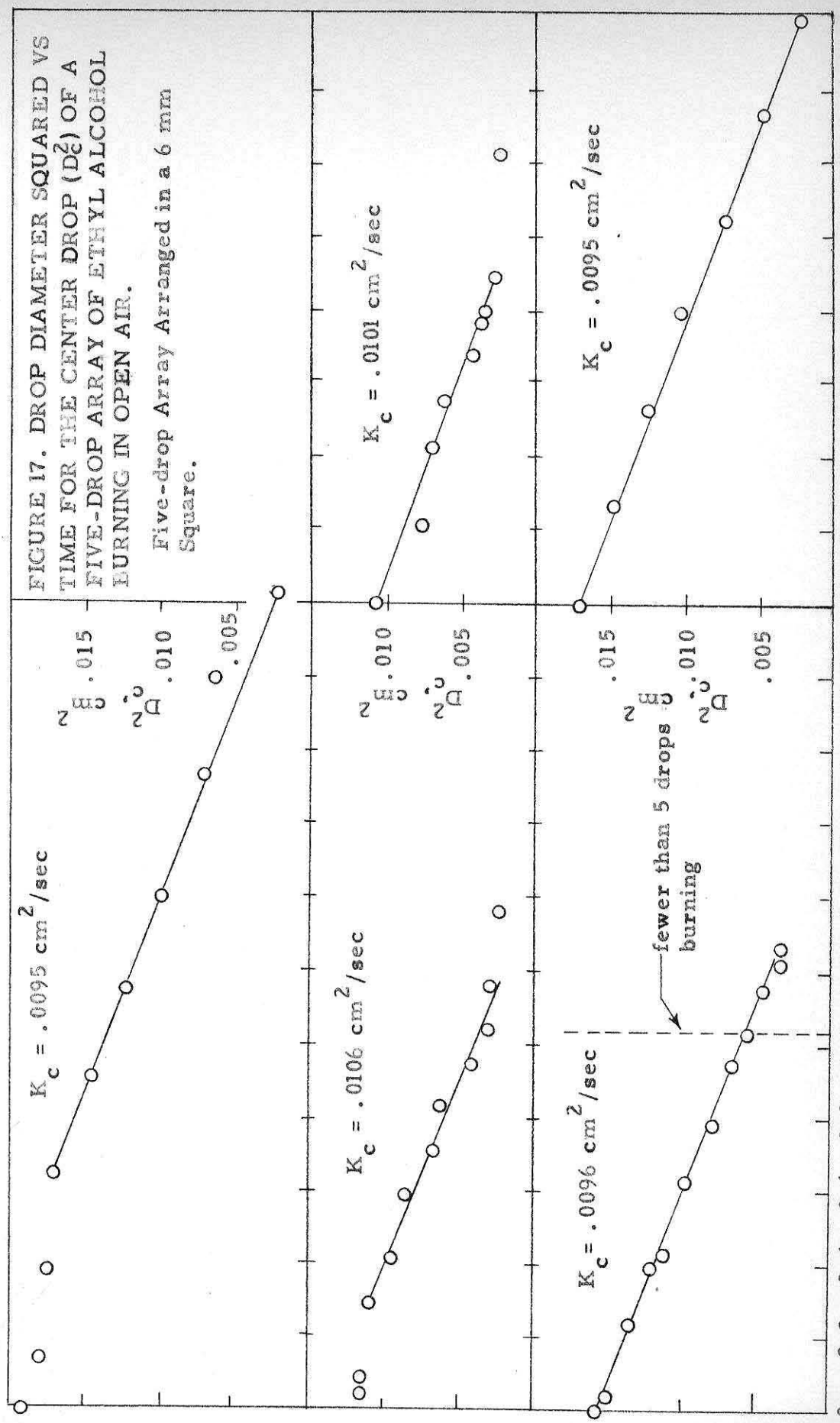

FIGURE 17. DROP DIAMETER SQUARED VS TIME FOR THE CENTER DROP (D_c^2) OF A FIVE-DROP ARRAY OF ETHYL ALCOHOL BURNING IN OPEN AIR.

Five-drop Array Arranged in a 6 mm Square.

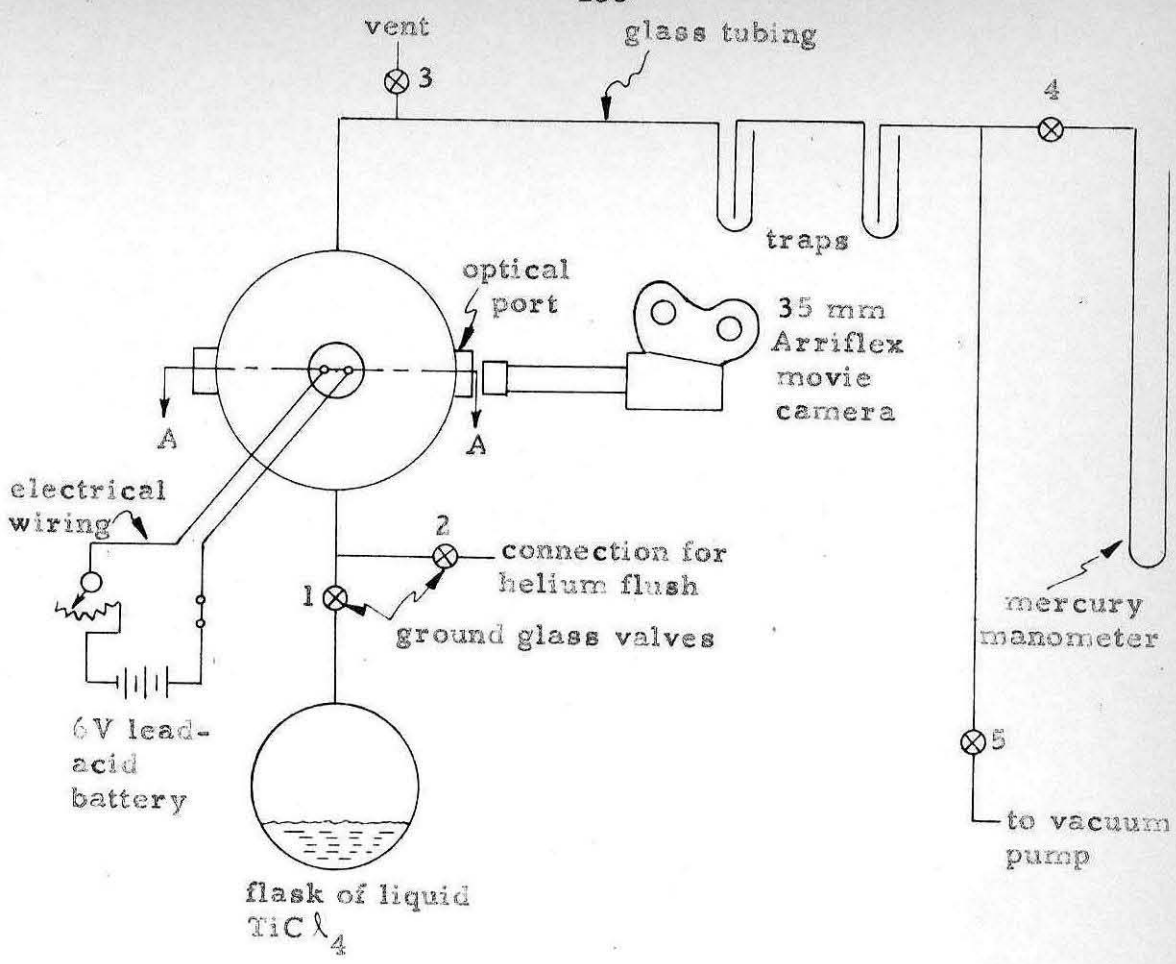

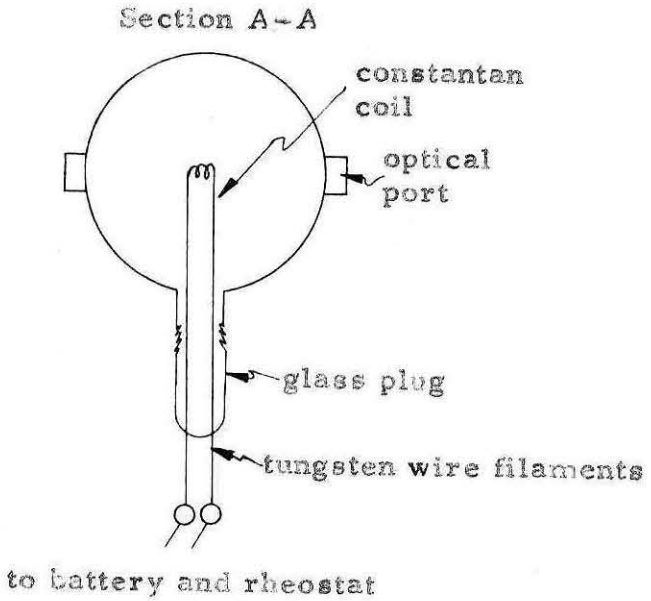

FIGURE 18. SCHEMATIC DIAGRAM OF APPARATUS USED FOR SODIUM-TITANIUM TETRACHLORIDE DIFFUSION FLAME EXPERIMENTS.

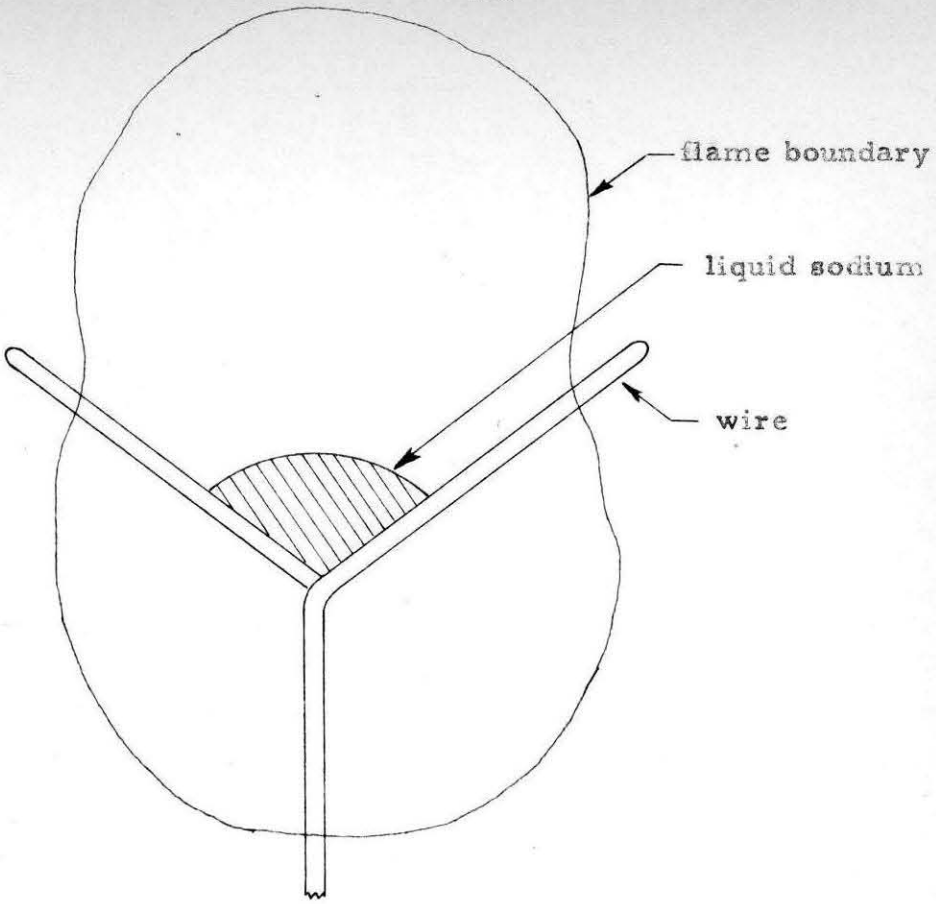

FIGURE 19a. END VIEW OF LIQUID SODIUM DROPLET SUPPORTED BY HEATING WIRES.

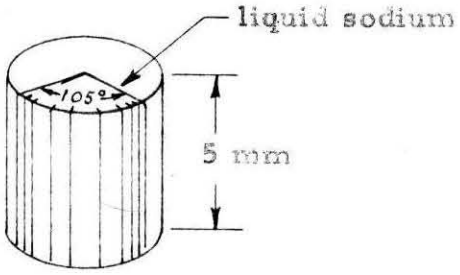

FIGURE 19b. TOP VIEW SHOWING THE LIQUID SODIUM.

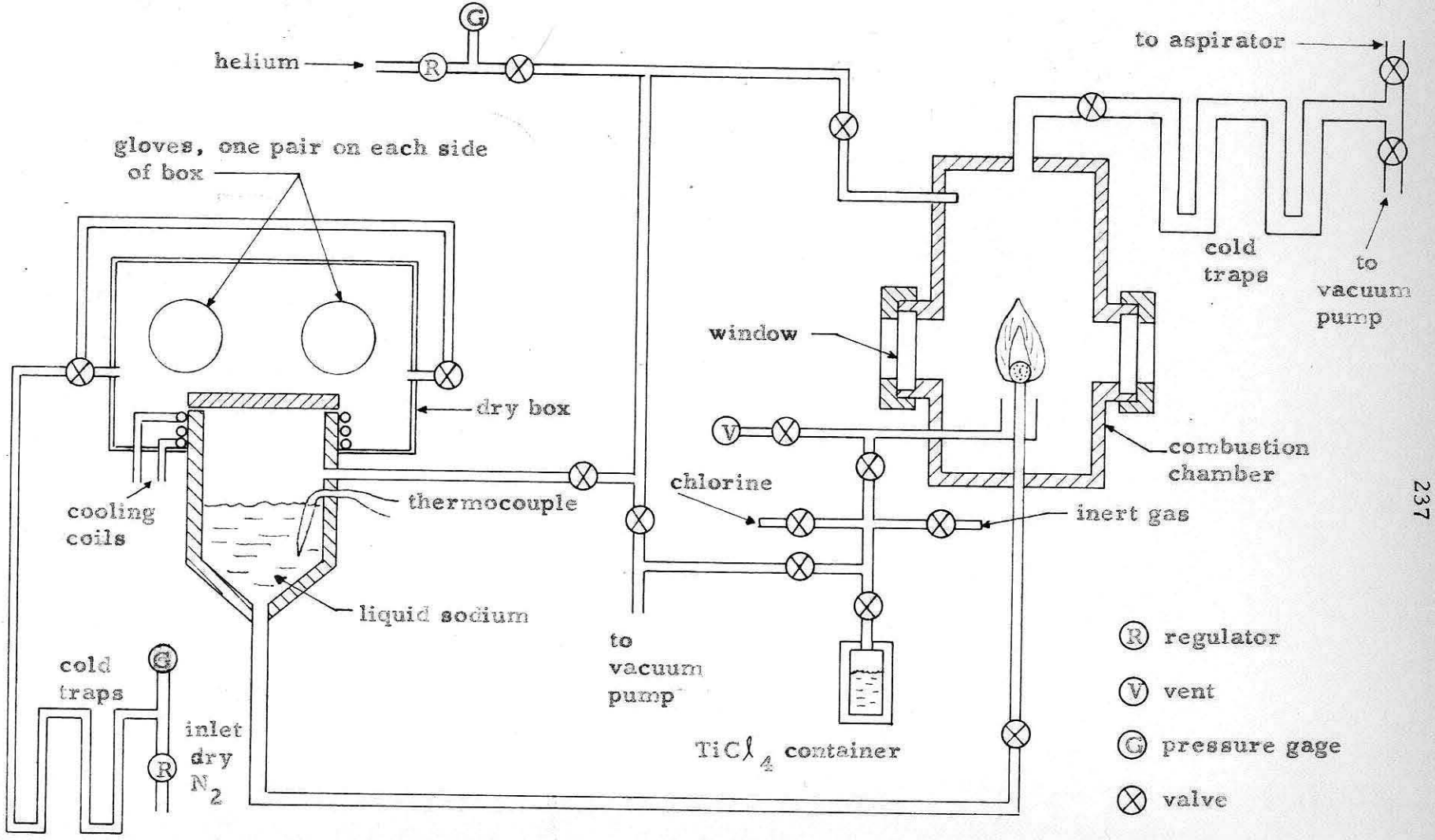

FIGURE 20. SCHEMATIC DIAGRAM OF AN APPARATUS FOR THE STUDY OF HETEROGENEOUS DIFFUSION FLAMES FORMED BETWEEN LIQUID SODIUM AND TITANIUM TETRACHLORIDE.

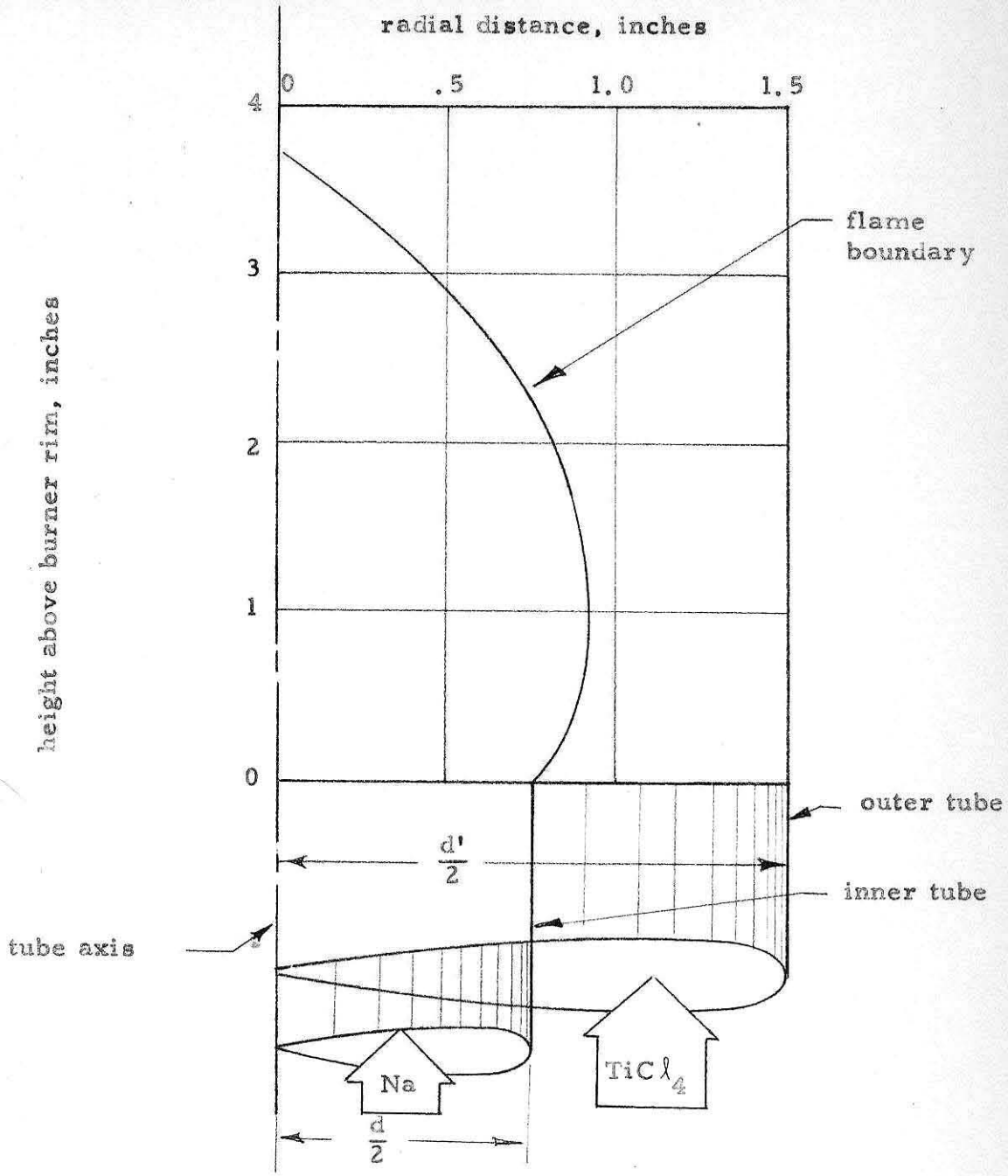

FIGURE 21. FLAME BOUNDARY FOR AN OVERVENTILATED DIFFUSION FLAME FORMED BETWEEN SODIUM AND TITANIUM TETRACHLORIDE.

Flow Velocity of Na=0.5 in/sec (in Inner Tube with 1.5 in Diameter) = Flow Velocity of $TiC\ell_4$ (in Outer Tube with 3 in Diameter);

$D = 0.05\ in^2/sec.$

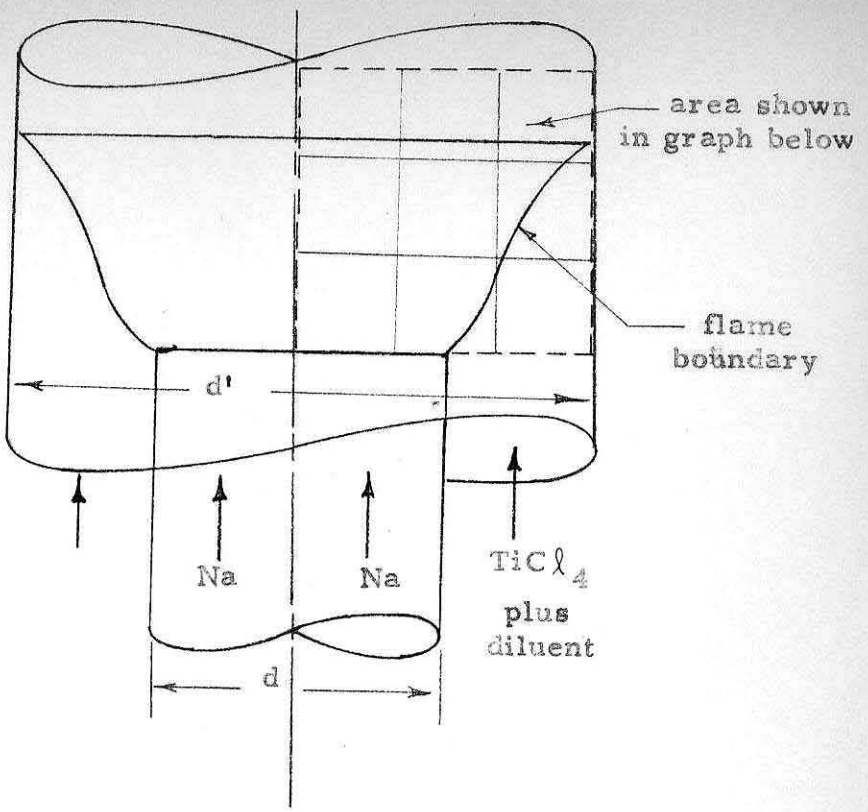

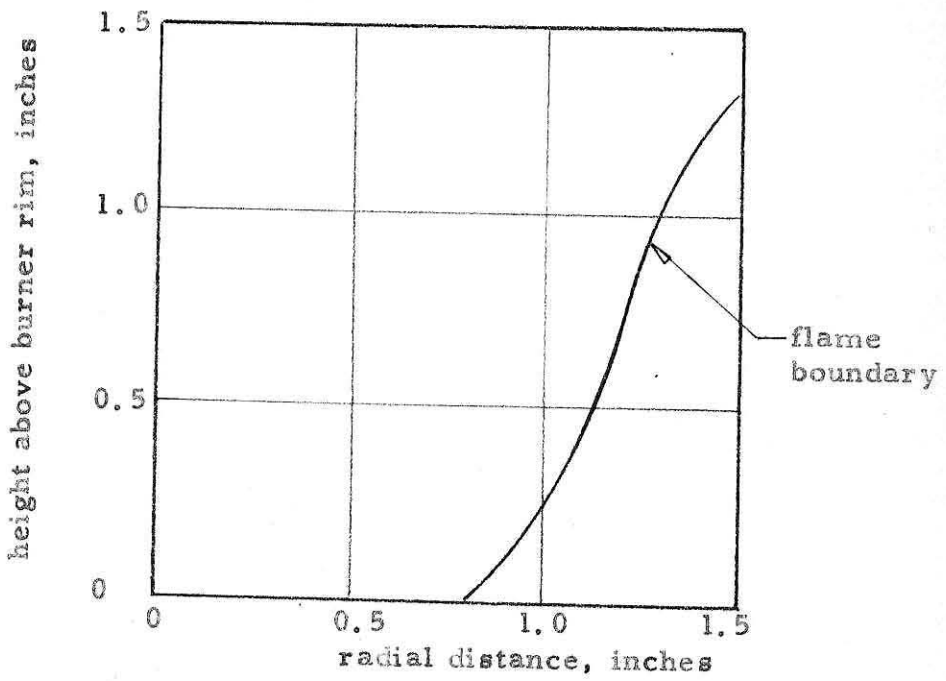

FIGURE 22. FLAME BOUNDARY FOR AN UNDERVENTILATED DIFFUSION FLAME FORMED BETWEEN SODIUM AND TITANIUM TETRACHLORIDE.

Flow Velocity of Na=0.5 in/sec (in Inner Tube with 1.5 in Diameter) = Flow Velocity of $TiC\ell_4$ plus Diluent (in Outer Tube with 3 in Diameter); Weight Fraction of Diluent = 0.5; D= 0.05 in^2/sec.

FIGURES

PART II

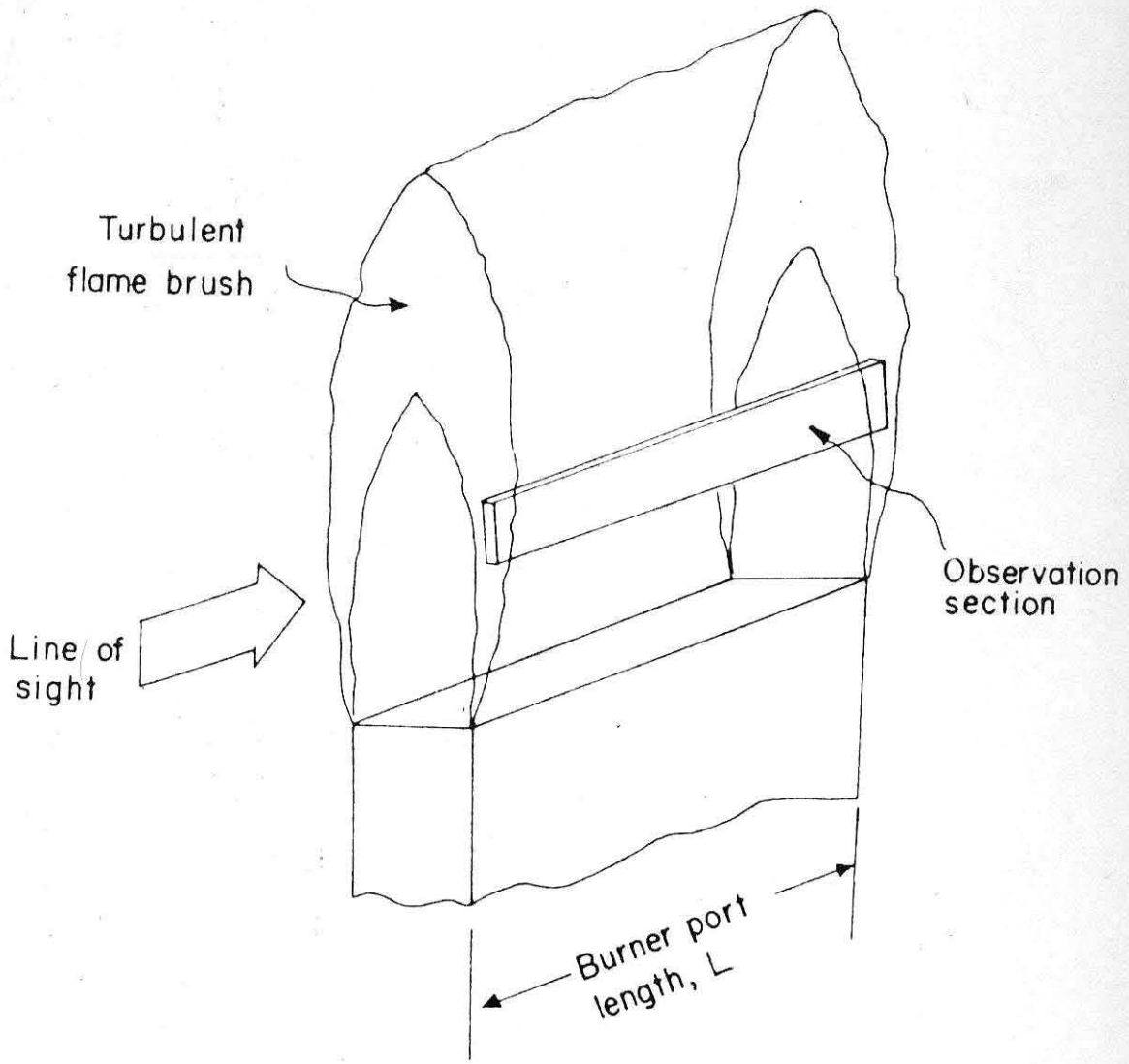

FIGURE 1. TURBULENT FLAME FORMED ABOVE A RECTANGULAR EXIT PORT AND A REPRESENTATIVE OBSERVATION SECTION (SCHEMATIC).

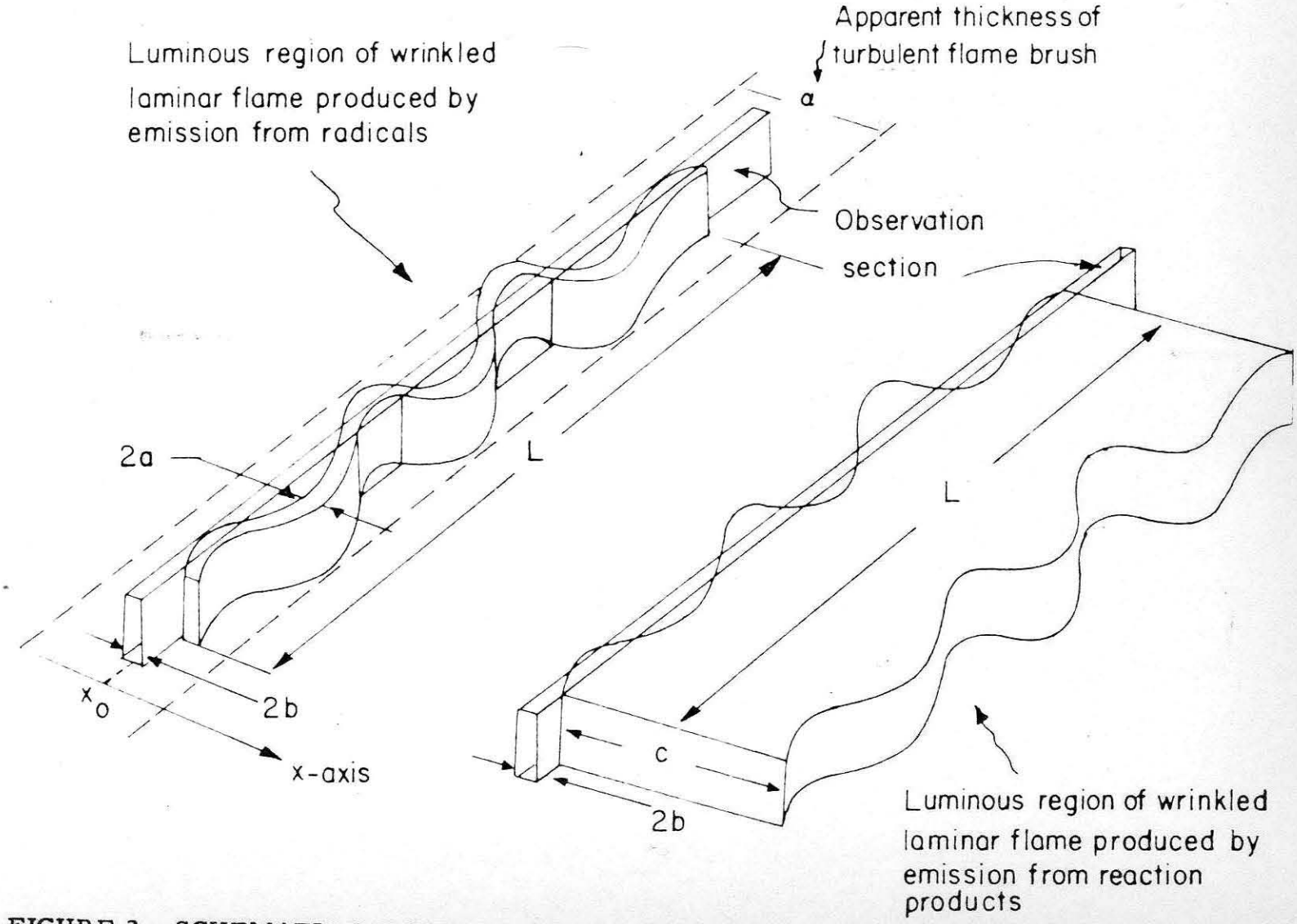

FIGURE 2. SCHEMATIC ILLUSTRATIONS OF THE IMPORTANT LENGTHS DEFINING EMISSION FROM A TURBULENT FLAME COMPOSED OF A WRINKLED LAMINAR FLAME.

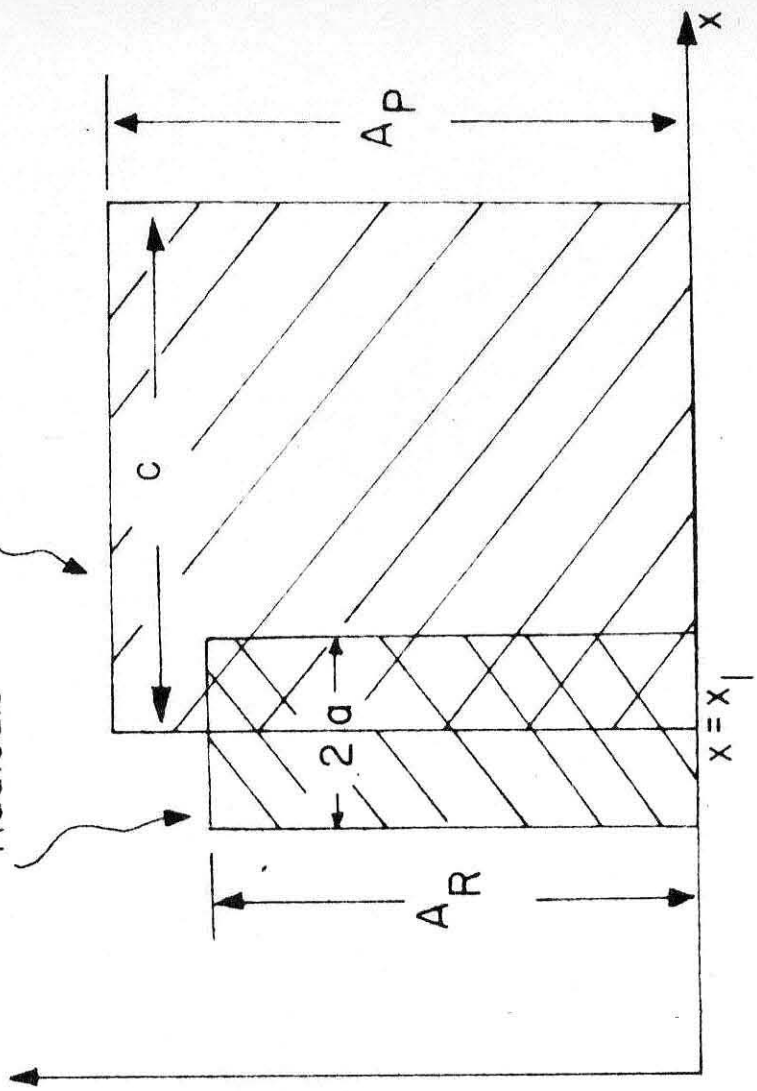

FIGURE 3. MODEL OF A STEADY-STATE LAMINAR FLAME.

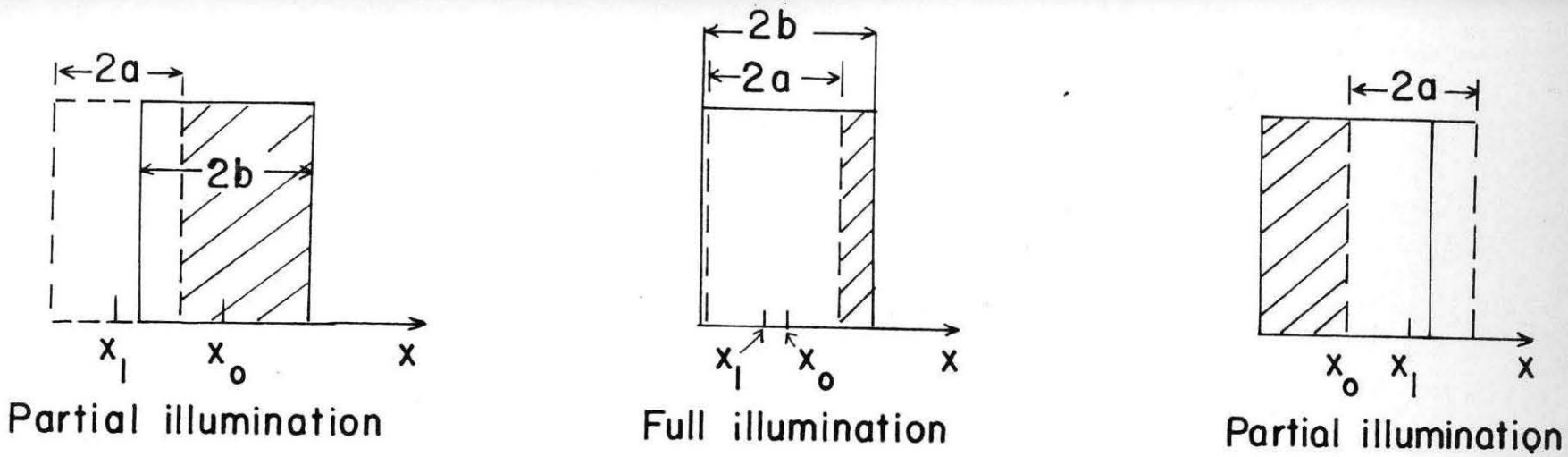

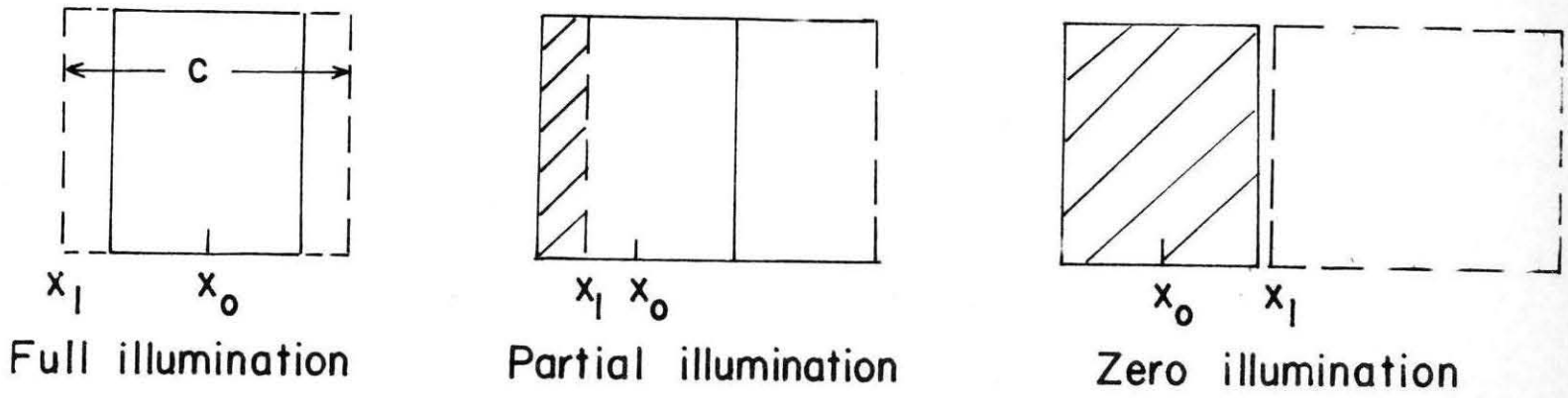

FIGURE 4. DEPENDENCE OF ENERGY PER SECOND RECEIVED ON THE SEPARATION BETWEEN THE SLIT CENTER AND THE LAMINAR FLAME CENTER.

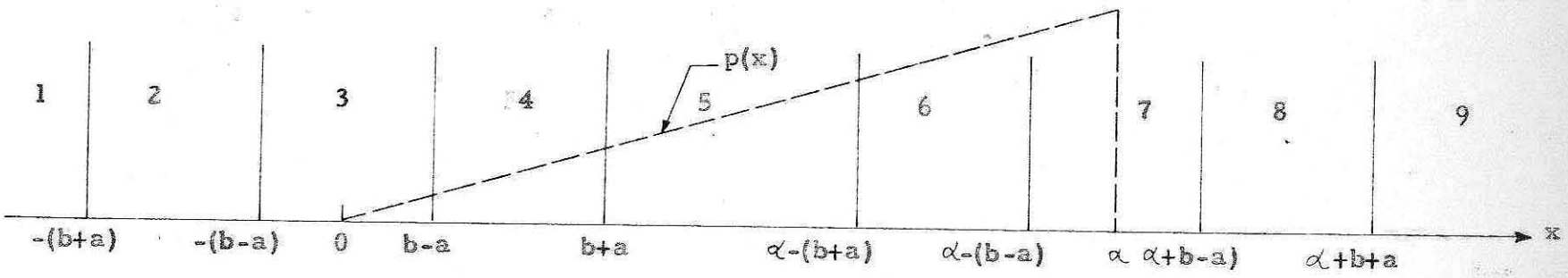

regions for the apparent radical emission profile

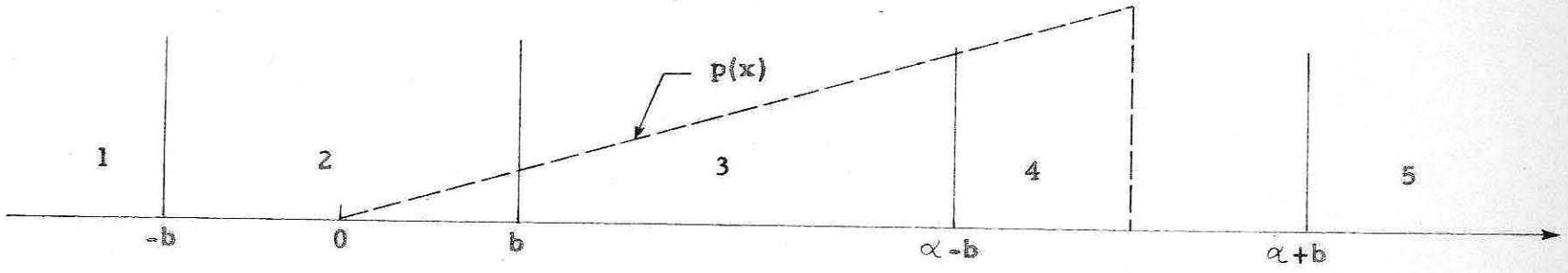

regions for the apparent product emission profile

FIGURE 5 . REGIONS WITHIN WHICH THE EQUATIONS FOR $E(x_o)$ ARE VALID.

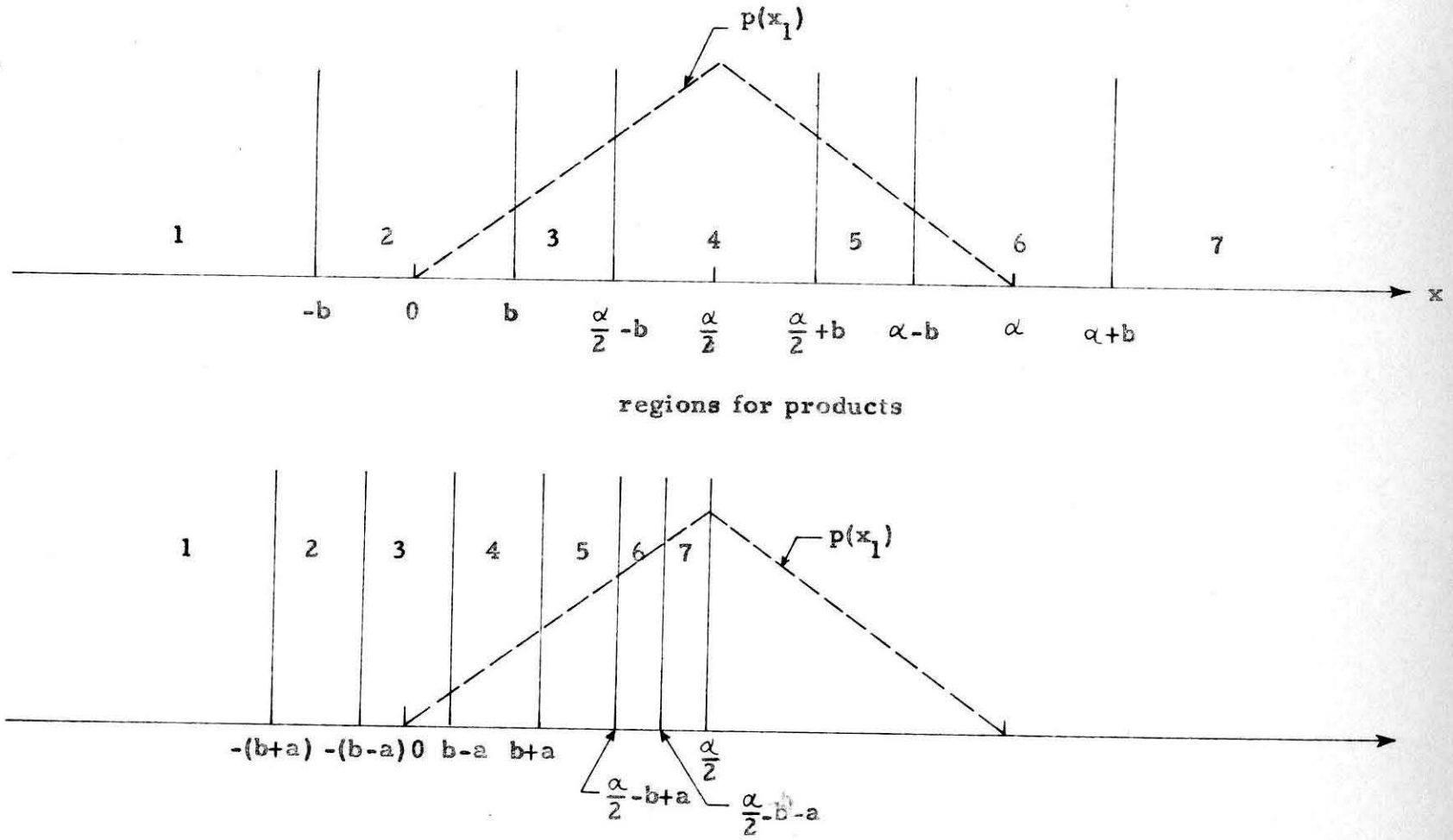

FIGURE 6 . COMPUTATIONAL REGIONS FOR PRODUCTS AND REACTANTS USING A SYMMETRICAL TRIANGULAR PROBABILITY FUNCTION.

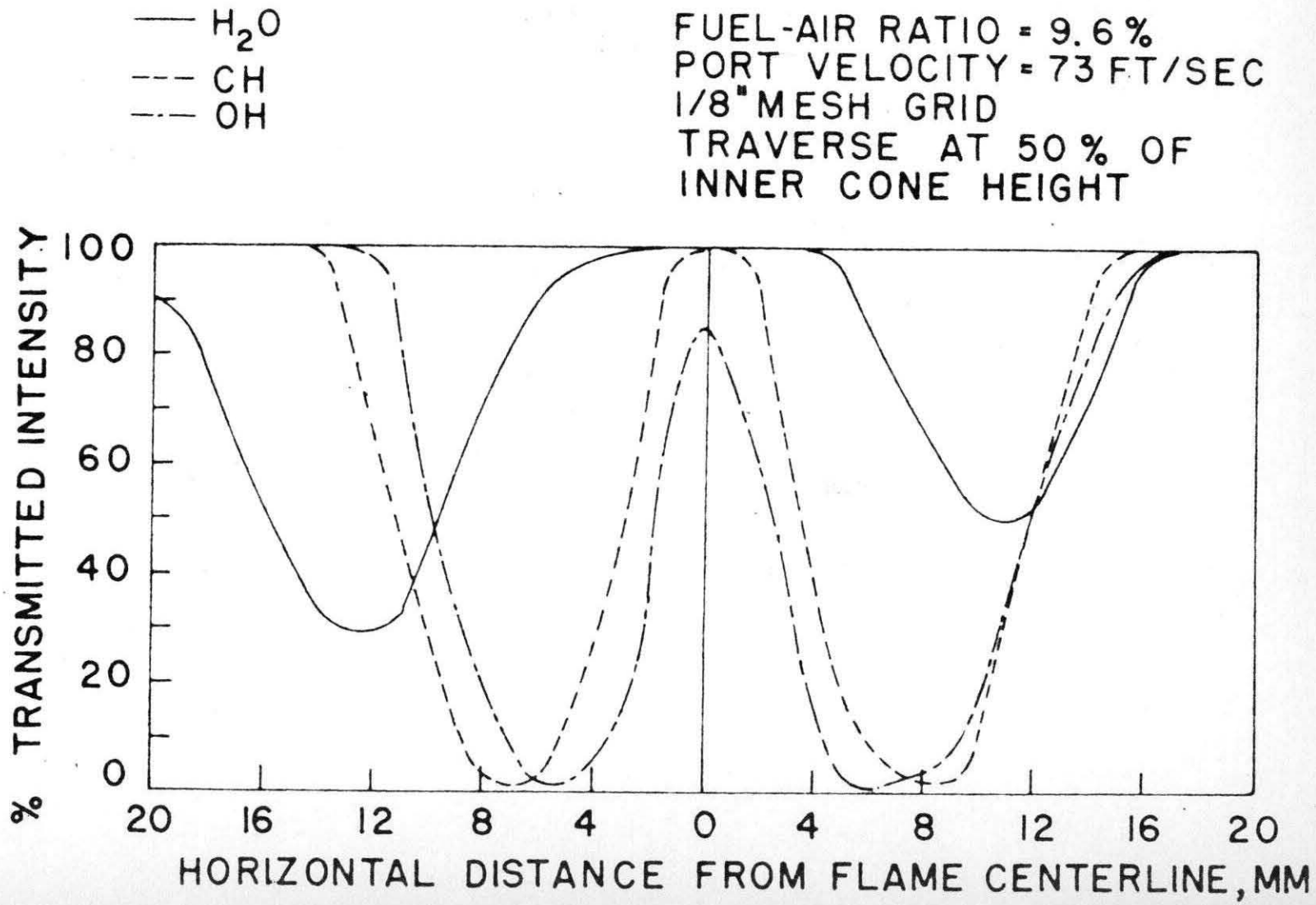

FIGURE 7. REPRODUCTION OF FIGURE 10 FROM REFERENCE (3). PERCENT TRANSMITTED INTENSITY AS A FUNCTION OF DISTANCE FROM THE FLAME CENTERLINE.

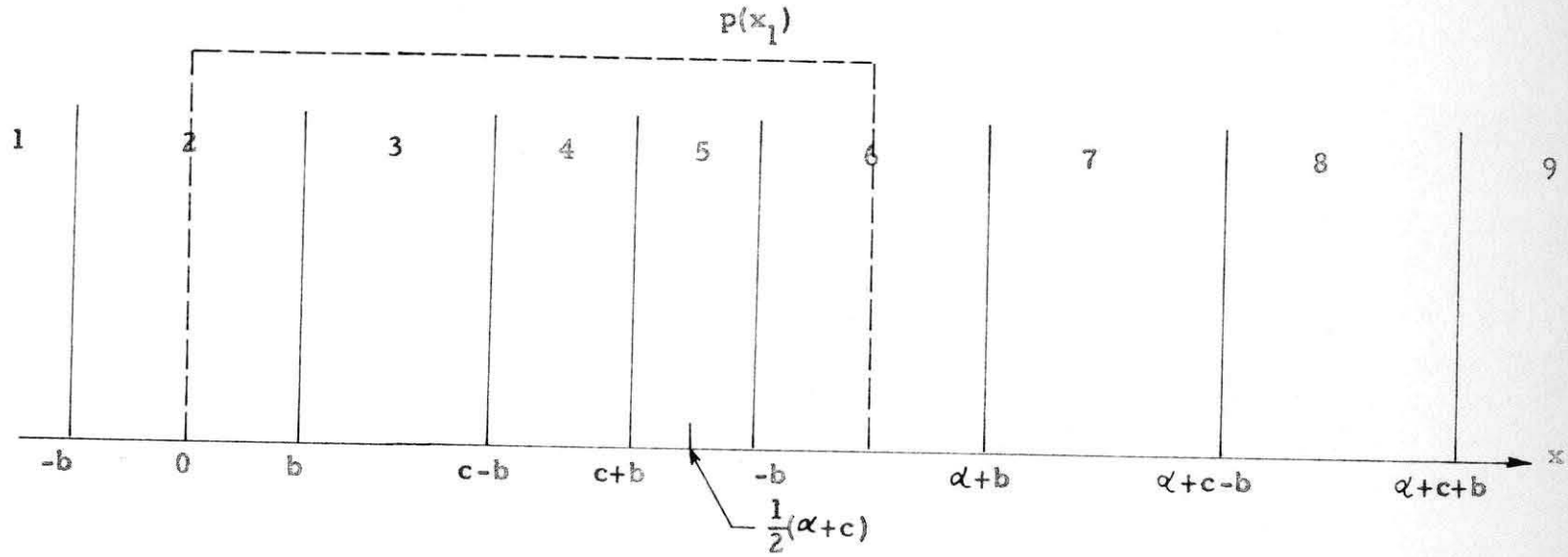

FIGURE 8 . COMPUTATIONAL REGIONS FOR $E_P(x_o)$ USING FINITE c VALUE.

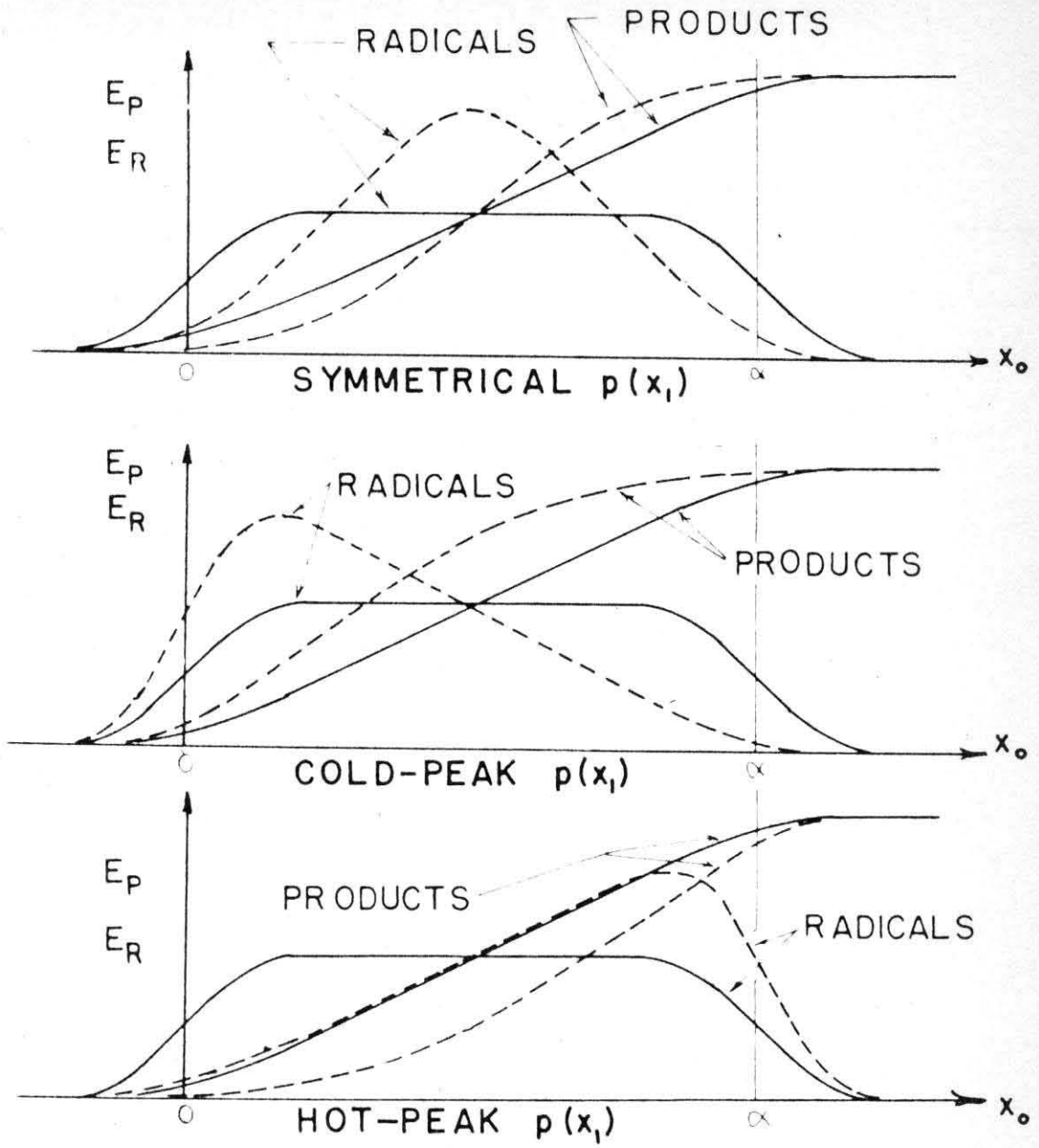

FIGURE 9. INSTRUMENTAL RESPONSE WHEN OBSERVATIONS ARE MADE WITH A SLIT WIDTH $b > a$ FOR VARIOUS PROBABILITY FUNCTIONS WITH INFINITE c. NOTE THAT THERE IS NO SIGNIFICANCE TO THE ABSOLUTE VALUES OF E_P AND E_R.

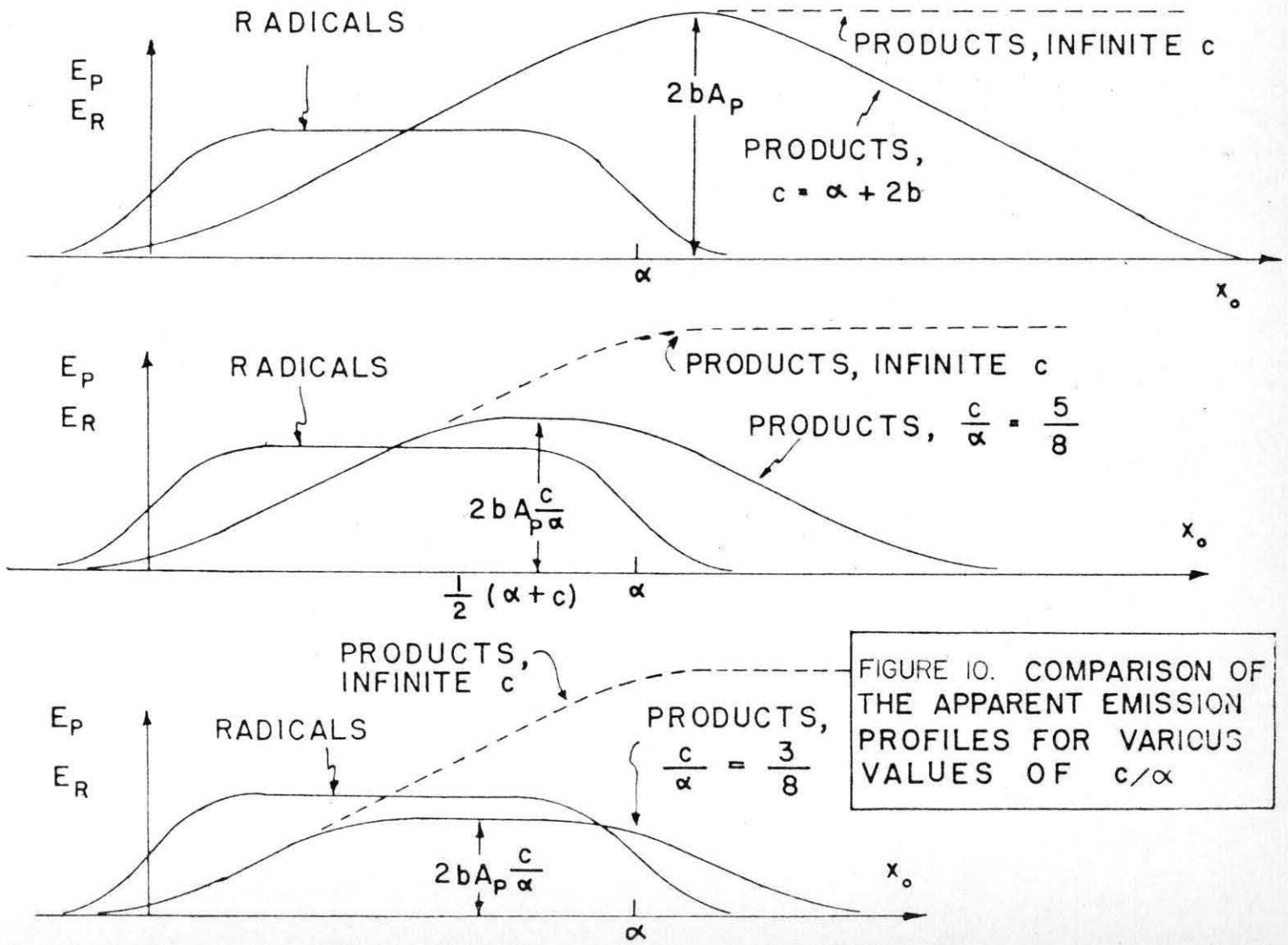

FIGURE 10. COMPARISON OF THE APPARENT EMISSION PROFILES FOR VARIOUS VALUES OF c/α

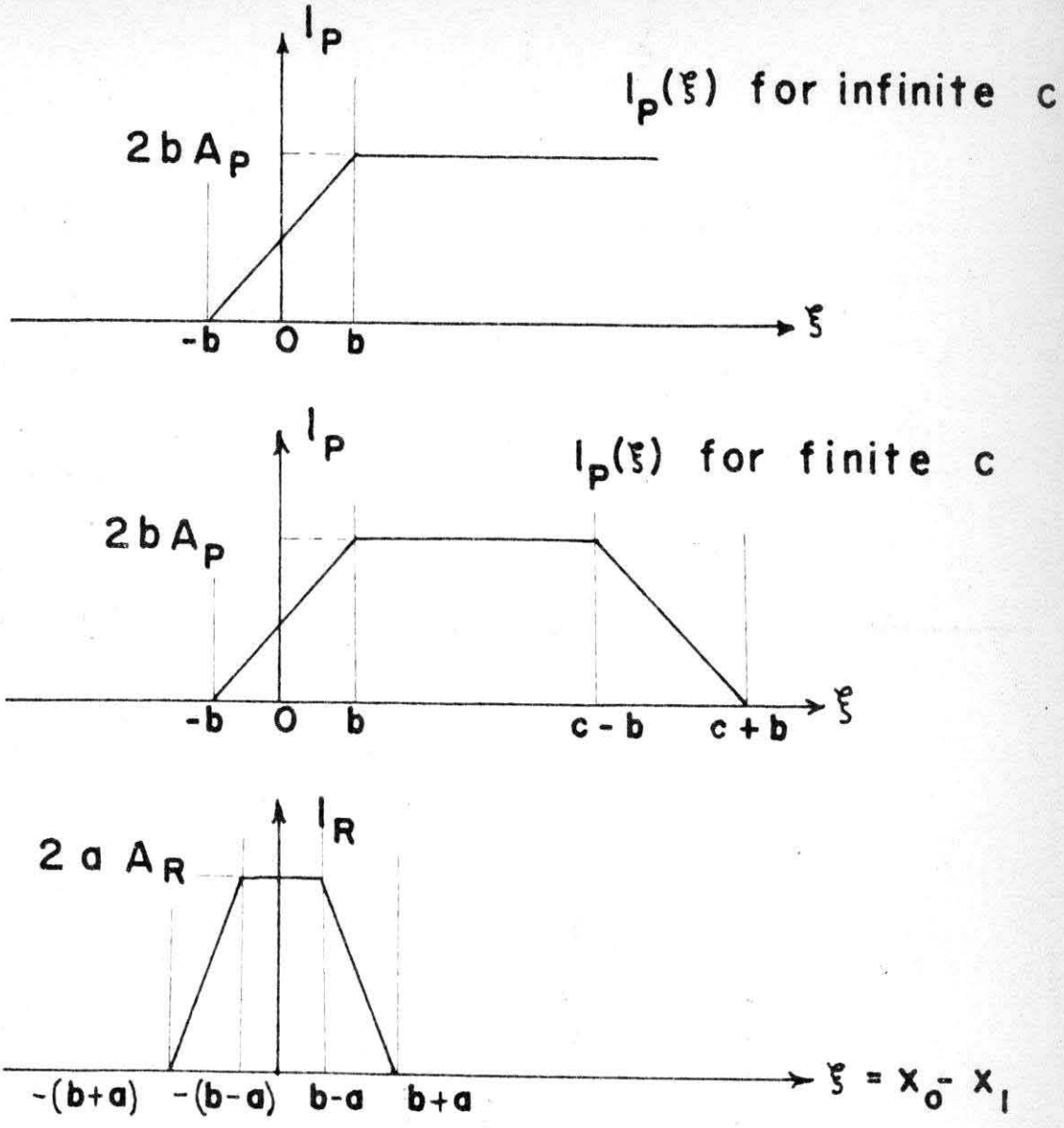

FIGURE 11. GRAPHS OF THE FUNCTIONS $I_R(x_o-x_1)$, $I_P(x_o-x_1)$ FOR FINITE c, AND $I_P(x_o-x_1)$ FOR FINITE c.

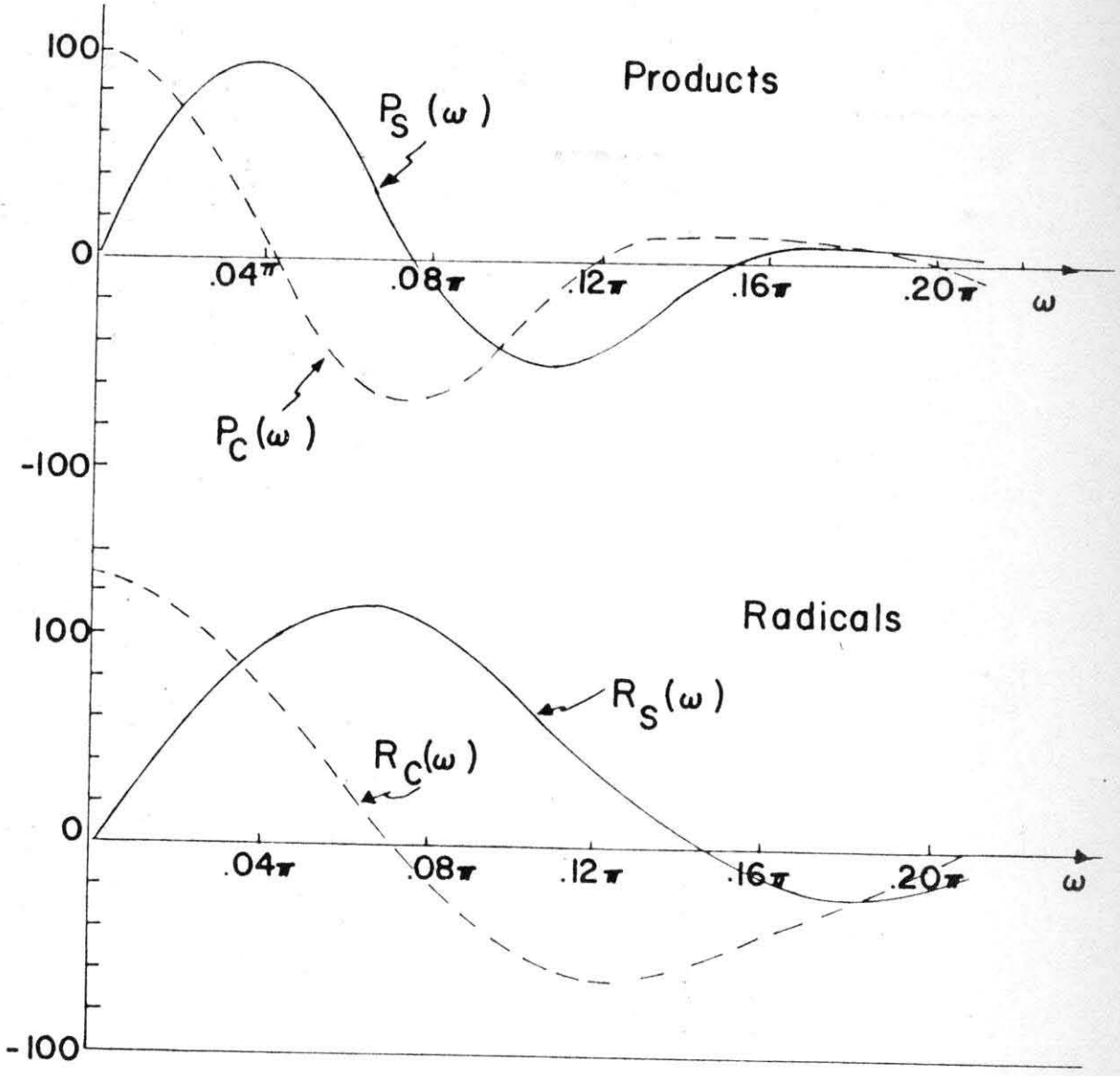

FIGURE 12. THE REAL AND IMAGINARY PARTS OF THE FOURIER TRANSFORM OF THE APPARENT EMISSION PROFILES PLOTTED AS A FUNCTION OF ω.

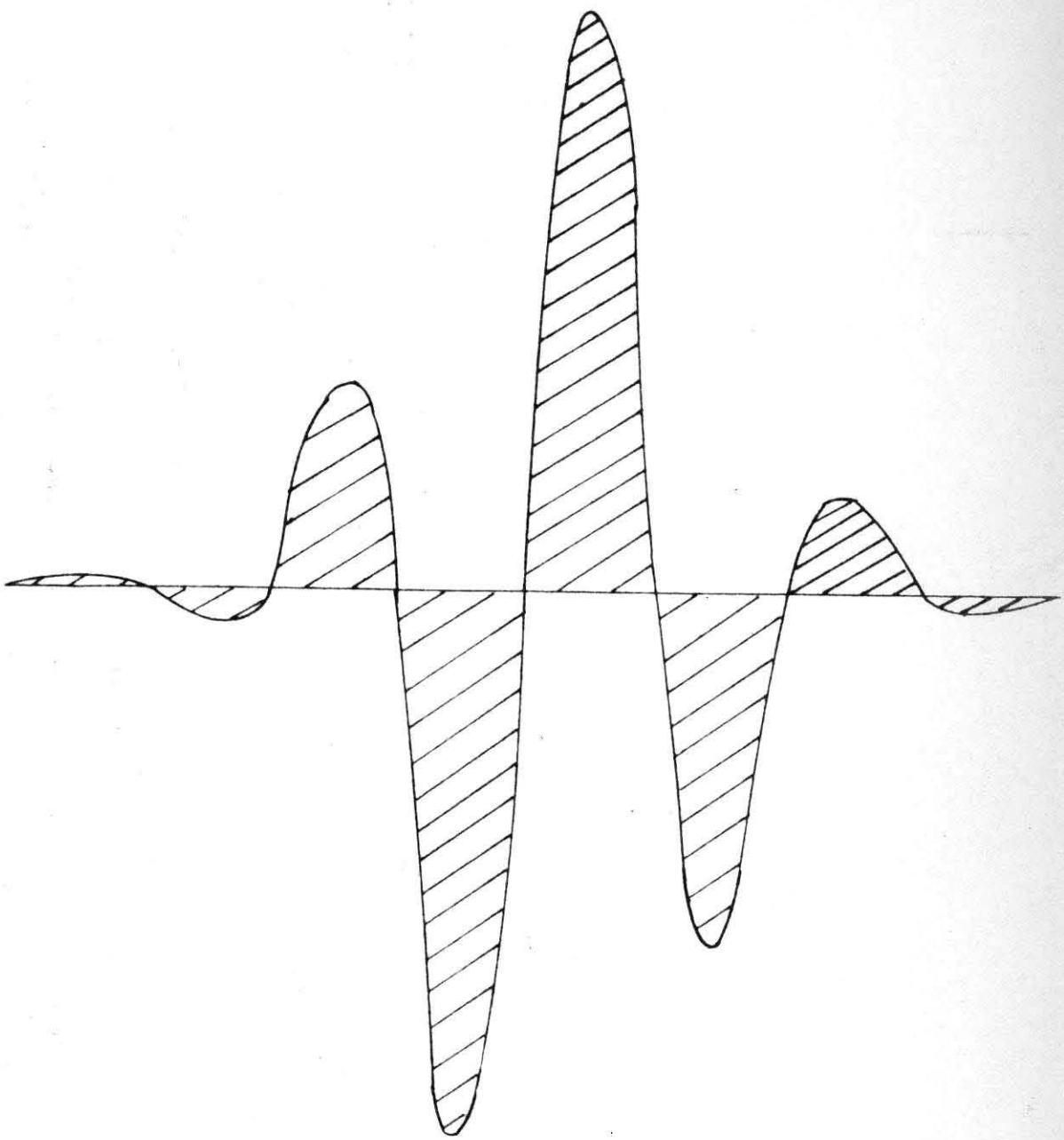

FIGURE 13. GRAPH OF THE INTEGRAND OF P_s FOR $\omega = 0.333\pi$.

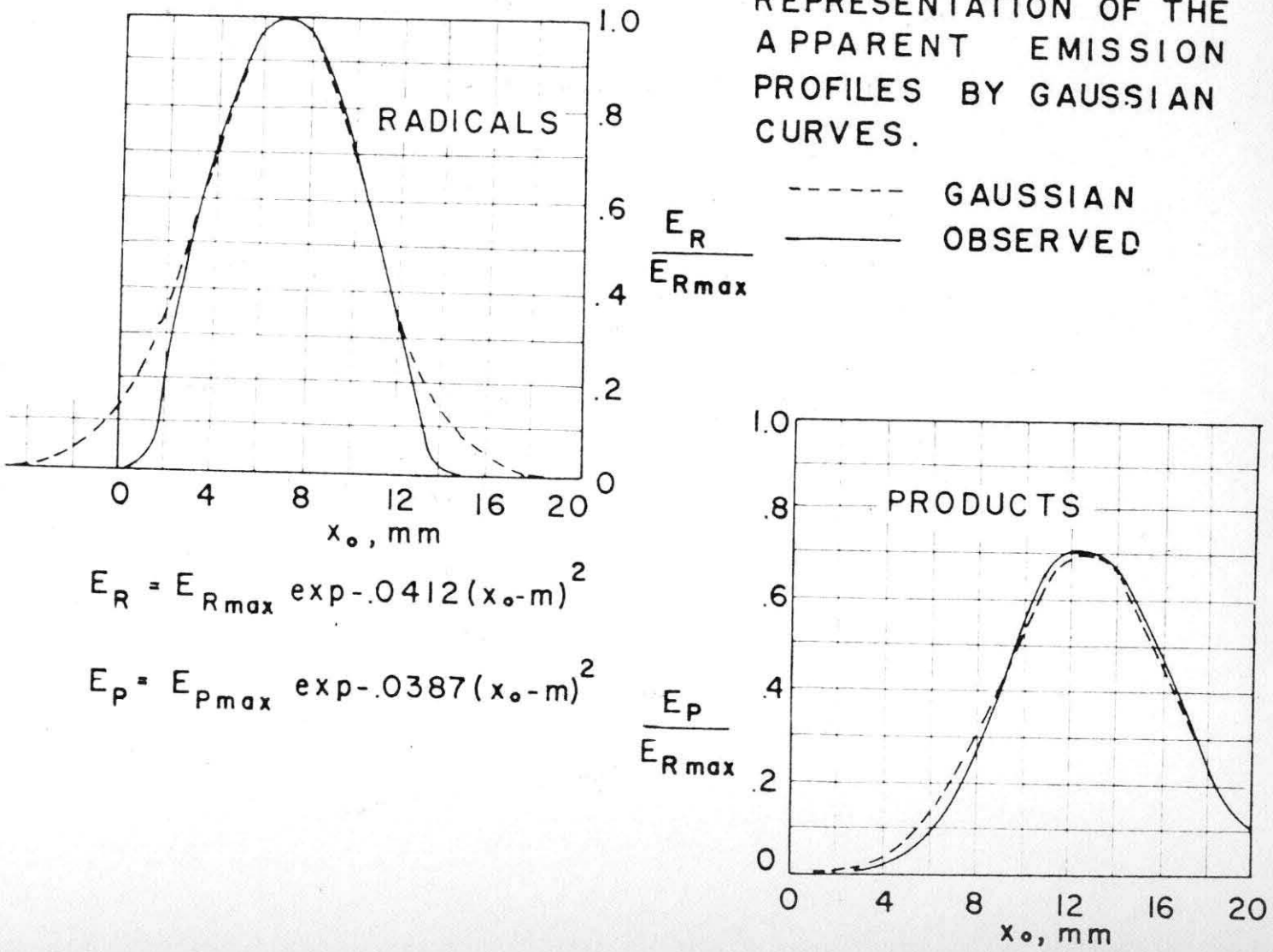

FIGURE 14. REPRESENTATION OF THE APPARENT EMISSION PROFILES BY GAUSSIAN CURVES.

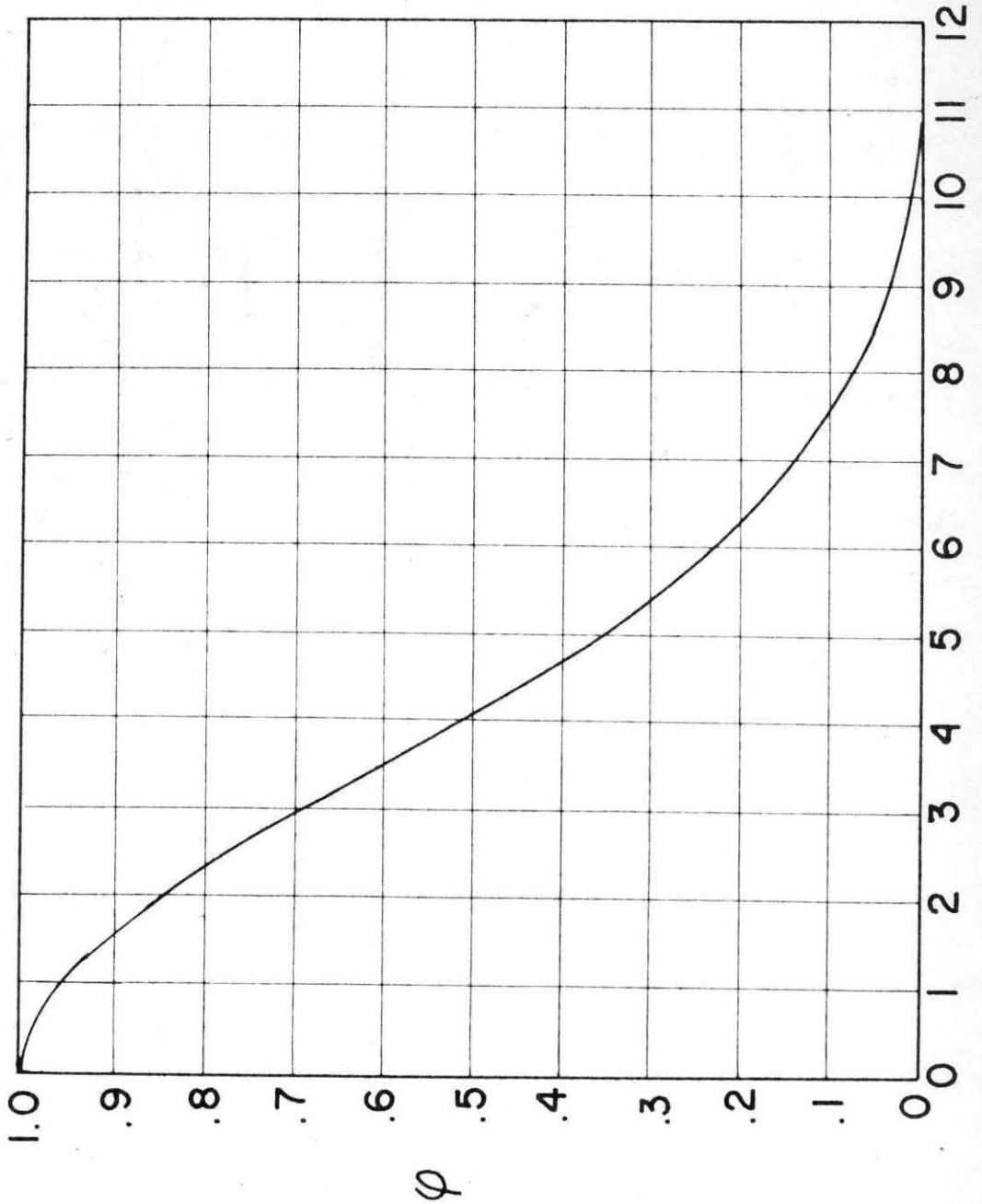

FIGURE 15. GRAPH OF THE FUNCTION $\varphi(x)$.

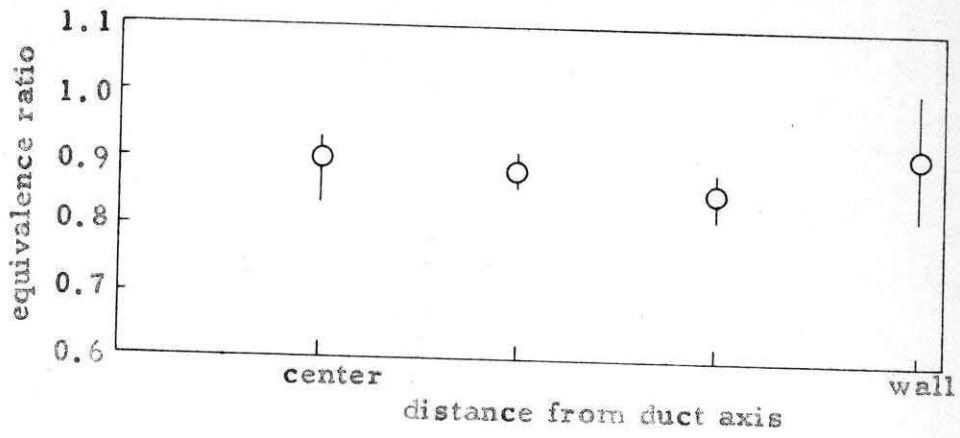

duct 1(1/4) inch standard pipe
jet pressure 30 psig
propane-air

FIGURE 16. THE OBSERVED EQUIVALENCE RATIO AS A FUNCTION OF RADIAL DISTANCE FROM THE DUCT AXIS FOR A STOICHIOMETRIC MAIN STREAM AND A STOICHIOMETRIC JET.

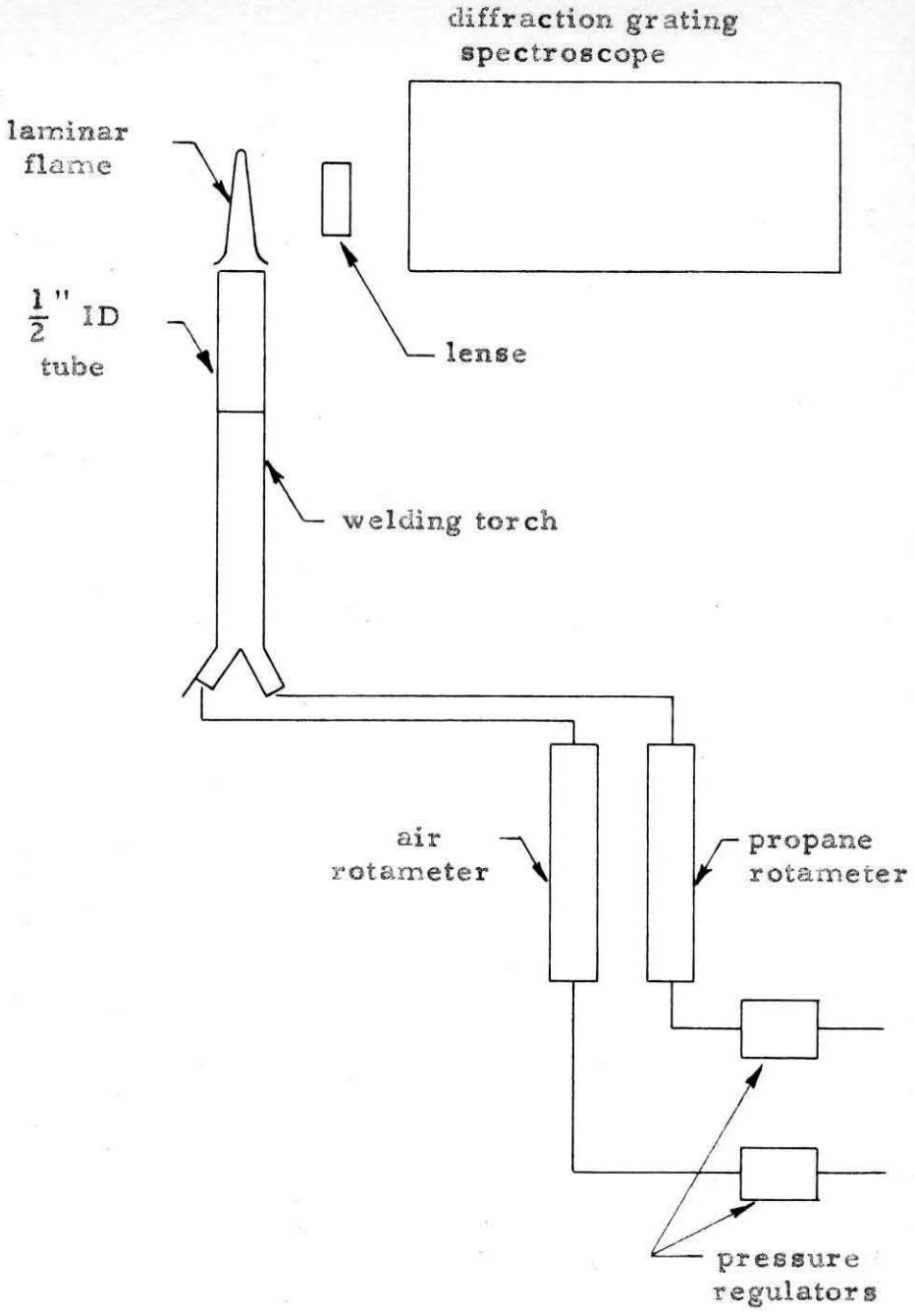

FIGURE 17. SCHEMATIC ILLUSTRATION OF THE APPARATUS USED FOR OBTAINING THE CALIBRATION CURVES.

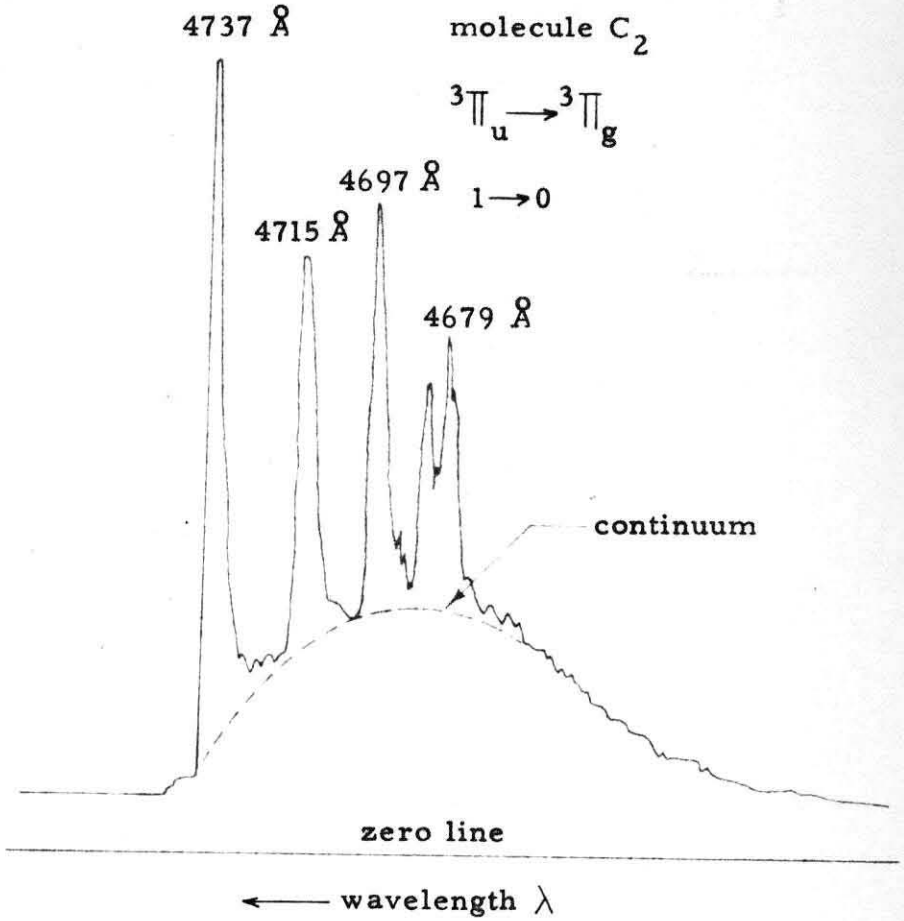

FIGURE 18. APPARENT EMISSION INTENSITY AS A FUNCTION OF WAVELENGTH.

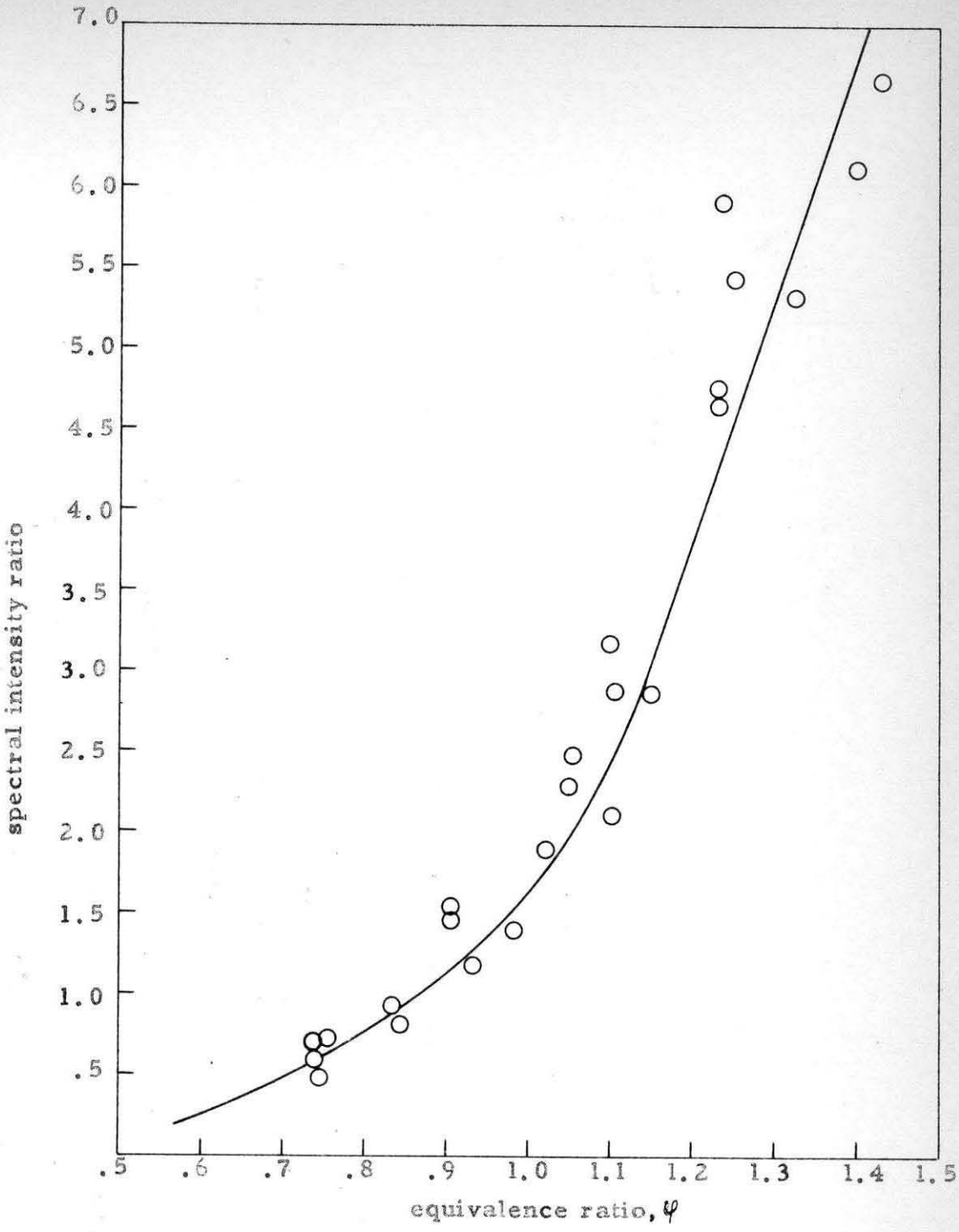

FIGURE 19. SPECTRAL INTENSITY RATIO AS A FUNCTION OF EQUIVALENCE RATIO FOR THE LINE WITH CENTER AT 4737 Å TO THE LINE WITH CENTER AT 4324 Å.

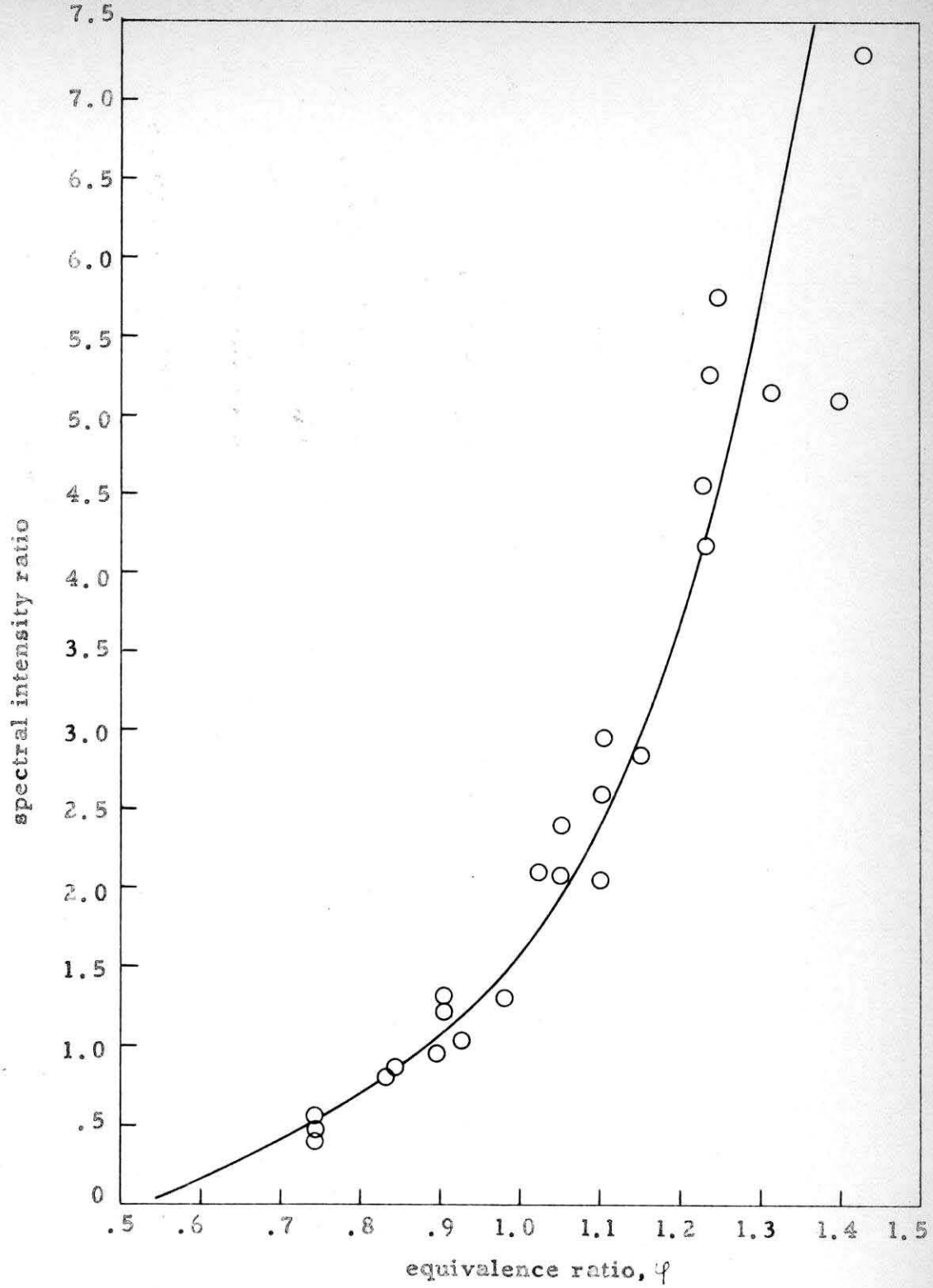

FIGURE 20. SPECTRAL INTENSITY RATIO AS A FUNCTION OF EQUIVALENCE RATIO FOR THE LINE WITH CENTER AT 4737 Å TO THE LINE WITH CENTER AT 4252 Å.

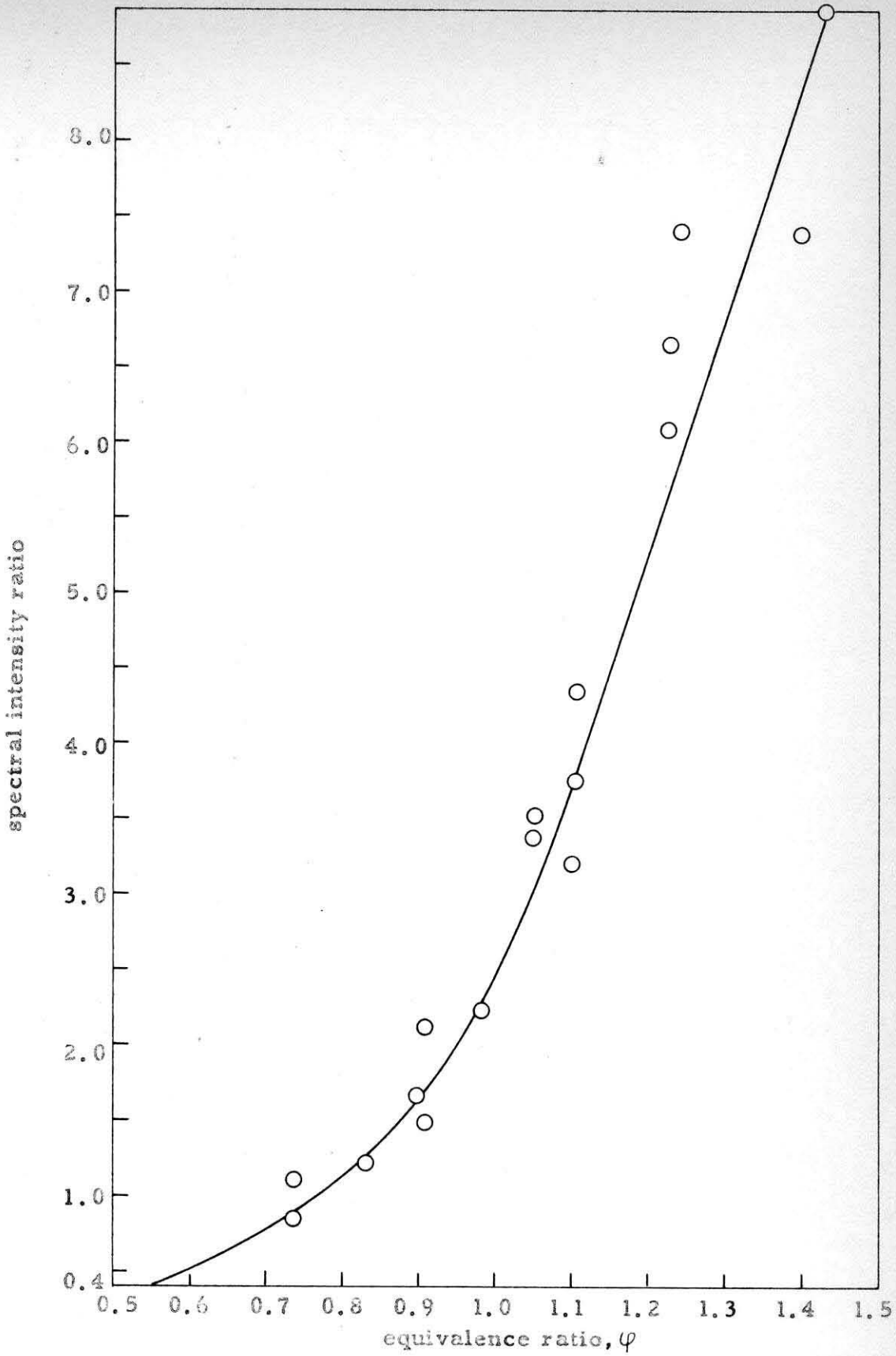

FIGURE 21. SPECTRAL INTENSITY RATIO AS A FUNCTION OF EQUIVALENCE RATIO FOR THE LINE WITH CENTER AT 5129 Å TO THE LINE WITH CENTER AT 4324 Å .

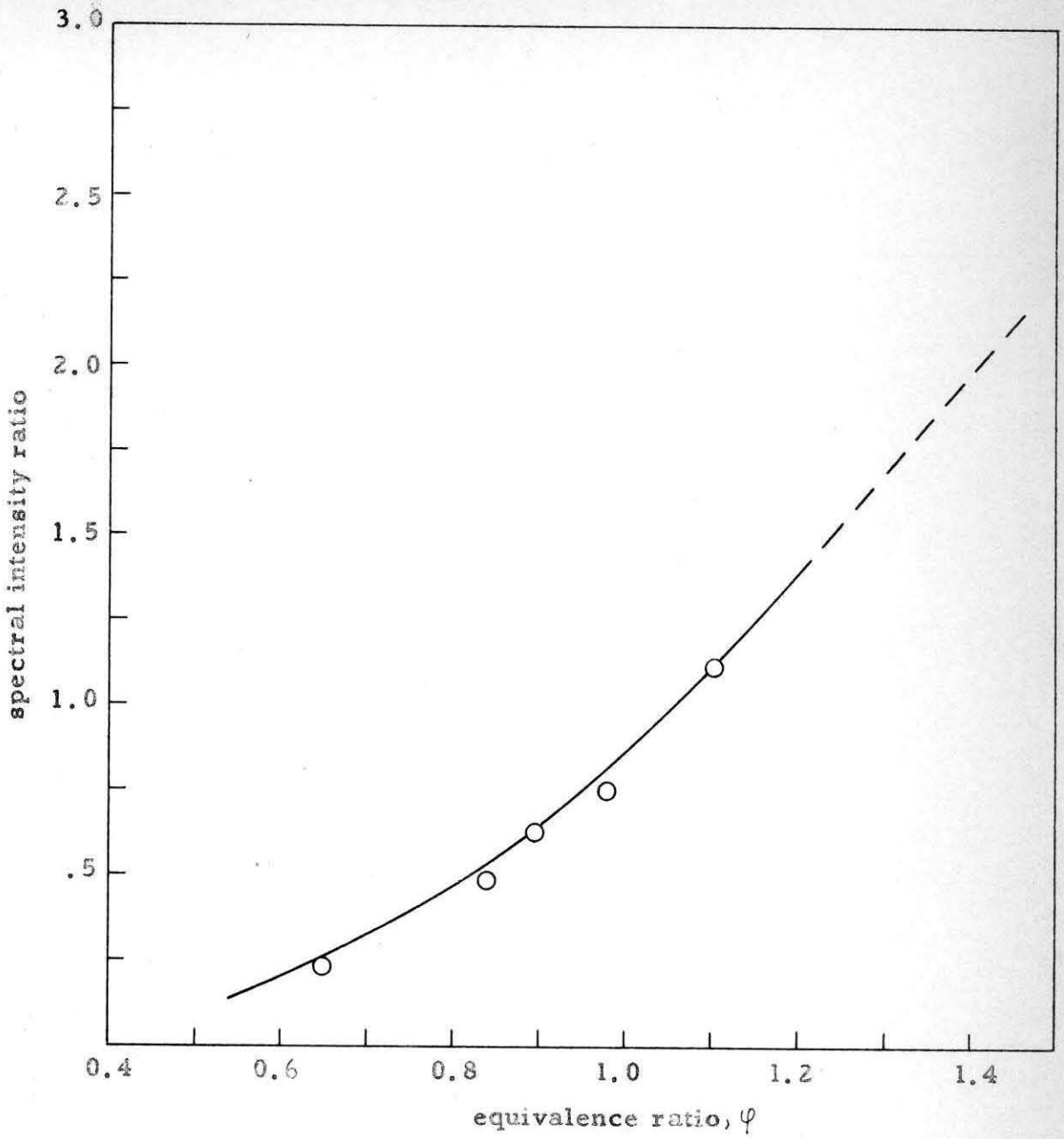

FIGURE 22. SPECTRAL INTENSITY RATIO AS A FUNCTION OF EQUIVALENCE RATIO FOR THE LINE WITH CENTER AT 5635 Å TO THE LINE WITH CENTER AT 4324 Å.

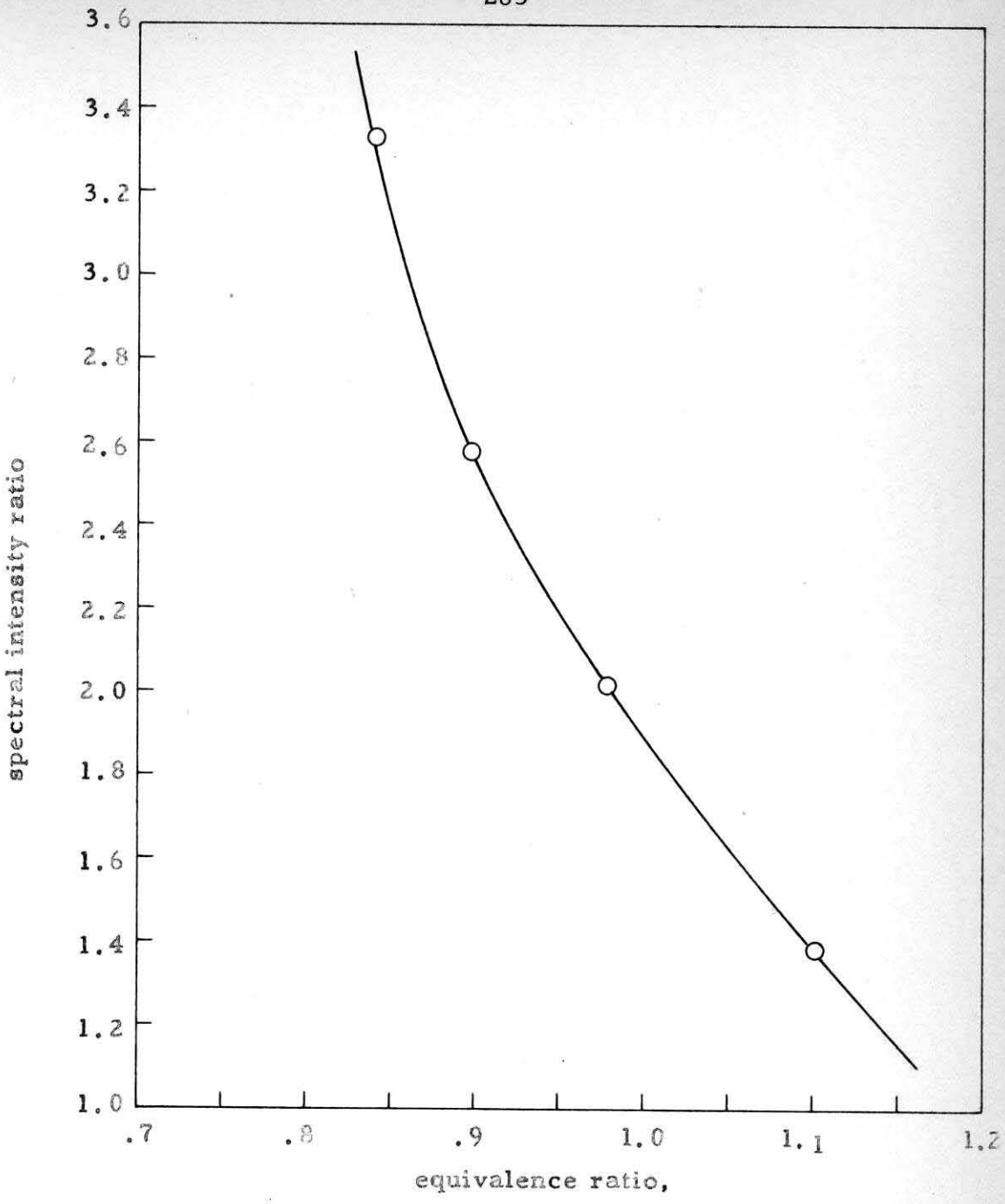

FIGURE 23. SPECTRAL INTENSITY RATIO AS A FUNCTION OF EQUIVALENCE RATIO FOR THE LINE WITH CENTER AT 6191 Å TO THE LINE WITH CENTER AT 4324 Å.

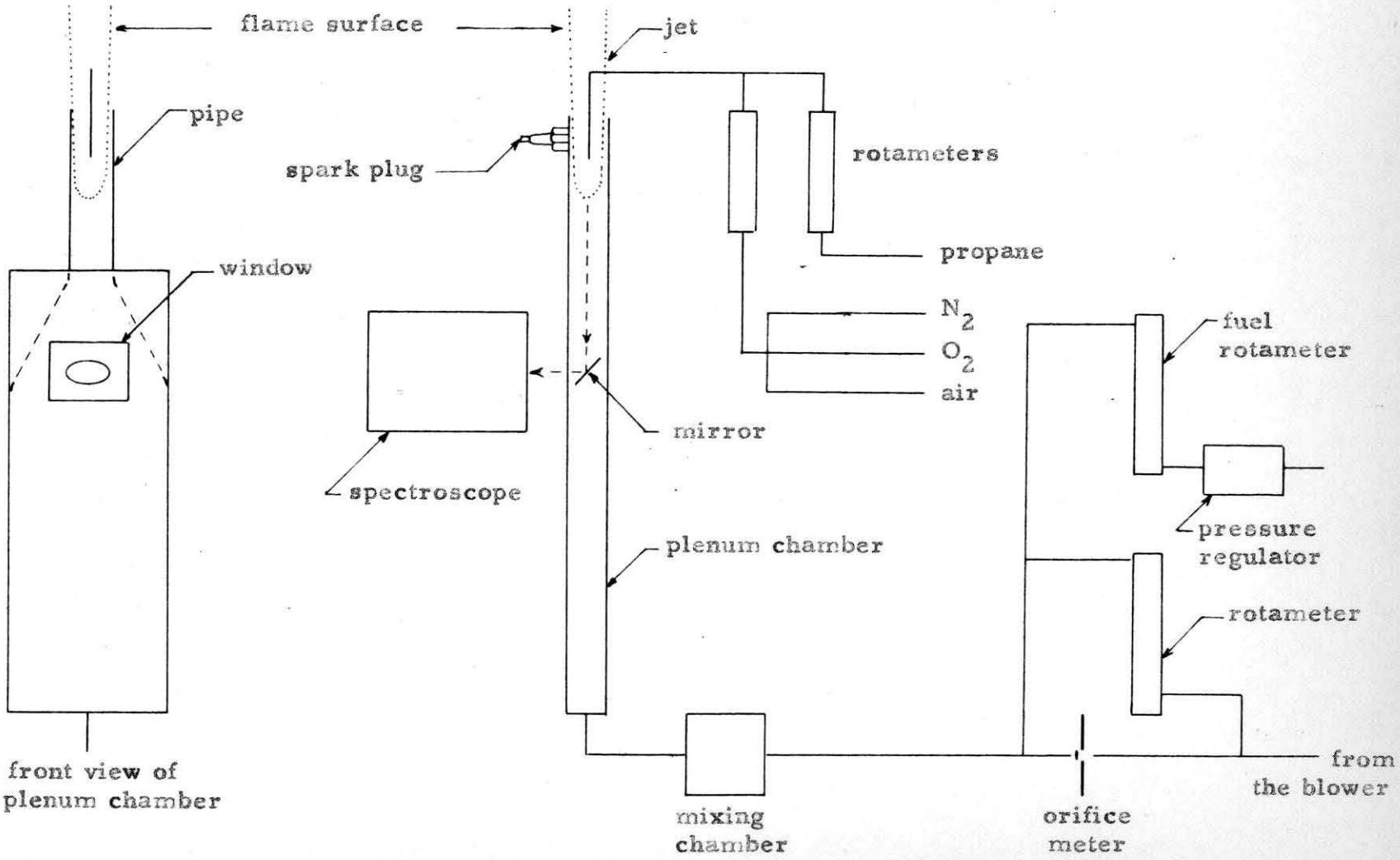

FIGURE 24. SCHEMATIC ILLUSTRATION OF THE APPARATUS USED FOR STUDIES OF A REVERSE-JET STABILIZED FLAME.

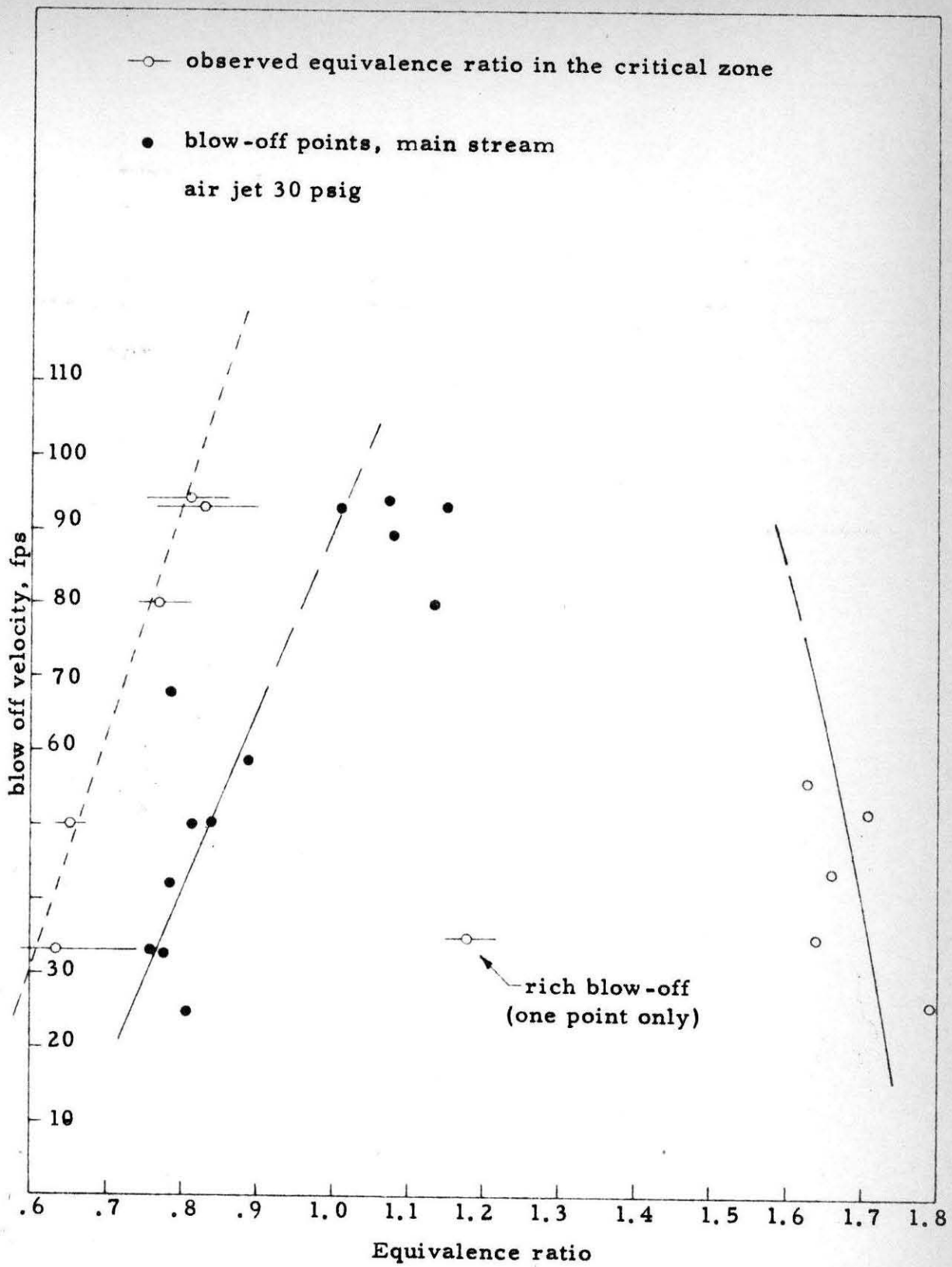

FIGURE 25. OBSERVED EQUIVALENCE RATIO IN THE CRITICAL ZONE AT BLOW-OFF FOR AN AIR JET.

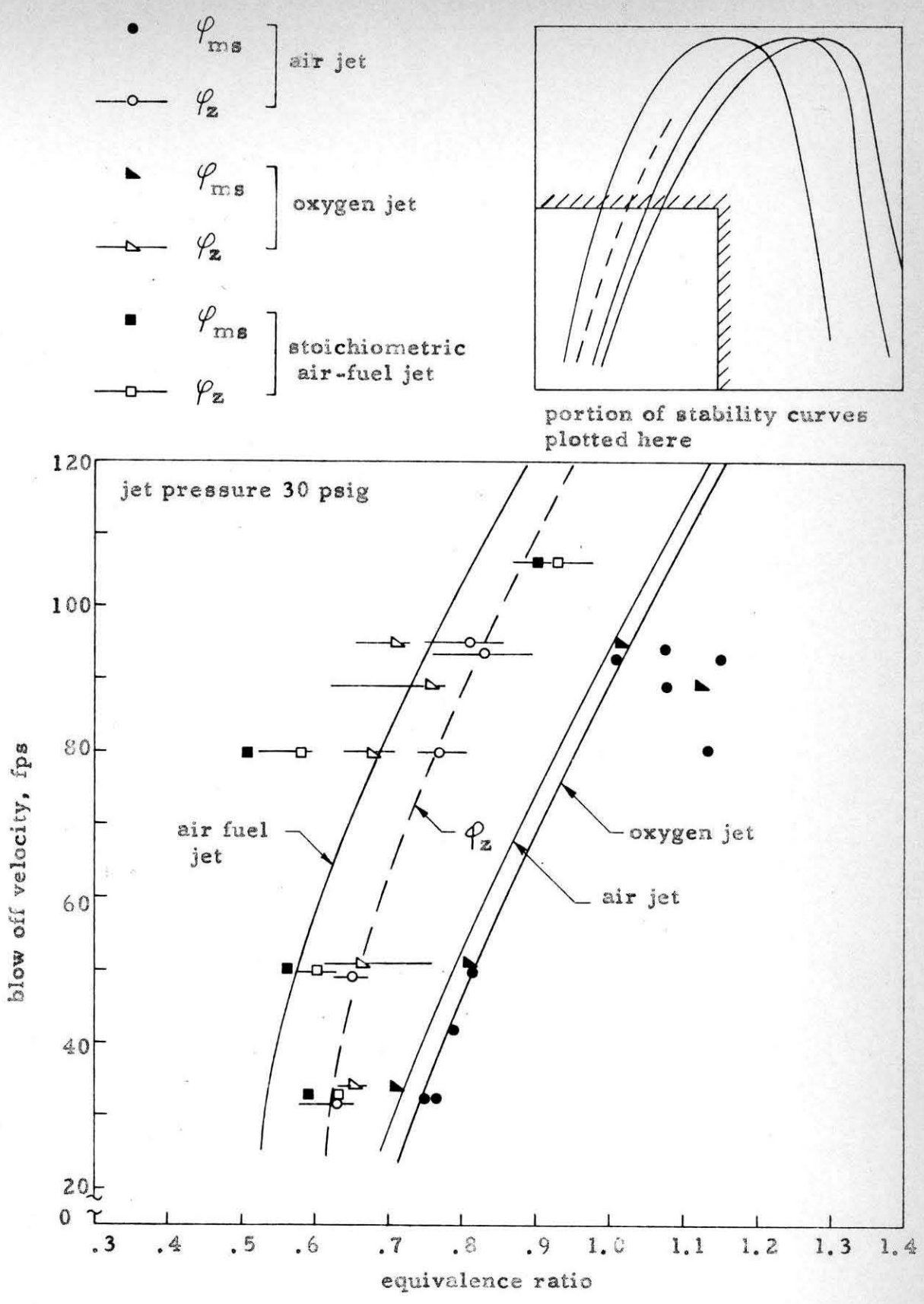

FIGURE 26. BLOW-OFF VELOCITY AS A FUNCTION OF MAIN STREAM AND CRITICAL ZONE EQUIVALENCE RATIOS.

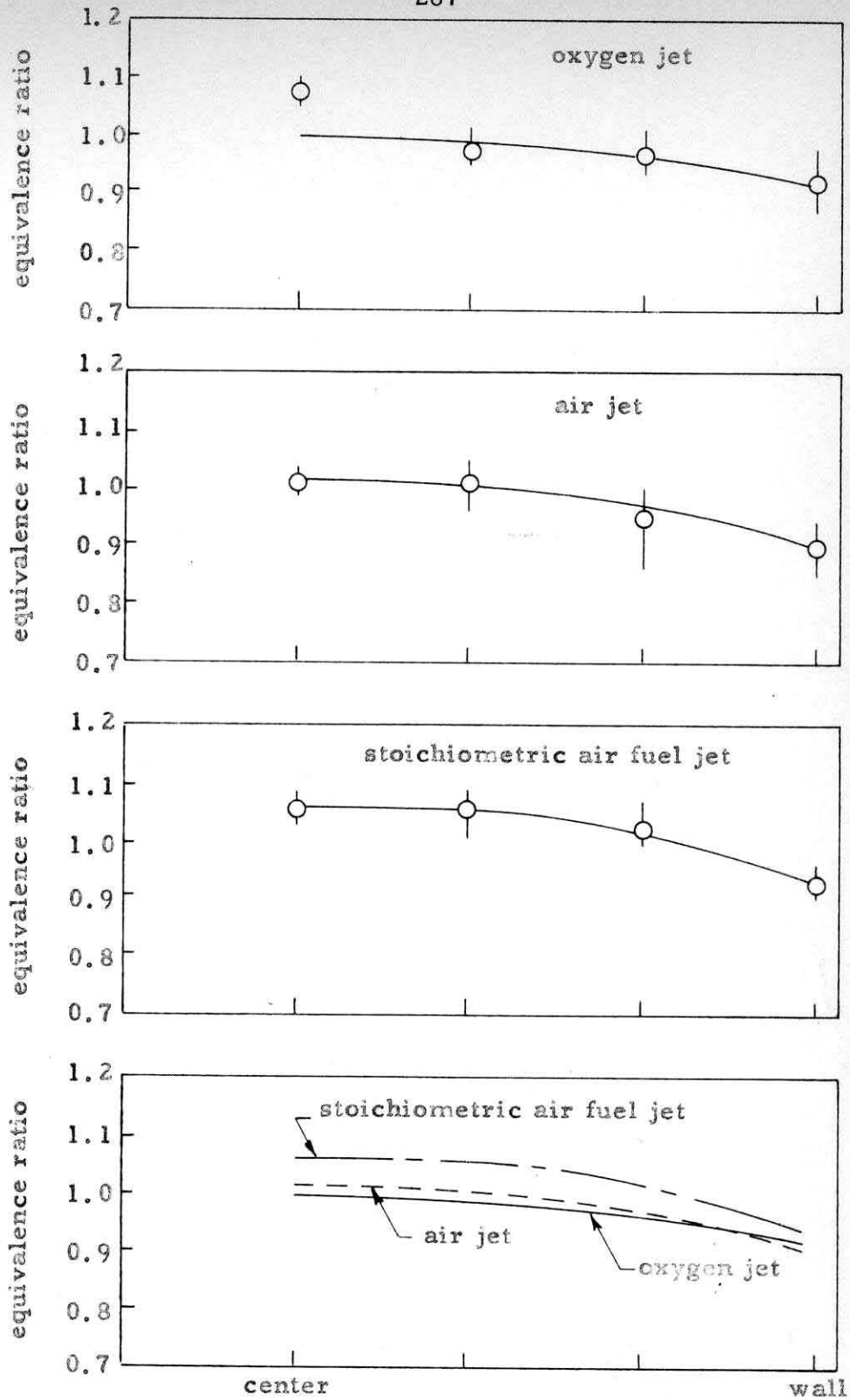

FIGURE 27. LOCAL EQUIVALENCE RATIO AS A FUNCTION OF RADIUS FOR A RICH MAIN STREAM (φ = 1.16) AND VARIOUS JET COMPOSITIONS (VELOCITY: 42 ft/sec, JET PRESSURE: 30 psig).

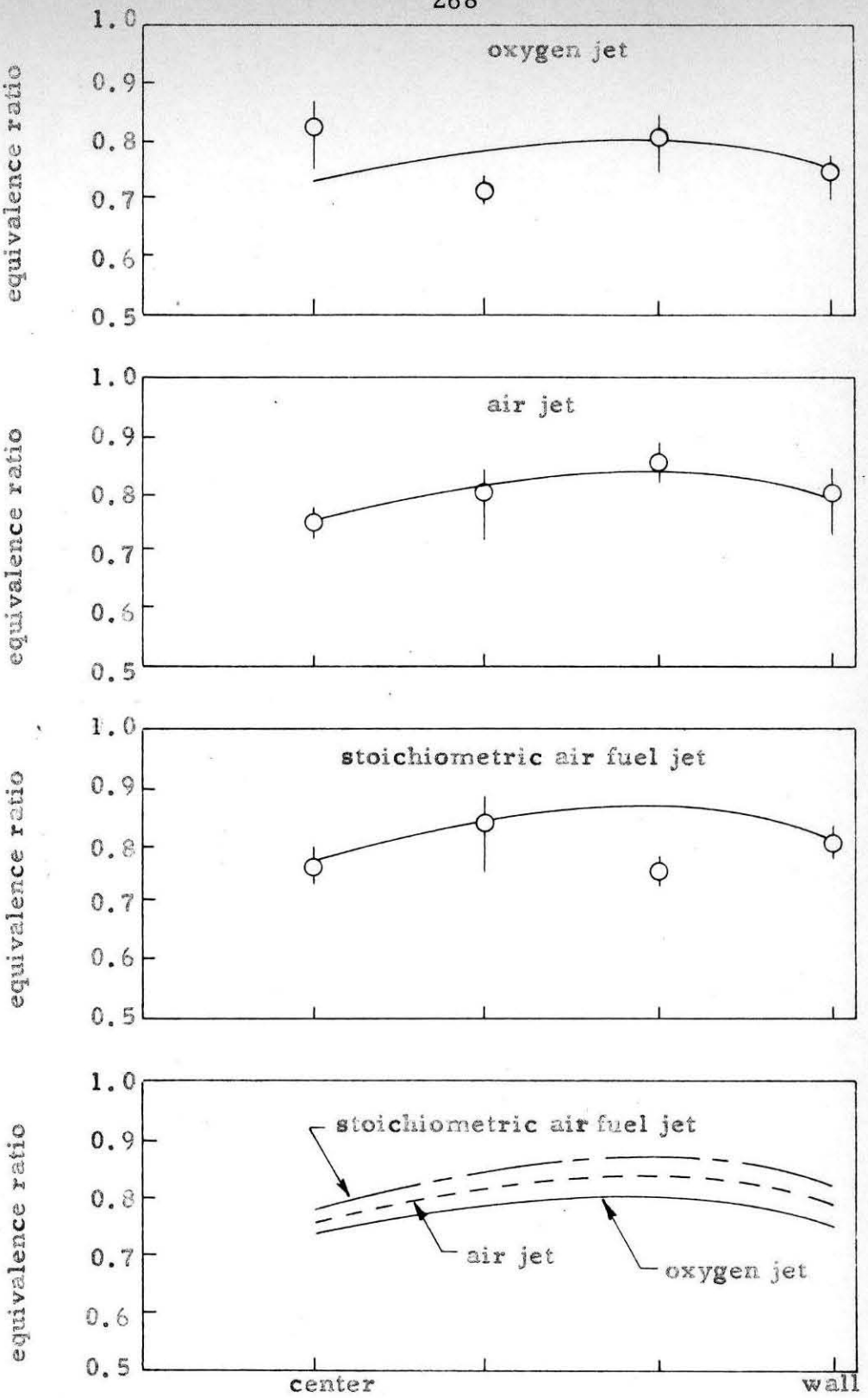

FIGURE 28. LOCAL EQUIVALENCE RATIO AS A FUNCTION OF RADIUS FOR A LEAN MAIN STREAM (φ = 0.92) AND VARIOUS JET COMPOSITIONS (VELOCITY: 42 ft/sec, JET PRESSURE: 30 psig).

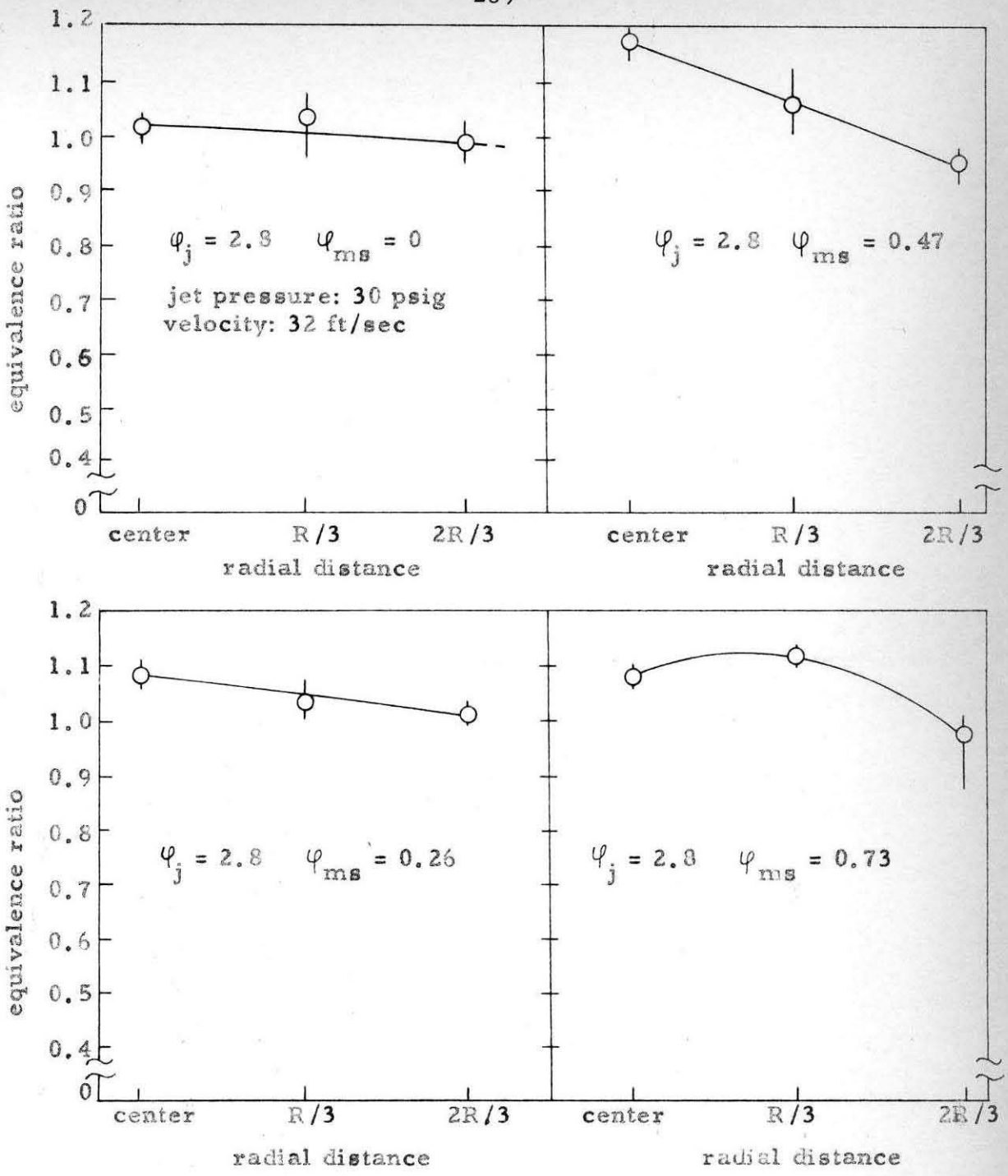

FIGURE 29. LOCAL EQUIVALENCE RATIO IN A PILOT FLAME AS A FUNCTION OF φ_{ms} AND RADIAL DISTANCE.

FIGURES

APPENDIX TO PART I

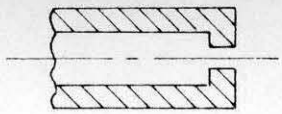

simple orifice

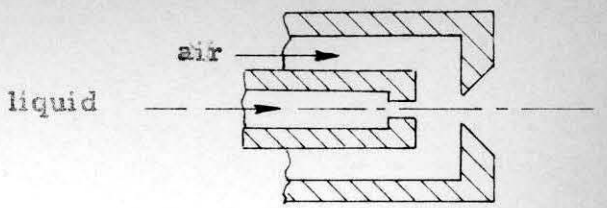

atomizer using secondary fluid

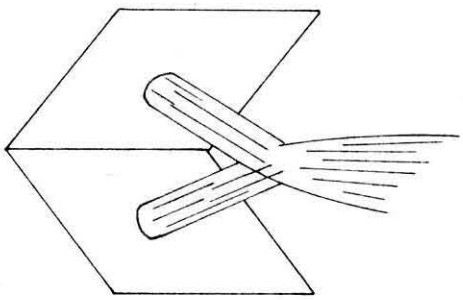

impinging jet

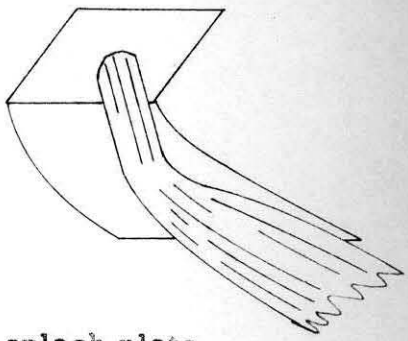

splash plate

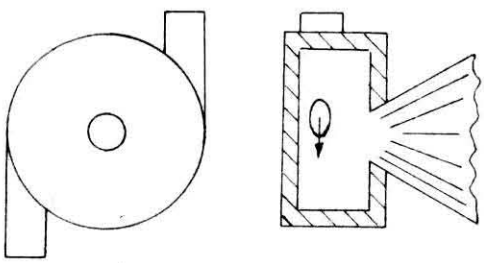

swirl chamber

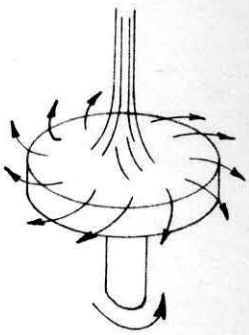

centrifugal atomizer

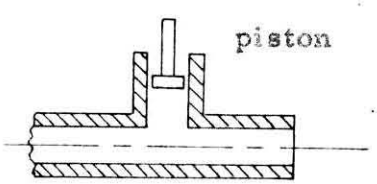

device for producing a train of large drops

FIGURE 1. SCHEMATIC ILLUSTRATIONS OF VARIOUS TYPES OF ATOMIZERS.

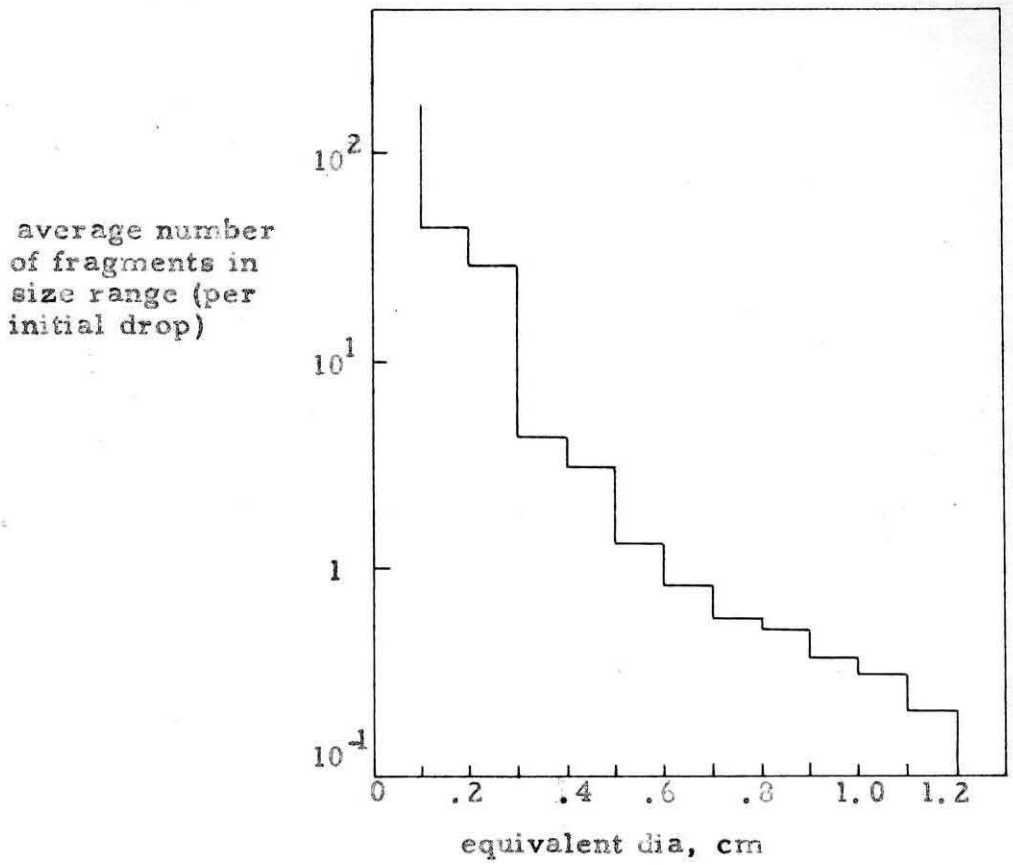

FIGURE 2 . HISTOGRAM SHOWING SIZE DISTRIBUTIONS OF FRAGMENTS. THE FRAGMENTS FROM 5 BREAK-UPS WERE MEASURED, GROUPED ACCORDING TO SIZE, AND ADJUSTED TO A PER DROP BASIS (UN-PHOTOGRAPHED SMALL DROPS ACCOUNT FOR 5-10% OF MASS).

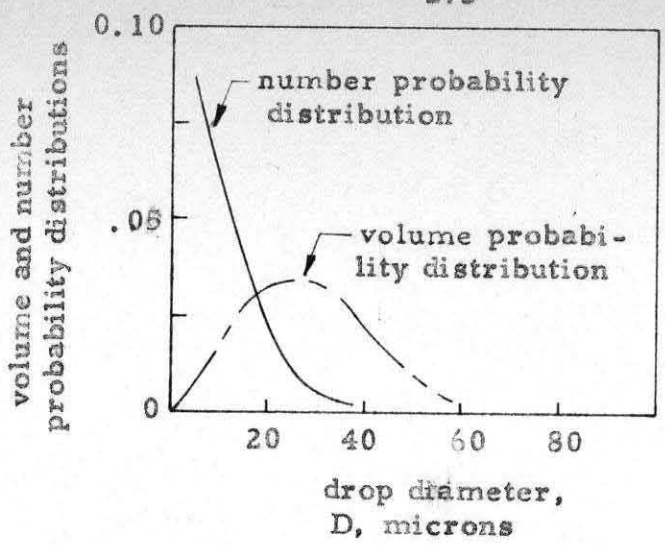

FIGURE 3 . PROBABILITY DISTRIBUTION FUNCTION FOR DROP SIZES.

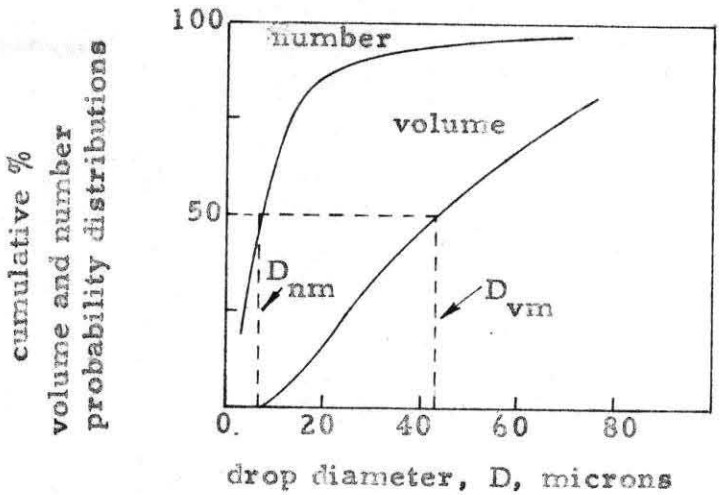

FIGURE 4 . CUMULATIVE FORM OF REPRESENTATION OF DROP SIZES.

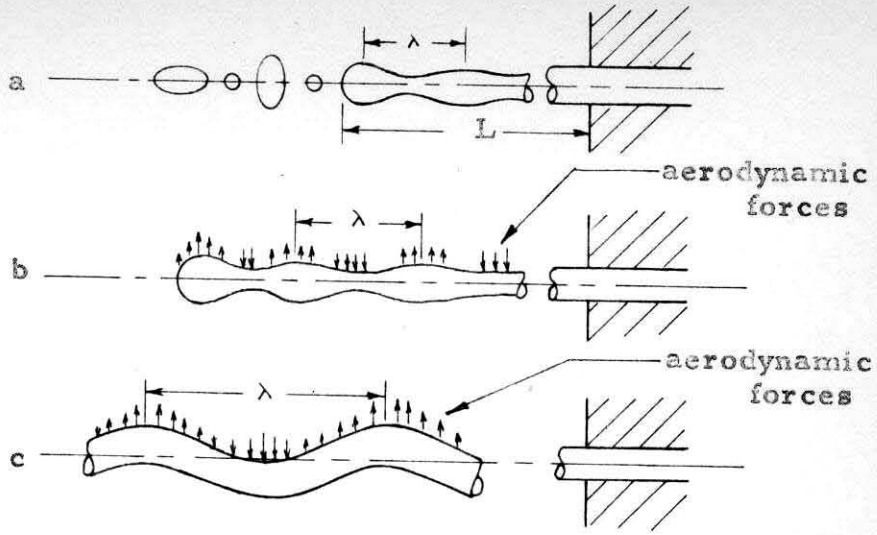

(a, drop formation without air influence; b, drop formation with air influence; c, wave formation through air influence).

FIGURE 5 . DISINTEGRATION OF A LIQUID JET.

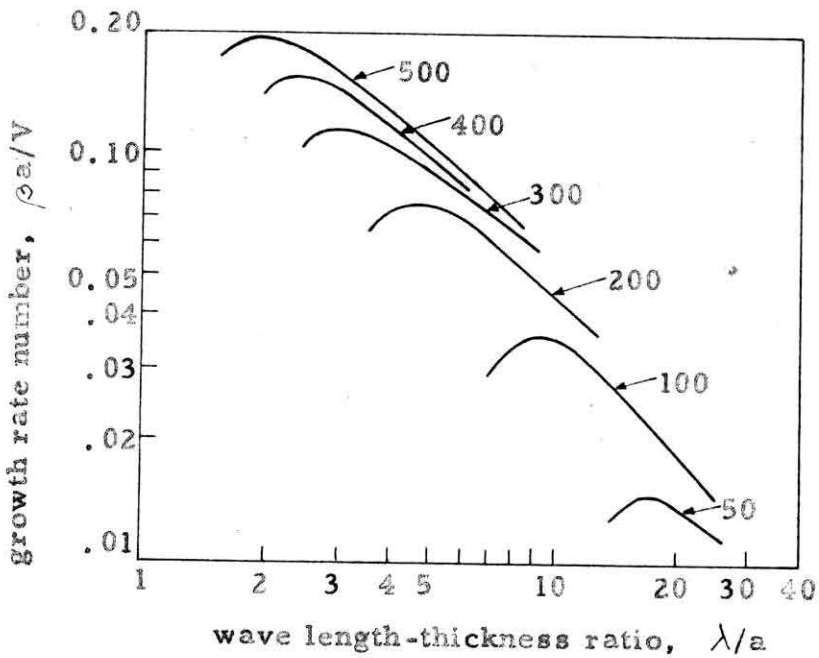

Ratio of density of ambient fluid to sprayed fluid is 0.01. Weber numbers are given for each curve.

FIGURE 6 . EFFECT OF WEBER NUMBER ON GROWTH RATE.

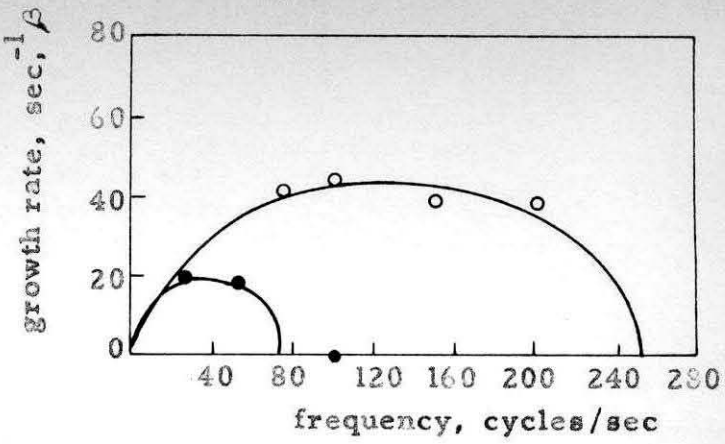

FIGURE 7 . COMPARISON OF THEORY AND EXPERIMENTS; GROWTH RATE AS A FUNCTION OF FREQUENCY.

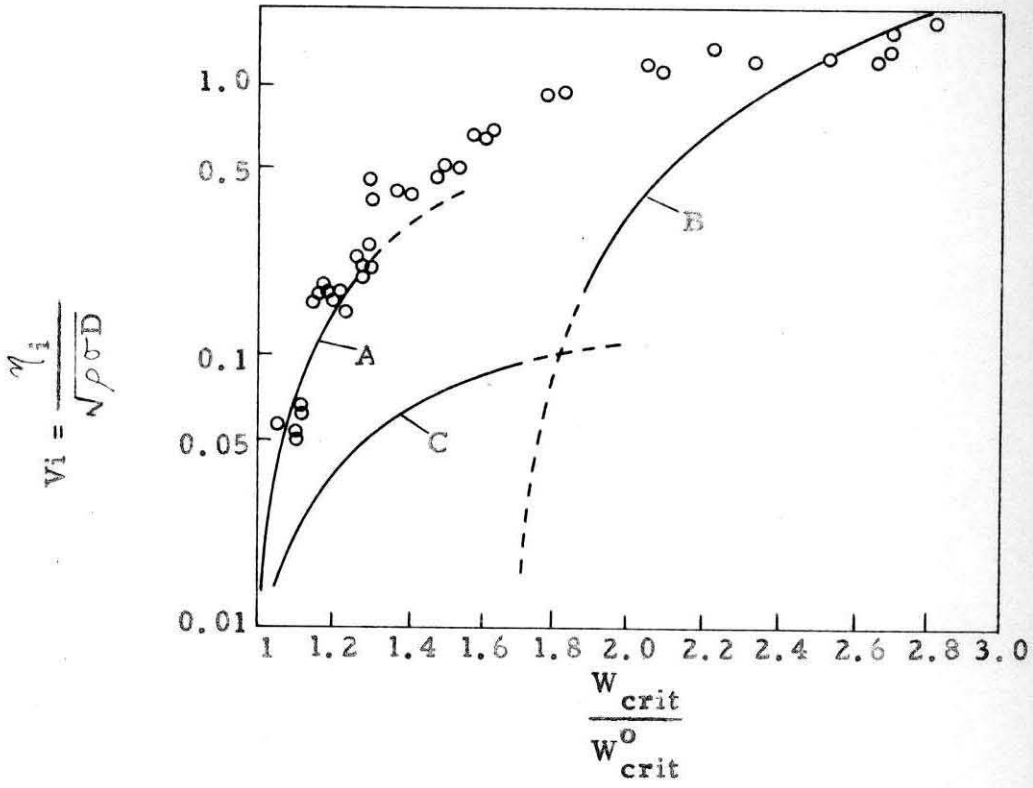

A theoretical curve for slight viscosity $Vi \leq 0.5$
B theoretical curve for great viscosity $Vi \geq 0.5$
C theoretical curve by Masugi

FIGURE 8 . EFFECT OF VISCOSITY ON W_{crit} FOR A DROP SUDDENLY EXPOSED TO AN AIR STREAM.

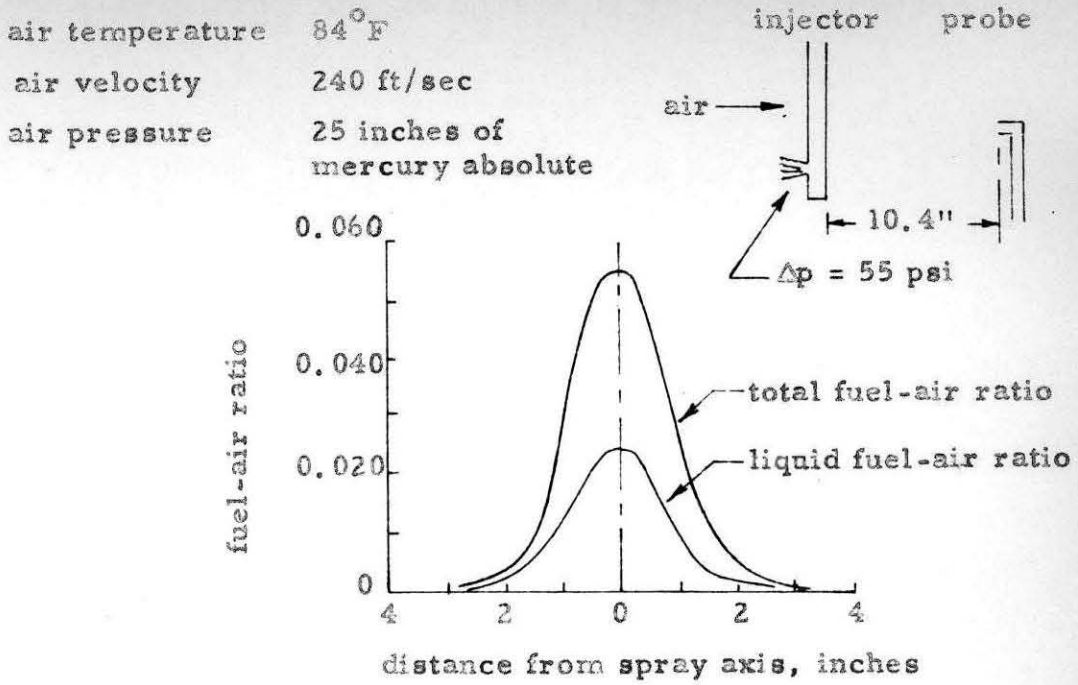

FIGURE 9. TOTAL AND LIQUID FUEL DISTRIBUTION DOWNSTREAM OF AN ISO-OCTANE SPRAY IN A DUCT.

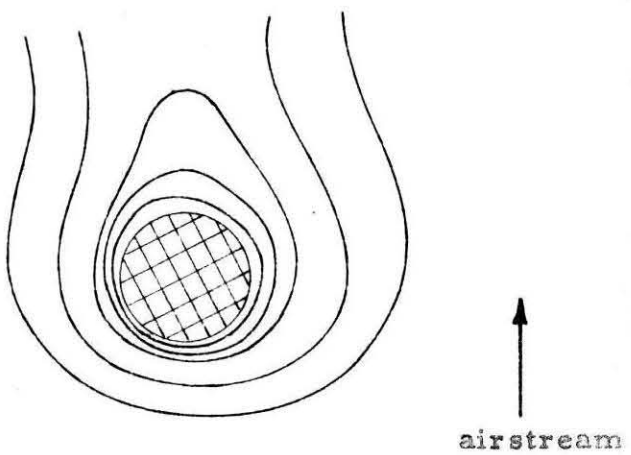

FIGURE 10. ISOTHERMS SURROUNDING AN EVAPORATING DROP IN A FORCED CONVECTION EXPERIMENT.

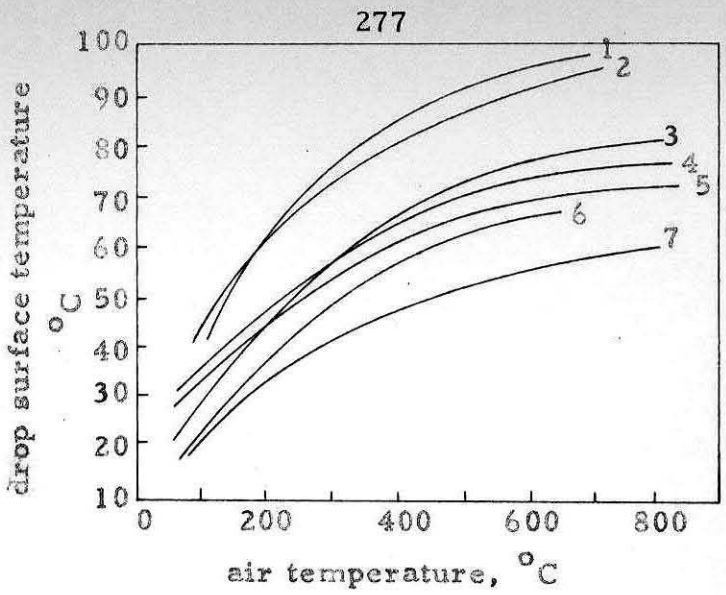

Copper-constantan thermocouples. Drop diameter 1 to 2 mm.

1. n-heptane
2. isooctane
3. benzene
4. water
5. ethyl alcohol
6. n-hexane
7. methyl alcohol

FIGURE 11. EXPERIMENTALLY MEASURED DROP SURFACE TEMPERATURES.

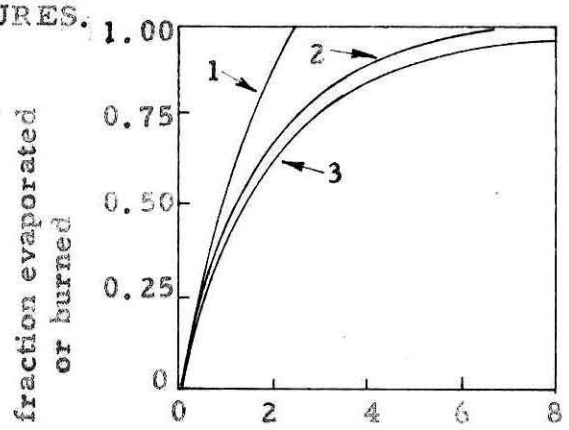

1. A model for a spray with all drops of size D_{31}.
2. A model for a spray with drops of constant size but decreasing number.
3. A spray with drop size distribution represented by the Nukiyama-Tanasawa distribution.

Note that the curves are drawn for fraction evaporated or burned. This applies to a process where drop diameter at any time is given by

$$D^2 = D_o^2 - Kt$$

FIGURE 12. THE FRACTION OF SPRAY EVAPORATED (OR BURNT) AS A FUNCTION OF TIME.

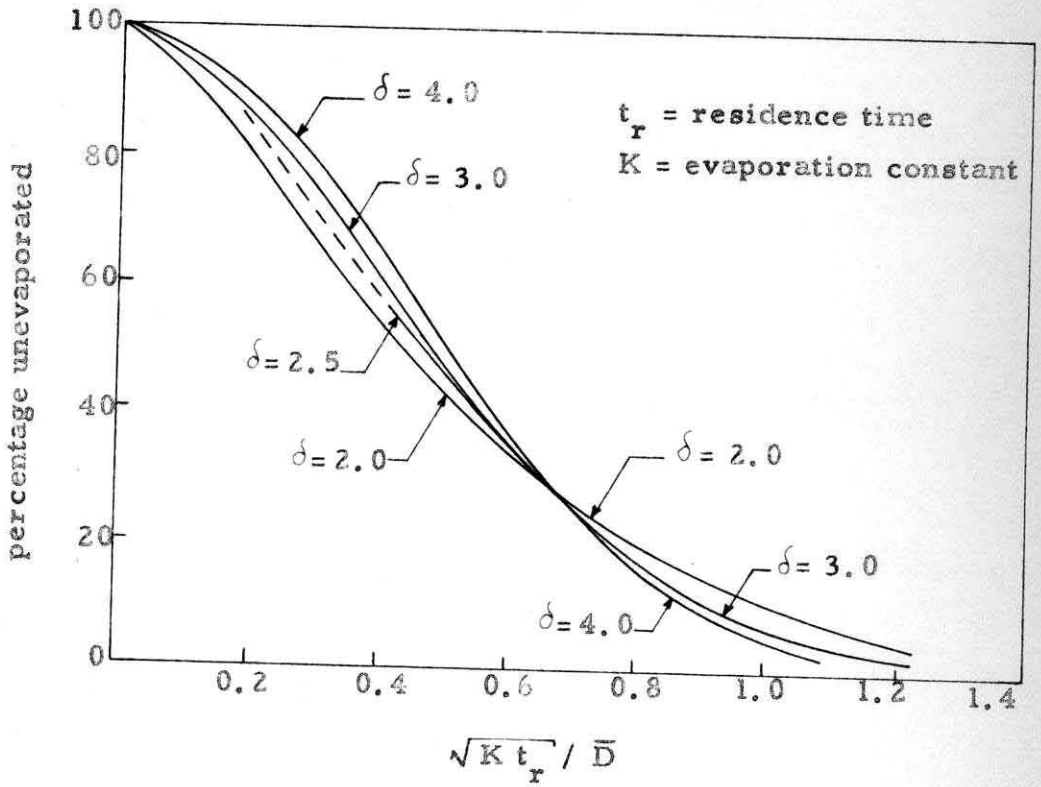

FIGURE 13. PERCENTAGE OF UNEVAPORATED (OR UNBURNT) FUEL AS A FUNCTION OF $\sqrt{K\,t_r}/\bar{D}$ AND δ FOR SPRAYS OBEYING THE ROSIN-RAMMLER DISTRIBUTION LAW (AFTER PROBERT, REF. 14).

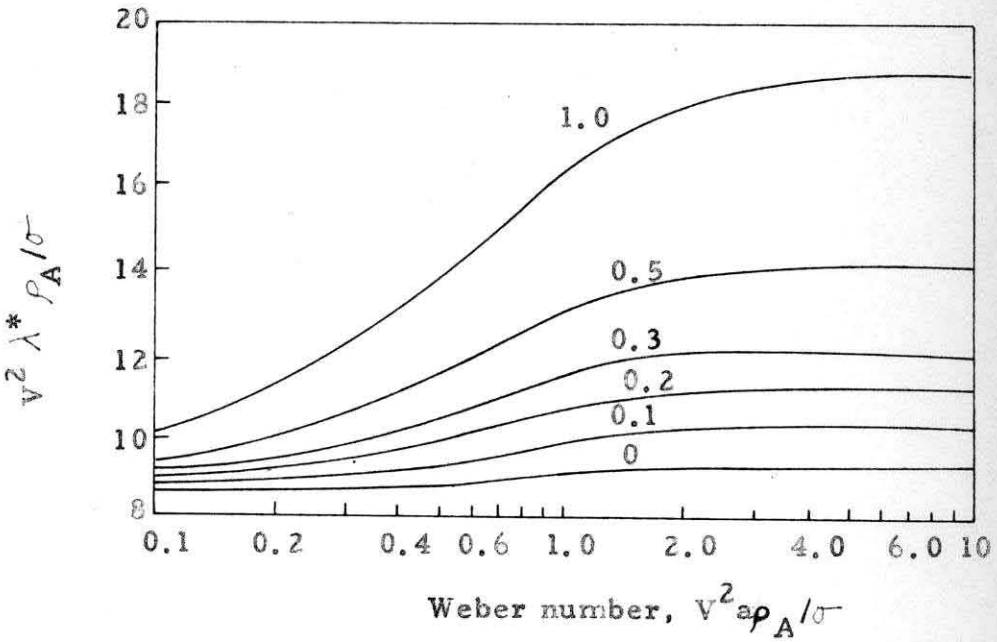

The curves are drawn for density ratios from 0 to 1.0.

FIGURE 14. EFFECT OF SHEET THICKNESS ON THE WAVE LENGTH CORRESPONDING TO MAXIMUM GROWTH RATE.

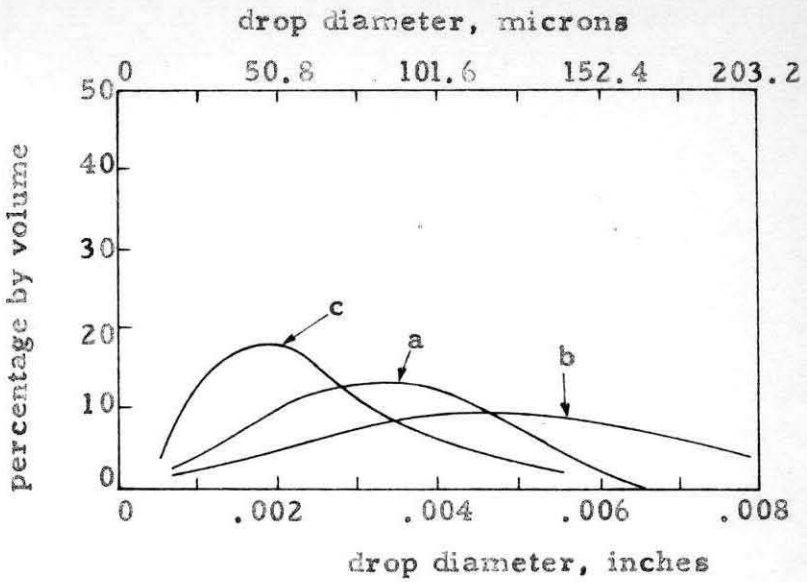

Test conditions were as follows:

effective injection pressure	1730 psi
impingement angle	74°
liquid sprayed	diesel fuel
chamber pressure (approx.)	12 atmospheres

Curves a and b apply to impinging jets of orifice diameter 0.028 inches. Both curves a and b were obtained under the same conditions except the weight of the valve stem, which prevents dribble, varied from 7.07g for curve a to 26.51g for curve b. Curve c applies to a single-jet atomizer with an orifice diameter of 0.030 inches.

Curve	Sauter mean diameter, microns
a	63.5
b	87.6
c	46.0

FIGURE 15. ATOMIZATION CURVES FOR INTERMITTENT SPRAYS FROM IMPINGING JETS AND FROM A SINGLE JET.

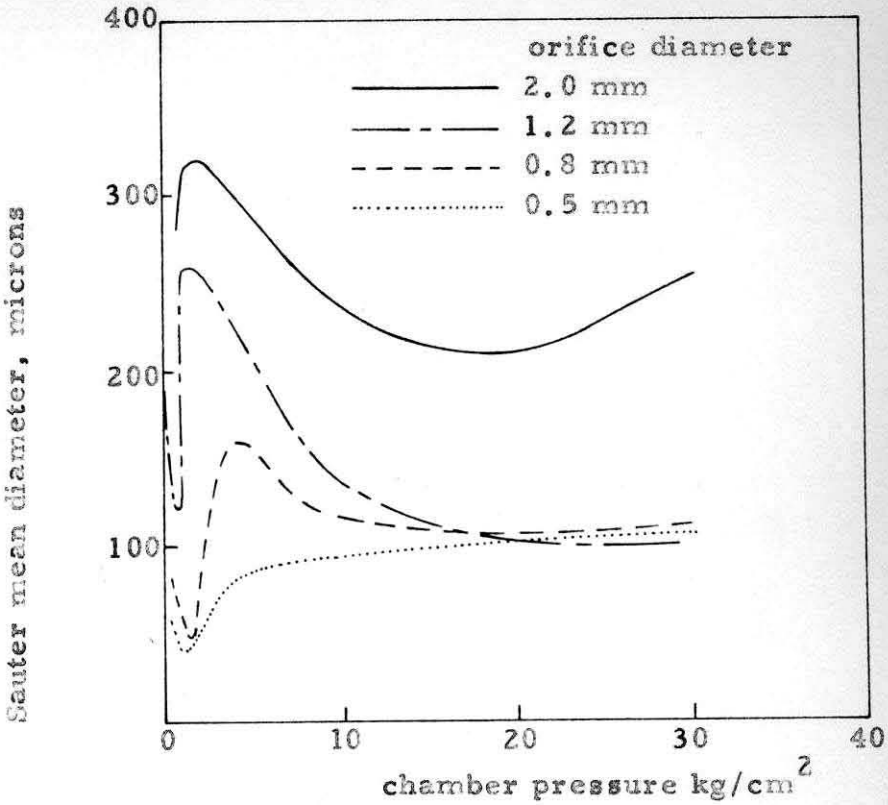

Conditions of the test were:

fluid	kerosene
fluid density at 20°C	0.791 g/cm²
impingement angle, 2θ	55°
injection pressure, Δp	6 kg/cm²
temperature, T	20°C

FIGURE 16. THE EFFECT OF CHANGES IN ORIFICE DIAMETER AND CHAMBER PRESSURE ON SAUTER MEAN DIAMETER.

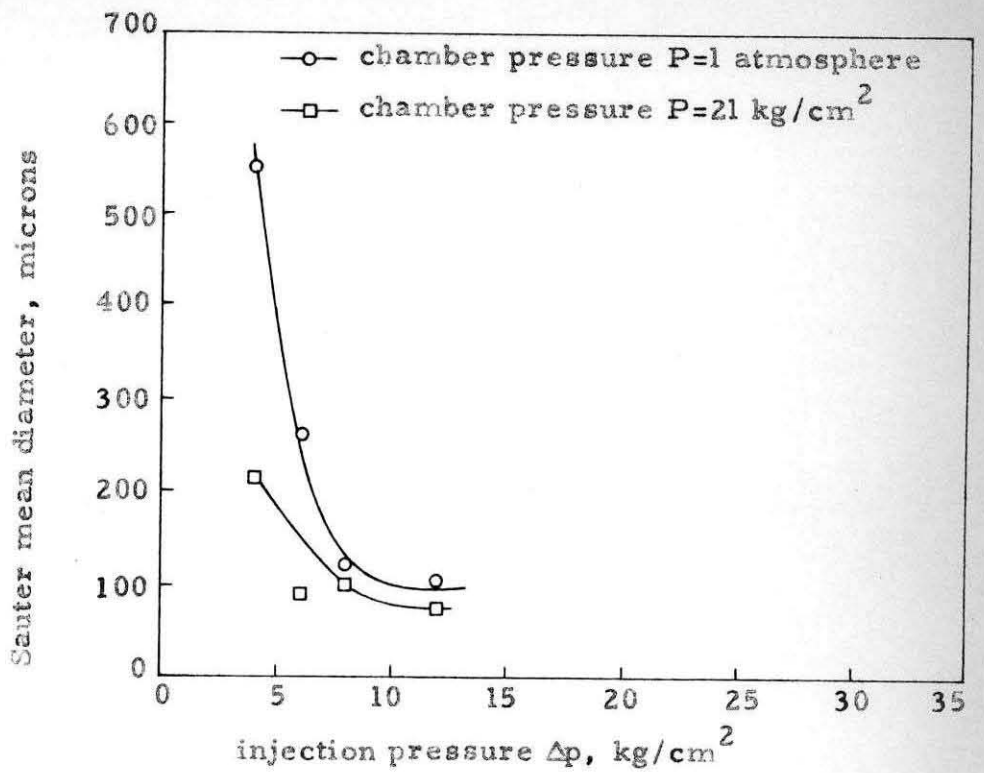

Conditions of the test were:

fluid	kerosene
fluid density at 20°C	0.791 g/cm^2
impingement angle, 2 θ	55°
orifice diameter, h	1.2 mm
temperature, T	20°C

FIGURE 17. THE EFFECT OF INJECTION PRESSURE ON SAUTER MEAN DIAMETER.

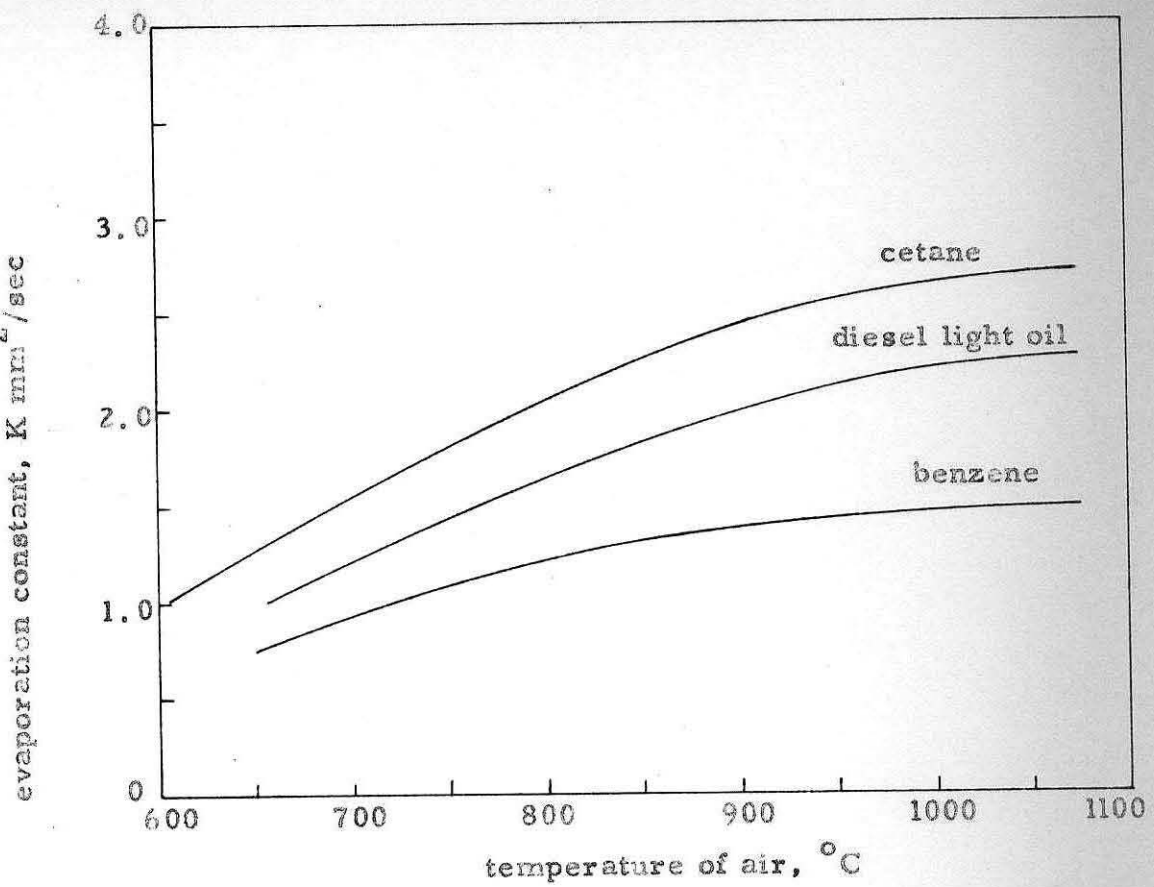

FIGURE 18. EFFECT OF AMBIENT AIR TEMPERATURE ON THE EVAPORATION CONSTANT, K

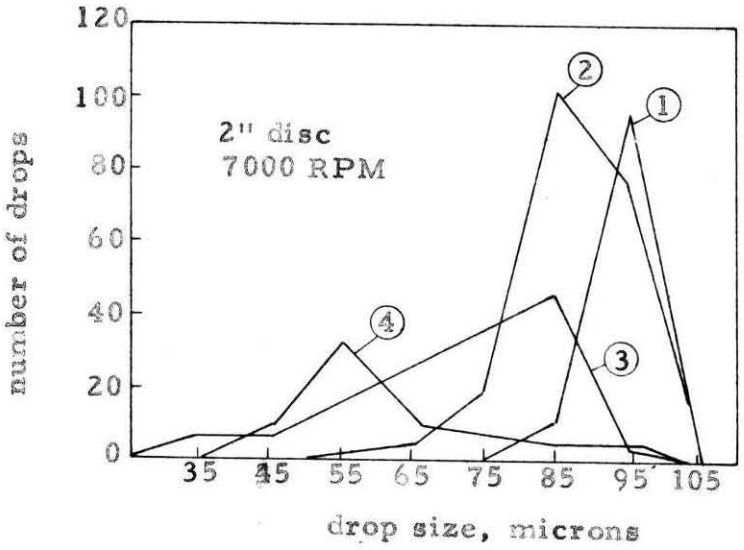

Curve number	Zones*	Number of drops	Mean diameter	Standard deviation
1	0-3	107	94.1	2.91
2	4-7	199	87.9	7.35
3	8-11	145	72.4	14.2
4	12-15	68	61.3	13.4

* The flame region was divided into 20 zones normal to the direction of drop motion. Each zone was 0.083 inches wide. The larger the zone number the farther the drops have traveled into the flame region.

FIGURE 19. DISTRIBUTION OF DROP SIZES IN THE COMBUSTION ZONES FOR KEROSENE (DECANE TO HEXADECANE MIXTURE) DROPS.

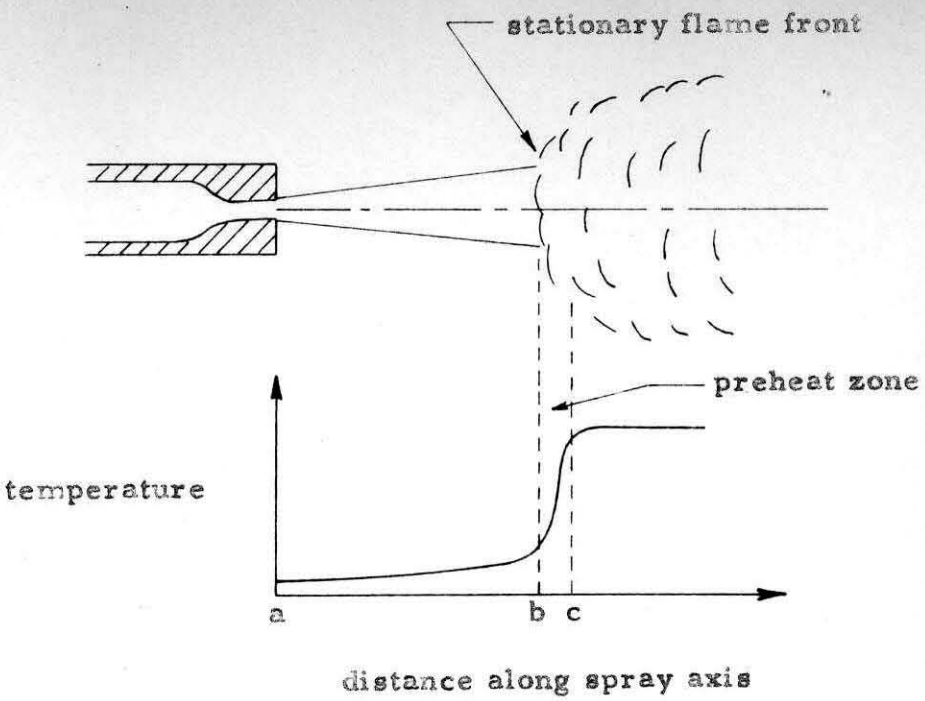

FIGURE 20. A QUALITATIVE REPRESENTATION OF THE TEMPERATURE WHICH DROPS EXPERIENCE IN A BURNING SPRAY.

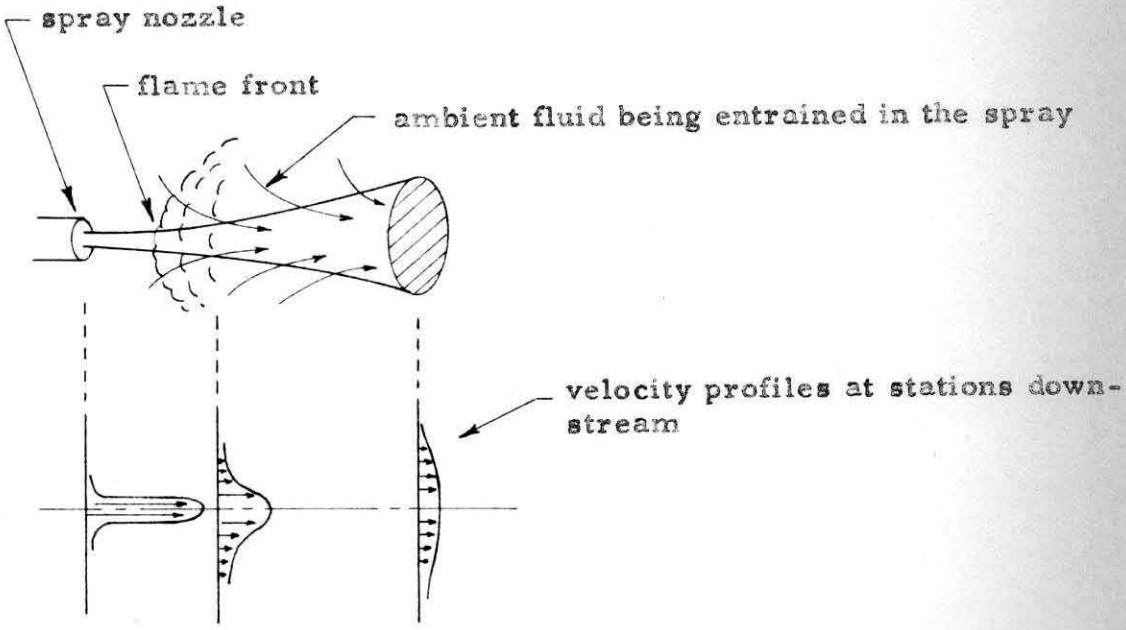

FIGURE 21. ENTRAINMENT OF THE CHAMBER GASES AND THE RESULTING VELOCITY PROFILES.

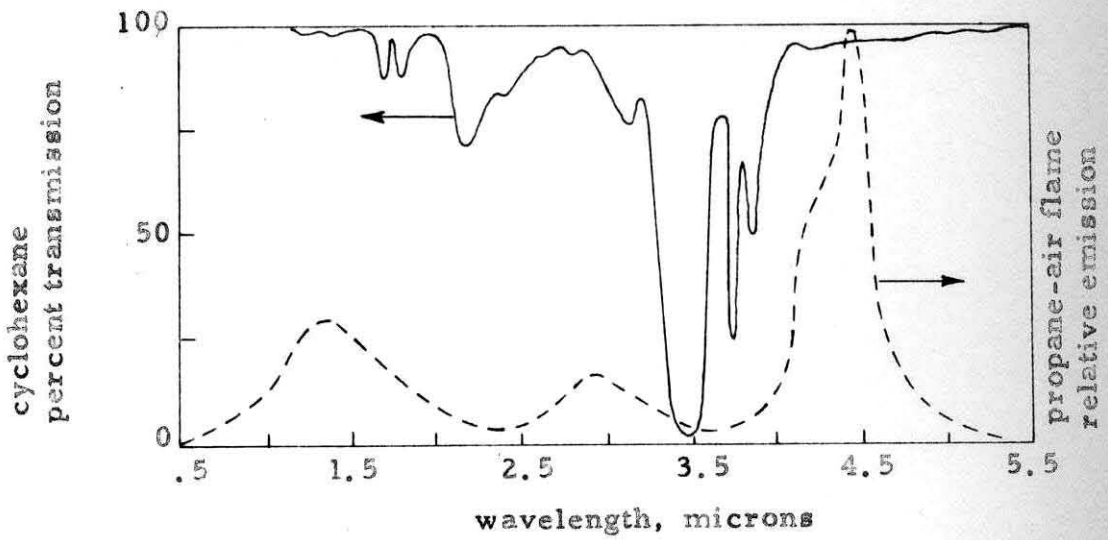

FIGURE 22. THE TRANSMISSION SPECTRUM OF CYCLOHEXANE AND THE EMISSION SPECTRUM OF A LUMINOUS PROPANE-AIR FLAME.

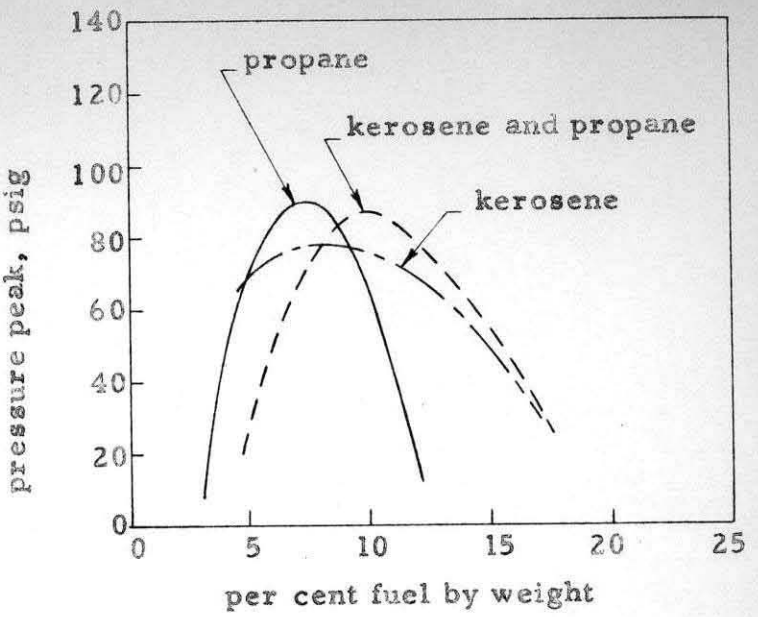

FIGURE 23. MAXIMUM PRESSURE CURVES FOR PROPANE-AIR AND KEROSENE MIST-AIR MIXTURES IN A CONSTANT VOLUME COMBUSTION BOMB.

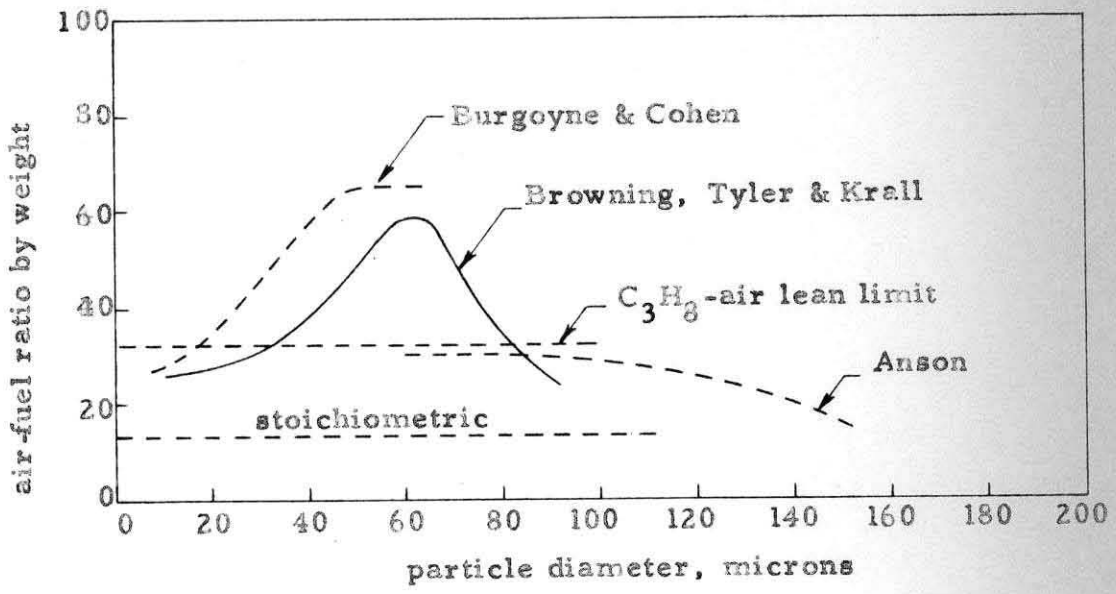

FIGURE 24. LEAN LIMIT AIR-FUEL RATIO AS FUNCTION OF PARTICLE SIZE.

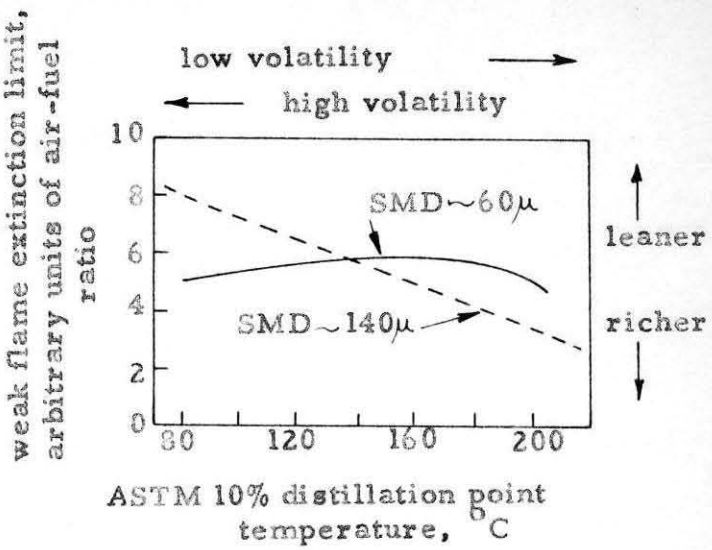

FIGURE 25. WEAK FLAME EXTINCTION LIMIT AS A FUNCTION OF FUEL VOLATILITY FOR FINE AND COARSE SPRAYS.